

**Magnetic Fabrics and Boundary Structure
at the Quetico/Shebandowan Subprovince Boundary,
near Kashabowie, NW Ontario**

by

Robert Nicholas Spark ©

Submitted in partial fulfillment of the
requirements for the degree of
Master of Science

Geology Department
Lakehead University
Thunder Bay, Ontario

April 10, 1990

ProQuest Number: 10611819

All rights reserved

INFORMATION TO ALL USERS

The quality of this reproduction is dependent upon the quality of the copy submitted.

In the unlikely event that the author did not send a complete manuscript and there are missing pages, these will be noted. Also, if material had to be removed, a note will indicate the deletion.



ProQuest 10611819

Published by ProQuest LLC (2017). Copyright of the Dissertation is held by the Author.

All rights reserved.

This work is protected against unauthorized copying under Title 17, United States Code
Microform Edition © ProQuest LLC.

ProQuest LLC.
789 East Eisenhower Parkway
P.O. Box 1346
Ann Arbor, MI 48106 - 1346



National Library
of Canada

Bibliothèque nationale
du Canada

Canadian Theses Service Service des thèses canadiennes

Ottawa, Canada
K1A 0N4

The author has granted an irrevocable non-exclusive licence allowing the National Library of Canada to reproduce, loan, distribute or sell copies of his/her thesis by any means and in any form or format, making this thesis available to interested persons.

L'auteur a accordé une licence irrévocable et non exclusive permettant à la Bibliothèque nationale du Canada de reproduire, prêter, distribuer ou vendre des copies de sa thèse de quelque manière et sous quelque forme que ce soit pour mettre des exemplaires de cette thèse à la disposition des personnes intéressées.

The author retains ownership of the copyright in his/her thesis. Neither the thesis nor substantial extracts from it may be printed or otherwise reproduced without his/her permission.

L'auteur conserve la propriété du droit d'auteur qui protège sa thèse. Ni la thèse ni des extraits substantiels de celle-ci ne doivent être imprimés ou autrement reproduits sans son autorisation.

ISBN 0-315-63190-2

1
ABSTRACT

The Quetico metasedimentary subprovince and the volcanic-plutonic Shebandowan belt to the south meet along an east-west steeply dipping boundary that is believed to have been affected by dextral transpressional deformation. It is also parallel to a steep metamorphic gradient from greenschist facies rocks to the north.

Macroscopic petrofabrics are difficult to observe along the belt to the west of Thunder Bay but magnetic susceptibility fabrics (low-field) are quite consistent. These define a gently plunging extensional fabric parallel to the belt boundary. Within the Kashabowie area, general field observations of subhorizontal stretching (and intersection) lineations, and cleavage directions are in agreement with magnetic susceptibility axis directions. Mineral separation reveals that all samples have multiple sources of magnetic susceptibility, dominated by metamorphic phyllosilicates. Consequently it is not possible to simply quantitatively relate the magnetic fabrics to strain magnitudes although the magnetic fabrics accurately monitor significant kinematic directions. Analyses of strain of low-grade detrital quartz grains, magnetic fabrics and general field observations recognize flattened oblate fabrics. Moreover oblique, subhorizontal lineations favour a transpressive kinematic model with compression normal to the belt boundary. The obliquity between mineral and magnetic lineations seem to indicate dextral transpressive deformation.

ii
ACKNOWLEDGEMENTS

This thesis was supervised by Dr. Graham Borradaile and funded from his NSERC operating grant #A6861. The author was also in receipt of scholarships from the Centre for Northern Studies (Lakehead University) which are gratefully acknowledged. Dr. Borradaile is thanked for introducing the writer to the field area and suggesting the research topic. His patience and unceasing support are greatly appreciated.

The author is grateful to the assistance of the many individuals in this project. Monica Barabonoff is thanked for cheerfully assisting in field work, sample preparation and drilling. Anne Hammond and Reino Viitala are also thanked for the speedy preparation of hundreds of superb thin-sections. Eleanor Jensen is also thanked for conducting the leaching experiments. The author is grateful to Al MacKenzie for instruction in the operation of the scanning electron microscope and for preparation of microphotographs and elemental X-ray maps. Thanks also to Sam Spivak for developing photographs at very short notice. Michelle Luscombe is thanked for helping to prepare this document.

The writer would also like to personally thank Dr. Edgar Froese (GSC) for being a constant source of encouragement and advice. Dr. R.G. Roberts (University of Waterloo) is thanked for inspiring insights into the fields of structural geology. I am eternally grateful for the support and inspiration given to me by Monica Barabonoff and my family. I thank my fellow graduate students for their support and "sense of humour".

TABLE OF CONTENTS

i)	ABSTRACT	i
ii)	ACKNOWLEDGEMENTS	ii
CHAPTER 1 - PREVIOUS STUDIES		
1.1	IntroductionI-1
1.2	Previous Geological MappingI-6
1.3	Recent Structural StudiesI-11
CHAPTER 2 - PRESENT STUDY		
2.1	Field Area Location and AccessII-1
2.2	Purpose and Scope of StudyII-5
2.3	Method of Investigation	
2.3.1	Field MethodII-6
2.3.2	Laboratory TechniquesII-7
CHAPTER 3 - GENERAL LITHOLOGICAL UNITS AND MINERALOGY		
3.1	Introduction and Geochronological RelationshipsIII-1
3.2	Metavolcanic LithologyIII-6
3.2.1	Mafic MetavolcanicsIII-6
3.2.2	Felsic MetavolcanicsIII-16
3.3	Metasediment LithologyIII-21
3.3.1	Clastic Metasediments and SchistsIII-23
3.3.2	MigmatitesIII-37
3.3.3	Granitic IntrusivesIII-41
3.4	Sedimentary Depositional EnvironmentIII-42
3.5	Regional MetamorphismIII-45
CHAPTER 4 - STRUCTURAL FIELD OBSERVATIONS		
4.1	Primary [S0] Bedding SurfacesIV-2
4.2	[S1] Cleavage SurfacesIV-2
4.3	[L1] Mineral LineationsIV-6
4.4	[S2] Late Shearing and KinkingIV-6
4.5	Bedding-Cleavage RelationshipsIV-10
4.5.1	Local Younging DirectionsIV-12
4.5.2	Structural Facing DirectionsIV-14
CHAPTER 5 - MAGNETIC SUSCEPTIBILITY ANISOTROPY (MSA)		
5.1	IntroductionV-1
5.2	Magnetic MineralogyV-4
5.2.1	Diamagnetic MineralsV-5
5.2.2	Paramagnetic MineralsV-5
5.2.3	Ferrimagnetic MineralsV-7
5.3	Magnetic Fabrics	
5.3.1	Magnetic Susceptibility Tensors and EllipsoidsV-9
5.3.2	Magnetic Fabrics and their RepresentationsV-10
5.4	Determination of Magnetic SusceptibilityV-15

5.5	Factors Controlling MSAV-16
5.5.1	Magnetocrystalline Anisotropy of Magnetic GrainsV-16
5.5.2	Shape Anisotropy of Magnetic GrainsV-18
5.5.3	Preferred Orientation of Magnetic Grains.	V-20
5.5.4	Particulate Flow.V-22
5.5.5	Effects of the MatrixV-24
 CHAPTER 6 - MSA AND METAMORPHIC DEFORMATION		
6.1	Introduction.VI-1
6.2	Re-orientation Due to Strain.VI-7
6.3	Preferred Crystallographic GrowthVI-8
6.4	Correlation between Principal Magnetic Susceptibility Directions and Principal Strain Directions.VI-10
6.5	Problems with MSA Quantitative Strain Estimates .	.VI-12
 CHAPTER 7 - MAGNETIC SUSCEPTIBILITY FABRICS OF THE STUDY AREA		
7.1	Magnetic MineralogyVII-1
7.1.1	Mineralogical Contributions to Bulk Magnetic SusceptibilityVII-3
7.1.2	Leaching Experiments.VII-10
7.1.3	Scanning Electron Microprobe X-ray Maps	.VII-12
7.1.4	Bulk Susceptibility In-situ Survey.VII-20
7.2	MSA Results	
7.2.1	Analytical Methods.VII-23
7.2.2	Principal Magnetic Susceptibility Directions.VII-26
7.2.3	Flinn Diagram Fabric AnalysesVII-35
7.2.4	Jelinek Plot Fabric Analyses.VII-38
7.3	Magnetic Fabric and Field Structure Correlation .	.VII-40
 CHAPTER 8 - STRAIN ANALYSES		
8.1	Rf/ ϕ DataVIII-2
8.2	Statistical Determination of Strain (Rs).VIII-9
8.2.1	Arithmetic, Geometric, and Harmonic Mean.	VIII-11
8.2.2	Robin's Analysis.VIII-13
8.2.3	Linearization Method.VIII-18
8.2.4	Comparison of Rs Estimation Techniques. .	.VIII-19
8.3	Strain/MSA Correlation.VIII-26
 CHAPTER 9 - TECTONIC IMPLICATIONS		
 CHAPTER 10 - SUMMARY.		
 REFERENCES		
 APPENDICES		
I	MSA Data	
II	Field S and L Data	
III	Semi-Quantitative Microprobe Magnetic Mineralogy Data	
V	Strain Results from Digitized Quartz Grains	

TABLE OF FIGURES

Figure 1-1 - Subprovinces of the Superior Province.I-3
Figure 1-2 - Location Map: Previous Work and Thesis Area.I-7
Figure 2-1 - Thesis study area (Quetico/Shebandowan Boundary)II-4
Figure 3-1 - Geochronological ChartIII-5
Figure 3-2 - Metavolcanic Outcrop Location Map.III-7
Figure 3-3 - Metavolcanic Outcrop Lithology MapIII-8
Figures 3-4a,b - Pillow Lava Photographs.III-13
Figures 3-4c - Pillow Lava Photographs.III-14
Figure 3-5 - Felsic Agglomerate Photograph.III-20
Figure 3-6 - Metasediment Outcrop Location Map.III-22
Figure 3-7 - Metasediment Outcrop Lithology MapIII-24
Figures 3-8a,b - Clastic Sediment Classification DiagramsIII-25
Figures 3-9a - Graded Bedding PhotographsIII-27
Figures 3-9b - Graded Bedding PhotographsIII-28
Figures 3-10a - Bedding/Cleavage Photographs.III-30
Figures 3-10b - Bedding/Cleavage Photographs.III-31
Figure 3-11 - Fishmouth Boudinage Photograph.III-33
Figure 3-12 - Paragneiss Segregation Banding PhotographIII-36
Figure 3-13 - Boudinaged and Rotated Quartz Vein PhotographIII-38
Figure 3-14 - Divisions within the Bouma Turbidite SequenceIII-44
Figure 3-15 - Metamorphic Isograd MapIII-46
Figure 4-1 - Bedding [S0] Stereonets.IV-3
Figure 4-2 - Cleavage [S1] StereonetsIV-5
Figure 4-3 - Lineation [L1] Stereonets.IV-7
Figure 4-4 - Kink [S2] StereonetsIV-9
Figure 4-5 - Pillow Tops Determination MethodIV-13
Figure 4-6 - Structural Facing Theory Diagrams.IV-15
Figure 4-7 - Structural Facing Map.IV-17
Figure 5-1 - Electron Spins in Magnetized MaterialsV-8
Figure 5-2 - MSA Ellipsoid Diagram.V-11
Figure 5-3 - The Flinn Diagram used for MSA plotsV-13
Figure 5-4 - The Hrouda-Jelinek or P'-T diagramV-14
Figures 5-5, 5-6 - Induced Magnetization Direction s.V-17
Figure 5-7 - Degree of Anisotropy vs. Grain Dimension Ratio Relationship for Various Values of Bulk SusceptibilityV-19
Figure 5-8 - Degree of Anisotropy vs. Grain MSA Relationship for Various Degrees of Preferred OrientationV-21
Figure 6-1 - Model of Magnetic Fabric Development during the Formation of Stylitic Cleavage.VI-9
Figure 6-2 - Rathore's Strain/MSA Correlations.VI-14
Figure 6-3 - Improved Representation of Strain/MSA Correlation.VI-16

Figure 7-1	- Bar Graph of Core vs. Powder Sample Bulk Susceptibility Values.VII-6
Figure 7-2	- Frantz Magnetic Separation Flow Chart.VII-7
Figure 7-3	- Bar Graph of Samples' Mineralogical Sources of Bulk Susceptibility.VII-9
Figure 7-4	- SMS Leaching Experiment - Depletion of Magnetic MineralsVII-11
Figure 7-5	- SEM X-ray Map: RS9C - greywacke.VII-15
Figure 7-6	- SEM X-ray Map: RS10 - higher grade greywackeVII-16
Figure 7-7	- SEM X-ray Map: RS10.5 - bi-gt schistVII-18
Figure 7-8	- SEM X-ray Map: RS10.8 - bi-gt-staur schistVII-19
Figure 7-9	- Bulk Susceptibility In-Situ Survey ResultsVII-22
Figure 7-10	- 12 MSA measurement orientationsVII-25
Figure 7-11	- Magnetic Fabric Stereonet (all axes).VII-27
Figure 7-12	- Kmin Plot and Density Contours.VII-29
Figure 7-13	- Kmax Plot and Density Contours.VII-30
Figure 7-14	- Kint Plot and Density Contours.VII-31
Figure 7-15	- Sarvas MSA DataVII-33
Figure 7-16	- Magnetic Fabrics of Various LithologiesVII-34
Figure 7-17	- Flinn Diagram (All MSA samples)VII-36
Figure 7-18	- Flinn Diagram (various lithologies)VII-37
Figure 7-19	- Jelinek Plot (All Msa samples).VII-39
Figure 7-20	- Jelinek Plot (various lithologies).VII-41
Figure 7-21	- Stereonet of Magnetic Lineations and Foliations .VII-44	
Figure 7-22	- Stereonet of Mineral Lineations and Foliations. .VII-45	
Figure 7-23	- Map comparing Magnetic vs. Mineral Lineations .VII-47	
Figure 7-24	- Superimposed Stereonet Displaying the Obliquity Between Magnetic and Mineral LineationsVII-49
Figure 8-1	- Special Arithmetic Functions on Zeiss Digitizer. .VIII-3	
Figure 8-2	- Parameters Used in the Rf/ ϕ Technique.VIII-4
Figure 8-3	- Summary of Rf/ ϕ Results.VIII-10
Figure 8-4	- Comparison of Arithmetic, Geometric and Harmonic Mean as Estimations of Strain (Rs)VIII-12
Figure 8-5	- Strain Estimates from the Various Analytical Methods.VIII-14
Figure 8-6	- Flinn Plot of Robin Analysis ResultsVIII-16
Figure 8-7	- Jelinek Plot of Robin Analysis ResultsVIII-17
Figure 8-8	- Flinn Data from the Linearization MethodVIII-20
Figure 8-9	- Flinn Diagram of Theoretical Initial (Ri) and Tectonic Strain (Rs) Values.VIII-21
Figure 8-10	- Jelinek Parameters for Theoretical Strain Values from Linearization MethodVIII-22
Figure 8-11	- Jelinek Plot of Theoretical Initial (Ri) and Tectonic Strain (Rs) ValuesVIII-23
Figure 8-12	- Comparison of the Strain Analysis Techniques. .VIII-25	
Figure 8-13	- Simple Linear Regression Plots for P'-Jelinek Parameters between Strain and MSAVIII-28
Figure 8-14	- Simple Linear Regression Plots for T-Jelinek Parameters between Strain and MSAVIII-29
Figure 8-15	- Possible Deformational Processes Significant in the Evolution of Magnetic FabricsVIII-31

Figure 9-1 - Diagrammatic Representation of
"Flower Structures".IX-6

I-1
CHAPTER 1 - PREVIOUS STUDIES

1.1 Introduction

Information concerning regional strain patterns within Archean greenstone belts is crucial to the understanding of the nature of tectonism and the evolution of adjacent metasedimentary and granite-greenstone belts. The paucity of outcrop and the poor preservation of primary sedimentary and volcanic features severely restricts the precise delineation of folds. Interpretation is further hampered both by a lack of strain markers and by the fine-grained nature of these ancient rocks. Since fossil and paleomagnetic indicators are unavailable, determination of relative belt motion must then depend upon other sources such as field structures that may be used as kinematic indicators, absolute and relative geochronology, and magnetic fabrics. Magnetic fabrics, and in particular, magnetic susceptibility anisotropy (MSA) have been previously demonstrated to clearly indicate finite strain directions.

This study applies the technique of MSA to the problem of regional tectonic strain patterns along an Archean sub-province boundary. This will also serve as a test of the viability of MSA as an accurate kinematic indicator in deformed Archean rocks. The problem addressed in this thesis concerns the structural relationship at the boundary between two subprovinces, the

Quetico metasedimentary belt and the Shebandowan-Wawa volcanic-plutonic belt, of the Superior Province within the Canadian Shield (fig. 1-1). This area was chosen as a valuable MSA application site due to its relatively low-grade metamorphism and consistent structure. The magnetic fabric data could then be compared with structures that are actually visible in the field. This investigation complements those performed between the Quetico metasedimentary belt and the Wabigoon volcanic-plutonic belt (Sarvas, 1987; Borradaile, et al., 1988).

Typically, Archean terranes consist of three major constituents:

- (i) greenstone-granite belts
- (ii) plutonic belts (contemporaneous or much older than adjacent greenstone belts)
- (iii) sedimentary belts (consisting of high-temperature metamorphosed sediments).

The evolution of greenstone belts and the nature of Archean tectonism has long been a source of controversy. Greenstone belt models have rapidly evolved over the last decade.

Early fixist belt models rationalized the greenstone stratigraphic progression by vertical orogenic activity controlled by the diapirism of igneous intrusive bodies through a pre-existing sialic crust (e.g. Anhaeusser, 1973; Gorman, et al., 1978). Later mobilist models utilized mantle convection and

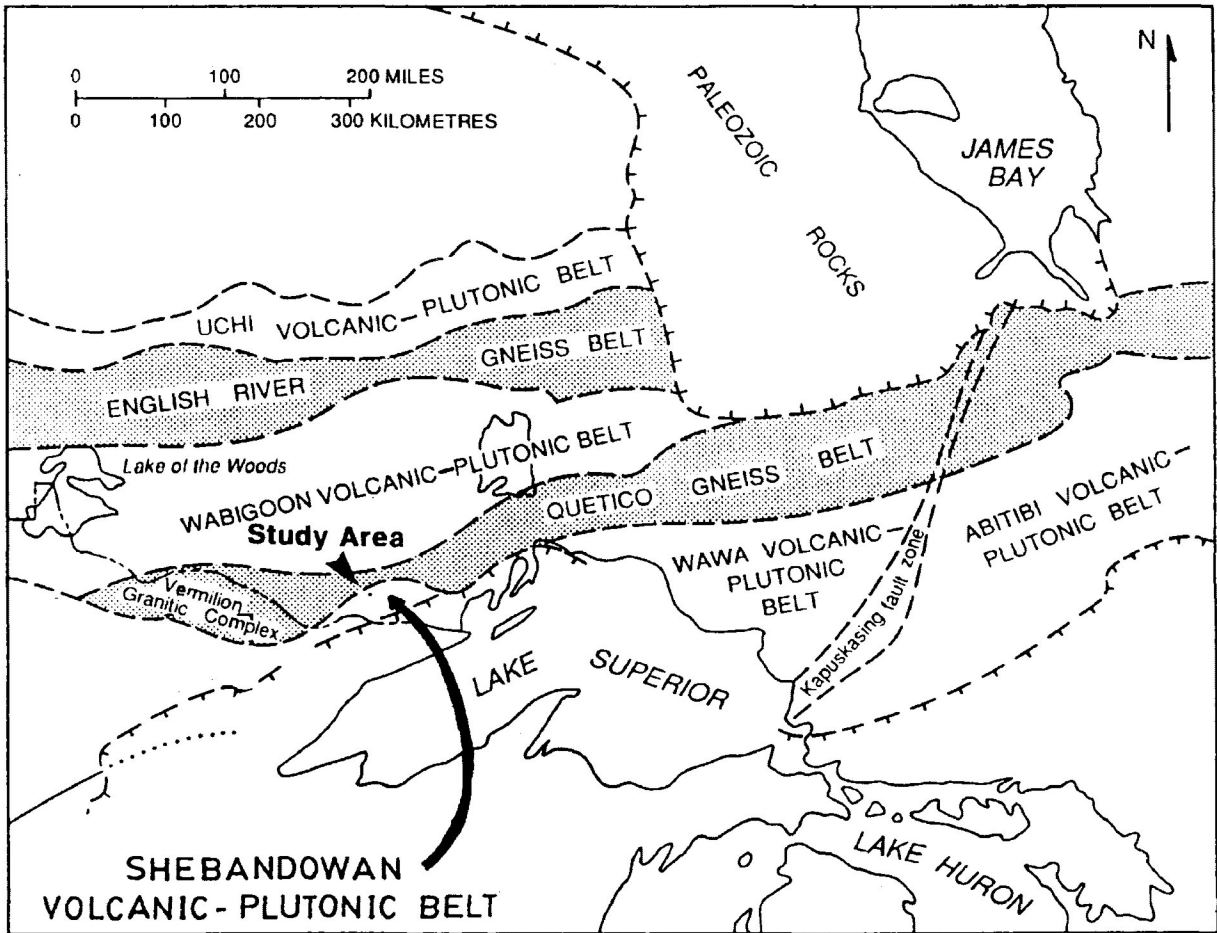


Figure 1-1: Map of subprovince boundaries within the Superior Province of the Canadian Shield and area of investigation (from Hudleston, et al., 1988).

its resultant horizontal lithospheric plate movement. Debate between the mobilists concerned the location of greenstone belt formation (ensialic rifting, island arc subduction, ocean floor spreading between sialic forelands, or back-arc marginal basin settings). Compressional or extensional mobilist origins were also disputed.

One school of thought was that the "subprovinces" within the Superior Province of the Canadian Shield originated compressionaly, as in fore-arc melanges or the amalgamation of island arc systems (e.g. Langford and Morin, 1976; Blackburn, 1980). Extensional mobilism, the other school of thought, also made use of plate tectonism and diapirism; as in extensional back-arc rifting (e.g. Tarney, et al., 1976). The belts were then thought to later deform into open folds, synclinoria, and various nappe structures (e.g. Poulsen, et al., 1980) and later vertical faults. These models all used diapirism as the major deformation force. Diapirism was utilized in further models involving the accumulation of massive amounts of tholeiitic magma through a fissured sialic crust (Goodwin, 1977). Recently, diapiric models involved the development of rift zones in pre-existing sialic cratons due to mantle-derived magmatism (Ayres and Thurston, 1985).

New models of this decade are quite unique. The recognition of the belts as "tectonic collages" is growing;

largely due to recent advances in geochronology. The most important deformational events are no longer believed to be dependent upon diapirism. The greenstone belt sequences are more accurately interpreted as a series of fault-bounded panels in an accretionary prism environment (Hall and Drury, 1989). This study area is thought to have undergone dextral transpression (Borradaile, et al., 1988; Hudleston, et al., 1988; Percival and Williams, 1989; Percival, 1989; Hall and Drury, 1989) as the sedimentary prism experienced horizontal shortening combined with simple shear across the belt. These oblique compressional events are commonly a result of oblique subduction or of the accretion of smaller lithospheric fragments.

The most current model for the Quetico belt (Hall and Drury, 1989) involves the accumulation and imbrication of sediments against an active fore-arc (now the Wabigoon subprovince) to the north. The present Quetico subprovince was trapped as an accretionary wedge from the south due to the subduction of oceanic rock, which later remained as the Shebandowan-Wawa subprovince.

1.2 Previous Geological Mapping

The Kashabowie-Shebandowan area has received much attention since the first discovery of copper, iron and gold deposits in 1870. It was the first major gold discovery in northwestern Ontario. Systematic regional mapping was initiated by the Geological Survey of Canada during the first few decades of this century. This work delimited the major rock units and outlined the substantial amount of exploration activity performed in the region as well as indicating new nickel-copper findings.

The Geological Branch of the Ontario Department of Mines, in 1961, began a program of systematic detailed remapping at a scale of 1:31,680 or one inch to a half mile. Initially, the Burchell Lake region was covered (area 2, fig. 1-2) (Giblin, 1964). General lithologies, structure, mineral deposits and folding of the metavolcanic and metasedimentary rocks about northeast-trending axes were observed.

Area 4 (fig. 1-2) comprises an eastward extension of regional mapping towards the western part of Middle Shebandowan Lake (Hodgkinson, 1968). Mapping included the description of the Shebandowan metavolcanic flows and pyroclastics. The Quetico metasediments were labelled as the Kashabowie Group of sedimentary rocks (greywacke and subordinate arkose altered to

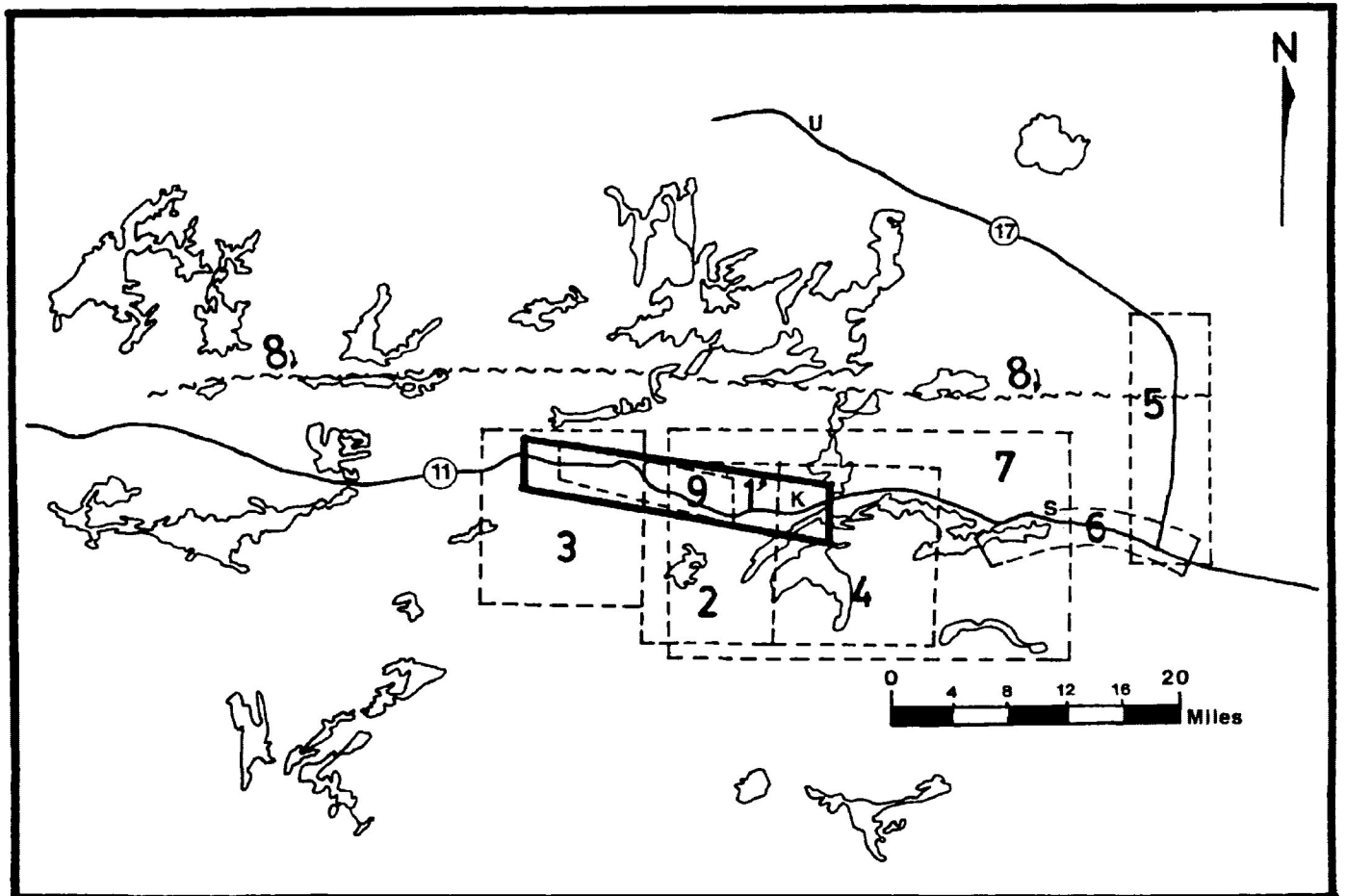


Figure 1-2: Location map of previous authors' work adjacent to and around the study area of this thesis (heavy lined box; K, S, and U are the towns of Kashabowie, Shebandowan and Upsala, respectively)

- Area 1 = thesis study area
- 2 = Giblin (1964)
- 3 = Harris (1970)
- 4 = Hodgkinson (1968)
- 5 = Kennedy (B.Sc. thesis, 1980)
- 6 = Shegelski (1980)
- 7 = Stott and Schwerdtner (1981)
- 8 = Kennedy (M.Sc. thesis, 1984)
- 9 = Pirie and Mackasey (1978)

schist). Harris (1970) performed mapping extending westward from Giblin's area for the Ontario Department of Mines and Northern Affairs.

Regional studies have continued this decade through various mapping projects by both the federal and provincial geological surveys. The Ontario Geological Survey investigated gold mineralization, lithology and structure in the Shebandowan area (Chorlton and Brown, 1984). An updated 1:250,000 scale Atikokan-Lakehead compilation map sheet (Thurston, 1985) was also produced by the Ontario Geological Survey. Recent investigations of the Quetico belt by the Geological Survey of Canada became part of a regional compilation of the western Superior Province (Percival, 1983; Percival and Stern, 1984; Percival, Stern, and Digel, 1985). Percival (1988) continued mapping in the area on a 1:250,000 reconnaissance scale.

More detailed work on various aspects of the Quetico and Shebandowan belts was conducted by several authors. Regional metamorphism within the Quetico metasedimentary belt (area 9, fig. 1-2) was examined by Pirie and Mackasey (1978). A path of regional metamorphism was determined from low greenschist facies along the belt margins through to higher grade migmatitic zones at the centre. Kennedy (1980) also examined metamorphic zonation in a B.Sc. thesis through a 30 kilometre stretch of the Quetico belt at Raith, Ontario (area 5, fig. 1-2). Structure and

metamorphism within the Quetico belt, west of the thesis area was also examined in B.Sc. theses by Dutka (1982), Stubley (1983), and Stewart (1984), near Atikokan, Ontario. Sawyer (1987) determined compositions of anatectically derived migmatite leucosomes from a suite of samples within the study area. Field and petrographic observations, combined with major, trace and REE compositions were obtained. This yielded information on partial melting and fractional crystallization processes after initial migmatite segregation.

Within the Shebandowan greenstone belt, volcanic stratigraphy and geological structure was examined in the immediate vicinity of the Shebandowan Ni-Cu mine (Morton, 1979). Detailed 1:4,800 scale mapping enabled Morton to infer a possible volcanic environment. The formation of possible Archean "red-bed" sequences was studied (Shegelski, 1980) at Lake Shebandowan (area 6, fig. 1-2). Complex folding of both volcanic groups (Keewatin and Timiskaming) was observed but contacts between the two remained unclear. Shegelski believed that the Keewatin platform (pillowed metabasalts analogous to modern island arc tholeiites) experienced orogeny, crustal thickening and stabilization prior to Timiskaming volcanism (calc-alkaline volcanics and alluvial-fluvial sediments). Red beds were deposited by the erosion of a newly emerged landmass. The Timiskaming volcanics were later redefined as "Shebandowan (Timiskaming-like) metavolcanics" (Brown, 1985; Borradaile and

Brown, 1987). The volcanic stratigraphy and structural relationships between the Keewatin and Shebandowan metavolcanics were re-examined as part of detailed mapping east of this area.

Geochronological studies were performed in both the Shebandowan belt and the Quetico belt. U/Pb isotopic data from areas adjacent to this study provides constraints on the timing of emplacement and deformational events supporting mobilist tectonic models. The date of 2704 ± 2 Ma (Corfu and Stott, 1986) was the maximum age given for the deposition of the younger "Timiskaming-type" calc-alkalic to alkalic volcanics and related troughs of alluvial-fluvial sediments. These unconformably overlie the Keewatin tholeiitic to calc-alkalic volcanic sequences dated at 2733 ± 3 Ma (Corfu and Stott, 1986) as a minimum extrusion age. Depositional, structural and metamorphic-plutonic histories (Percival, 1989) were reviewed and developed further to illustrate possible large-scale tectonic processes. The Quetico is believed to represent a sedimentary accretionary complex (Percival and Williams, 1989). The Quetico sedimentary wedge is thought to have been imbricated during the accretion of the present Shebandowan-Wawa greenstone belt towards what is now the Wabigoon greenstone belt. Low pressure metamorphism would then occur by the thermal relaxation and melting of the accretionary pile.

1.3 Recent Structural Studies

Numerous authors have recently studied the structural geology surrounding the thesis study area. Detailed structure was initially observed as part of systematic mapping by the Ontario Department of Mines (Giblin, 1964; Hodgkinson, 1968; Harris, 1970). Many geological features were attributed to "complex faulting". The Postans and Crayfish Creek faults were identified from air photo lineaments to explain the metasediment-metavolcanic boundary. The supposed fault-bounded contacts cannot be found in outcrop, but were described as "depressions in the ground" (Hodgkinson, 1968). Hodgkinson also inferred widespread folding, possibly isoclinal, within the metavolcanics, based partially on reversals in younging directions of pillow lava and graded bedding. The folding mechanism was attributed to diapiric action of granitic plutons.

Sawyer (1983) also attributed folds to large-scale vertical diapiric tectonics. The southern edge of the Quetico belt was shown to contain recumbent nappe-like folds. Evidence of resultant stratigraphic inversion was interpreted as the consequence of relative uplift during an early phase of gravity-driven, northwest-directed tectonics. However, Sawyer (personal communication, 1989) has reconsidered the nature of the subprovince boundary to be related more to dextral transpression.

Two phases of regional deformation were inferred within the Shebandowan belt (Stott 1985; Stott and Schwerdtner, 1981). These were delimited by the change in the plunge of the lineation. Coherent boundaries were mapped (fig. 1-2; area 7) between these two megascopically discrete strain domains. These boundaries were thought to represent strain discontinuities and the site of precious metal concentrations (Stott and Schnieders, 1983). The strain domains were interpreted as zones of a single deformation phase [D1] and zones of a superimposed second phase [D2]. However, no outcrops of interfering polyphase fabrics have been found. Although there may only be one single deformation phase, the boundaries do delimit zones of different tectonic symmetry (ie. L>S versus S>L tectonites). This mapping included the first application, in this region, of magnetic susceptibility anisotropy (MSA) to show variations in strain patterns. Magnetic fabric analyses, through the centre of the Shebandowan greenstone belt, revealed many of the strain domains and their boundaries.

MSA ellipsoids were determined also for the Quetico fault (fig. 1-2; area 8) through the Wabigoon and Quetico subprovinces (Kennedy, 1984). The ellipsoids were oblate and coaxial with strain ellipsoids. Microfaults and asymmetrical quartz c -axis petrofabrics indicated a dextral transcurrent motion. Kennedy's detailed study of the Quetico fault zone included: its sense of motion, the nature of strain, deformation mechanisms, and its brittle-ductile deformation transitions.

Magnetic fabric, in addition to thin-section and scanning electron microprobe analyses were completed for the metavolcanics within the Shebandowan belt (Borradaile and Brown, 1987).

Magnetic fabrics indicated a single, penetrative cleavage of consistent trend. Tight isoclinal folding, with subvertical and east-west trending fold axial traces, was found to affect all Archean Shebandowan rock types during a single tectonic episode.

The Quetico-Wabigoon boundary structure was also recently examined (Sarvas, 1987; Borradaile, et al., 1988; Poulsen, et al., 1980), west of the thesis study area. A number of regional folds were delineated within the Quetico metasediments at its northern boundary (Borradaile, et al., 1988). Investigations included: bedding-cleavage relationships, local younging directions, minor fold asymmetries, and structural facing directions. Macroscopic, isoclinal sheath folds, possessed axial traces that nearly paralleled the belt boundary. This supported pervasive dextral transpression at the boundary. Magnetic fabrics confirmed the existence of a single penetrative flattening tectonic microfabric (Sarvas, 1987), with a subordinate partially preserved fabric in places related to bedding.

CHAPTER 2 - PRESENT STUDY2.1 Field Area Location and Access

This thesis studies a controversial boundary between two subprovinces of the Canadian Superior Province. Originally, the subdivision of the Superior Province (Stockwell, 1964) separated the volcanic-plutonic terranes from adjacent, east-west trending, higher grade migmatized sedimentary belts, on the basis of recognizable tectonic features. Stockwell defined the "Quetico belt" as a linear belt of east-trending metamorphosed sediments. Stockwell's definition distinguished it from the more curvilinear greenstone belts and elliptical plutons of the Shebandowan-Wawa subprovince to the south and the Wabigoon subprovince to the north. The subprovince boundaries were later clarified, based more on lithological origin and characteristics (Card and Ciesielski, 1986). The Superior Province was reclassified into: volcano-plutonic, metasedimentary, plutonic, and high-grade gneiss subprovince types.

The subprovince boundary examined in this study lies between the Shebandowan volcano-plutonic belt to the south, and the Quetico subprovince of metasediments and associated granitic intrusions to the north. Previously, the subprovince boundary was thought to involve a locally conformable fault-bounded

contact (Giblin, 1964; Hodgkinson, 1968; Harris, 1970). However, evidence for this is not clear. Subprovince boundaries cannot be delineated simply on the basis of metamorphic grade, along faults, or between local metasedimentary - metavolcanic interfaces.

The Shebandowan greenstone belt extends westward, as an extension of the Wawa greenstone belt across Lake Superior, and continues to the southwest into Minnesota. It consists of an Archean supracrustal belt of metamorphosed volcanic and sedimentary rock and comprises the most southernly exposed subprovince of the Superior Province. The belt is approximately northeast-trending and contains a variety of volcanics rocks. Mafic to felsic flows and pyroclastics of tholeiitic to calc-alkaline chemical affinities exist in part with basaltic flows that are typically massive, pillowed or brecciated (Goodwin, 1972).

The Quetico belt spans nearly 1200 km and varies in width from 10 to 100 kilometres. It emerges from beneath the western Paleozoic cover as the Vermilion Granitic Complex in northern Minnesota and continues to the east through Ontario as the Quetico subprovince. Further east, it continues beneath the late Precambrian rocks of the Nipigon basin, and terminates abruptly at the Kapuskasing structural zone. Within this subprovince, the

"Quetico metasediments" are defined as medium-grade submarine fan sandstones forming a monotonous sequence with rare internal structure (Wood, 1980). A high proportion of detrital quartz, useful for strain estimation in this study, is thought to represent a product of reworking prior to final sedimentation, or a product of a quartz-rich source.

The thesis study area (fig. 2-1) is an oblique transect through low greenschist facies Shebandowan metavolcanics and into increasingly higher metamorphic grades within the Quetico metasediments. The transect ends at the medium amphibolite grade migmatitic gneisses at the core of the Quetico belt. This area represents an easily accessible window through a subprovince boundary. The transect runs along the #11 Trans Canada Highway from the town of Kashabowie, approximately thirty kilometres west towards Huronian Lake at the divide between the Arctic and Atlantic watersheds. Access to the area is enhanced by several old logging roads, hydro-electric and telephone corridors, as well as boat access through numerous small lakes. However, areas studied were restricted to the better quality exposures along Highway 11.

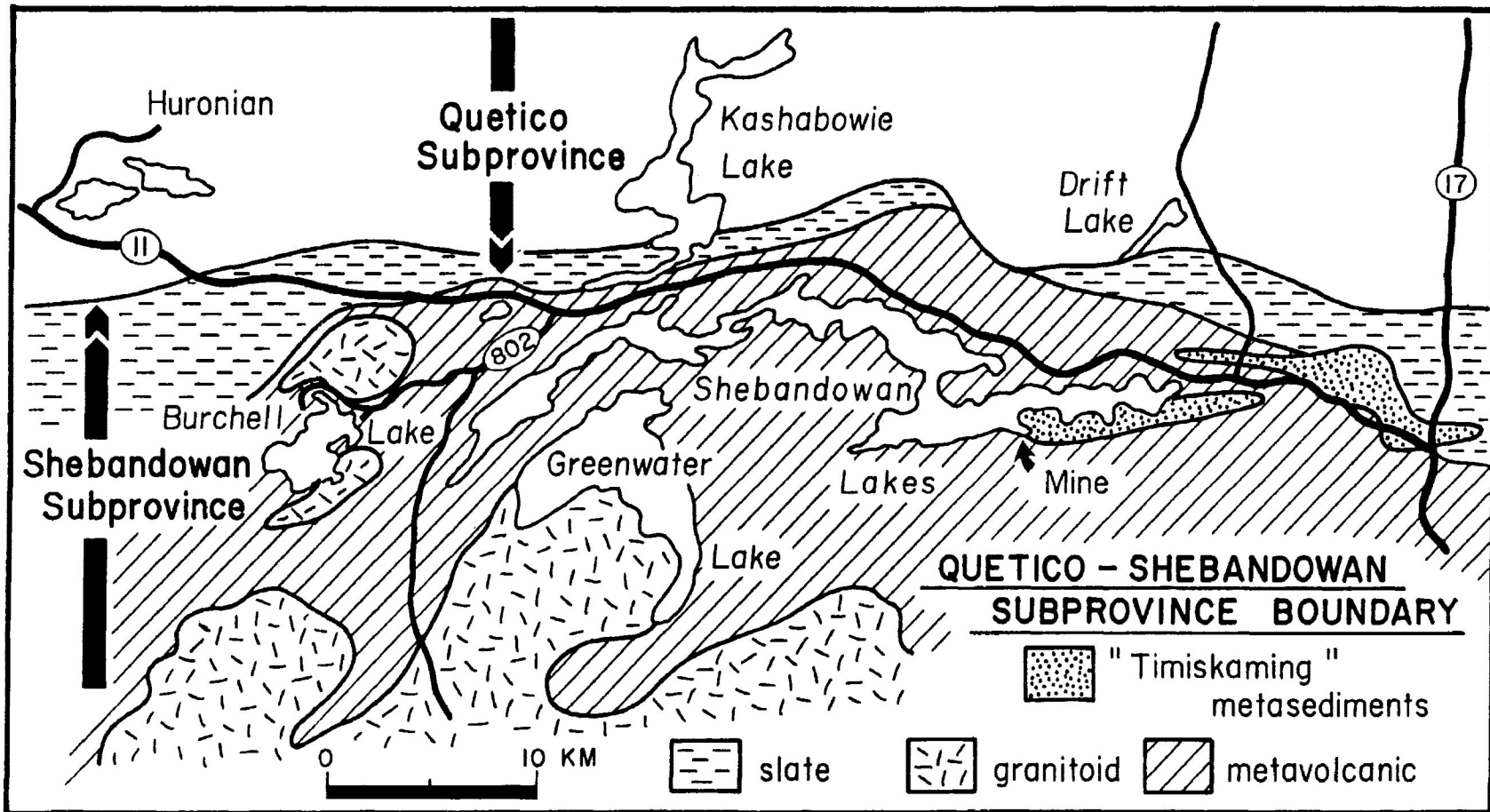


Figure 2-1: Map of the thesis field area and surrounding geology. The study area runs along highway #11 roadside exposures as part of an oblique transect from Kashabowie through the Quetico/Shebandowan boundary to Huronian Lake.

2.2 Purpose and Scope of Study

This study examines structure and magnetic fabric variations across the Quetico/Shebandowan subprovince boundary. Insights into the tectonic history may be revealed through the regional distributions of principal strain directions; especially utilizing the directional variability of magnetic susceptibility. This study tests the viability of magnetic susceptibility anisotropy (MSA) as an accurate kinematic indicator and compares results derived from mesoscopic and microscopic techniques. The present study includes:

- (1) detailed mapping on outcrop by outcrop scale
- (2) collection of over 200 oriented samples
- (3) initial bulk susceptibility measurements across the area using a portable susceptibility meter
- (4) preparation of numerous thin-sections for optical and scanning electron microscope
- (5) MSA determination and analysis from oriented samples
- (6) determination of magnetic mineralogy
- (7) correlation of MSA data with magnetic mineralogy
- (8) correlation of MSA with observed petrofabrics and macroscopic structural elements
- (9) correlation of MSA, if possible, with calculated strain

2.3 Method of Investigation

2.3.1 Field Method

Field work was completed during part of the fall of 1988 and during two months in the summer of 1989. Mapping concentrated on structural observations, including the measurement of bedding and cleavage orientations, mineral lineation trends, local younging directions, and other minor structures (ie. kink banding, sense of movement of ductile shears, and minor folds where present). Carefully oriented samples of all rock types were collected. The horizontal strike and dip of any planar surface was marked on the samples. Some oriented cores for MSA analyses were initially obtained in the field using a portable drill.

The analysis of relative dominance of planar versus linear preferred mineral orientations was carried out both in the field and by microscope thin-section examination. The relative strength between mineral lineation and schistose foliation, from a single sample, forms a continuous spectrum termed the "L-S Fabric System" (Flinn, 1965). It possesses spectral end-members of purely linear prolate ("L-tectonite") fabrics and purely flattened oblate ("S-tectonite") fabrics. Intermediate cases within the L-S fabric system can be described by $L > S$, $L = S$, or $L < S$

tectonic intervals. Visual L-S field approximations are crude and are generally verified by inspection of thin-sections parallel and perpendicular to the observed mineral lineation. Such estimates are valuable tools for mapping tectonic strain variations (Schwerdtner, et al., 1977). Often rocks with small grain sizes, or too weak a deformation, may not readily allow identification of planar and linear fabrics by conventional means. In such cases, the technique of magnetic susceptibility anisotropy (MSA) can provide useful qualitative correlations between magnetic fabrics, mineral fabrics, and strain.

2.3.2 Laboratory Techniques

Laboratory techniques within this study concentrated on magnetic susceptibility anisotropy. The use of MSA in this area was advantageous due to an absence of widespread strain indicators, poorly preserved primary sedimentary and volcanic features, and frequently some very small grain sizes. MSA techniques could then reveal principal strain direction variations and the range of fabrics across the subprovince boundary.

Magnetic mineralogies were evaluated by magnetic separation, leaching techniques and scanning electron microprobe. Qualitative correlations between MSA and strain were attempted. Strain was measured from detrital quartz granules in vertical and

horizontal thin-sections using various strain analysis methods. Experimental procedures for the various laboratory techniques will be described in later chapters. These techniques contribute to analyses of strain and fabric relationships and variations with respect to lithology and mineralogy.

CHAPTER 3 - GENERAL LITHOLOGICAL UNITS AND MINERALOGY3.1 Introduction and Geochronological Relationships

Within the study area, two main bedrock lithologies lie along two belts: the Archean Quetico metasediments and the Shebandowan-Wawa Archean metavolcanic belt to the south. Keewatin volcanics make up the older Shebandowan-Wawa belt. They display typical Archean cyclical sequences (Thurston and Chivers, 1990) found within other greenstone belts of the Superior Province. These volcanics are overlain by locally unconformable "Timiskaming-type" alluvial-fluvial metasediments occurring in two east-trending belts (Shegelski, 1980; Borradaile and Brown, 1987). The volcanic stratigraphy in this area is unclear, being complicated by, deformation, alteration and multiple intrusions of gabbros and diorites.

To the north lies the Quetico metasedimentary belt, which is itself bounded by the granite-greenstone terrains of the Wabigoon belt to the north. The Quetico belt consists of pelitic and wacke metasediments formerly grouped under the umbrella term "Coutchiching Series" (Lawson, 1913). The original stratigraphic relationships with the volcanic sequences to the south are unknown. The entire area has experienced late Archean "Kenoran" regional metamorphism. According to Stott (1985), two phases of

deformation were distinguished. The first deformation phase [D1] imposes a vertical schistosity, upright folds, and relatively steep west-plunging and southwest-plunging mineral lineations. This deformation style confines itself mainly to the southern half of the Shebandowan belt (Stott, 1985). The north half of the belt predominantly displays a vertical schistosity, but with east-plunging sub-horizontal lineations, and some discrete shear zones (Stott, 1985). This, Stott attributed to [D2] although nowhere are the two sets of structures seen to interfere. This deformation style largely affected the adjacent Quetico belt and caused the carbonatization and sericitization alteration related to the major ore deposits in the area (Stott and Schnieders, 1983).

Some late Archean granitic plutons later intruded the area. They are undeformed and retain primary granitic textures. A late pluton, at Burchell Lake (Fig. 2-1), caused the deflection and slight curvature of surrounding [D2] deformed volcanics and metasedimentary rocks to the north. A few small diabase and lamprophyre dykes were the most recent intrusions in the area.

The relative ages of the metavolcanic and metasedimentary sequences have been debated for over a century. Lawson (1913) originally considered the Coutchiching sediments to be older, apparently overlying the volcanics of the Wabigoon belt in the

Rainy Lake area. At one location, this apparent "sequence" was later found to be structurally inverted (Poulsen, et al., 1980), resulting in stratigraphically younger "Quetico-type" metasediments.

Recent U-Pb zircon and titanite geochronological data has produced approximate ages for the deposition of sedimentary and volcanic sequences as well as for periods of deformation and plutonism in the Shebandowan-Wawa belt. Dating of a porphyry sill within mafic metavolcanics, just east of Kashabowie, yielded an age of 2733 ± 3 Ma (Corfu and Stott, 1986). This indicates a minimum extrusion age for the volcanics and a maximum possible age for [D1] deformation. The overlying Timiskaming-type volcanics and sediments yielded maximum deposition ages of 2704 ± 2 Ma (from a trondhjemite clast within a conglomerate), and $2689 \pm 3/-2$ Ma (from large cognate inclusions within a pyroclastic breccia)(Corfu and Stott, 1986).

The dating of the two deformation phases helps bracket the ages of the units. The tonalitic Shebandowan Lake pluton intruded prior to, or during deformation. The post-tectonic circular tonalite stock at Burchell Lake intruded after the final phase of deformation. Dates from these plutons, as well as the dating of the post-[D1] and pre-[D2] Timiskaming-type deposits, establishes age ranges for the deformation phases (D1: 2696-2689

Ma; and D2: 2689-2684 Ma)(Corfu and Stott, 1986).

Geochronology from the Quetico belt is much less precise. In fact, earlier geochronological work failed to resolve Lawson's Keewatin/Coutchiching controversy. Total rock Rb-Sr dating of Keewatin Series rocks from the Rainy River area gave an age of 2595 ± 45 Ma and a Coutchiching Series age of 2625 ± 85 Ma (Peterman and Goldich, 1970). But with recent advances in U-Pb geochronology analysis, zircon, titanite and rutile yield much more precise resolution of major crustal events. A wide range of ages for the Quetico metasediments still exists due to the detrital and xenocrystic nature of its lithic clasts and single mineral grains. The very oldest detrital zircons (3059 ± 3 Ma) (Davis, et al., 1989) indicate a still older sialic sediment source area. The youngest detrital zircon age (2704 ± 3 Ma) (Davis, et al., 1989) would then infer an upper age limit for the deposition of the Quetico sediments. A lower limit is established by the earliest cross-cutting intrusions that date at 2692 ± 2 Ma (Davis, et al., 1989).

The oldest sequences north of the Quetico, in the Wabigoon granite-greenstone subprovince, have U-Pb dates ranging from 2725 ± 2 Ma to $2728 \pm 4/-3$ Ma (Davis, et al., 1989). Age relationships, in figure 3-1, are summarized. Since sedimentary sources may be from distant areas, the Quetico sediments can then

Age (Ma)	Wawa	Quetico	Wabigoon
2650		Pegmatite ^a (D ₃)	
2670	Late granites ^a (D ₂)	Pink, white granites ^a (D ₂)	Late granites ^a (D ₂)
2690	"Timiskaming" volcanics ^a (D ₁)	Granodiorite sills ^a	Seine conglomerate ^b (D ₁)
2710	"Keewatin" volcanics	Sedimentation (D ₁) ^b	"Keewatin" volcanics ^a
2730			
2750	Early intrusions ^a "Keewatin" volcanics ^a		Early intrusions ^a "Keewatin" volcanics ^a
2990			Unconformity, Steep Rock Group ^b Marmion tonalite ^a Lumby Lake volcanics ^a

^aDated unit.

^bBracketed unit.

Figure 3-1: Summary of relative age relationships of geological units and deformation events in the Shebandowan-Wawa, Quetico and Wabigoon subprovinces of the Superior Province, Canadian Shield. (from Percival, 1989)

be visualized as younger and allochthonous, rather than existing as older basement to the volcanic sequences.

3.2 Metavolcanic Lithology

The metavolcanics of the Shebandowan-Wawa belt span from east of the Shebandowan Lakes, to the onset of the Quetico metasediments west of Whitefish Lake (see metavolcanic outcrop location map, fig. 3-2). They occupy about one third of the thesis study area and consist of a complex intermingling of both mafic and felsic metavolcanic varieties. Their spatial relationship most likely derives from both isoclinal folding and cyclical stratigraphy.

3.2.1 Mafic Metavolcanics

The rocks of this group occur mainly in two bands. A NW band flanks the Quetico/Shebandowan boundary and the second runs north of Upper Shebandowan Lake (fig. 3-3). Small outliers of mafic flows are found incorporated within the Quetico metasediments to the west of the boundary. Regional greenschist metamorphism has altered these, massive and pillowed flows and pyroclastics, from a basaltic composition to chlorite and amphibolite schists. Many primary textures are still discernible. In many localities, original flow textures exist

Metavolcanic Outcrop Location Map

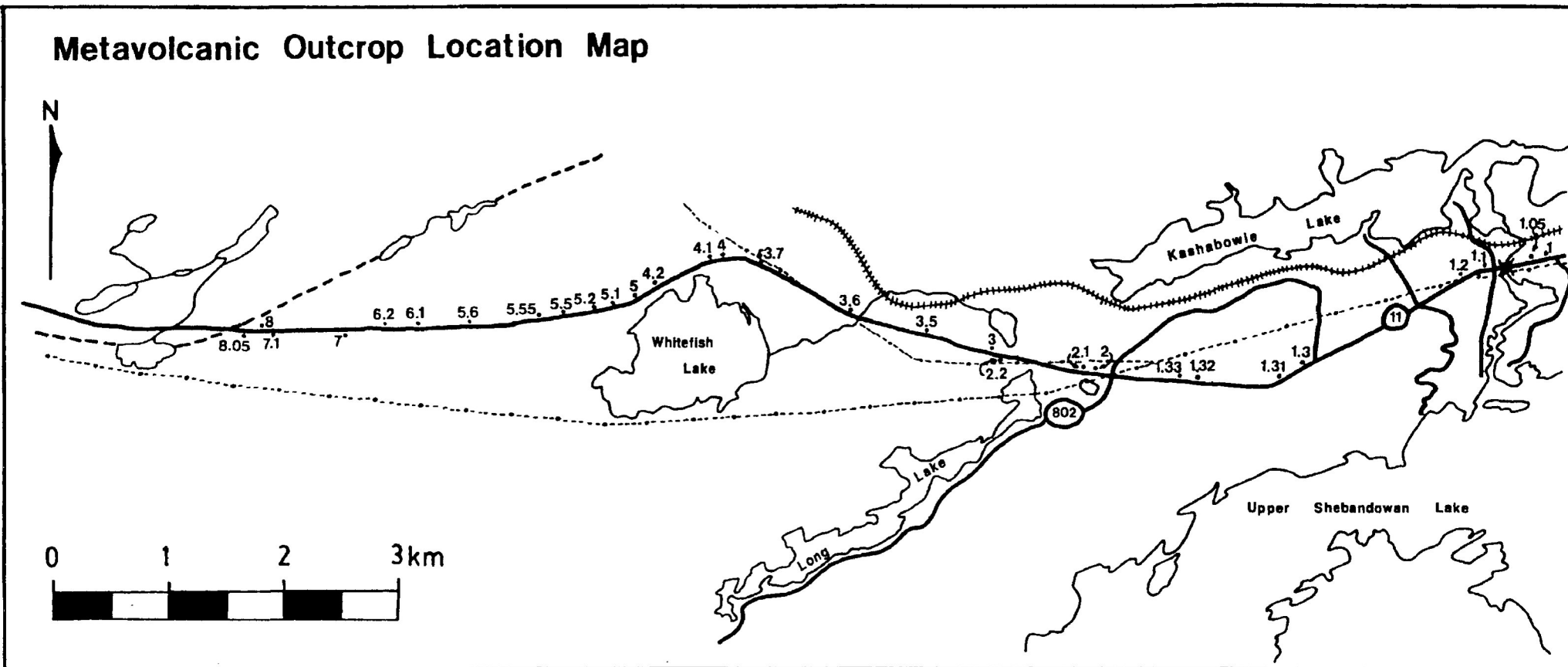


Figure 3-2: Metavolcanic outcrop location map for thesis area east of the Quetico metasedimentary belt (boundary shown as dashed line). Highways #11 and #802, the proximity of hydro lines, railway tracks and some lakes are added for reference. All station localities have an "RS-" prefix in the text. Samples and thin-sections also have an "RS-" prefix or a "C-" prefix (core drilled at outcrop).

Metavolcanic Outcrop Lithology Map

N   Mafic Volcanics  Felsic-Intermediate Volcanics  Gabbroic Intrusives

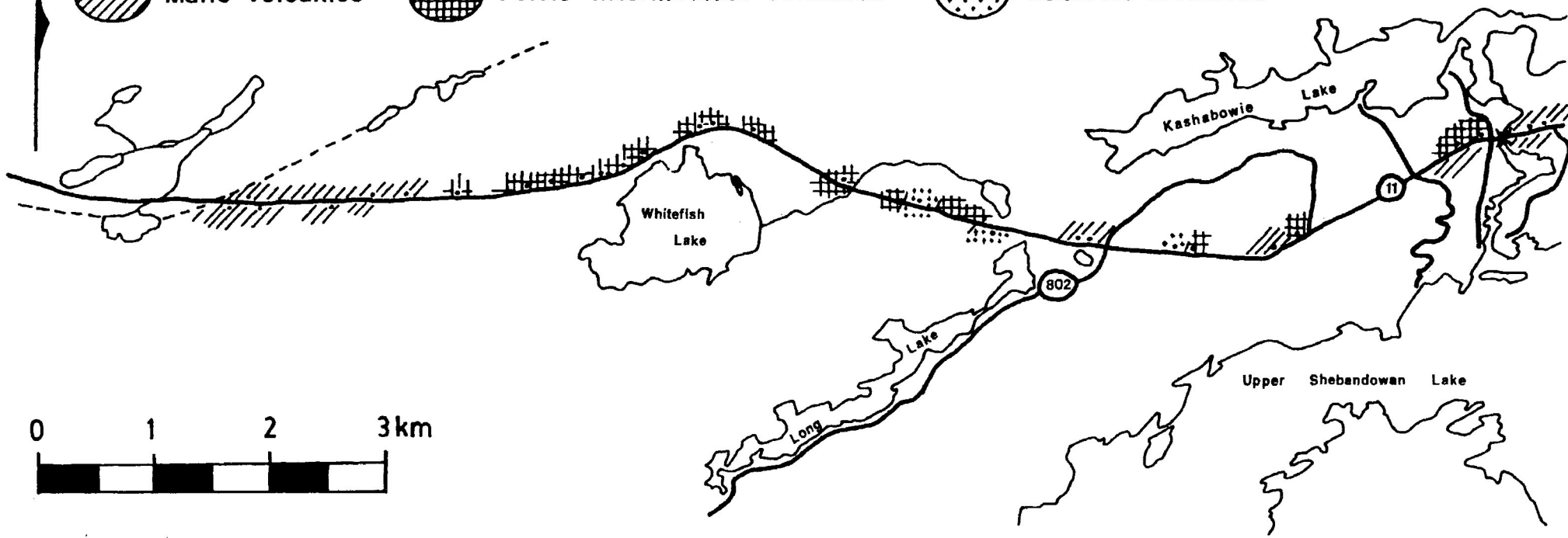


Figure 3-3: Metavolcanic outcrop lithology map for thesis area east of the Quetico metasedimentary belt (boundary shown as dashed line). Shown above are the major outcrop units of: the highly siliceous felsic metavolcanics near Whitefish Lake, the sheared belts of mafic and felsic metavolcanics near Upper Shebandowan Lake, and the NW belt of mafic metavolcanics adjacent to the Quetico metasedimentary belt boundary.

and locally layered and graded bedding, pillows, and amygdules are still visible.

All the mafic metavolcanics possess a high proportion of minerals typical of greenschist facies metamorphism (chlorite, actinolite, and epidote). Many original ferromagnesian minerals have suffered chloritization. Feldspar phenocrysts are usually sericitized and often saussuritization has completely replaced the feldspar phenocrysts. The few remaining olivine phenocrysts are small (generally 0.1-0.2mm), and were fractured and rounded by magmatic corrosion. Feldspar laths exhibit broken and shattered terminations. Regionally, and at outcrop scale, the intensity of deformation seems quite variable. Stott (1985) found that the rocks south of the Shebandowan Mine were much less deformed than similar rocks north of Upper Shebandowan Lake.

Several pyroclastic outcrops are apparent within this unit. Tuffs (stations RS2, RS2.1 and RS7) and agglomerates (station RS6.2) exhibit very well-flattened lenticular fragments. These ovoids of recrystallized quartz display excellent S-tectonite flattening in near-horizontal and vertical directions. Large chlorite laths have grown within the strain shadows of these augen. The agglomerate fragment size is about 1x4 cm on average while the tuffaceous outcrops exhibit pyroclast sizes generally within the lower lapilli tuff range (less than

2x6 mm in size). The lapilli consist of late quartz and calcite with convolute boundaries. The tuffs and agglomerates contain mainly saussuritized, corroded and fragmented feldspar phenocrysts with fibrous clusters of chlorite and actinolite. Epidote, opaques, glass relicts, some quartz, olivine phenocrysts, and broken poikilitic biotite laths were contained within the largely micaceous matrix. Alteration produced abundant sericite, as well as, secondary quartz and carbonate veining. Magnetic separation produced portions of magnetite, hematite, and pyrite. Generally, these rocks are not very deformed and possess relict flow textures and groundmass debris trails. Graded bedding at station RS2 was found to be slightly oblique to cleavage. Anastomosing chlorite and actinolite fibres vaguely define a cleavage containing single crystals and crystal fragments. Locally, the tuffs are quite fissile with chloritic "sheared" bands visible.

Altered flows were observed on both mafic metavolcanic bands. A sizeable porphyritic flow lies north of Upper Shebandowan Lake (at stations RS1 and RS1.2). More massive flows occur in the NW belt (at stations RS6.1 and RS6.2). Like the tuffs, the porphyritic flows have an anastomosing fabric with some zones of greater intensity. Within these shear zones the rock is more carbonatized, more fissile and has siliceous knots and augen. Thin-sections reveal a dominantly plagioclase

composition (60%-70% volume). Plagioclase phenocrysts were zoned and rimmed on outcrop exposures. In thin-section, it is intensely sericitized, has lamellar twinning and is present also within the groundmass. Small rounded and fractured olivines and some opaques were the only other visible phenocrysts. Olivine was probably rounded by magmatic corrosion. It occasionally occurs as clusters which could represent accumulations from the magma chamber wall. Chlorite (penninite), actinolite, and sericite constitute most of the remaining volume. This micaceous component produces a good preferred orientation and an anastomosing fabric wraps around the phenocrysts. Relict flow textures are still visible. Amygdaloids are abundant and are filled by secondary calcite. The scanning electron microprobe indicated the presence of rutile, zircon, albite, apatite, magnetite, and epidote. Magnetite, hematite, and pyrrhotite were magnetically separable.

Some flows were entirely massive and coarse grained, yet quite altered. Presently they are amphibolites and probably originated as gabbroic flows (stations RS6.1 and RS6.2). They are fissile and chloritic in places; probably representing small shear zones. All original mafics seem to have been replaced by greenschist assemblage minerals. Nearly half of the rock volume appears to consist of altered plagioclase. Alteration makes identification difficult and may in part be due to the relatively

close proximity of this outcrop to the Burchell Lake tonalite pluton to the south. Remaining mineralogical constituents are mainly chlorite and actinolite which envelope large (1-2 mm) plagioclase phenocrysts.

The massive flows of RS6.1 and RS6.2 seem to grade into pillowed flows (stations RS7, RS7.1, RS8, and RS8.05) over a relatively short distance. Both massive and pillowed flows appear principally along the north margin of the NW mafic metavolcanic belt. A strike-length of three miles was observed by Gibling (1964) for the pillowed flow units. Some pillows are distorted but several are suitable for reliable top determinations. Good selvages and cusps were seen (figures 3-4a, 3-4b and 3-4c). Pillows at RS7 possess several quartz infilled vesicles (1mm diameter on average). Most plagioclase phenocrysts are heavily sericitized and have broken terminations. Small (0.1mm) corroded olivine phenocrysts also still exist. A majority of the rock has been pseudomorphed by chlorite and actinolite. A number of small quartz, epidote, and calcite veins cut through the pillows and often have brittle offsets. Groundmass constitutes nearly a third of the rock and is composed of plagioclase, sericite, some quartz, opaques and glassy debris. Scanning electron microprobe reveals the additional presence of apatite, sphene, zircon, pyrite, and cobaltite. Magnetic separation techniques yielded magnetite, hematite, and pyrrhotite



Figure 3-4a: Pillow lavas at station RS7. The compass points north. Cusps trend towards the top of the photo and younging is estimated at 330 degrees. Pillow "bedding" trends at about 050 degrees. (Highway #11 is just beyond the top of the photo).

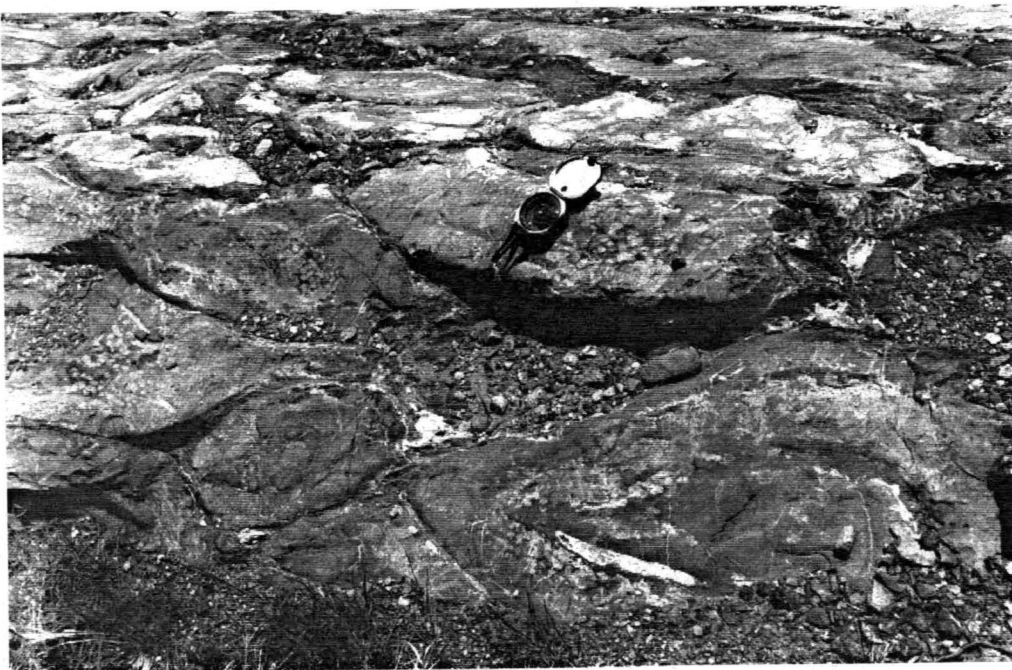


Figure 3-4b: Relatively undeformed pillows at station RS8. Compass points north. Cusps are towards the top of the photo and younging trends at about 322 degrees. The "bedding" of the pillows is oriented at about 242/83.

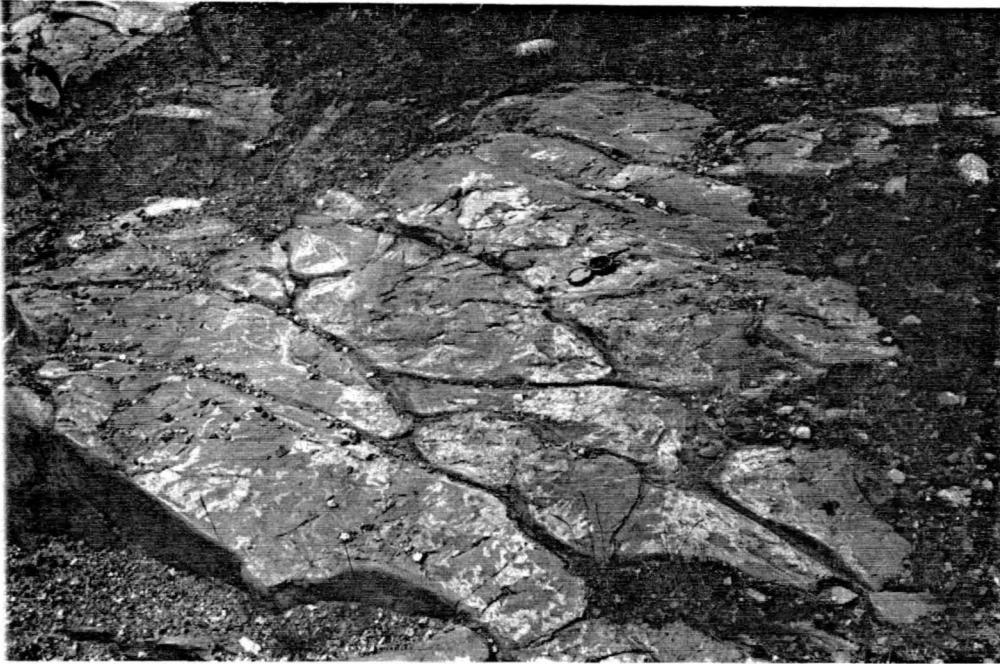


Figure 3-4c: Additional pillow exposure at station RS8. Compass points north. Younging trends at 325 degrees with pillow "bedding" oriented at 238/78.

fractions. A crude banding exists but no cleavage was visible. Large radiating fibrous actinolite laths and chlorite seem to be randomly oriented in thin-section.

Chlorite and actinolite schists are present in most outcrops experienced local shearing. Larger, outcrop-scale schist units occur at stations RS2, RS6.2, RS7.1 and RS8. A few lenses of these schists appear within the Quetico subprovince. At RS8, a very fissile chlorite schist lies along strike from the pillowed flows across highway 11. They are petrologically alike. Pillow sequences elsewhere are cut by local small shears and contain chlorite schist. A larger schist unit at RS7.1 is extremely fissile and sericitic. Chlorite and actinolite flakes as well as phenocrysts of plagioclase, quartz, and carbonate infillings are stretched almost to the point of mylonitization. Secondary calcite entered the rock at the time of interaction between pillow lava and seawater. Since all grains, including calcite are severely stretched; therefore, these shear zones mark sites of subsequent kinematic reactivation. The stretching is horizontal and is more pronounced. It is an L>S tectonite. A plagioclase phenocryst displayed good dextral kinematics in plan view. It has a snowball texture with inclusion trails and microcrysts clearly indicating dextral rotation. A large portion of the sheared area has infillings of late third stage carbonate and quartz derived from hydrothermal solution.

3.2.2 Felsic Metavolcanics

The felsic metavolcanics consist of rhyolites, porphyritic rhyolites, tuffs, agglomerates, and their altered equivalents. They are generally more resistant to erosion than the chloritic mafic volcanics, and remain as large round clustered outcrops. The main felsic metavolcanic outcrop cluster (stations RS3 to RS5.6) occurs near Whitefish Lake between the two mafic volcanic bands (figures 3-2 and 3-3). Smaller sheared metavolcanic outcrops are present near the town of Kashabowie (stations RS1.1, RS1.3, and RS1.32).

Visible pyroclast sizes range from elongated agglomerates (maximum size about 30 cm), to smaller, lenticular and rounded lapilli (mostly 4-6 mm), to tuffaceous pyroclasts (1-2 mm diameter). Many primary bedding features are preserved, despite local ductile behaviour that has further distorted and elongated some of the pyroclasts. Micaceous minerals form a preferred orientation and create a schistose fabric parallel with the elongation of the recrystallized pyroclasts. Often the rocks are very fissile and the pyroclasts reveal good S-tectonite flattening. Thin units of sericite and chlorite schists often occur within outcrops. Alteration in places can be quite extensive. Recrystallization of quartz and various degrees of sericitization of feldspar phenocrysts are evident in all sample

thin-sections.

Near Kashabowie, the felsic metavolcanics are locally very fissile and have experienced kinking and several brittle offsets. The outcrop fabric is generally anastomosing, although schistose, with some minor shears. Small quartz veins were dextrally, in plan view, rotated through boudinage (RS1.1). Late brittle sinistral offsets were also observed. The felsic metavolcanics are generally rhyolitic but contain occasional chloritic mafic inclusions in this area. The largest pyroclasts found within agglomerate portions were 10 cm long and demonstrated good flattening. Several small gossan zones contain small (<1 cm) pyrite and chalcopyrite areas. A small sulphide-bearing zone runs through stations RS1.2 and RS1.2-2. It contains larger clusters (<5 cm) of pyrite hosted by sheared quartz veining.

In thin-section, albite is the predominant mineral. Possible phenocrysts of sanidine and microcline were observed. These alkali feldspars occur commonly within late-crystallizing rhyolites. Nearly half of the rock's volume is occupied by a schistose matrix containing very fine grained (<0.02 mm) recrystallized quartz, fragmented feldspars, and lesser amounts of sericite, chlorite, and epidote. Larger quartz phenocrysts are rounded, embayed and display undulose extinction. Other

phenocrysts include small rounded olivines, opaques, and a few anhedral tourmaline grains. Secondary calcite fills some amygdaloids and fractures. Sericite exhibits a strong preferred orientation and wraps around feldspar phenocrysts. Tectonic flattening creates several augen structures with few asymmetries. A few albite phenocrysts that contain calcite and sericite poikiloblasts exhibit crude dextral rotation in plan view. A possible secondary cleavage exists in the form of kinematically inconsistent crenulations.

Felsic metavolcanics were not extensively sampled. These rocks were extremely siliceous and also lacked Fe-bearing phyllosilicates and Fe-oxides; hence, these rocks would prove useless for magnetic fabric analyses. One test sample was obtained, however, from station RS3.

Outcrops from RS3 to RS4 consist of fairly homogeneous felsic rhyolites. Again, several kink folds were noted. Some bands contain lenticular bombs over three centimetres in length, (one centimetre average). The rock possesses a very fissile cleavage but a random orientation of acicular actinolite crystals. These rocks demonstrate S>L tectonite characteristics also in thin-section. Quartz occupies nearly 80% of the rock volume both as large rounded phenocrysts and as tuffaceous clusters with convolute boundaries. Some tuff and lapilli

contain mixtures of quartz and calcite or consist entirely of calcite. Some pyroclasts seem flattened, while others are totally rounded. This suggests recrystallization and/or relict flow fabrics.

Outcrops of a pink-coloured felsic rhyolite are exposed near Whitefish Lake (station RS4.1) and continue westward to station RS5.6. The rhyolite becomes more porphyritic and eventually becomes a flattened agglomerate towards RS5.6, where it meets the NW mafic metavolcanic band. It becomes less felsic and more intermediate in composition as the proportions of chlorite, tourmaline, and actinolite increases. Otherwise, the mineralogy is fairly constant; comprising of sericite, quartz, feldspar, and opaques. Actinolite needles become more prominent towards the west. They reach sizes greater than one centimetre. Their alignment also becomes more prominent and attains a nearly parallel lineation with a relatively steep plunge and eastern trend. Blobs of pyrite, chalcopyrite, and flecks of specular hematite are visible locally. Feldspar phenocrysts range in size from about one to five millimetres, but their alteration becomes more profuse towards the west. Sericitization and calcite infilling increases until complete pseudomorphing is nearly achieved. Agglomerate bombs are quite variable in size and abundance (fig. 3-5). Fabrics are very convolute and anastomose in those bands containing numerous bombs. The bombs contain



Figure 3-5: Bombs within the pink felsic to intermediate agglomerate at station RS5.5. The hammer handle points approximately north.

fragmented and sericitized feldspar laths as well as recrystallized quartz and calcite. Average bomb sizes seen in section are about 8x3 cm within a matrix of sizes ranging between 0.01 and 0.25 mm. Beyond the western margin of these felsic metavolcanics and to the west of the NW mafic metavolcanic band, lies the inferred Quetico/Shebandowan subprovince boundary.

3.3 Metasediment Lithology

The "Quetico-type" pelitic and wacke metasediments were defined by Wood (1980) in the Rainy Lake area, west of this study area. They were initially grouped under the umbrella term "Coutchiching Series" (Lawson, 1913). Locally, these metasediments were referred to as the Kashabowie Group of monotonously uniform, massive, well-bedded greywackes (Hodgkinson, 1968). The Quetico metasediments occupy nearly two thirds of the thesis transect area (see metasediment outcrop location map, fig. 3-6). Inwards from the belt boundary, the clastic sediments gradually increase in metamorphic grade to form coarse biotite schists and paragneisses as the quartz/feldspar groundmass becomes recrystallized and porphyroblasts form. A few foreign lenses exist within the Quetico belt. An inclusion of porphyritic basalt flow metavolcanic occurs at RS10.1. Outcrop-scale amphibolite pods are also present towards Stetham Lake.

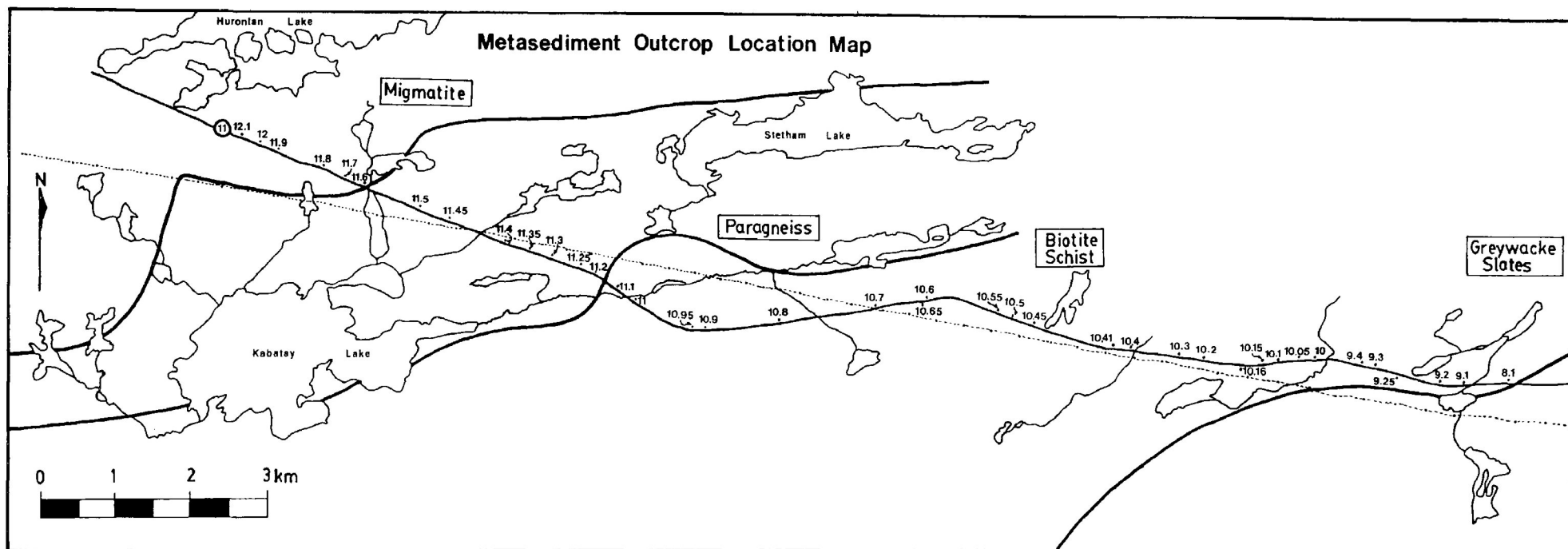


Figure 3-6: Metasediment outcrop location map for thesis area west of the Shebandowan-Wawa greenstone belt. Highway #11, the proximity of hydro lines, and some lakes are added for reference. All station localities have an "RS-" prefix in the text. Samples and thin-sections also have an "RS-" or a "C-" prefix (for core drilled at outcrops). Boundaries separating migmatite, paragneiss and greywacke/schist regions are compiled from: Giblin (1964), Harris (1970), and Percival (1988).

3.3.1 Clastic Metasediments and Schists

Fairly unaltered clastic sediments exist near the Shebandowan-Quetico lithological boundary (fig. 3-7). The clastic sediments consist of thin units of siltstone, mudstone, and shale and their metamorphic equivalents (e.g. argillites and slates) (fig. 3-8a). They are frequently interbedded with each other. Many of their primary sedimentary textures and structures were retained. Progressive metamorphism increases inward to the belt axis, grading towards recrystallized biotite schists.

The classification of sandstones and wackes becomes difficult due to the polygenetic origin of the matrix. Based on Pettijohn's classification scheme (fig. 3-8b), the sandstones from this area resemble arkosic wackes since quartz clasts are abundant and lithic fragments are relatively rare. However, sedimentary classification schemes do not account for the substantial metamorphic contribution to the matrix. With regard to metamorphism, the Quetico metasediments would then consist of arkosic metagreywacke, and finer grained slates and argillites.

The wacke and siltstone outcrops bordering the Shebandowan subprovince (stations RS8.1 and RS9.1) are well-bedded and still possess many primary sedimentary structures. A few occurrences of graded bedding, soft sediment deformation, and

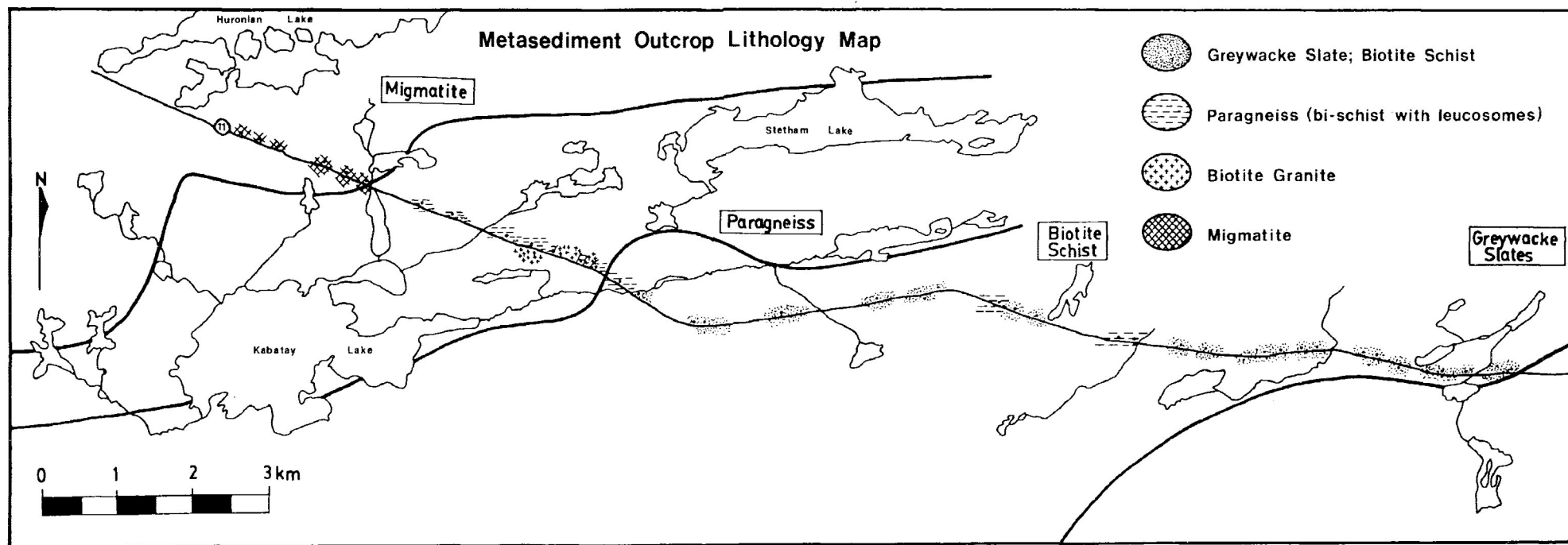


Figure 3-7: Metasediment outcrop lithology map for thesis area west of the Shebandowan-Wawa greenstone belt. Shown above are the major outcrop units of: (i) clastic metasediments: greywacke slates and recrystallized schists, (ii) paragneisses, (iii) intrusive biotite granite, and (iv) migmatites near the centre of the Quetico belt. Boundaries separating migmatite, paragneiss, and greywacke/schist regions are compiled from: Giblin (1964), Harris (1970), and Percival (1988).

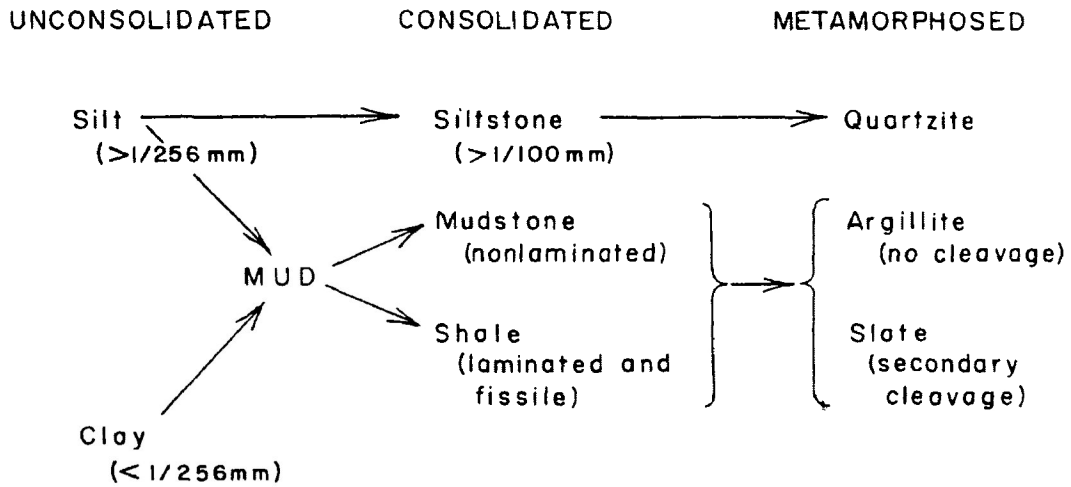


Figure 3-8a: Terminology of the argillaceous sediments (note: both slate and argillite can develop from either mudstone or shale). (from Pettijohn, 1975)

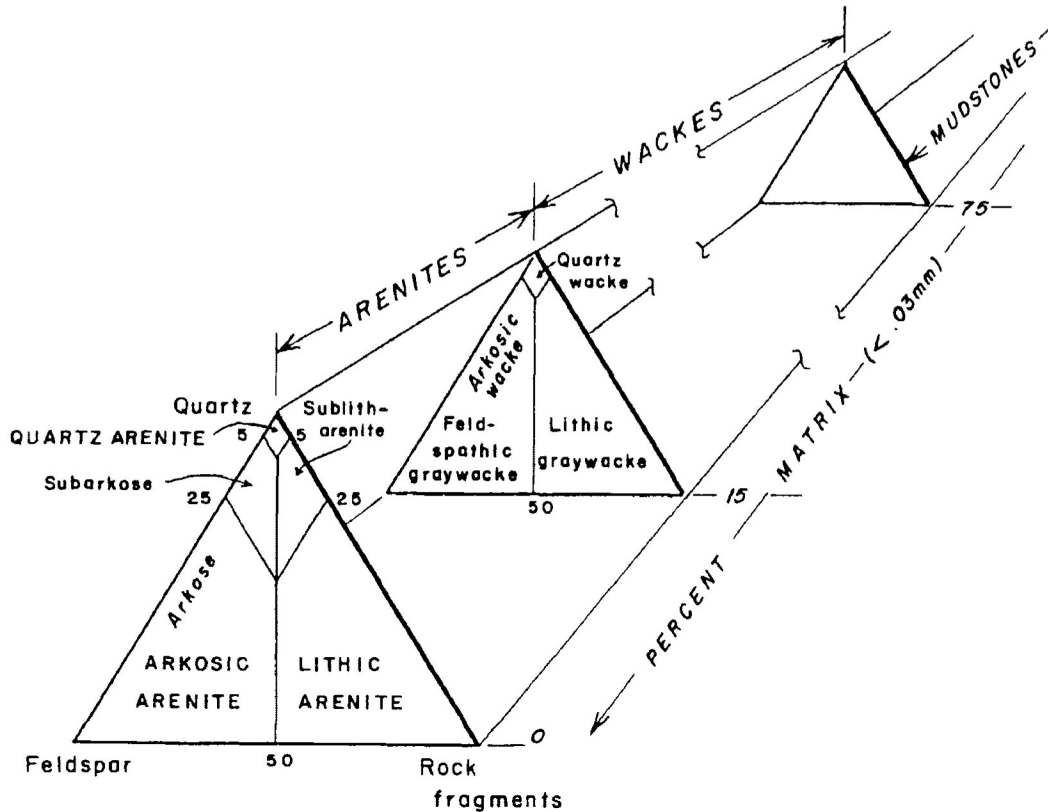


Figure 3-8b: Classification scheme of terrigenous sandstones. (from Pettijohn, 1975)

fine siltstone-mudstone laminations are visible (figs. 3-9a and 3-9b), but cross-bedding and ripple marks are absent. The beds have distinct bases and are on average 50-100 cm thick. Cleavage is initially weak, but becomes more manifest by station RS9.1.

The mineralogy of the wackes consists simply of quartz, biotite (detrital and porphyroblastic), and plagioclase. Retrograded quartz and albite are also visible. Rare detrital microcline alkali feldspars are also present. All these minerals comprise both the clasts (angular to subrounded clasts; usually <1 mm dia.), and the fine-grained matrix (<0.1 mm dia.). The matrix usually composes 50-70% of the rock volume and contains additional microlaths of chlorite and white micas. The scanning electron microprobe reveals lesser amounts of: muscovite, apatite, rutile, calcite, chlorite, ilmenite, zircon, sphene, epidote and sericite. Magnetite, hematite, pyrrhotite and pyrite were observed through magnetic separation. In thin-section, large detrital biotite laths (1 mm) appear ragged and torn and possess many pleochroic halos. They contain recrystallized quartz within poikiloblasts and symmetrical strain shadows. Bedding is difficult to discern from continuous cleavage in thin-section. This cleavage arises from a combination of the preferred crystallographic orientation of the phyllosilicates and the preferred dimensional orientation of larger clasts. A mild flattening style of deformation, near the belt boundary, is



Figure 3-9a: Outcrop showing wacke graded bedding at station RS8.1 (closest outcrop to the pillowed metavolcanics of the Shebandowan belt). Pelitic bases grade up to finer mudstone tops. Scour marks, common in turbidity current environments, are evident at the mudstone-sand base turbidity current interface. Younging is towards the north approximately top of the photo).

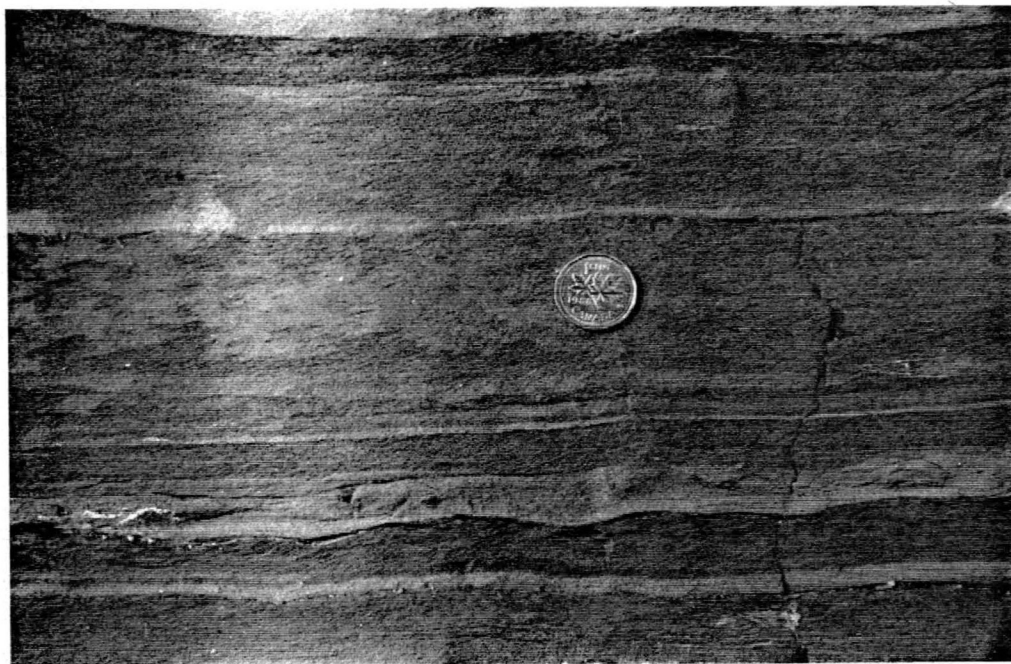


Figure 3-9b: Additional wacke graded bedding exposure at station RS8.1. A superimposed cleavage upon bedding fabric begins its appearance at this outcrop. Yet, the graded bedding and soft sediment deformational features are still well preserved. Younging is towards the north (approximately top of photo).

apparent since no lineation component is visible from horizontal and vertical thin-sections. A few crude examples of rotated snowball texture (dextral in plan view) within biotite porphyroblasts are visible in thin-section. Feldspar clasts contain euhedral sericite crystals and are variably saussuritized. Quartz clasts are generally more rounded and have undulose extinction.

Beyond RS9.2, the greywacke becomes somewhat crenulated and any obliquities between bedding and cleavage are nearly indistinguishable. Graded beds are still visible since the growth of porphyroblasts has not yet been sufficient to obscure younging directions. Examples of well-formed cleavage-bedding obliquities occur at RS8.1, RS9.1, and RS10 (figs. 3-10a and 3-10b). The schistosity fabric refracts slightly at the interface between separate beds. This is most likely due to differences in bedding normal compaction on either side of bed contacts. Shear strain appears to be more intense within more pelitic zones. Increasing metamorphism, and the growth of microblasts obscures any reliable younging directions beyond RS10. These outcrops contain boudinaged quartz swaths but become very prominent by RS9.4. The necklines between the boudins are filled by quartz, pyrite and chlorite crystals. Late sinistral kinking and late dextral shears (plan view) are visible.

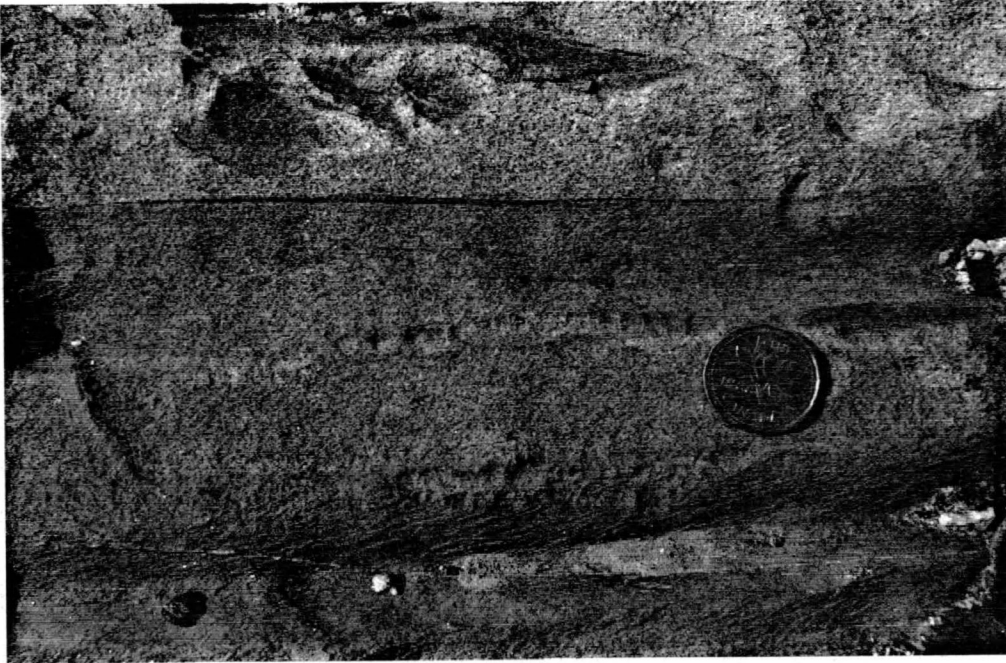


Figure 3-10a: Outcrop displaying bedding/cleavage relationship at station RS9.1. The "1" on the coin points north. Bedding trends at 072 degrees and is marked by fine grained silty laminae separating coarser units in the photo. The cleavage (trending at 062 degrees) is evident in the recessional groove below the coin. Since younging is approximately north, the structural facing direction is east.

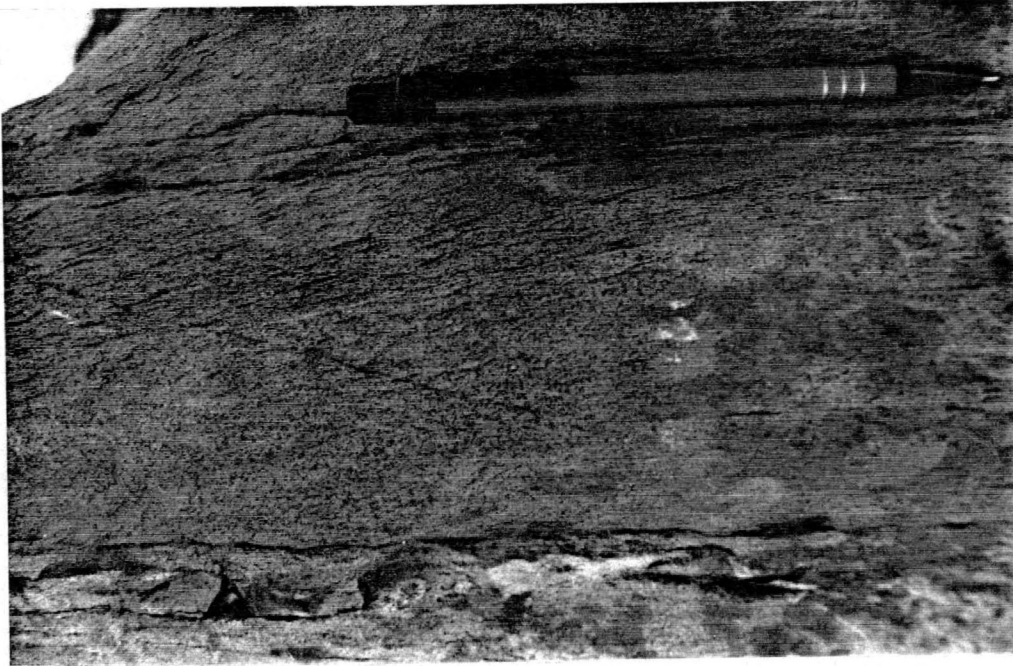


Figure 3-10b: Additional bedding/cleavage relationship from station RS9.1. Bedding (072) is indicated by the pencil parallel to the parting along bed interfaces. Cleavage within the bed above the pencil is slightly oblique (062). Top of the photo is approximately north.

The mineralogy beyond RS9.2 remains fairly consistent. Proportions of matrix and strain intensity (reflected in part by detrital quartz grain shapes) vary across the region. Local quartz recrystallization occurs near RS10. The xenoblastic quartz crystals between muscovite laths depict a granoblastic-polygonal texture. Two generations of biotite are clearly evident. Detrital, primary biotite laths are larger (1.5 mm max. dia.) and possess quartz strain shadows that show no kinematically significant asymmetries. The laths contain internal inclusion trails which are variably oriented. Secondary porphyroblastic biotite is also present and displays a preferred orientation along with muscovite.

The metasediments have generally metamorphosed to biotite-quartz-feldspar schists by station RS10.3. Naturally, at this point, biotite becomes quite abundant. Kinking, brittle offsets and quartz-filled tension gashes exist at these outcrops. Fish-mouth boudinage, where the matrix flows in a ductile manner into the boudin interspace, occurs with increasing frequency (Fig.3-11). Often the interspace also contains coarse quartz plugs. The graded beds are partially preserved; however, the more pelitic layers are unrecognizable due to the formation of larger porphyroblasts. These schists develop a well-defined schistosity from the preferred crystallographic orientation of the phyllosilicates and is supported by the preferred dimensional

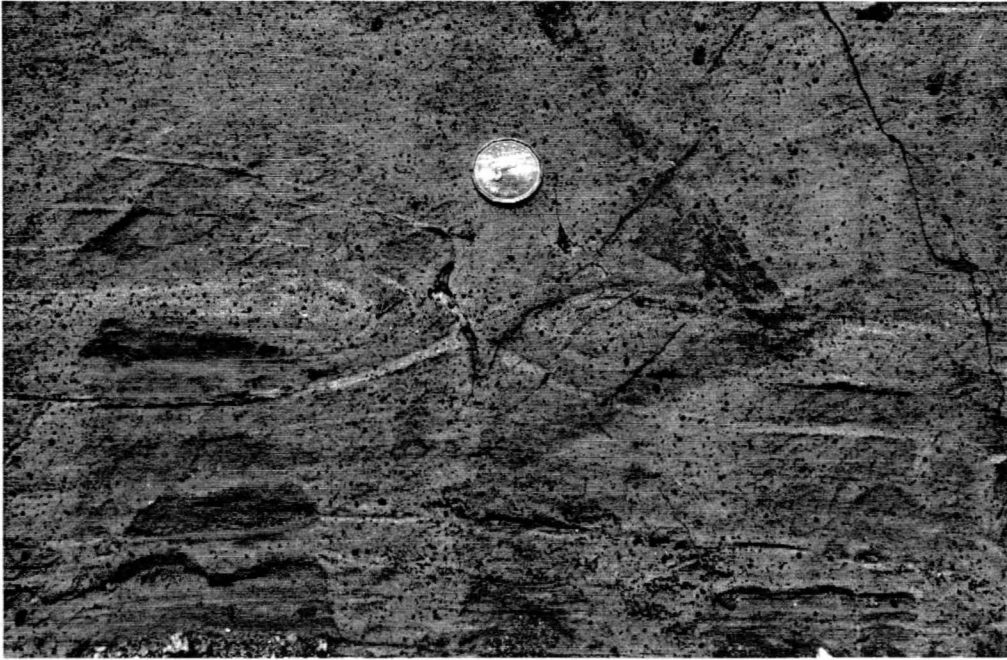


Figure 3-11: Fishmouth boudinage from outcrop RS10.3. Usually the boudin interspace area contains coarse quartz plugs. Top of photo is approximately NW.

orientation of remaining detrital quartz and feldspar clasts. The feldspars are sufficiently altered as to make identification nearly impossible.

Schist mineralogy is similar to its wacke predecessor. However, various metamorphic porphyroblasts appear, often along cleavage-parallel horizons. Embayed quartz clasts often recrystallize to form granoblastic-polygonal aggregates (especially beyond RS10.5). The matrix consists of this quartz, in addition to fine-grained sodic plagioclase, chlorite intergrown with biotite, K-feldspar, zoned zircons and monazite. By magnetic separation in a Franz-separator, pyrrhotite, magnetite, and pyrite were obtained. Green hornblende (1-2 mm long prisms) and anhedral garnets begin to appear at RS10.4. Rocks containing hornblende seem devoid of chlorite and sericite. Station RS10.65 has thin horizons of fibrolitic masses and needles of sillimanite (2 mm long strands) and garnet-rich layers (<2 mm dia.). Porphyroblasts of staurolite (some 4-5 mm long) begin to appear locally at RS10.7. They possess abundant quartz inclusions in an irregular arrangement. Station RS10.95 contains some prismatic andalusite (1 mm) and rare cordierite porphyroblasts with pleochroic haloes and polysynthetic twinning. Large garnets (<3 mm) are also present here. Beyond RS11, schists and paragneisses basically contain garnet and biotite as the main metamorphic matrix minerals.

Paragneisses develop from homogeneous biotite schists and appear regularly beyond RS11. Two types of paragneiss seem to be present within this area. Calc-silicate gneisses (stations RS10.4, RS10.41 and RS10.55) occur within the schists. Paragneisses with granitic leucosomes occur with increasing metamorphic grade (stations west of and including RS11.1).

Metamorphic differentiation within the schists produces large nearly monomineralic horizons (biotite, garnet, amphibole, etc.), or else a strongly defined (but lenticular and irregular) segregation banding of calc-silicate gneisses. These bands appear as conformable, light-coloured layers or as ovoid structures. These can break into boudins under tensile conditions due to their higher competency relative to the less competent biotite schist (fig. 3-12). The bands are also boudinaged in the third (near-vertical) dimension. They contain green hornblende (1-2 mm long laths), small anhedral garnets with many quartz inclusions, calcite, embayed quartz, plagioclase, microcline, rare biotite, and epidote. These units are more coarsely grained than surrounding schists and lack any sort of dimensional preferred orientation of calcite or ferromagnesian minerals.

Paragneiss segregation bands beyond RS11 consist of granitic rather than calcic bands. Since a gradual change occurs

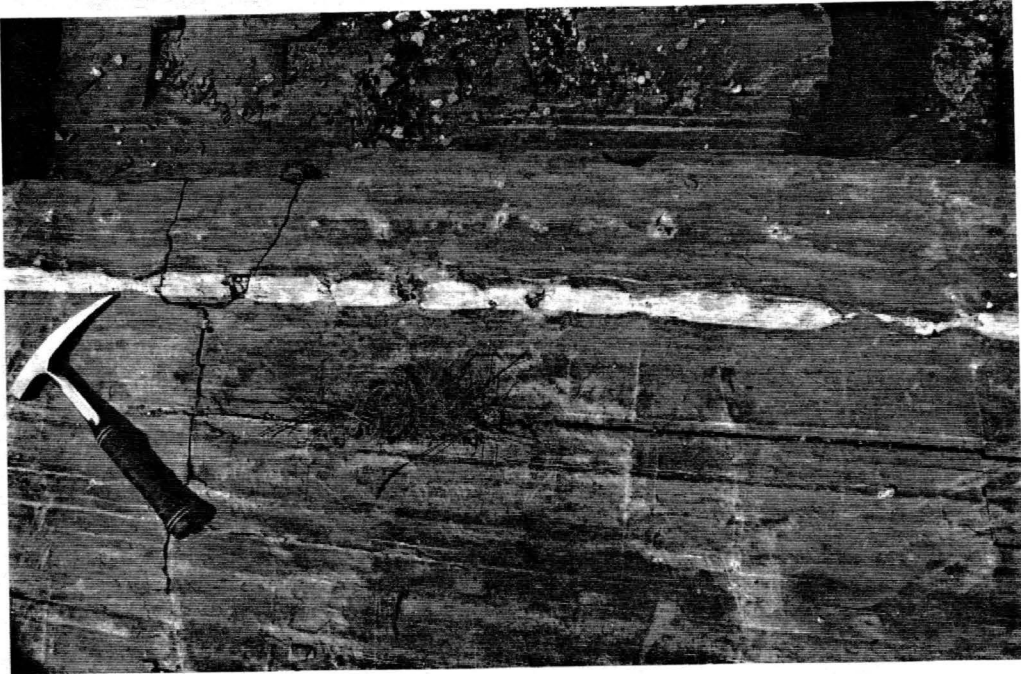


Figure 3-12: Slightly rotated and boudinaged calc-silicate layer from outcrop RS10.4. The host rock is a very fissile paragneissic biotite schist. Hammer points to the site of coarsely recrystallized quartz between boudins. (photo from south side of Hwy 11; top of photo is approximately NW).

towards nebulitic and anatectic, and finally migmatitic textures within the central Quetico belt, these paragneiss segregation bands probably are anatectically derived granitic leucosomes (plus quartz sweats). They are more competent and frequently display rotation and boudinage (fig. 3-13). These lighter-coloured, erosion-resistant bands mainly comprise coarse grained quartz and feldspar with some biotite. They demonstrate a weak preferred orientation. Some of these bands were mapped previously as "lit-par-lit granitic injections" (Giblin, 1964; Harris, 1970). The genesis of these layers is not readily apparent, and is beyond the scope of this study.

3.3.2 Migmatites

Areas formerly mapped as "lit-par-lit" magmatic injection gneisses could be more accurately described as layered or stromatic migmatites (Ashworth, 1985). The term 'migmatite' refers to medium to high grade metamorphic rocks, that are macroscopically heterogeneous; consisting of pale-coloured quartzofeldspathic bodies (leucosome) and bodies of dark-coloured and mafic-rich lithology (melanosome). Melanosome and leucosome, both being products of migmatization, can together be termed "neosome". The "paleosome" is the remnant of the protolith from which the neosome derives. The paleosome may remain intact, as in the case of metatexite migmatites; which retain original



Figure 3-13: Quartz vein showing slight rotation (kinematic sense ambiguous) at outcrop RS10.6. An erosion resistant thin calc-silicate layer runs across the bottom of the photo. (Hwy 11 along top of photo; photo top is about SSE).

fabrics (e.g. bedding, compositional and lithological layering).

Harris (1970) had used relative percentages of metasediments within Quetico outcrops to ascertain lithologies. His metasedimentary units contained >75% metasediments, migmatites had 25-75%, and granitic units had <25% metasediments. The entire migmatite area (stations RS11.6-RS12.1) consists of a combination of: biotite schist, coarse-grained leucogranite, foliated biotite granites and pegmatites. The transformation between biotite schist, paragneiss, and foliated biotite granite was thought to represent the progressive anatexis of the metasediments (Harris, 1970; Percival, et al., 1985). Through anatexis, the biotite schist paleosome experienced partial melting 'in situ', with small-scale melt segregation. Migmatites formed by 'in situ' partial melting commonly produce diatexites (which had experienced extensive partial melting, and leucosome portions predominate and original pre-migmatization structures are entirely disrupted). Sawyer (1983, 1987) observed diatexites near Huronian Lake, where previously it had been argued that no clear evidence for 'in situ' anatexis existed within outcrop structures (Percival, et al., 1985).

Sawyer (1987) performed detailed analyses of leucosomes that were discordant to the host rock layering. Discordancy implies some degree of melt intrusion. He observed compositional

and textural zoning within the discordant leucosomes. Normal, symmetrical leucosomes within the study area possess numerous, thick biotite-rich streaks or schlieren. The outcrops also include several pods and fragments of amphibolite within relatively homogeneous anatectic melts. The mineralogy of the leucosomes consists of chlorite intergrown with biotite, quartz, plagioclase, microcline and muscovite.

The formation of granites and migmatites within the thesis area may have been partially formed by the metasomatism of the Quetico metasediments (Hodgkinson, 1968). However, the partial anatexis of aluminous metasediments is also favoured (Harris, 1970; Morin, 1973; Percival, et al., 1985; Sawyer, 1987). This concept is supported by the persistence of fabrics through schists, paragneiss areas, and metatexite migmatite. Fragmented inclusions of amphibolite and metasedimentary layers within the granites and migmatites, in addition to, the presence of schlieren and migmatitic contortions also support progressive anatexis. The actual process(es) of migmatite formation is still highly controversial. The syntectonic, conformable, quartz-feldspar veining of stromatic migmatites and paragneisses may have formed through metamorphic differentiation with possible metasomatic influences. Elsewhere, discordant leucosomes, near RS12, were shown to have originated from partial melting and later influenced by fractional crystallization (Sawyer, 1987).

These post-date the penetrative regional deformation evident within lower grades of Quetico metasediments.

3.3.3 Granites

Three types of granite are present within the thesis study area (older foliated biotite-hornblende granite, pink migmatitic leucosomes, and younger muscovite granites and pegmatites). They seem to differ mainly in terms of structure and texture. The granite mineralogy remains fairly consistent: equivalent proportions of quartz, plagioclase and microcline phenocrysts. Variable proportions of coarse muscovite, biotite and intergrown chlorite also exist. Accessory minerals can include small garnets and tourmaline. The megacrysts are usually recrystallized or polygonized into lesser strained subgrains.

The oldest of the three granites is foliated, gneissose and contains a relatively large proportion of biotite (15-20%), some hornblende and a few muscovite laths (stations RS11.2, RS11.25, RS11.5). This granite has well-defined S-fabric, probably derived from bedding or schistosity or both. It is comparably finer grained and appears as inclusions within younger granites.

The second granite type consists of a pink, largely

massive, coarser grained biotite granite related to leucosome formation within central Quetico migmatites (stations RS11.6-RS12.1). It displays some migmatitic segregation but rarely any schistosity. Some bands are quite coarse and are sometimes difficult to distinguish from other pegmatites. This granite has characteristically large amounts of microcline (up to 50%) and occasional large biotite books and magnetite. Quartz and feldspar compose a fused granoblastic-polygonal matrix. This granite does cross-cut itself and other leucosomes in the form of coarser pegmatitic veins.

The youngest granite is a massive, sometimes very coarse and pegmatitic, white-grey granite. This unit can appear as large pegmatite dykes or as medium grained irregular intrusions. It intrudes along a band of stations (RS11-RS11.45) amongst schists and biotite granite remnants; but is not apparent within the migmatites. Very large muscovite books are common, as well as microcline, perthitic albite, quartz, plagioclase, biotite, and a few small garnets.

3.4 Sedimentary Depositional Environment

In the Quetico metasediments this study has not revealed any major internal tectonic structures. A single planar cleavage schistosity and mineral or shape lineation fabrics. The Quetico

metasediments display many of the primary sedimentary features associated with turbidity current deposits (Wood, 1980). Such features in this study include locally preserved graded bedding with abrupt bases with some soft sediment deformation structures.

The interlayered sequences of wackes, slates and argillites correspond to A, B, or ABE-type turbidites (Wood, 1980) derived from the Bouma Sequence model for classical turbidites (fig. 3-14). The apparent absence of agitated shallow water structures supports a deep water depositional environment. The parallel bedding and absence of channelization, typical of classical turbidites, indicates smooth-fan environments near outer smooth suprafan lobes and basin plains (Walker, 1984).

The compositions of clasts within the Quetico metasediments imply a mixed volcanic-plutonic provenance (Ojakangas, 1985; Wood, 1980). Sediment sources were probably epiclastic with some degree of autoclastic, penecontemporaneous reworking of pyroclastics. Any of the few observed lithic fragments have ambiguous identities due to the combined effects of diagenesis, burial and regional metamorphism.

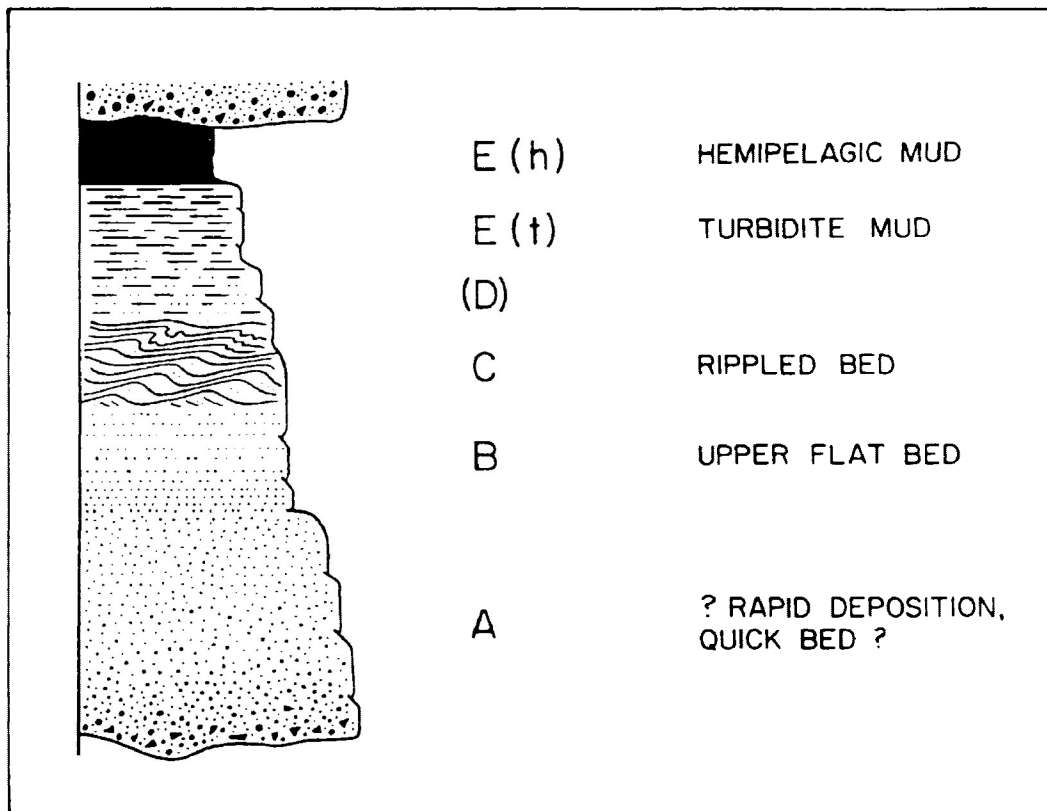


Figure 3-14: Divisions of the Bouma sequence for classical turbidites:

- A) - massive or graded
 - B) - sandy parallel laminations
 - C) - rippled and/or convoluted
 - D) - delicate interlaminations of silt and mud
 - Et) - mud introduced by turbidity current
 - Eh) - hemipelagic background mud of the basin
- (from Walker, 1984).

3.5 Regional Metamorphism

The Quetico metasediments and the Shebandowan volcanics and related intrusives to the south meet along an east-west steeply dipping boundary. Dextral transpression is believed to have affected the boundary. Figure 3-15 shows lithology belts paralleling a steep metamorphic gradient. The symmetrical metamorphic zonation ranges from low greenschist facies in the Shebandowan belt, through the upper stability limit of chlorite, and through the isograds of biotite, garnet and staurolite. To the north, the metamorphic gradient peaks at medium-pressure amphibolite facies. Paragneisses form within the central Quetico belt and anatectic melt produced migmatites in places.

Throughout the entire Quetico belt, all sequences possess the characteristic zonation of low pressure facies series to andalusite-sillimanite facies culminating in migmatite and granite intrusion, usually spanning a distance under five kilometres (Percival, 1989; Pirie and Mackasey, 1978). The spatial arrangement of isograds seems related to the width of the belt. In narrower portions, the isograds are more closely spaced and probably dip steeply; whereas widely spaced isograds in wider portions could dip more gently (Percival and Stern, 1984). It was inferred by Percival (in Percival and Stern, 1984) that the

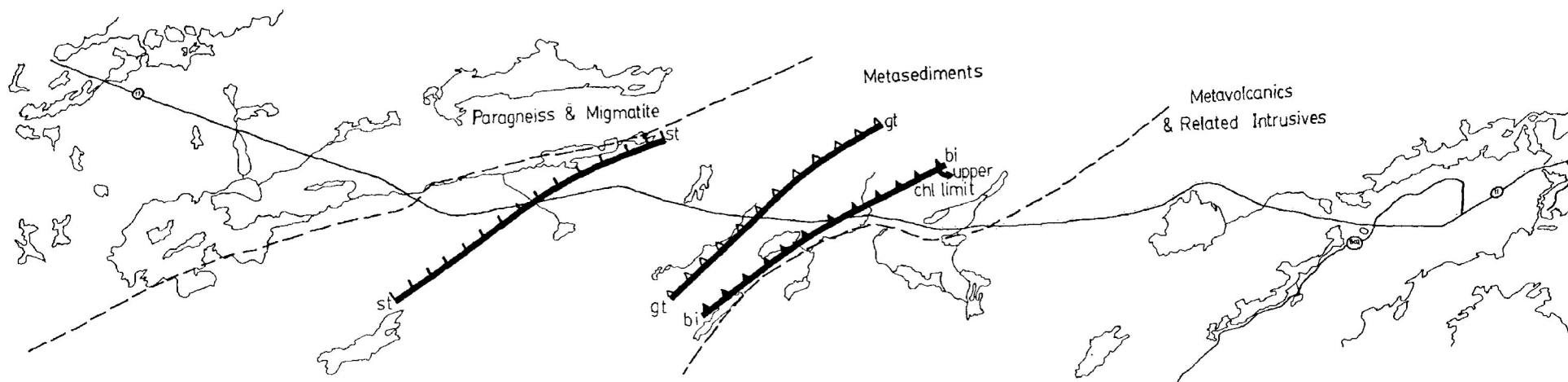


Figure 3-15: Metamorphic isograd map of relatively steep metamorphic gradient parallel to lithological belts at the Shebandowan-Quetico boundary. Lithological boundaries compiled from: Gibling (1964), and Harris (1970). Isograd data taken from Pirie and Mackasey (1978) and this study.

Quetico schists were metamorphosed at depths of less than 10 km by intrusive granite pluton heat sources that were transported to higher structural levels. Migmatites and granites that were derived from sedimentary sources at mid-crustal depths had possibly deeper crustal level heat sources (Sawyer, 1987).

Pirie and Mackasey (1978) performed extensive metamorphic analyses within this study area as well as other regions within the Quetico belt. Their study reveals that the grade of metamorphism at the southern Quetico boundary is higher than the grade at the northern boundary in the vicinity of the Quetico Fault. Contact metamorphism from the Burchell Lake Pluton might possibly form an additional contribution to locally restricted metamorphism in this area.

The lowest grade outcrops within the thesis area consist of greenschist facies metavolcanics and adjacent metasediments. These sediments contain a stable pelitic assemblage of sericite, chlorite, and epidote. Two generations of biotite are visible: coarse, stubby and ragged porphyroblasts showing variable orientation, surrounded by smaller laths displaying a preferred crystallographic orientation. The larger biotite laths contain many pleochroic halos, poikiloblastic quartz and are flanked by symmetrical strain shadows. Feldspar clasts are variably sericitized and quartz clasts possess undulose extinction.

Inward from the belt margin, chlorite and sericite decrease in abundance and biotite stabilizes. The upper stability limit of chlorite and sericite roughly coincides with the biotite isograd (Fig. 3-15) near station RS9.1. Further inward, quartz veins become more prominent in outcrops. Local quartz grain recrystallization of formerly embayed quartz grains is achieved at RS10 in the form of a granoblastic-polygonal texture. Graded bedding is obscured, beginning at RS10.3, due to the formation of larger porphyroblasts. Hornblende and garnet are more prominent at RS10.4. Other metamorphic mineral appearances include: fibrolitic sillimanite (at RS10.65), staurolite (at RS10.7), and some andalusite (at RS10.95) and a few identifiable cordierite porphyroblasts with pleochroic haloes (also at RS10.95). However, beyond RS11, the schists contain garnet and biotite as the main metamorphic minerals.

Pirie and Mackasey (1978) had observed fibrolite within andalusite (not seen in this study), suggesting andalusite-sillimanite transition conditions of 550° C and 3 kb. They also postulated conditions of 660° C and 3.5 kb obtained from a biotite-garnet-cordierite-sillimanite "melt" assemblage within rocks from outcrops at the onset of migmatization.

CHAPTER 4 - STRUCTURAL FIELD OBSERVATIONS

Structural field analysis within the field area is hampered by the absence of readily recognizable marker horizons. The combined use of MSA techniques, younging directions and bedding-cleavage relationships, in addition to field observations assist in describing regional structure. Both metavolcanic and metasedimentary rocks possess only a single, penetrative tectonic fabric that is present as a slaty cleavage or phyllitic schistosity. Coarser psammitic units have a crude continuous cleavage. With increasing metamorphic grade, schistosity becomes more predominant and paragneissic segregations form.

The entire transect contains a similarly oriented penetrative cleavage generally striking E-W with nearly vertical dips. Primary sedimentary and volcanic depositional features are preserved locally. Increased metamorphic recrystallization towards the centre of the Quetico belt gradually obliterates all primary bedding features. Anatexis and recrystallization within the migmatites at the western extremity of the transect creates difficulties for structural measurement and interpretation. McLellan (1984) has shown that the presence of as little as 30% melt, can drastically alter the deformational response of the rock to that of a viscous melt flow mechanism. The failure to recognize the geometrically variable structures as syn-anatectic

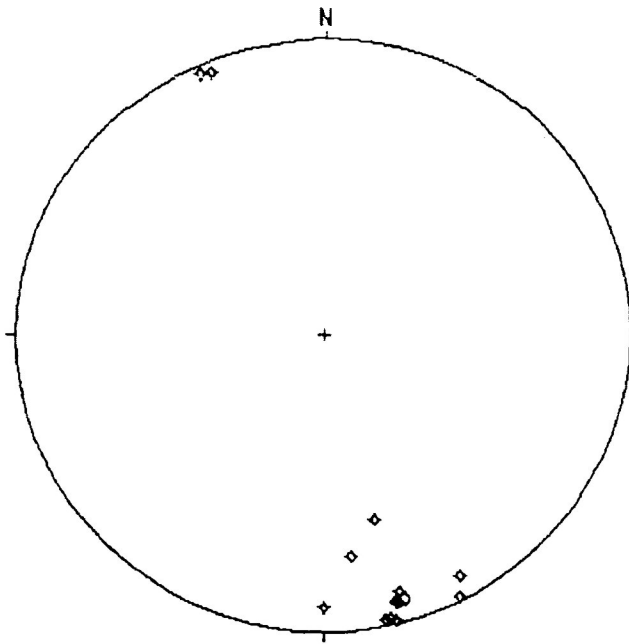
folds may result in the misinterpretation of the structural history of the migmatites with respect to regular folding in surrounding lower-grade areas. These anatectic folds may mimic structures similar to those formed by polyphase deformation. Consequently, only a few very consistent structures were measured at migmatite outcrops.

4.1 Primary [S0] Bedding Surfaces

Many primary bedding features within the turbiditic metasediments and pyroclastic metavolcanics are locally preserved. The metavolcanics display bedding in places and show abundant flow textures despite local ductile behaviour that has further distorted and elongated some pyroclasts. The metasediments, of lowest metamorphic grade adjacent to the metavolcanics, possess consistently oriented bedding [S0] surfaces (Fig. 4-1). The beds vary only slightly and have an average orientation of 074/83NW. Bedding measurements are listed in Appendix II.

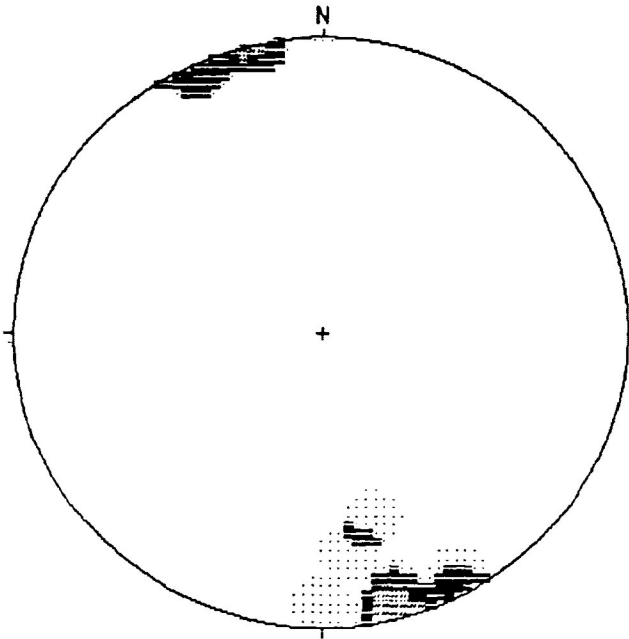
4.2 [S1] Cleavage Surfaces

Like bedding, the cleavage surfaces for both the metavolcanics and metasediments possess a relatively consistent orientation throughout the study area. Some local variation



BEDDING [S0] FIELD MEASUREMENTS

Projection	Schmidt
Number of Sample Points	13
Mean Lineation Azimuth	163.6
Mean Lineation Plunge	7.0
1st Eigenvalue	12.35
2nd Eigenvalue	0.47
3rd Eigenvalue	0.18
LN (E1 / E2)	3.265
LN (E2 / E3)	0.951
(LN(E1/E2)) / (LN(E2/E3))	3.435
Spherical variance	0.3232
Rbar	0.6768



BEDDING [S0] FIELD MEASUREMENTS

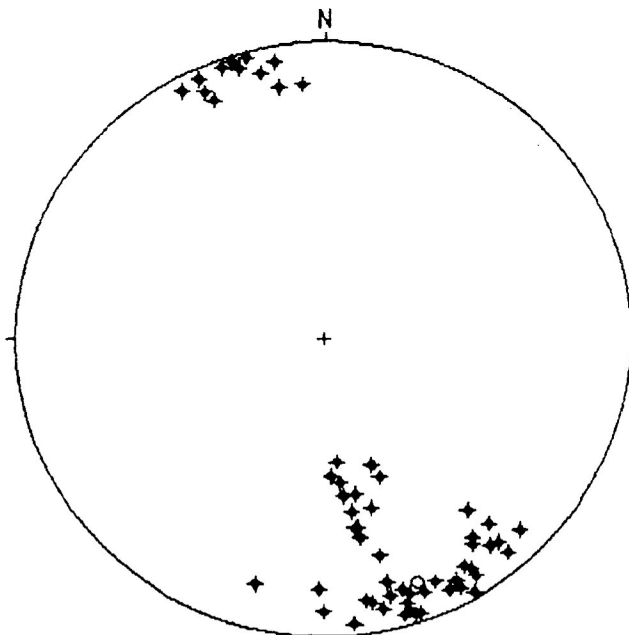
Step Function Grid	
Number of Sample Points	13

	0.0 to 12.0 %
	12.0 to 24.0 %
	24.0 to 36.0 %
	36.0 to 48.0 %

Figure 4-1: Upper stereonet displays consistently oriented poles to bedding planes. Average bedding orientation is 074/83NW. Plotted beds include only those clearly identifiable as [S0] bedding surfaces. Lower stereonet is a density plot of the above data.

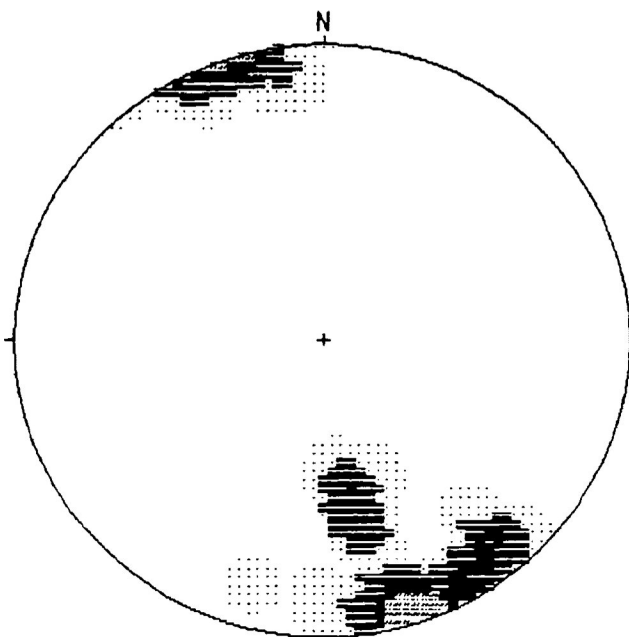
occurs around the margin of the Burchell Lake Pluton. In very low and higher metamorphic grade rocks, bedding and cleavage is difficult to distinguish. In places, a fine grained schistosity or slaty cleavage creates a small but perceptible dihedral angle with bedding.

Cleavage within the metavolcanics is relatively consistent with the metasediment trends. The average cleavage orientation is 070/77NW for the entire transect (Fig. 4-2). Cleavage measurements for each outcrop are listed in Appendix II. Cleavage in these rocks, regardless of lithology, comprises of a combination of a preferred crystallographic orientation of phyllosilicates and a preferred dimensional orientation of larger clasts. The metavolcanic outcrops have zones of intense fissility. Sheared pyroclastics reveal a very good S-tectonite flattening. Very low grade coarse clastic beds can contain a crude, widely spaced stylitic cleavage. Initially, cleavage is weak, but becomes more manifest by station RS9.1. Beyond RS9.2, bedding/cleavage obliquities become dubious (with a few rare exceptions). A few examples of dextral (when viewed in plan) kinematic indicators are visible in thin-section. Rotated porphyroblasts with inclusion trails were discovered from thin-sections from about four outcrops. In higher grade schists, over ten good Z-folded quartz veins were visible on relatively horizontal outcrop surfaces.



FOLIATION [S1] FIELD MEASUREMENTS

Projection	Schmidt
Number of Sample Points	60
Mean Lineation Azimuth	159.7
Mean Lineation Plunge	12.8
1st Eigenvalue	52.46
2nd Eigenvalue	5.20
3rd Eigenvalue	2.34
LN (E1 / E2)	2.312
LN (E2 / E3)	0.797
(LN(E1/E2)) / (LN(E2/E3))	2.903
Spherical variance	0.4223
Rbar	0.5777



FOLIATION [S1] FIELD MEASUREMENTS

Step Function Grid
 Number of Sample Points 60

	0.0 to 6.0 %
	6.0 to 12.0 %
	12.0 to 18.0 %
	18.0 to 25.0 %

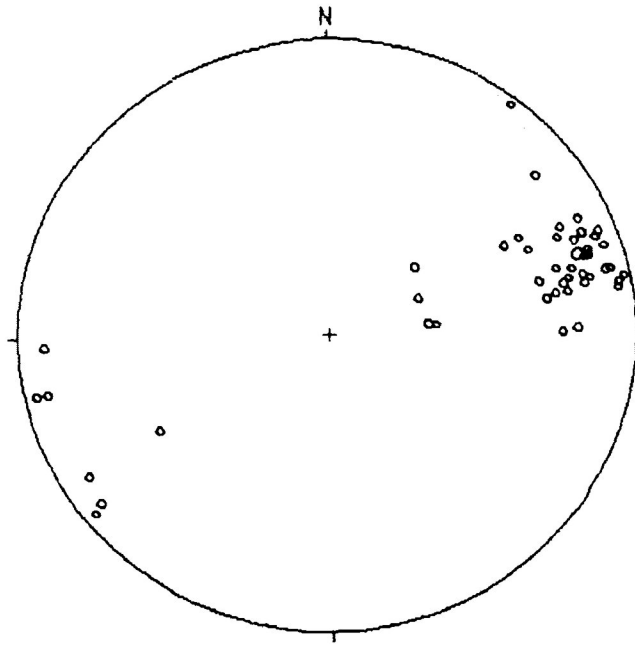
Figure 4-2: Upper stereonet displays clustered poles to [S1] cleavage for the entire thesis transect of both metavolcanic and metasediment lithologies. Average cleavage orientation is 070/77NW. Lower stereonet is a density plot of the above data.

4.3 [L1] Mineral Lineations

Penetrative "stretching" lineations of aligned L-S fabrics of chlorite and actinolite, as an integral part of the schistose fabric, are common within the mafic metavolcanics. Lineations in felsic metavolcanics are less abundant and must be carefully distinguished from non-penetrative slickenfibres. The lineations from both metavolcanics and metasediments show very similar, gently east-plunging, orientations (Fig. 4-3). However, they may originate differently. The metavolcanic lineations possibly derive from shearing. The metasediments display only one, more consistently oriented lineation. It is in some cases a bedding-cleavage intersection lineation with an orientation parallel to both bedding and cleavage planes. All linear data from the transect are listed in Appendix II. The regional average lineation is about 072-15.

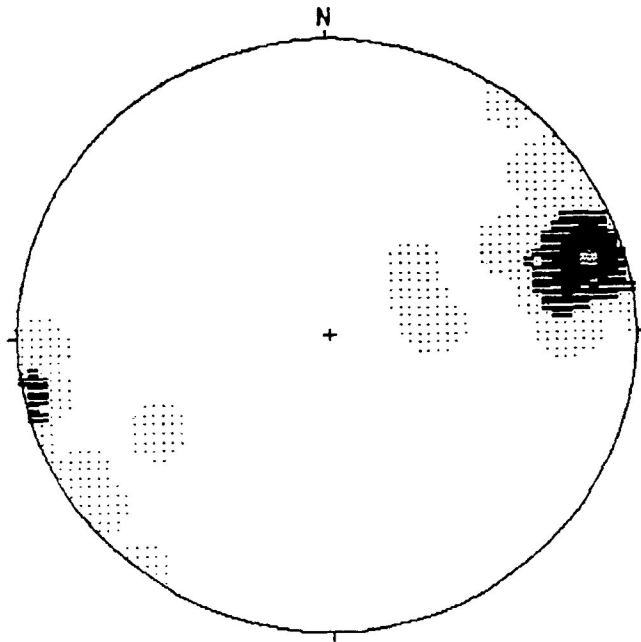
4.4 [S2] Late Shearing and Kinking

Several occurrences of small-scale structures characteristic of brittle or semi-brittle deformation are evident across the transect. They disrupt bedding and cleavage structures and probably represent the last regional episode of deformation. These small-scale structures include: en echelon tension gashes, brittle-ductile shears and kink bands. They are



LINEATION FIELD MEASUREMENTS

Projection	Schmidt
Number of Sample Points	47
Mean Lineation Azimuth	72.1
Mean Lineation Plunge	14.8
1st Eigenvalue	41.38
2nd Eigenvalue	4.36
3rd Eigenvalue	1.25
LN (E1 / E2)	2.249
LN (E2 / E3)	1.248
(LN(E1/E2)) / (LN(E2/E3)) ..	1.803
Spherical variance	0.3109
Rbar	0.6891



LINEATION FIELD MEASUREMENTS

Step Function Grid	
Number of Sample Points	47

	0.0 to 10.0 %
	10.0 to 20.0 %
	20.0 to 30.0 %
	30.0 to 40.0 %

Figure 4-3: Upper stereonet displays metavolcanic and metasediment [L1] stretch (and intersection) lineations. The lineations show a gently east-plunging subhorizontal preferred orientation with 072-15 as an average orientation. Lower stereonet is a density plot of the above data.

all referred to as [S2] surfaces arbitrarily assigned to a late [D2] episode of deformation.

Recently, Peterman and Day (1989) studied local Proterozoic reactivation of the late Archean Quetico Fault. Using Rb-Sr techniques, they were able to date the formation of pseudotachylite within the fault at 1947 ± 23 Ma (Peterman and Day, 1989). Proterozoic reactivation of pre-existing faults seems to coincide with episodes of compressional tectonics associated with orogenic events at the margins of the Superior Province (q.v. Hoffman, 1988). The NW-directed compression from these events, seems to relate to the orientation of many brittle kink bands and some brittle and brittle-ductile shears across the area.

The [S2] orientations (e.g. kink band orientations; Fig. 4-4) are fairly variable. However, most [S2] structures were seen in outcrop to possess generally NW or NE orientations; implying possible conjugate sets. These surfaces produce small and localized displacements. They appear irregular and discontinuous in outcrop and are not very noteworthy at mappable scales.

Kink bands generally are less than 3 cm in width. They are usually north-trending or range in orientation between 315-

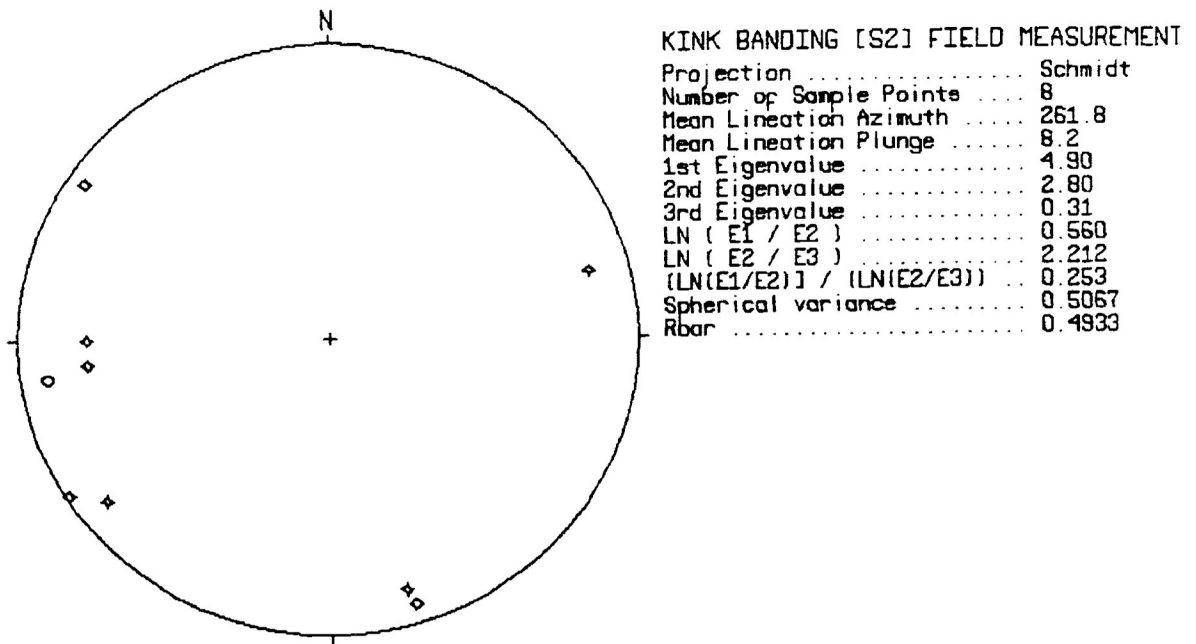


Figure 4-4: Upper stereonet plot is of a few [S2] kink band poles that had consistent orientations. A crude average orientation would occur at 352/82E. Generally of NW and NE trend, the scatter of the data may be due to conjugate kink sets.

330° and 015-030°, with subvertical dips. A crude average from some kink bands in Figure 4-4 yields an orientation of 352/82E. Both sinistral and dextral kinematic sense was observed within kink band offsets (maximum 3 cm offset).

Brittle offsets and brittle-ductile shears displayed both sinistral and dextral kinematic senses. They have variable orientations, and no conjugate sets are determinable. Some brittle offsets contain unfilled or coarsely quartz-filled tension gashes. These [S2] surfaces also vary in orientation generally between trends of 330° and 030°. The shear zones are discontinuous, but locally bend or offset cleavage and bedding with small displacements. The dimensions of the shear zones vary but rarely exceed 60 cm in length.

4.5 Bedding-Cleavage Relationships

The thesis area is dominated by one pervasive east-west striking "continuous" cleavage. It cuts across primary bedding fabrics, where preserved. Bedding-cleavage relationships combined with local younging indicators can assist in the delineation of folds and inverted stratigraphy. Such relationships are rare in outcrop in this area, due to many hindrances such as: paucity of outcrop, recrystallization of graded metasedimentary beds, and some very small dihedral angles

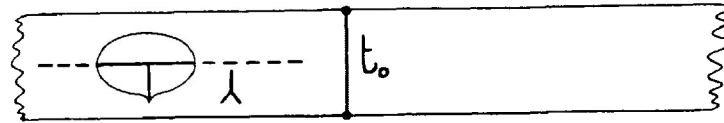
between bedding and cleavage. These restrictions severely limit the data available for extensive study. Actual major fold closures were never observed in outcrop. Small folds were also rarely found. The exception being a single small intrafolial fold (at station RS10.05) where bedding-parallel cleavage cuts a more pelitic minor fold (3 cm across) closure.

The general scarcity of superimposed microfabrics suggests an absence of regionally significant polyphase deformation. Farther west, within the Quetico belt, polyphase deformed terrains have been examined (Poulsen, et al., 1980). Multiple deformation episodes may also exist in the Shebandowan-Wawa subprovince (Stott and Schnieders, 1983). The boundaries of the Quetico belt were shown elsewhere to have experienced complex folding. The Quetico/Wawa boundary to the east, in the Hazelwood Lake area, is deformed by two episodes of steeply plunging isoclinal folding (Kehlenbeck, 1983). The northern Quetico boundary with the Wabigoon subprovince incorporates sheath folds developed during dextral transpressive deformation (Borradaile, et al., 1988); but they also developed during a single tectonic episode. However, within the area of this study, no evidence for large-scale stratigraphic inversion or substantial, region scale refolded folds has been revealed (see also Giblin, 1964; Pirie and Mackasey, 1978; Borradaile and Schwerdtner, 1984).

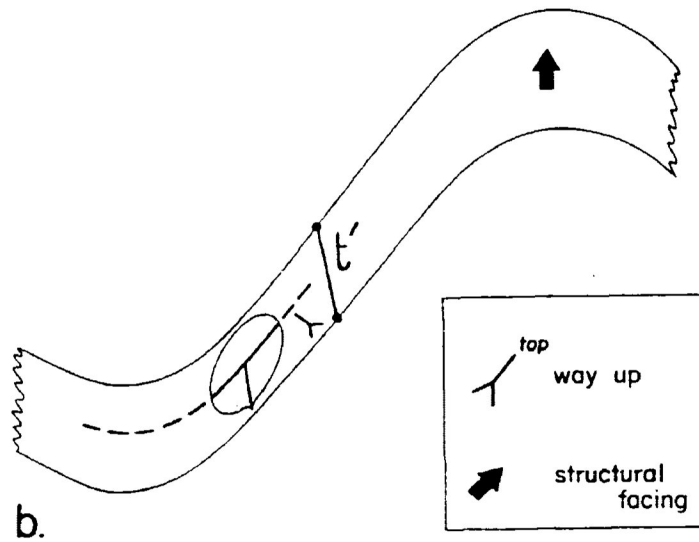
4.5.1 Local Younging Directions

A few outcrops containing graded bedding and pillows yielded local younging directions. Younging criteria for graded bedding in low-grade metasediments was based on the idealized Bouma turbidite sequence (Walker, 1984). A fining-upwards "way-up" direction within single beds or laminae could then be determined. Younging directions become less reliable with increased metamorphic grade for the following reason. Metamorphism promotes the porphyroblastic recrystallization of finer sediments selectively; this may cause an apparent reversal in younging directions. Younging data, from this study, were taken from reliable, outcrop exposures exhibiting recognizable original graded beds.

Way-up directions within the metavolcanic belt were procured from graded beds of pyroclastic debris flows and from cusped pillows. Younging is well exposed at one tuff locality and three pillow outcrops. The pillows are located near the contact with the metasediments and appear relatively undeformed. Strained pillows have altered shapes and require special attention when establishing younging directions (Borradaile, 1982). Initially, the long axis of the pillow denotes bedding. After straining, this axis may no longer reliably indicate bedding due to alteration of shape and cusp position. The



a.



b.

Figure 4-5: Determination of younging directions from deformed pillow lavas. After deformation (b), cusp position and shape no longer clearly indicate younging. Instead, approximate way-up direction is given by a line, perpendicular to its long axis, away from the side of the pillow with the cusp.
(from Borradaile, 1982)

approximate way-up direction, in strained or unstrained pillows, is given by a line directed away from the side of the pillow with the cusp and perpendicular to the long axis (fig. 4-5).

4.5.2 Structural Facing Directions

The rarity of finding both way-up directions and a fold closure on the same outcrop; coupled with the general outcrop paucity and effects of metamorphic alteration, makes the delineation of major fold structures nearly impossible. The technique of "structural facing" (Shackleton, 1958) describes the younging direction of strata at the hinges of primary folds. This method was applied to beds where minor fold closures were not necessarily visible in outcrops (Borradaile, 1976). It was demonstrated that, if the cleavage is axial planar, then the projection of the younging direction onto the axial planar cleavage is parallel to the structural facing direction of primary folds (see figures 4-6a and 4-6b). Structural facing has been further applied to terrains experiencing polyphase deformation (Poulsen, et al., 1980).

The direction of structural facing then indicates the overall younging of the folded stratigraphic sequence. The structural facing of a fold is defined then as the direction of the younging of strata along a line perpendicular to the trace of

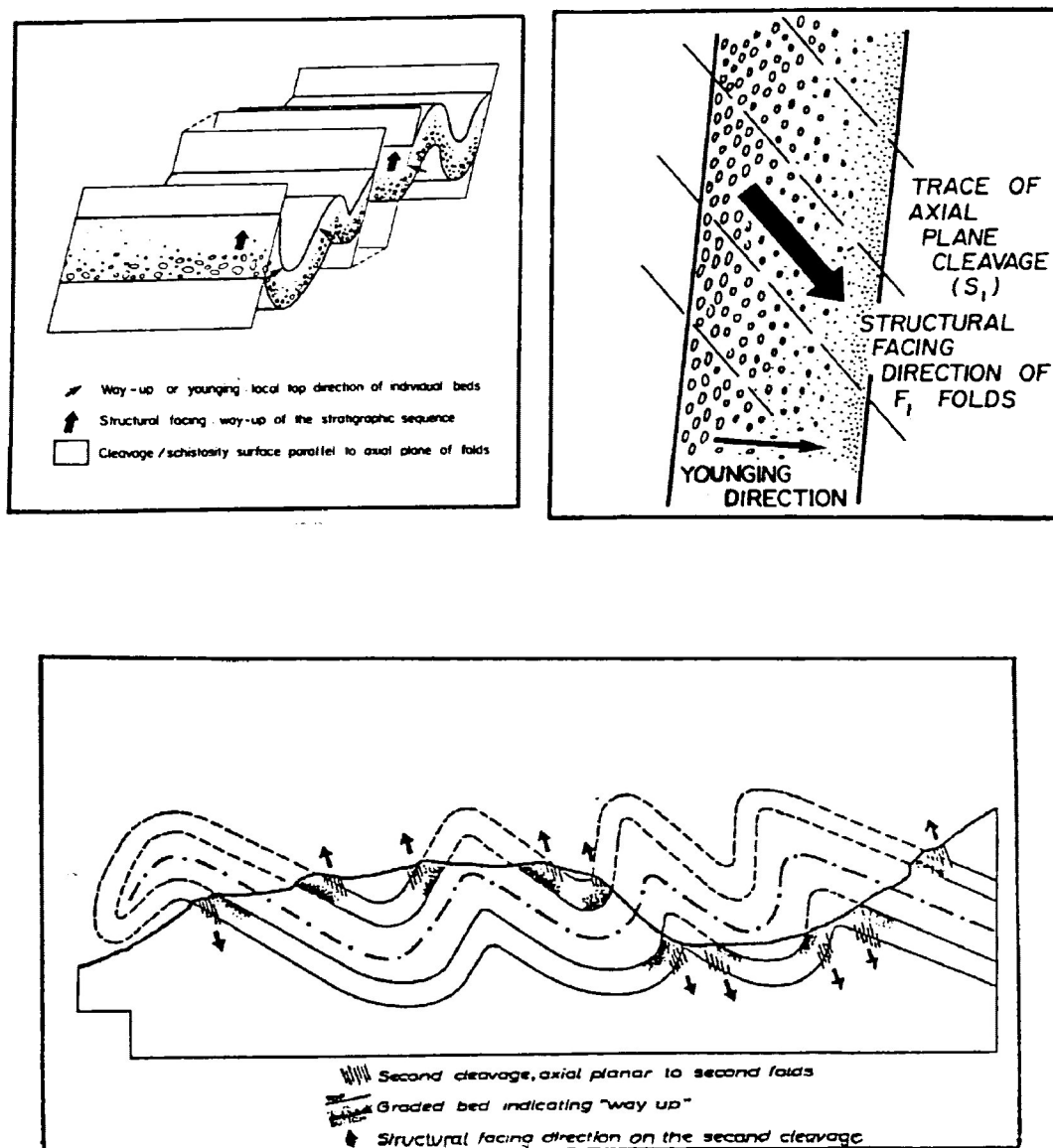


Figure 4-6: Theory of "Structural Facing";

- (a) - Structural facing is determined by younging direction on axial planar cleavage. Though younging directions vary throughout the fold, structural facing remains constant.
(from Borradaile, 1976)
- (b) - Plan outcrop view of bedding/cleavage relationship. Structural facing direction is the projection of the younging direction onto cleavage parallel to the axial plane of folds.
(from Poulsen, et al., 1980)
- (c) - Example of an overturned fold and the resulting reversal in structural facing polarity.
(from Borradaile, 1976)

the bedding in the cleavage (ie. the bedding-cleavage intersection lineation). The consistency of this direction, despite variable local younging indicators, is exemplified in Figure 4-6c. Reversals in structural facing imply secondary folds formed in previously folded strata.

All local younging directions, where visible within the transect, are generally north-trending (Fig. 4-7). The structural facing directions are also consistent. Within the metasedimentary belt, they have an east-facing component; generally in a gently upward-facing orientation. The directions of structural facing from the metavolcanics are less reliable. They young to the north but have west and upward-facing directions.

The easterly upward structural facing in this area corresponds to the dominant structural facing directions, elsewhere, at the northern Quetico/Wabigoon boundary (Borradaile, et al., 1988). These orientations were attributed to syn-kinematic or to reactivation movements along the Quetico Fault. However, the steep upright sheath folds found at that boundary, have no counterparts in this study area. No strong evidence has been uncovered to suggest large-scale stratigraphic inversion (ie. major fold nappes) or upright sheath folds within this study area. Similarly, within the metavolcanics, north-younging upward

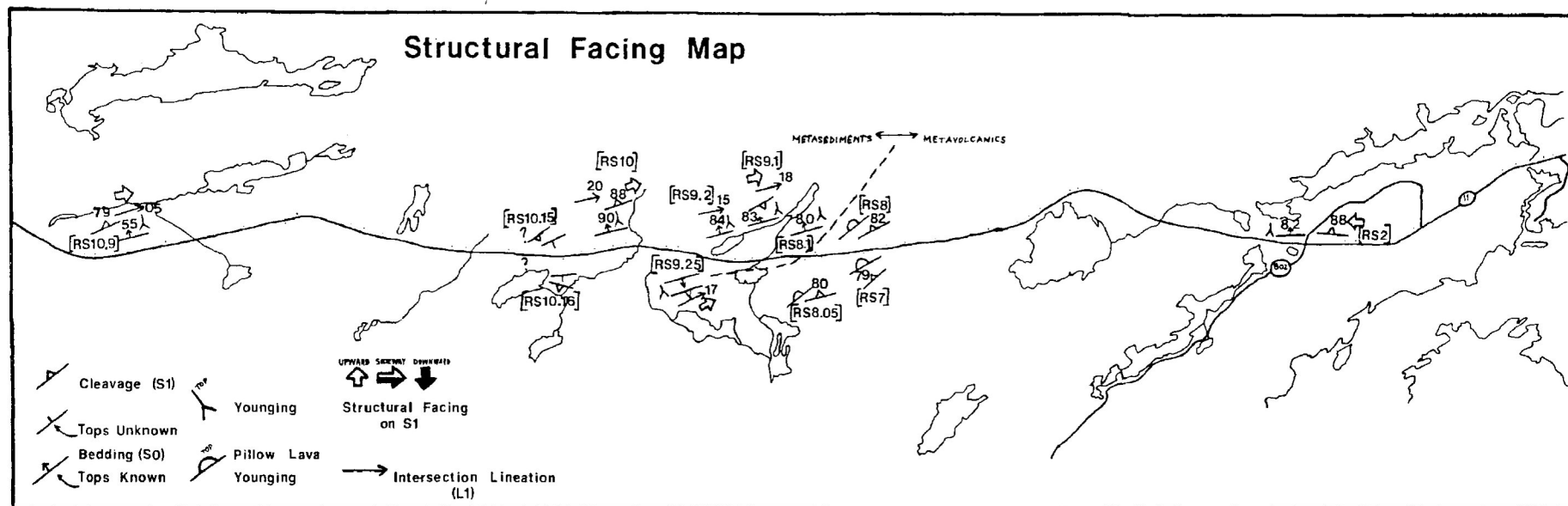


Figure 4-7: Structural facing and younging indicators across the transect. Stations numbers are given in square brackets. RS2 data derived from rhyolite-agglomerate bedding with superimposed cleavage. RS7, RS8 and RS8.05 were pillow lavas with top indicators (cleavage at these sites were local sheared fabrics). The remaining stations to the left of the dashed line were turbiditic metasediments with discernible graded bedding in places, and bedding, cleavage and intersection lineations.

facing directions to the west are relatively consistent. The data is too sparse to make significant regional interpretations. Eastward structural facing directions (both south and north-younging) were observed, to the east, at Middle and Lower Shebandowan Lakes (Borradaile and Schwerdtner, 1984). This apparent reversal in structural facing direction within the Shebandowan-Wawa metavolcanics may be due to the curvature of hinge lines of major folds within the synformal structures that were originally described by Giblin (1964) in the study area.

CHAPTER 5 - MAGNETIC SUSCEPTIBILITY ANISOTROPY (MSA)5.1 Introduction

The phenomenon of magnetic anisotropy has only been studied recently as an aid to petrofabric analysis. Magnetic susceptibility was observed as a geologically significant fabric detector based on information obtained on how a sample interacts with an applied magnetic field (Graham, 1966; Bhatal, 1971). Recent innovations, especially in the fields of computer-based technology, have allowed the measurement of magnetic susceptibility with greater precision and much greater speed.

Magnetic susceptibility anisotropy (MSA) was initially examined in order to avoid specimens with strong anisotropy as these are difficult to interpret in terms of remanent magnetism. It was also realized that the original rock susceptibility can be modified during structural deformation (Graham, 1966). MSA was then investigated in igneous, sedimentary, and deformed metamorphic rocks as a cause of systematic deviations in magnetization vectors that are a consequence in studies of remanence. The geological applications were greatly expanded (Hrouda, 1982) to include the fabric of various ferrimagnetic and paramagnetic minerals within the rock and the effects of tectonic strain upon the MSA. It has been found that a susceptibility

ellipsoid with principal susceptibility axes often roughly corresponds to principal strain directions.

Within a crystal, magnetic susceptibility can be represented as a tensor. The principal values and orientations depend upon the orientation of the crystal lattice. Hence, lattice orientation controls the measured value of susceptibility measured in any given direction, with the exception of certain high susceptibility ferrimagnetic materials such as magnetite; in which case the shape of the mineral controls the susceptibility. Generally, the greatest length of the grain is approximately the direction of maximum magnetic susceptibility, with the minimum susceptibility lying perpendicular to it, whether the susceptibility is shape or lattice-controlled.

Magnetic susceptibility anisotropy exists within rocks where the individual magnetic crystals possess some preferred orientations of either long axes (magnetite) or crystallographic axes (other minerals). A sample containing a range of susceptibilities, if measured, would yield the vector sum of the various anisotropies of all contributing grains, or the bulk susceptibility. MSA is detected by observing the interaction of a sample with an applied magnetic field. The consequential automatic and immediate vector summations, over the bulk of the rock make MSA a valuable technique for petrofabric study.

The interaction of the sample of magnetic minerals with an applied magnetic field of certain magnitude (H), produces an internal field of magnetization of measurable magnitude (J). For weak external magnetic fields, the induced magnetization follows a linear relationship: $J = k \cdot H$, where the proportionality constant, (k), is the magnetic susceptibility. The directional variability of (k) is the crucial property of the anisotropy of magnetic susceptibility.

Six various causes of anisotropy in rocks were distinguished (Bhatal, 1971):

- (i) Shape Anisotropy: where non-equidimensional magnetic grains have a preferred orientation of long axes and/or crystallographic axes.
- (ii) Magnetocrystalline Anisotropy: where magnetization lies along certain crystallographic axes within an aligned set of crystals.
- (iii) Anisotropy of Domain Alignment: caused by the orientation of magnetic domains with respect to the applied field, a special case of (ii).
- (iv) Anisotropy of Linear or Planar Strings of Magnetic Grains: a special case of (i).
- (v) Exchange Anisotropy: describes ferrimagnetic and antiferromagnetic domain interaction.
- (vi) Stress-Induced Anisotropy: involves

magnetostriction, a dimensional or magnetic change due to an applied stress.

However, the most important prerequisite for MSA, is the presence of various magnetic minerals.

5.2 Magnetic Mineralogy

Magnetic minerals, usually containing iron or manganese, are common in almost all rocks. They can be classified as diamagnetic, paramagnetic, and ferrimagnetic (Strangway, 1970; Owens and Bamford, 1976). The physical and spatial alignment of the magnetic minerals constitute the lithological magnetic fabric. Ferrimagnetic minerals, such as magnetite, hematite, and pyrrhotite, are the most essential for rock magnetism. However, for the analysis of magnetic anisotropy some paramagnetic silicates are equally important (Owens and Bamford, 1976; Hrouda, 1982; Borradaile, et al., 1987). Diamagnetic and paramagnetic minerals display only induced magnetization and have low to moderate susceptibilities (about $10E-06$ and $10E-04$ SI units [volume basis] respectively). Ferrimagnetic minerals have a very strong susceptibility ($>10E-02$ SI units). They can also support a remanent magnetization.

These various types of susceptibility are determined by a mineral's atomic and electronic structure. The force of an

external magnetic field upon a sample effects electron motion. This is the motion responsible for the creation of magnetic dipoles that result in a secondary induced magnetic field.

5.2.1 Diamagnetic Minerals

The orbital electrons, about an atom of a magnetic mineral, generate simple dipoles. In the case of diamagnetic minerals, these dipoles are randomly oriented, resulting in a lack of net magnetism. When these minerals are exposed to an external magnetic field, the force acting on the orbital electrons slows them down. This effect weakens the magnetic dipole and produces a small negative susceptibility (k) value.

Weak magnetic responses arise from diamagnetic minerals such as quartz, feldspar, and calcite. If both diamagnetic and even small amounts of paramagnetic impurity are present together in a rock, the stronger paramagnetic fraction can overwhelm the diamagnetic anisotropy.

5.2.2 Paramagnetic Minerals

Electrons spin on their own axes, and in paramagnetic minerals this contributes greatly to the magnetic properties, in addition to the simple diamagnetic orbital electron motion. This

motion creates a dipole with a strength that remains constant in the presence of an external magnetic field. In substances with unpaired orbital electron spins (ie. in substances with an odd number of electrons or odd atomic number), the individual electrons act as small permanent magnets. These will reorient themselves from randomness to the direction of the magnetic field. The realignment of the spin axes is the paramagnetic effect and it increases the total magnetism. Substances with even atomic numbers possess diamagnetic properties. The paramagnetic effect is even more pronounced in the transition series of elements. Their overlapping electron shells contribute up to five unpaired electrons and large magnetic effects.

Only a few ions display significant paramagnetic properties in natural minerals: Mn^{2+} , Fe^{3+} , and Fe^{2+} . Common paramagnetic silicates (ie. amphiboles, chlorites, micas and other ferromagnesian) can account for a major portion of most metamorphosed rocks. Ferrimagnetic iron oxides with high magnetic susceptibility can be absent, or present in only trace amounts in these rocks. Consequently, the anisotropies of the paramagnetic silicates are relatively high (Borradaile, et al., 1986; 1987) and may dominate the overall magnetic susceptibility anisotropy.

5.2.3 Ferrimagnetic Minerals

The mutual alignment of spin axes within magnetic minerals is related to an exchange energy. Some substances maximize this energy by aligning spins so that neighbouring atoms have parallel spin (fig. 5-1a). Such substances possess properties of ferromagnetism, where a strong internal spontaneous magnetization is created and maintained even in the absence of an external magnetic field.

Naturally occurring rocks seldom have simple ferromagnetic minerals. Instead, a complex arrangement of atomic spins within the crystal lattice produces the possibility of both positive and negative energy effects occurring simultaneously (fig. 5-1c). The combination of unequal numbers of parallel and anti-parallel spin alignments results in a highly magnetic, ferrimagnetic material (ie. magnetite, hematite, pyrrhotite). In rare cases, exchange energy is minimized in antiferromagnetic crystals where equal numbers of parallel and anti-parallel spins cancel out the overall magnetization (fig. 5-1b).

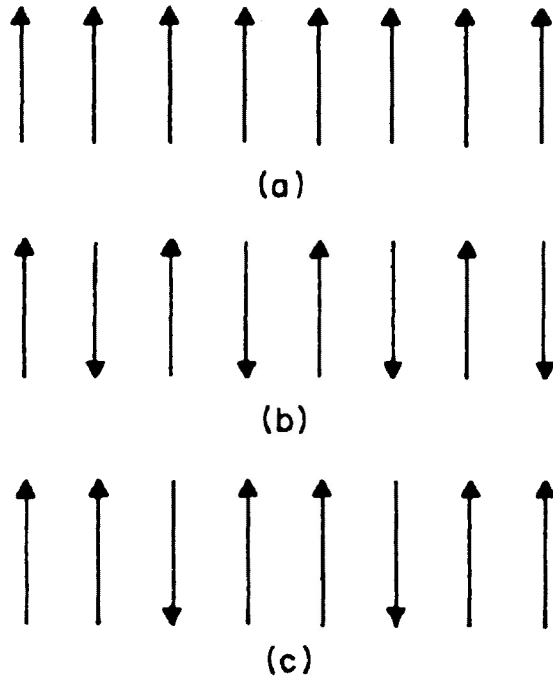


Figure 5-1: Electron spin orientations in various types of strongly magnetized material.

- (a) Ferromagnetism - parallel spins, with a strong internal spontaneous magnetism, even in the absence of an external magnetic field.
- (b) Antiferromagnetism - equal numbers of electron spins in parallel and anti-parallel orientations, cancelling out the overall magnetization.
- (c) Ferrimagnetism - most common magnetic condition where more spins are aligned in a parallel manner than anti-parallel.

(from Strangway, 1970)

5.3 Magnetic Fabrics

5.3.1 Magnetic Susceptibility Tensors and Ellipsoids

The magnetic moment per unit volume of a rock (J), within a weak magnetic field (H) is given by:

$$J = J_r + J_i$$

where: J_r = the remanent moment of magnetism, which is unaffected by the weak field (H).

J_i = the induced moment of magnetism

(Bhatal, 1971).

For an isotropic substance, J_i has the same direction as H . However, J_i varies from the direction of H in anisotropic substances within a weak magnetic field. This variance, a measure of magnetic susceptibility (k) under these conditions, can be expressed by:

$$J_i = k \cdot H$$

The susceptibility actually can be considered to be a single additive combination of different susceptibilities based on the volumetric proportions of the various magnetic mineral types (Borradaile, 1987a).

The range of susceptibilities can be expressed as a

symmetrical second order tensor:

$$\begin{array}{ccc} k_{11} & k_{12} & k_{13} \\ k_{21} & k_{22} & k_{23} \\ k_{31} & k_{32} & k_{33} \end{array}$$

defined by three principal orthogonal axes: k_{11} , k_{22} , and k_{33} . They represent maximum, intermediate, and minimum susceptibilities respectively.

The shape and magnitude of a magnetic susceptibility ellipsoid (fig. 5-2) can then be represented by the orientation of the three principal magnetic susceptibilities. Various other parameters can also be used to augment this representation (Hrouda, 1982; p. 42). MSA analyses utilize the magnitude of magnetic susceptibility ellipsoid and the values of the principal orthogonal axes to graphically represent the magnetic fabrics, which are controlled by the fabric of magnetic minerals in the rock.

5.3.2 Magnetic Fabrics and Their Representation

Magnetic lineations and foliations constitute a magnetic fabric based on the shape and orientation of the magnitude of magnetic susceptibility ellipsoid. The magnetic fabric can be qualitatively correlated with the shape and orientation of strain ellipsoids (Hrouda, 1982).

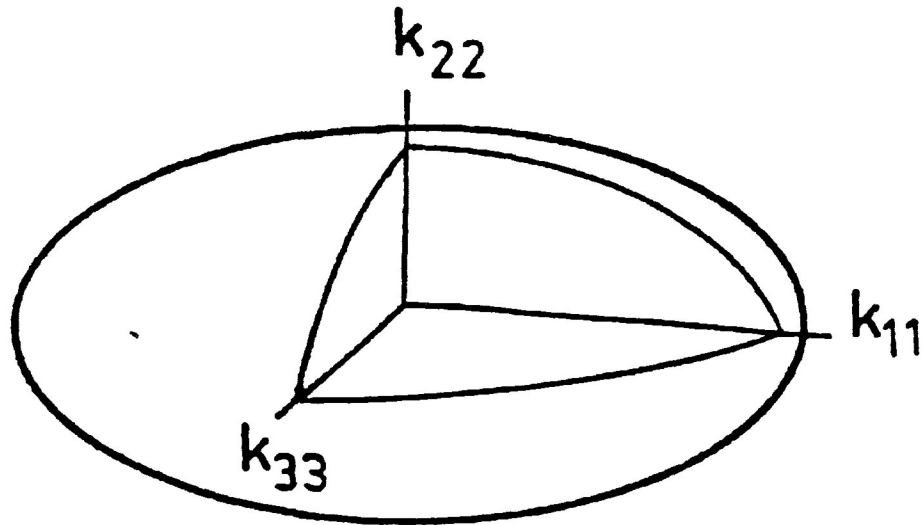


Figure 5-2: Magnitude of magnetic susceptibility ellipsoid represented by the orientation of the three principal magnetic susceptibilities where:

$$\begin{aligned}K_{\max} &= K_{11} \\K_{\text{int}} &= K_{22} \\K_{\min} &= K_{33}\end{aligned}$$

Two types of magnetic anisotropy plots have been developed for MSA analysis, to graphically represent the shape of the susceptibility ellipsoid (Hrouda and Janak, 1976; Hrouda, 1982). The first type of plot is based on an MSA version of the Flinn Diagram with "a" and "b" axes (where $a = k_{\max}/k_{\min}$ [the "magnetic lineation"], parallel to the mean of k_1 ; and $b = k_{\text{int}}/k_{\min}$ [the "magnetic foliation"], perpendicular to the mean of k_3) (fig. 5-3). Each plotted point on the diagram represents an ellipsoid of specific shape and degree of anisotropy (which increases with distance away from the origin). This technique is valuable for its ease of qualitative correlation with strain paths on a Flinn Diagram deformation plot.

The second technique for plotting magnetic anisotropy is the Hrouda-Jelinek or P-T' diagram. The axes used are P' (the increasing degree of anisotropy) and T (the sense of anisotropy), (fig. 5-4) where:

$$P' = \exp \left(\left[2 \left(\{a-K\}^2 + \{b-K\}^2 + \{c-K\}^2 \right) \right] \right)$$

$$T = 2 \left[\frac{(b-c)}{(a-c)} \right] - 1$$

where: a, b, c = the natural logarithm of principal susceptibilities in descending order

K = the logarithm of the mean susceptibility

$T = 1$ -> uniaxial oblate ellipsoid sense

$T = 0$ -> intermediate ellipsoid sense

$T = -1$ -> uniaxial prolate ellipsoid sense

(Borradaile, et al., 1987).

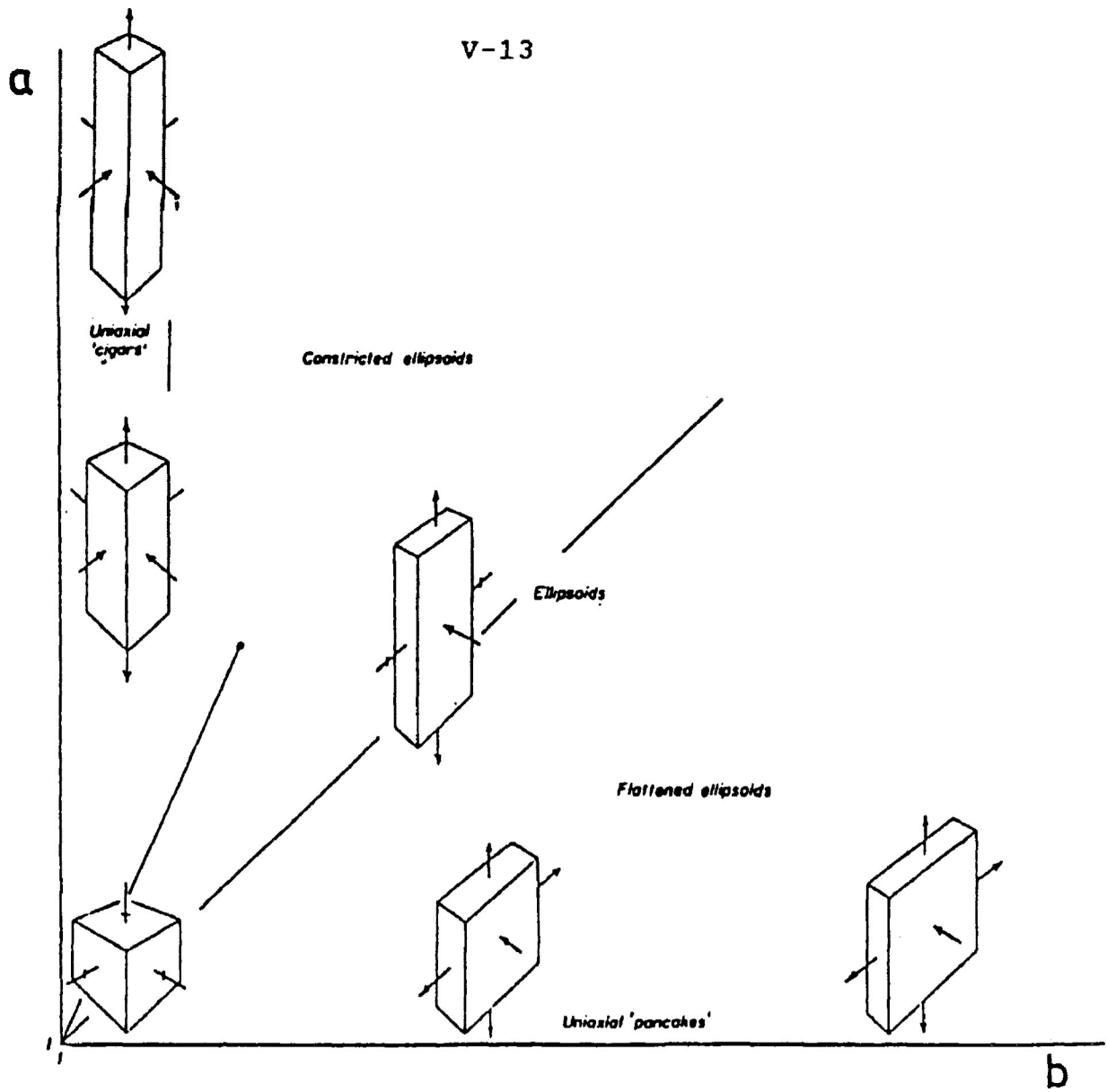


Figure 5-3: Flinn diagram used for graphical representation of magnetic anisotropy plots. (from Ramsay and Huber, 1983)

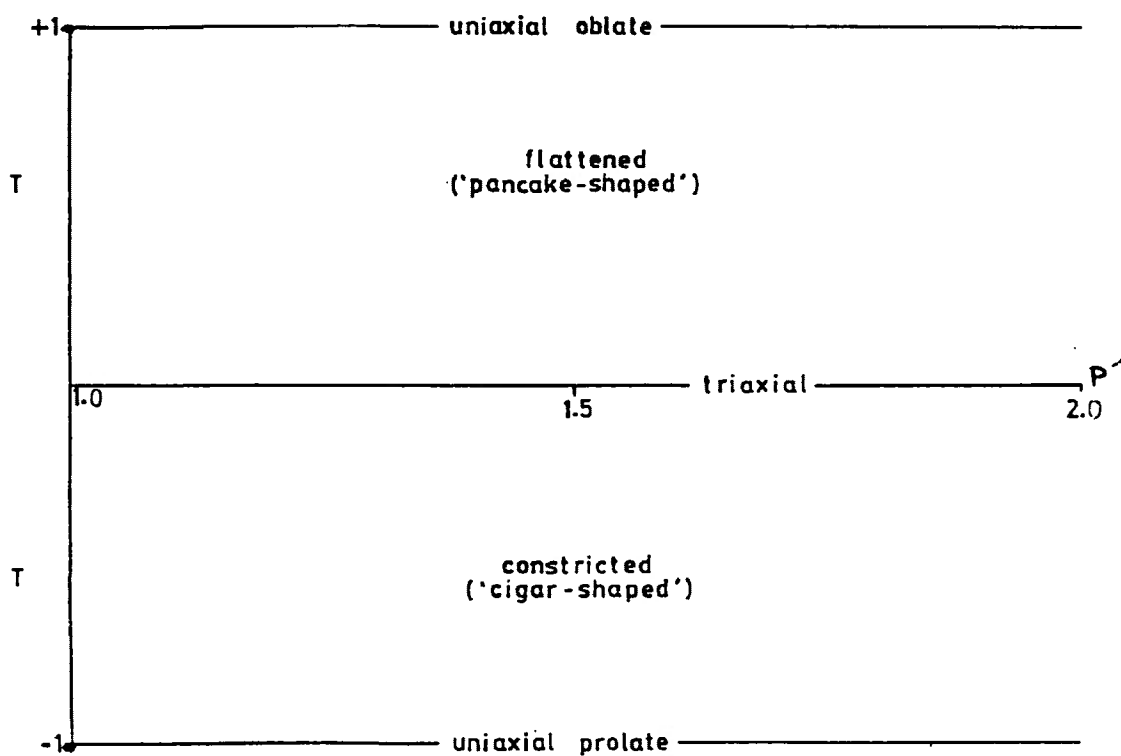


Figure 5-4: Hrouda-Jelinek, or P'-T diagram equal area distribution for all susceptibility ellipsoids where they are plotted with respect to sense of anisotropy (T) versus the degree of anisotropy (P').

The latter technique is more advantageous if one wants to see the variance of the degree of anisotropy. The Hrouda-Jelinek plot provides an equal distribution for all the ellipsoids regardless of shape or degree of anisotropy. The Flinn Diagram approach offers poor resolution of ellipsoids with smaller degree of anisotropy.

5.4 Determination of Magnetic Susceptibility

At Lakehead University, the Sapphire Instrument SI-2 AMS meter has a magnetic field suitable for examination of the paramagnetic component of MSA. It essentially consists of a sensing coil with an inner volume of 160 cubic centimetres, an attached control system and accompanying data-acquisition circuitry.

Bulk magnetic susceptibility is measured by placing a cylindrical oriented sample in the coil. A timed electrical circuit induces a secondary field which generates an electrical current within the field. The induced current is measured and recorded. This process is repeated in a pattern of twelve different orientations in order to compute an averaged susceptibility tensor. Coil inductances are compared between each sample reading with an "air" reading. These are used in comparison with a regularly calibrated MnO₂ standard with known

susceptibility and similar volume to the standard specimens used.

5.5 Factors Controlling MSA

Of the factors that control MSA, magnetocrystalline and shape anisotropy are the most important (Bhatal, 1971; Hrouda, 1982). Preferred orientation of magnetic grains is a lesser factor. Two other additional aspects that influence MSA are matrix effects (Rochette, 1988) and particulate flow (Borradaile and Tarling, 1981; 1984).

5.5.1 Magnetocrystalline Anisotropy of Magnetic Grains

Just as slip can occur more easily along certain crystallographic slip planes within a crystal lattice, magnetization can also align electron spin axes with less energy along certain planes. Analogous to crystal slip systems, there exist "easy" and "hard" directions of magnetization (fig. 5-5). Magnetization tends to follow the "easy" directions whereas it is more difficult to produce magnetic saturation along the "hard" directions (Bhatal, 1971). The result is an anisotropy where the crystal lattices are aligned with respect to magnetocrystalline anisotropy; independent of crystal shape.

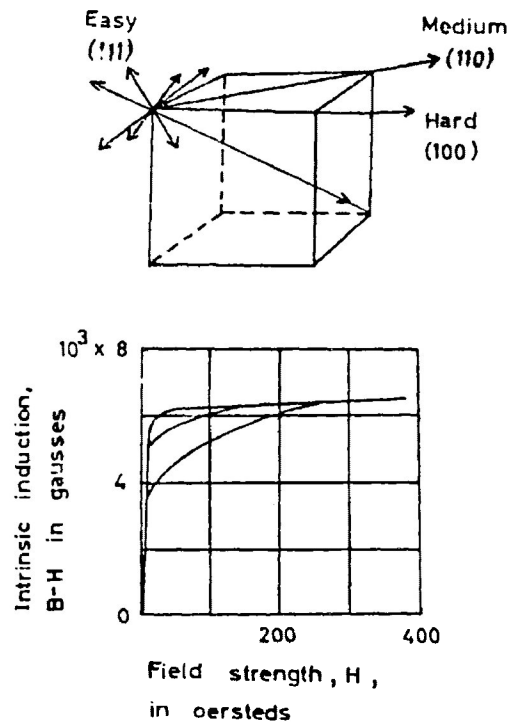


Figure 5-5: "Easy" and "hard" magnetization directions relative to crystallographic planes in a single crystal; in this case, a single crystal of nickel. (from Bhatal, 1971)

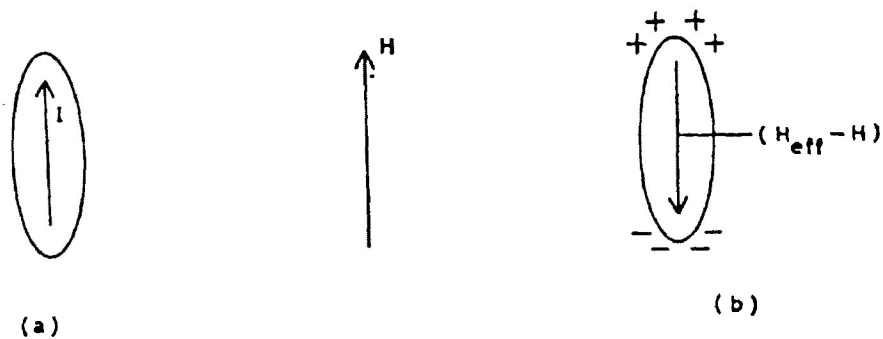


Figure 5-6: (a) a magnetically isotropic non-equant grain. (b) after being influenced by an external magnetic field (H), a uniform internal magnetization is produced and free magnetic poles form at the most distant ends of the grain. (from Bhatal, 1971)

5.5.2 Shape Anisotropy of Magnetic Grains

The shape anisotropy of grains is aligned with respect to a preferred orientation of either long axes or crystallographic axes. Non-equidimensional grains impart a directional dependence of magnetostatic energy. Magnetostatic energy is the energy required to maintain free magnetic poles. This energy requirement is minimized when the poles are as far apart as possible.

In a perfectly ideal equidimensional grain, no poles will develop. Conversely, an ideally isotropic magnetocrystalline crystal of non-equant shape will try to create free magnetic poles at opposite ends of the crystal surface (fig. 5-6). The internal magnetization will parallel the long axis of crystals in the presence of an external magnetic field, in such cases of non-equant grain size.

Magnetostatic anisotropy can sometimes mask the crystalline anisotropy of section 5.5.1. Magnetostatic effects seem confined to strongly magnetic (magnetite-type) minerals (Bhatal, 1971). Hrouda (1982) graphically demonstrated that weakly magnetized crystals with low susceptibility are hardly effected by magnetostatic anisotropy (fig. 5-7). Thus, most

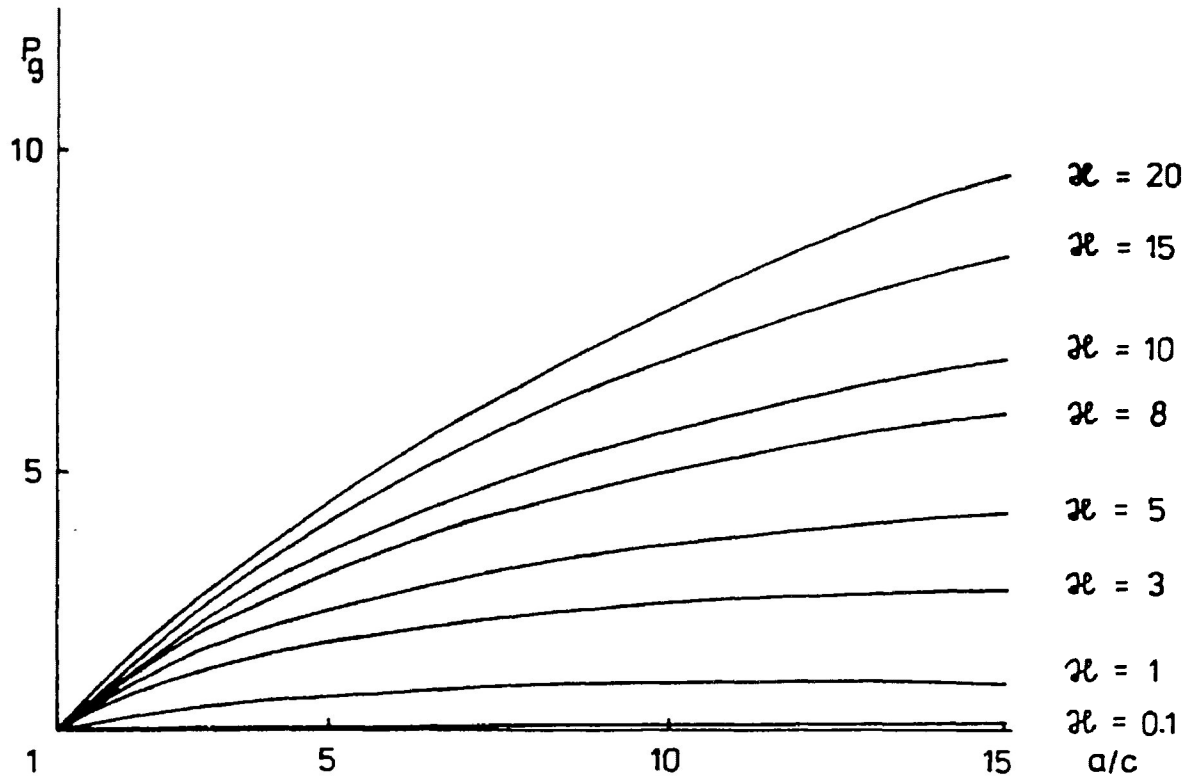


Figure 5-7: The relationship between the degree of anisotropy (P_g) and the dimensions of the grain ratio (a/c) of various (H) values of bulk susceptibility. (from Hrouda, 1982)

paramagnetic minerals are dominated by magnetocrystalline anisotropy (i.e. preferred mineral orientation).

5.5.3 Preferred Orientation of Magnetic Grains

Preferred orientation can take two forms: (i) preferred crystallographic orientation (pco), and (ii) preferred dimensional orientation (pdo). The magnetic susceptibility of a magnetite-bearing rock can be influenced by both grain shape anisotropy and the preferred orientation of magnetic grains. In many metamorphic rocks, where magnetite tends to occur in trace amounts, the "pco" of the paramagnetic rock-forming silicates controls the anisotropy of susceptibility and overpowers the "pdo" of magnetite-type grains (Borradaile, et al., 1987).

The relationship between the degree of preferred orientation of elongated grains with grain MSA and rock MSA was graphically depicted by Hrouda (1982), (fig. 5-8). As long as the grain anisotropy degree of magnetite does not exceed 5, the MSA of the rock would be controlled by both grain shape anisotropy and by the preferred orientation of the long axes of grains (Hrouda, 1982).

Progressive deformation and the effects of plastic deformation on magnetism was observed in diamagnetic calcite

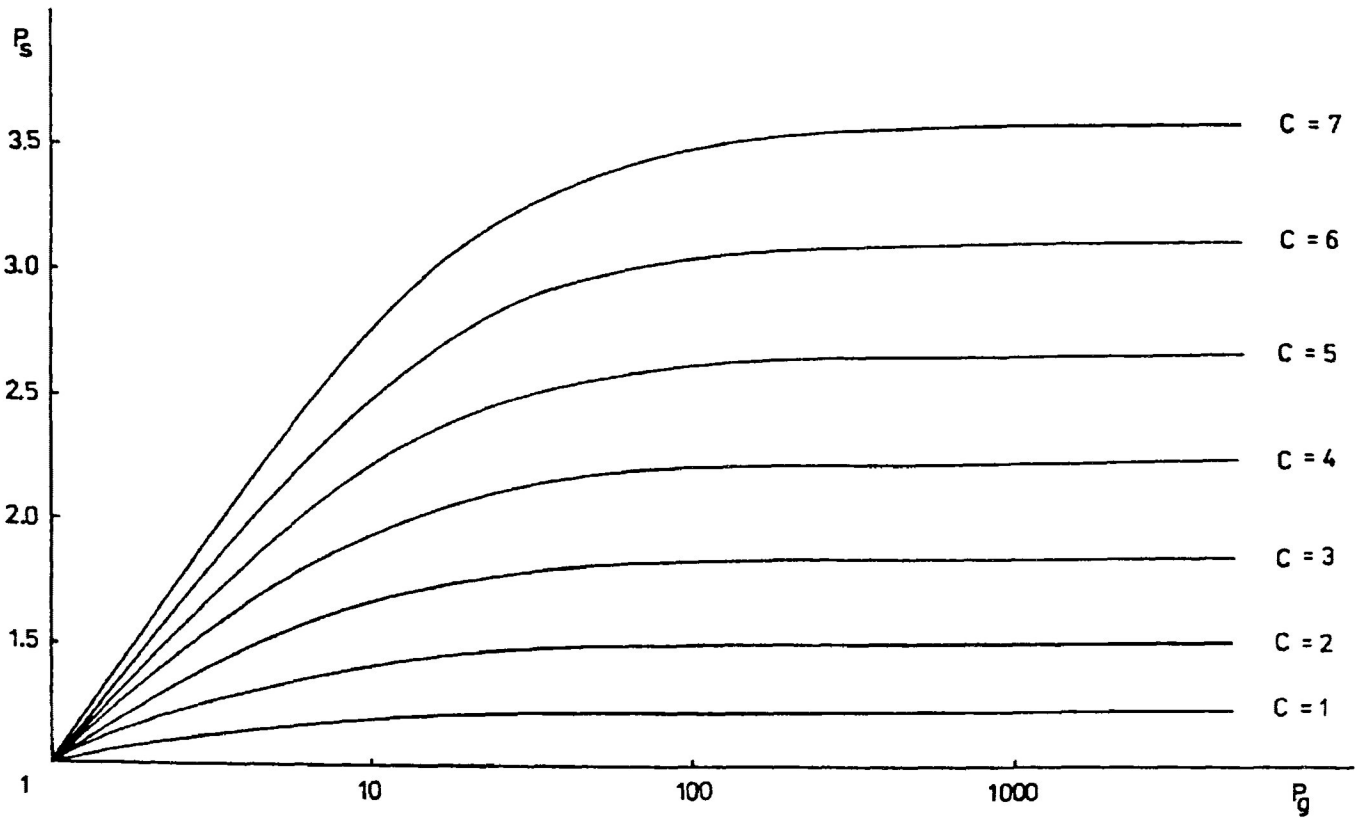


Figure 5-8: The relationship between degrees of MSA for a rock (P_s) versus the grain MSA (P_g) for various values (C) representing the degree of preferred orientation of elongate grains within the rock. (from Hrouda, 1982)

crystals from deformed samples of Carrara marble (Owens and Rutter, 1978). It was found that magnetic anisotropy results were consistent with conventional optical fabrics. A very pronounced pattern of crystallographic preferred orientation was observed to develop, in addition to intracrystalline gliding, when the levels of confining pressures were high enough to suppress cataclastic (dilatant) behaviour. The Carrara marble is composed of diamagnetic calcite crystals. Such material possesses a low negative ($-k$) susceptibility. Thus, in this case of the Carrara marble, the maximum absolute susceptibility axes plotted within ten degrees of the compressional axes (as opposed to the positive susceptibility alignment along the extensional axis usually found in paramagnetic and ferrimagnetic materials).

5.5.4 Particulate Flow

Three types of particulate flow (Borradaile, 1981) influence preferred orientation and magnetic susceptibility anisotropy. There exists two end members of particulate flow: dependent and independent particulate flow. The third type, controlled particulate flow, is intermediate to the other two.

During dependent particulate flow, grain movement relative to one another is only due to the incompatibility of deformation of adjacent grains. After deformation, the grains

take new shapes, based on their crystallographic slip systems, and no longer fit together. Deformation tends to rotate the slip planes of the grains towards parallelism.

Grain movement during independent particulate flow does not involve any grain deformation. Flowage, a macroscopic ductility, is the only method responsible for the promotion of sliding. Some sort of supporting effect, as in the overcoming of friction by fluid pressure, is needed to lower normal stresses across the grain boundaries.

Controlled particulate flow involves movement caused by incompatible deformation of adjacent grains in addition to the contribution of higher fluid pressures. However, of these agents of sliding, grain deformation is the rate-controlling step. The rate at which obstructions are removed will control the rate of particulate flow.

Fluid pressure decreases and re-equilibrates over time. This phenomenon is important since it marks the transition from controlled to dependent particulate flow. Hence, a majority of the grain deformation that occurs in the metamorphic process of L-S fabric development actually occurs in the latter stages of the metamorphic episode. Any magnetic fabrics would then also represent only the last few increments of strain during

metamorphism.

Synthetic fabrics were measured at various stages of progressive deformation by Borradaile and Alford (1987). It was found that during pure shear stress experiments, the grains deformed quite complexly in very non-coaxial flow patterns. A strain heterogeneity was observed between different types of minerals and different grains.

Despite heterogeneous strain partitioning, a strong preferred orientation has been preserved through particulate flow. Thus, orientations of the principal strains are still tracked by magnetic susceptibility ellipsoids (This has been shown in natural rocks by Borradaile and Tarling, 1984). Particulate flow is a factor that does influence MSA, and must be paid attention to when studying weakly deformed rocks and rocks involving extensive particulate flow during deformation. This has to do with the effects of pressure solution.

5.5.5 Effects of the Matrix

One final contributing factor of MSA is that of the matrix. Overall magnetic susceptibility can be broken down into two additive components:

$$K = K_f + K_l$$

where: K_f = the ferrimagnetic susceptibility

K_l = the low field susceptibility

K_l is generally due to paramagnetic minerals and make up, as discussed in section 5.2.2, a considerable bulk of the matrix of the rock. This is especially true for metamorphic phyllosilicate- containing rocks. An overview of K_l in rocks is given by Rochette (1988) and by Rochette and Vialon (1984). The magnetic susceptibility of some paramagnetic metamorphic minerals is discussed by Borradaile, et al., (1987).

Early work on MSA tended to ignore K_l in favour of K_f determination and its more obvious remanent properties. The matrix was often overlooked due to the false assumption that K_l was negligible compared to K_f . The matrix will be overpowered and will be negligible when $K \gg 10E-03$ SI units / cubic cm (Rochette, 1988).

K_l can be estimated with proper experimental technique. The only method to directly examine the matrix or paramagnetic component is to use a sufficiently high magnetic field. K_l is independent of the field whereas the ferrimagnetic component reaches saturation and produces a zero differential susceptibility. K_l can also be estimated by destroying the rock and physically separating the minerals (see section 7.1.1).

CHAPTER 6 - MSA AND METAMORPHIC DEFORMATION6.1 Introduction - Uses in Primary Features

The magnetic susceptibility technique of bulk anisotropy lends itself to many applications in the study of primary features such as massive ore deposits, sedimentary paleocurrent indicators, volcanic flow and plutonic emplacement. The one-step measurement of bulk anisotropy eliminates some of the tedium normally required for the analysis of many individual grains or crystals.

The use of MSA in study of massive ore emplacement and consolidation is possible if there is no geological evidence of post-ore metamorphism. The magnetic anisotropy of massive pyrrhotite in Ni-Cu ore deposits associated with the Sudbury Irruptive was studied by Schwarz (1974) near Timmins, Ontario. High anisotropies were found due to the preferred orientation of "C" axes of pyrrhotite caused by ductile deformation associated with tectonic processes.

MSA can also provide information concerning the depositional process of ferromagnetic grains. Hamilton and Rees (1971) addressed the problem of distinguishing between depositional and deformational origins of magnetic fabrics. MSA

studies that indicate primary paleocurrent directions are reviewed by Hrouda (1982) and by Hrouda, et al., (1988). Hydrodynamics is the driving force behind MSA paleocurrent analysis. Water currents tend to orient the longer axes of the grains parallel to the flow line.

Similar flow patterns develop for volcanic flow studies. Volcanic rocks may have relatively low susceptibilities, similar to those of some sediments. However, some mafic lavas have relatively high susceptibilities ($>10E-03$ SI). Flowing lava is thought to produce a dimensional orientation of ferrimagnetic minerals that can be visualized by magnetic anisotropy (Hrouda, 1982). The directions of the principal susceptibilities are established from lava flow and/or the shapes of volcanic bodies. Magnetic lineations and foliations approximately parallel the planes of flow within sills, dykes and lava flows.

For example, estimates of flow direction were obtained from the MSA of calc-alkaline welded tuffs in the central San Juan Mountains of southern Colorado (Ellwood, 1982). The lineation of magnetic grains indicated the mean of the maximum susceptibility which revealed inferred axes of uniaxial flow within the tuffs. MSA was also used to distinguish between two possible modes of formation of a doleritic intrusion in Spitsbergen (Halvorsen, 1974). The intrusion was in the shape of

a "circular envelope". The visible outcrops were believed to be either the remains of an irregular sunken sill (where the maximum magnetic susceptibility plane would have been horizontal), or else the remains of a ring dyke (where the maximum susceptibility plane would have been vertical or very steeply inclined). MSA analyses divulged a horizontal maximum susceptibility plane. Thus, the dolerite intrusion represented a sill.

The knowledge of the generation of igneous features, such as basaltic columns, can be increased through studies of MSA. Ellwood (1979) studied horizontal columnar segments from two Icelandic near-vertical dykes. Short MSA axes were found to be vertically oriented while long axes were horizontal. This results from vertically exerted forces caused by the overlying column overburden rather than the effects of flow on grain alignment. These discrete columns would then be formed as a stacked pile that gradually gains a column overburden stress.

Plutonic rocks can also possess MSA-detectable primary flow fabrics emplaced during magma flow (Hrouda, 1982). Studies of MSA in these rocks can help discern a mode of emplacement. For example, Cogné and Perroud (1988) used MSA to help argue for a syntectonic emplacement of the Flamanville granite in the Armorican Massif, NW France. The pluton contained no internal deformation, but the margins had pronounced cleavage and

elliptical inclusions. Good correlation between the cleavage and principal susceptibility axes supported the syntectonic diapir hypothesis.

The magnetic anisotropy of weakly deformed rocks is much higher than that of sedimentary or volcanic rocks. The high degree of anisotropy is due to either: (i) grain rearrangement or, (ii) ductile deformation, or (iii) the preferred crystallographic growth of ferrimagnetic and paramagnetic minerals influenced by the dominant field of metamorphic stress. Higher grades of metamorphism did not result in increased degrees of anisotropy. Hence, the mechanisms of orientation are relatively independent of metamorphic grade (Hrouda, 1982).

As discussed above, it is important to distinguish primary depositional magnetic fabrics from those that underwent ductile deformation. Hamilton and Rees (1971) examined the modification of MSA during progressive deformation. Another important point to consider is the effectiveness of the MSA technique as an indicator of strain. Graham (1966) was the first to demonstrate a correlation between principal susceptibility axes and principal strain axes. Graham also showed that, during progressive deformation, the magnetic susceptibility ellipsoid will change shape and orientation. The change of shape is quite complex, from oblate to triaxial form and back to an oblate

ellipsoid, with increasing deformation (Hrouda, 1976; Hrouda, 1982; Hrouda and Janak, 1976).

In low grade metamorphic rocks, both bedding and a slaty cleavage may be present. The magnetic foliation lies within the cleavage with minimum susceptibility axes parallel to the cleavage poles. The maximum susceptibility axes are parallel to the physical lineation as well as the intersection lineation between cleavage and bedding. However, this does not mean that the maximum strain is in this direction. Borradaile and Tarling (1981) showed that pressure solution, especially, causes the magnetic lineation to be parallel to the intersection lineation; but this is not the maximum strain direction. In higher grade rocks, the schistosity is the only cleavage present and the magnetic foliation is usually parallel to it. Generally, the maximum susceptibility axis is defined by the long axes of silicate grains that define a lineation. Minimum susceptibility is perpendicular to this foliation.

The MSA technique is very applicable to mylonites due to their fine grained and recrystallized nature. The relationship between mesoscopic and magnetic fabrics within the centre of mylonite zones yields good correlations (Goldstein, 1980; Goldstein and Brown, 1988). A lack of parallelism was noted at the margins of the zones. Relationships between strain and

magnetic fabrics helped support a model of mylonite origin and propagation outwards due to simple shear, followed by later flattening stages.

The determination of kinematic sense of simple shear along a shear line, using MSA, was introduced by Rathore and Becke (1980). The underlying premise of this technique is the similarity of how the k_3 minimum susceptibility direction and the minimum strain direction rotate during simple shear.

Mapping by "magnetic isograds" was developed by Rochette (1987) in Jurassic black shales in the Swiss Alps. Magnetic isograds appear due to the existence of rapid jumps in magnetic susceptibility due to the breakdown of detrital magnetite and the transformation of pyrite into pyrrhotite. The presence or absence of iron-bearing silicates, magnetite, or pyrrhotite paralleled the metamorphic facies zonation (zeolite to amphibolite facies). A "pyrrhotite-in" isograd was the only one clearly detectable during the study. Rochette states that a "magnetite-out" isograd should also be possible. The variation due to the appearance of iron-bearing paramagnetic silicates in progressive metamorphism was too gradual to detect any jumps in susceptibility.

6.2 Re-orientation due to Strain

The re-orientation mechanisms are well documented by several authors. The mechanisms are discussed briefly in sections 5.5.3 and 6.1. Coupled with preferred crystallographic growth, both these mechanisms offer the ability for the principal susceptibility directions to attempt to co-align with principal strain directions.

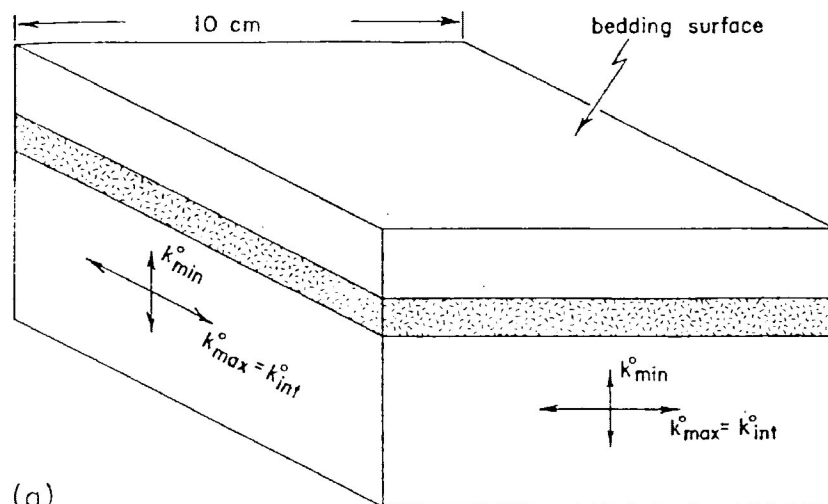
March's model (that a group of randomly oriented will rotate into a preferred orientation, in which long axes are perpendicular to the direction of maximum shortening) provides a reasonable model for some rock fabric. Mechanical rotation can take place by the rotation of comparatively rigid, non-equidimensional grains in a less rigid matrix or by the deformation of constrained crystals with glide properties. Not all grains behave passively but tend to quickly align with the early principal strain orientations and then change shape (Borradaile and Tarling, 1984). Different rheologies and initial orientations, with respect to applied stress, cause some grains to deform and/or rotate more quickly than others towards the preferred crystallographic direction. Strain analyses of individual grains or crystals does not represent the strain of the whole rock since much of the strain is taken up by

particulate flow (Borradaile, 1981) (section 5.5.4). Due to the complications of particulate flow (grain boundary sliding and diffusive mass transfer processes), the reorientation can be very complex.

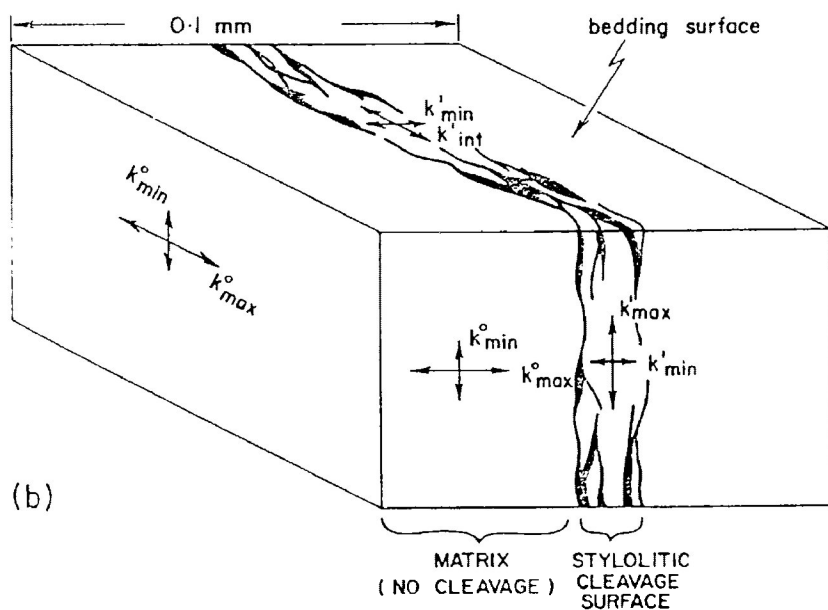
6.3 Preferred Crystallographic Growth

With the onset of deformation upon primary rock features, the correlation between principal finite strain directions and magnetic fabrics is quite complex. Borradaile and Tarling (1981) examined the development of magnetic fabric within embryonic stylitic cleavage in weakly deformed rocks. Their study shows how tectonic and primary magnetic fabrics interact in situations of weak deformation.

Originally the undeformed sediments had a k_{max} direction that was parallel with bedding. However, where stylitic cleavage developed the magnetic fabrics were different and more anisotropic (fig. 6-1). The k_{max} directions were oriented parallel with the new cleavage. Localized tectonism produces a magnetic fabric interference with the pre-existing magnetic fabrics (due to the initial deposition of weakly aligned clastic magnetite). Tectonism produces a stylitic cleavage that concentrates clastic magnetite within an insoluble residue. The magnetite then aligns dimensionally, parallel to cleavage



(a)



(b)

MATRIX
(NO CLEAVAGE) STYLOLITIC
CLEAVAGE
SURFACE

Figure 6-1: Model of magnetic fabric development during the formation of stylolitic cleavage.
 (a) the undeformed rock showing primary sedimentary magnetic fabric.
 (b) development of localized tectonic magnetic fabric. Overall a net maximum bulk susceptibility is produced.
 (from Borradaile and Tarling, 1981)

surfaces. New magnetite also grows so that k_{max} is parallel to the maximum extension in the cleavage. Thus, a net overall maximum susceptibility (k_{max}) is a superposition in weakly deformed rocks; where the kind of the tectonic fabric and the k_{max} of the sedimentary magnetic fabric lie in a direction parallel to the bedding-cleavage intersection (Borradaile and Tarling, 1981). As deformation becomes stronger, the effect on MSA of preferred crystallographic growth (as well as pressure solution, and particulate flow effects) increases.

6.4 Correlation between Principal Magnetic Susceptibility Directions and Principal Strain Directions

Most MSA studies undertaken agree upon a good correlation between the principal direction orientations of both magnetic susceptibility and finite strain. In all cases, k_{min} is roughly oriented perpendicular to schistosity (which defines the XY plane of the strain ellipsoid). However, k_{max} is not always parallel to the elongation direction (the X direction of the strain ellipsoid). It is sometimes perpendicular to it. One of the main correlative problems lies with the few cases where k_{max} and k_{int} show no relationship with the principal strain directions of the fabric. This maybe due to a complication of interference by bedding fabrics (Borradaile and Tarling, 1981).

As described in section 5.5.4, principal susceptibilities usually track principal strain directions despite the heterogeneous nature of particulate flow and strain partitioning (Borradaile and Tarling, 1984). Goldstein and Brown (1988) found only a qualitative correspondence between foliation and lineation orientations, and susceptibility ellipsoids.

Kligfield, et al., (1981, 1982) attempted to quantitatively correlate the mean axial ratios of strain and susceptibility ellipsoids. For strain indicators they used reduction spots and oolites. They do, however, admit that the relationship varies, probably due to changes in the mechanisms of deformation. Outright failures in attempted quantitative correlations were documented in other studies (Hirt, et al., 1988; Rochette and Vialon, 1984; Lamarche and Rochette, 1987; Borradaile and Tarling, 1984; Borradaile and Mothersill, 1984), especially where there were pressure solution processes prevalent.

Yet, some studies propose a quantitative relationship between strain and magnetic anisotropy (Rathore, 1979, 1980, 1983; Rathore and Henry, 1982; Cogné and Perroud, 1988). The problems with such quantitative correlations are outlined in the next section, 6.5.

6.5 Problems with MSA Quantitative Strain Estimates

Geological problems and the numerical treatment of MSA data cause problems that arise for the use of MSA for quantitative estimates of strain. The fact that large strains have been shown to be accommodated differently by various mineral and grain types (Borradaile and Tarling, 1984) poses geological problems for the quantitative correlation at lower and moderate strain levels. Hirt, et al., (1988) found that a direct quantitative comparison of both mean susceptibility ellipsoids and finite strain ellipsoids was not accurate at the sample level due to these problems with strain heterogeneity. Lamarche and Rochette (1987) found that the interaction of different planar and linear structural elements and their consequential mineralogical origin of a magnetic fabric (as described by the development of stylonitic cleavage in Borradaile and Tarling, 1981) prevented the use of their data for quantitative estimates of strain. Rochette and Vialon (1984), similarly, found that contributions to tectonic fabric from pressure solution processes, and the frequent occurrence of planar or linear clusters of opaque grains within solution planes also ruled out quantitative strain correlations.

Magnetic susceptibility ellipsoids were extensively compared to analyses of strained accretionary lapilli from the

Borrowdale Volcanic Sequence in England (Borradaile and Mothersill, 1984). As expected, the principal directions of the magnetic susceptibility ellipsoid were very similar to the direction of maximum extension of the specimens. The direction of minimum susceptibility was usually perpendicular to the cleavage and the plane of flattening.

Rathore (1979) correlated MSA and strain using a logarithmic parameter (fig. 6-2). He plotted natural strains (N_i) against the logarithms of all the principal susceptibility deviations from their "isotropic" norm (M_i). The resulting linear correlation is possible when the N_i values are plotted against all the M_i values (fig. 6-2). However, the physical significance of this is not obvious. Rathore's regression line connects three distinct data clusters (minimum, intermediate, and maximum data values). It is fairly easy to obtain a well-defined regression line that connects the three separate "scattergrams". In the case of the Welsh slate study (Rathore, 1979), where the maximum and intermediate values were roughly equivalent, it is even simpler to define a regression line between two points (the two scattergrams).

Borradaile and Mothersill (1984) propose that there was no acceptable quantitative correlation with their data. The problem may lie in previous assumptions of simple strain

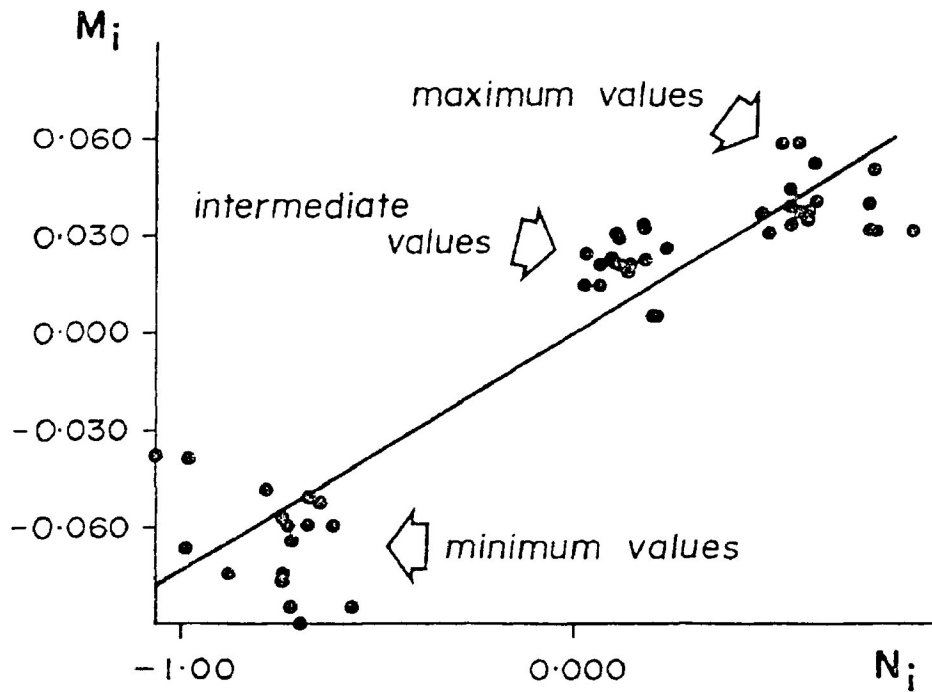


Figure 6-2: Rathore's logarithmic correlation between strain and MSA, using a linear correlation to connect the three data clusters.
(from Borradaile and Mothersill, 1984)

responses where rigid-body rotation was homogeneously applied throughout, and that it was responsible for both magnetic and strain fabrics simultaneously. Strain partitioning heterogeneities and particulate flow effects may have been overlooked.

If each of the three scattergrams is used as a source for a regression line (fig. 6-3), a more justifiable correlation may be produced. However, this should be tested with several data sets during future work.

The use of microfabric analysis in conjunction with magnetic susceptibility anisotropy measurements yields great promise for the analysis of strain, especially in geological situations where strain markers are absent or not easily obtainable. In highly deformed terrain, where reduced grain size and/or recrystallization may obscure conventional strain markers, magnitude of magnetic susceptibility ellipsoids can be constructed to aid in the understanding of changes of shape in any sized field area. Even in the presence of strain indicators, a known qualitative correlation between strain and MSA, makes MSA analysis a useful tool. MSA has the advantage of instantaneous and simple bulk anisotropy reading of a whole rock specimen, over the tedious grain by grain analysis of petrofabrics.

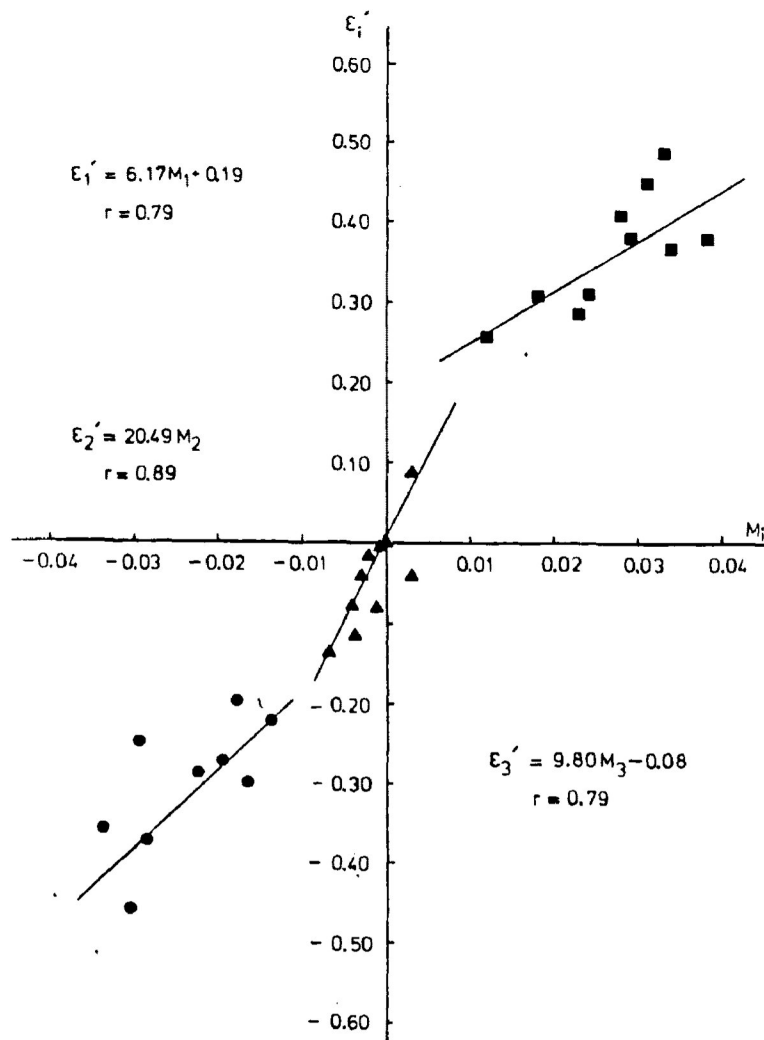


Figure 6-3: Possibly a more justified method of defining correlation, using separate correlations through each data cluster.
 (from Hirt, et al., 1988)

CHAPTER 7 - MAGNETIC SUSCEPTIBILITY FABRICS OF THE STUDY AREA7.1 Magnetic Mineralogy

The interpretation of magnetic fabrics depends upon the knowledge of the major sources of susceptibility in rocks. Each constituent mineral possesses a characteristic bulk susceptibility and a certain degree of anisotropy of susceptibility (Borradaile, et al., 1987). The coil used in determining magnetic susceptibility detects anisotropies due to shape or lattice orientations of susceptible minerals. The measurement of MSA involves the summation of the magnetic contributions of all the mineral constituents to create an average bulk fabric description.

The contributions to whole-rock susceptibility were originally attributed to ferrimagnetic iron-oxides; mainly magnetite and hematite (Rathore, 1979, 1980; Kligfield, et al., 1982; Goldstein, 1980). However, in most metamorphic rocks, iron-oxides are present only in traces, as accessory minerals or may even be absent. Ferrimagnetic minerals possess a very strong magnetic response and are controlled more by mineral shape (pdo) than by crystallographic orientation (pco), which controls the diamagnetic and paramagnetic components. Magnetite has an immense magnitude of bulk susceptibility; however, its anisotropy

is negligible due to its shape. The susceptibility due to magnetite and hematite can predominate in the comparatively rarer cases where grains are grouped to form elongate domains by pressure solution or other methods of metamorphic differentiation (Borradaile and Tarling, 1981). The importance of pyrrhotite as a ferrimagnetic contributor to MSA is documented by Rochette (1987). Pyrite adds very little to lithological MSA but is significant only as a site for the creation of pco-dominated pyrrhotite through progressive metamorphism.

Recent work has acknowledged the notable contribution, in general cases, of paramagnetic minerals to MSA (Borradaile and Sarvas, 1990; Rochette and Vialon, 1984; Borradaile, et al., 1986; Jover, et al., 1989). In most metamorphic rocks, iron-oxides usually are <<1 wt% of the rock. In these cases, the influence of less susceptible but more anisotropic matrix-forming silicates can predominate. The paramagnetic mineral attributes of high magnetocrystalline anisotropy and a strongly preferred crystallographic orientation is especially relevant to the MSA of syn-metamorphic tectonites. However, the minerals originating by metamorphic growth may not entirely reflect the bulk strain history of the rock but may in part derive from metamorphic processes. Magnetite grains, if detrital, may more accurately depict the bulk strain of a rock. This MSA response, however, will be masked by susceptibilities of the paramagnetic and

diamagnetic matrix components (ie. phyllosilicates). Hence, the ferrimagnetic and matrix segments each possess principal susceptibility directions and anisotropies that will not necessarily coincide; yielding a complex superimposed magnitude ellipsoid of susceptibility.

These discrepancies between fractions may present difficulties, in deformed and metamorphosed rocks, when attempting to correlate strain ellipses, with magnitude ellipsoids of susceptibility. Another source of incongruity arises from compositional variability. Specimens can produce varying anisotropy data despite experiencing similar strain and possessing similar fabrics.

7.1.1 Mineralogical Contributions to Bulk Magnetic Susceptibility

In order to ascertain to what extent MSA relates to a preferred orientation of matrix-forming phyllosilicates, tests were performed to determine the possible sources of bulk magnetic susceptibility. These tests involved: (i) the measurement of bulk susceptibility of individual minerals that were physically separated by a Frantz magnetic separator; (ii) leaching experiments; and (iii) scanning electron microprobe X-ray maps.

Previously, the techniques of magnetic remanence and Curie-point determinations were used to determine magnetic mineralogy. These methods are successful only in identifying ferrimagnetic portions since they completely ignore the paramagnetic contribution to susceptibility. They also fail to supply a reliable indication of the volumetric significance of any of the magnetic minerals comprising the total lithological MSA. It is more advantageous to crush the rock and physically separate the minerals so that measurements of bulk susceptibility on individual minerals can be performed.

Eight samples were chosen to represent typical lithologies in the field area:

- (i) RS1: porphyritic mafic metavolcanic
- (ii) RS1.2-1: sheared agglomerate metavolcanic
(chosen for anomalously high magnetite content)
- (iii) RS2: mafic bedded lapilli tuff
- (iv) RS8: chloritized pillow basalt
- (v) RS9: greywacke containing bedding and cleavage
- (vi) RS10: slightly higher grade greywacke
- (vii) RS10.5: greywacke with garnet and hornblende
- (viii) RS10.8: biotite-garnet-staurolite schist.

The samples were obtained from unused core remaining from MSA analyses. Samples were crushed for a length of time sufficient to break up polymineralic grains. Bulk susceptibility was

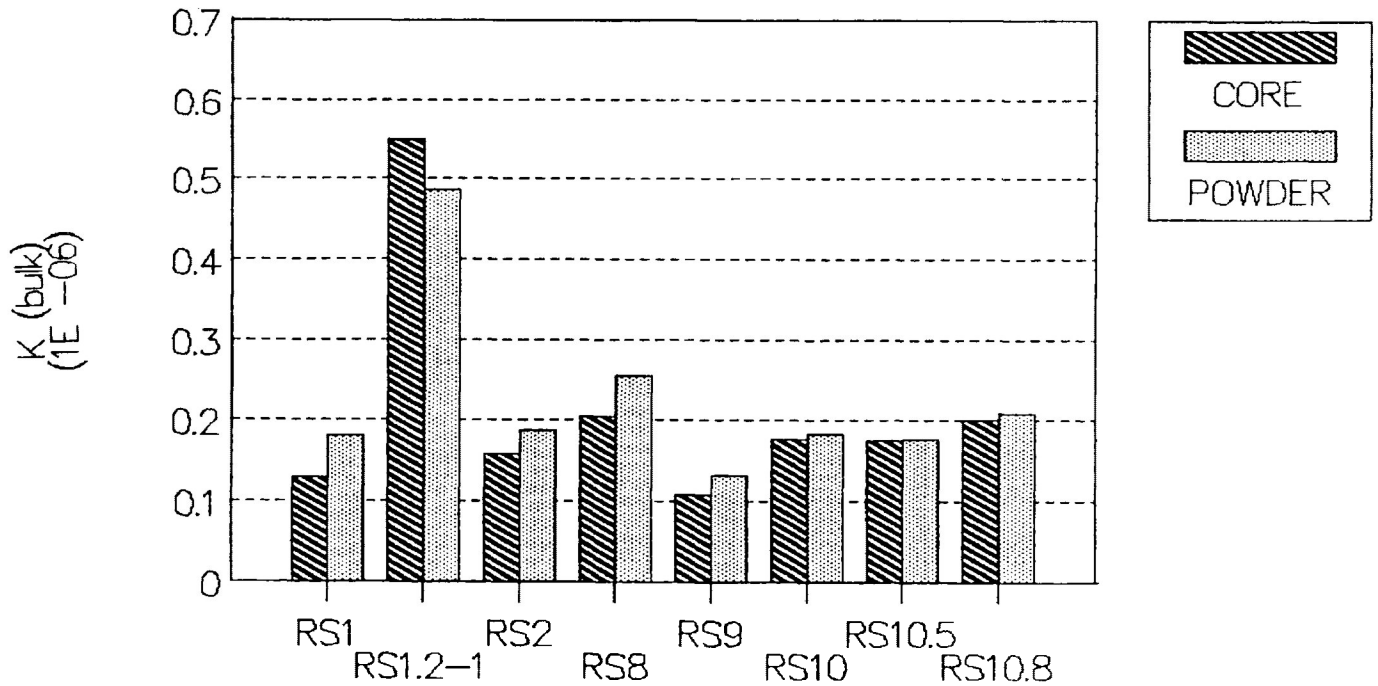
measured in the form of whole core specimens and as pulverized samples, measured in plastic cubes (see Figure 7-1 for weights and susceptibilities of rock and powdered samples). Crude bulk susceptibility measurements were made in the standard "SI2" coil. Five repeat measurements were made to produce a mean magnetic susceptibility. Figure 7-1 shows very little difference between rock and powder bulk susceptibilities.

The eight samples were separately crushed in an agate mortar. Sieving isolated two size fractions and removed fine dust and very coarse polymineralic fragments from the generally monomineralic fractions. The two size fractions [coarse fraction 1.75 ϕ (0.3 mm) to 2.75 ϕ (0.149 mm); and fine fraction 2.75 ϕ (0.149 mm) to 3.75 ϕ (0.074mm)] were washed with distilled water to liberate grains of surface dust. It is possible that some minerals may not have been fully represented since some may crumble more finely to dust than others. However, there appear to be no appreciable differences in minerals present or their volumes (Fig. 7-2) between the two size fractions.

A large hand magnet was used to separate highly magnetic grains (magnetite, hematite, and pyrrhotite). Optical examination of the separated components revealed that these grains were relatively rare as separate minerals (<1 wt%; Fig. 7-3). The powdered samples were run through the Frantz

Bulk Susceptibilities

BULK (K) FROM "MS" PROGRAM



=====
Bulk Susceptibility Determination (using "MS" program)

SAMPLE #	CORE WT (g)	CORE BULK K MS (m/kg)	CORE SDEV	CRUSH WT (g)	CRUSH BULK K MS (m/kg)	CRUSH SDEV
RS1	80.11	1.2866E-07	5.463E-10	7.78	1.8063E-07	2.335E-09
RS1.2-1	63.68	5.4904E-07	9.172E-10	9.02	4.8549E-07	3.467E-09
RS2	79.45	1.5766E-07	5.981E-10	7.775	1.8750E-07	2.617E-09
RS8	72.45	2.0411E-07	4.436E-10	8.615	2.5481E-07	4.615E-09
RS9	78.26	1.0812E-07	3.065E-10	8.34	1.3127E-07	4.486E-09
RS10	37.53	1.7718E-07	2.246E-10	7.335	1.8348E-07	1.773E-09
RS10.5	28.21	1.7550E-07	5.384E-10	9.035	1.7705E-07	1.175E-09
RS10.8	33.67	2.0015E-07	3.890E-07	9.33	2.0808E-07	2.117E-09

Core Readings = obtained from core drilled from hand sample

Crushed Readings = pulverized samples
= air readings used empty plastic cubes

Figure 7-1: Sample weights and bulk susceptibility measurements for both whole-rock samples and powder samples after crushing and sieving. The bar graph shows the similarities between the bulk susceptibilities before and after pulverizing.

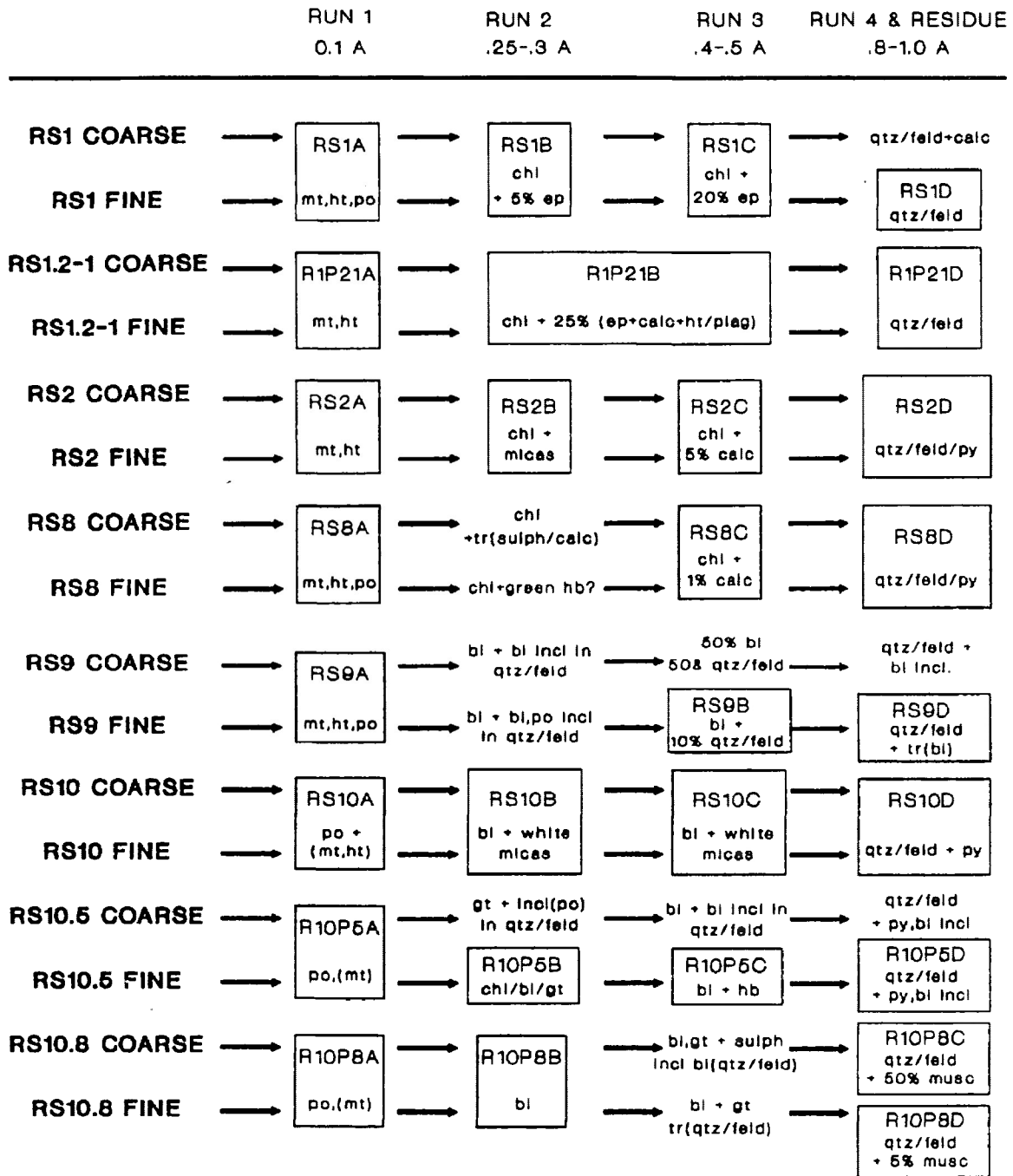
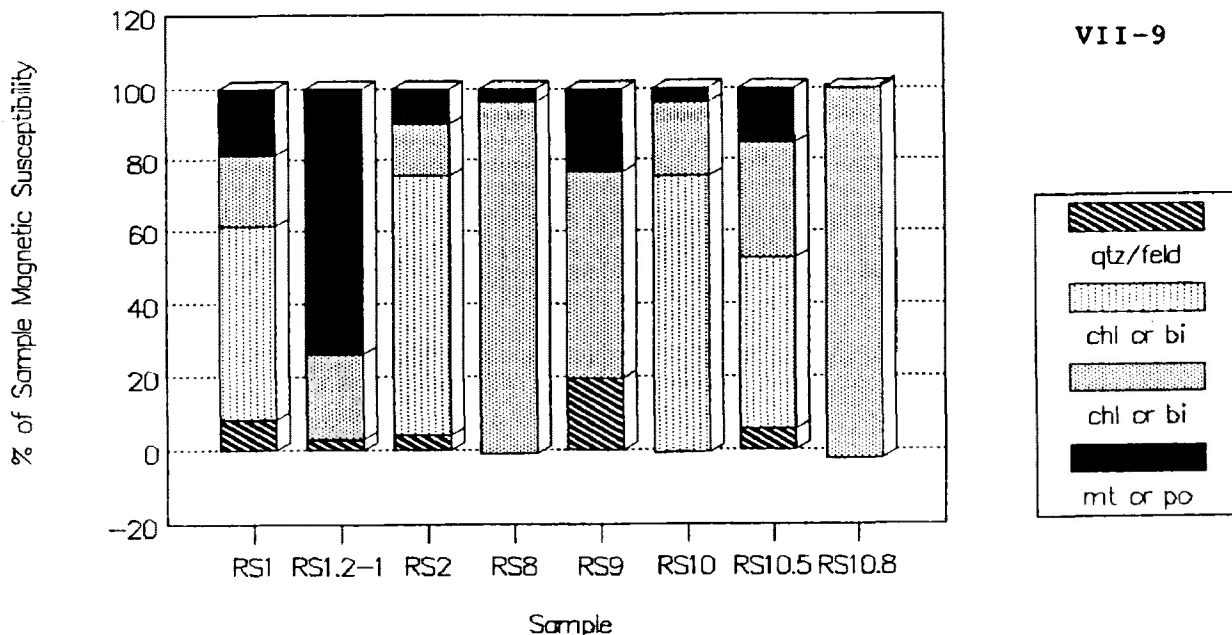
MAGNETIC SEPARATION

Figure 7-2: Magnetic separation flow chart for coarse and fine sieve fractions for each sample. Four runs of the powders through the Frantz Isodynamic Separator of variable amperages are shown as four columns. Boxed separates represent relatively monomineralic magnetic separates that could be weighed and measured for bulk susceptibility.

Isodynamic Separator utilizing settings recommended by Rosenblum (1958). Four runs were made using variable amperages and constant slope (Fig. 7-2). The first run, at very weak amperage (0.1 A), separated remaining ferrimagnetic grains that had escaped the hand magnet sweeps. The second and third runs were successful in isolating paramagnetic phyllosilicates. The final run separated a diamagnetic fraction of quartz, feldspar (and sometimes pyrite, and muscovite) from a final inseparable residue. The compositions of the separates were verified under binocular microscope and were hand-picked where necessary to achieve purity.

Usually, if compositionally similar, the coarse and fine fractions of each sample were combined. This yielded four magnetic separates for each sample (see "boxed" separates in Figure 7-2). The four separates for each sample were weighed and inserted into plastic bottles. Bulk susceptibility measurements were made of these bottles within a smaller, more sensitive "SMS-coil". Nine repeat measurements yielded mean bulk susceptibilities. Weights and MS measurements for each sample's magnetic separates are listed in Figure 7-3. The four separates (representing diamagnetic, paramagnetic, and ferrimagnetic portions) were recalculated to 100%; with each portion representing a percentage of the entire magnetic susceptibility of the sample.



SMS EXPERIMENTS

Frantz Magnetic Mineral Separations

** MAGNETIC SUSCEPTIBILITY IN UNITS: -3 3 **
 ** (mass basis) 10 m / kg **

RS1 SEPARATION Mineral Separate	Weight (g)	Mag Suscep	Wt X MS	Percentage Sample MS
mt, po	0.01	3.2426E-02	3.24E-04	18.8
chl + <5% ep	0.742	4.5782E-04	3.40E-04	19.7
chl + 20% ep	3.62	2.5355E-04	9.18E-04	53.3
qtz, feld	3.69	3.8245E-05	1.41E-04	8.2
100.0				

RS1.2-1 SEPARATION Mineral Separate	Weight (g)	Mag Suscep	Wt X MS	Percentage Sample MS
mt	0.08	6.0789E-02	4.86E-03	73.9
chl + 25% ep, calc	4.65	3.2651E-04	1.52E-03	23.1
qtz, feld	1.94	1.0217E-04	1.98E-04	3.0
100.0				

RS2 SEPARATION Mineral Separate	Weight (g)	Mag Suscep	Wt X MS	Percentage Sample MS
mt	0.002	1.0001E-01	2.00E-04	10.0
chl + micas	1.1	2.6067E-04	2.87E-04	14.4
chl + 5% calc	7.847	1.8229E-04	1.43E-03	71.6
feld, qtz + py	2.445	3.2531E-05	7.95E-05	4.0
100.0				

RS8 SEPARATION Mineral Separate	Weight (g)	Mag Suscep	Wt X MS	Percentage Sample MS
mt, po	0.005	1.0730E-02	5.37E-05	3.8
chl + <1% calc	6.292	2.1990E-04	1.38E-03	97.3
qtz, feld, py	0.1	-1.5441E-04	-1.54E-05	-1.1
100.0				

SMS EXPERIMENTS

Frantz Magnetic Mineral Separations

** MAGNETIC SUSCEPTIBILITY IN UNITS: -3 3 **
 ** (mass basis) 10 m / kg **

RS9 SEPARATION Mineral Separate	Weight (g)	Mag Suscep	Wt X MS	Percentage Sample MS
mt, po	0.003	6.7455E-02	2.02E-04	23.4
bi + 10% qtz/feld	1.35	3.6683E-04	4.95E-04	57.1
qtz/feld + (bi)	8.76	1.9288E-05	1.69E-04	19.5
100.0				

RS10 SEPARATION Mineral Separate	Weight (g)	Mag Suscep	Wt X MS	Percentage Sample MS
po + (mt)	0.005	8.7625E-03	4.38E-05	4.1
bi + (white micas)	0.71	3.0803E-04	2.19E-04	20.6
bi + (white micas)	3.225	2.5033E-04	8.07E-04	76.1
qtz/feld + (py)	0.6	-1.4963E-05	-8.98E-06	-0.8
100.0				

RS10.5 SEPARATION Mineral Separate	Weight (g)	Mag Suscep	Wt X MS	Percentage Sample MS
po + (mt)	0.004	1.9257E-02	7.70E-05	15.4
chl + bi + gt	0.39	4.1390E-04	1.61E-04	32.2
bi + hb	0.72	3.2544E-04	2.34E-04	46.7
qtz/feld (bi incl)	4.125	6.9210E-06	2.85E-05	5.7
100.0				

RS10.8 SEPARATION Mineral Separate	Weight (g)	Mag Suscep	Wt X MS	Percentage Sample MS
po (mt)	0.003	-4.8484E-03	-1.45E-05	-0.7
bi	4.93	4.4226E-04	2.18E-03	102.9
qtz/feld, 50% musc	0.335	-7.7724E-05	-2.60E-05	-1.2
qtz/feld, <5% musc	5.62	-3.8662E-06	-2.17E-05	-1.0
100.0				

Figure 7-3: The relative bulk susceptibilities of the four magnetic separates (representing diamagnetic [qtz/feld], paramagnetic [chl/bi], and ferrimagnetic [mt/po] portions of the rock samples) are expressed as a mass percentage, representing relative proportions of the entire magnetic susceptibility of each sample.

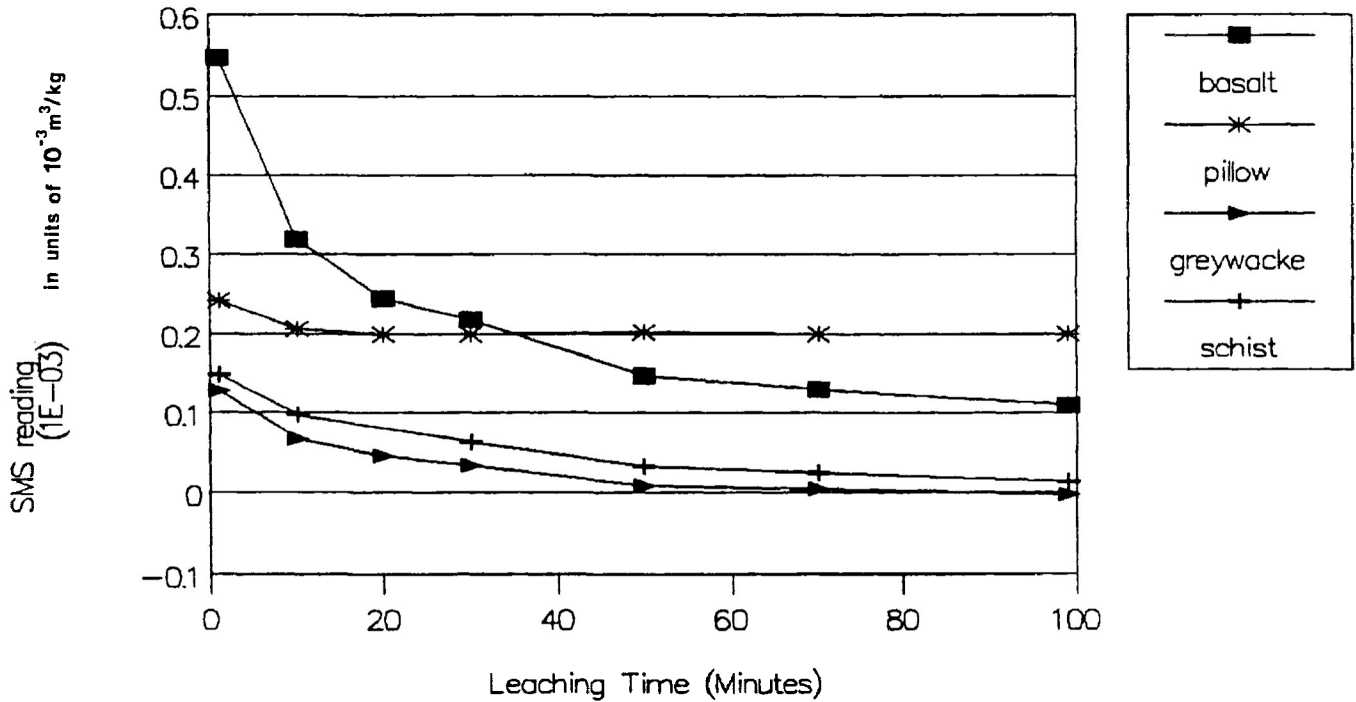
The results from bulk susceptibility measurements of the Frantz separates reveal that all the samples have multiple sources of magnetic susceptibility. Figure 7-3 shows an overwhelming majority of the sample's magnetic susceptibility is taken up by the more anisotropic and more voluminous chlorite and biotite paramagnetic portion. Therefore, iron-bearing phyllosilicates predominate over the less significant diamagnetic and ferrimagnetic portions of these metamorphosed rocks. Sample RS1.2-1 is the only exception, since it was especially chosen for its anomalously high amounts of magnetite and sulphides.

7.1.2 Leaching Experiments

A relatively new method of examining magnetic mineralogy was performed on some typical powdered samples. They consisted of the finer powder ($<3.75\phi$ (0.074mm)) remaining from the crushing and sieving operations. A typical schist (RS10.8), greywacke (RS9), chloritized pillowed basalt (RS8), and a basaltic (magnetite-rich) metavolcanic (RS1.2-1) were leached by hydrochloric and acetic acids for various time intervals (Fig. 7-4). Bulk susceptibility measurements were performed after each time interval, in the smaller and more sensitive SMS-coil with nine repeat measurements to calculate mean susceptibility.

SMS LEACHING EXPERIMENTS

hydrochloric and acetic acids



SMS LEACHING EXPERIMENTS

- Leaching Intervals in Hydrochloric and Acetic Acids

Time: (minutes)	Bulk Magnetic Susceptibilities in units of $10^{-3} \text{ m}^3/\text{kg}$			
	SAMPLE: RS1.2-1	RSB	RS9	RS10.8
0	5.4660E-04	2.4145E-04	1.2808E-04	1.4750E-04
10	3.1848E-04	2.0650E-04	6.6365E-05	9.7154E-05
20	2.4393E-04	1.9915E-04	4.6073E-05	
30	2.1751E-04	1.9972E-04	3.3242E-05	6.2619E-05
50	1.4673E-04	2.0170E-04	8.9060E-06	3.2039E-05
70	1.2921E-04	1.9908E-04	4.0364E-06	2.4308E-05
100	1.0943E-04	1.9934E-04	-2.7970E-06	1.3156E-05

Figure 7-4: Iron depletion curves for various ultra-fine rock sample powders after leaching by hydrochloric and acetic acids.

It has been found that samples containing ferrimagnetic iron-oxide minerals experience rapid decrease in bulk susceptibility due to iron-leaching processes. The iron-bearing silicates retain their iron longer, resulting in a much flatter leaching curve. As shown in Figure 7-4, the basaltic metavolcanic has a characteristic magnetite depletion. In contrast, the two metasediment samples (schist and greywacke) possess an iron-bearing matrix and exhibits a slow and gradual depletion. The chloritized pillow basalt also retained iron within a paramagnetic phyllosilicate matrix. After nearly 30 minutes of leaching it had reached a stable level of bulk susceptibility with remaining iron being tightly bound within phyllosilicate lattices.

7.1.3 Scanning Electron Microprobe X-ray Maps

X-ray elemental mapping provides a useful qualitative verification of magnetic mineralogy with respect to the gross distribution of elements within various minerals of a sample. This technique makes use of direct electron bombardment on polished thin-sections within an energy-dispersive scanning electron microprobe. The electron-specimen interaction produces different types of electrons and electromagnetic waves. Backscattered electrons are detected by the microprobe as signals and can be displayed on a screen or photographic film to infer

compositional information. Backscatter electrons are elastically scattered by the sample through a large angle (usually can bounce back very close to the primary beam). They are indicators of average elemental number. Larger elemental numbers relate to bigger atoms which yield a greater intensity of backscatter electrons at characteristic angles. The brightness of areas on the cathode ray tube and on photographs are proportional to the current intensities.

The energy-dispersive spectrometer produces the simultaneous display of multi-element spectra. Spectral peaks are utilized in elemental identification and semi-qualitative mineral analyses. Six samples were used to typify lithology within the thesis area:

- (i) RS1.22C - porphyritic basalt flow metavolcanic
- (ii) RS8C - chloritized pillow basalt
- (iii) RS9C - greywacke
- (iv) RS10 - higher grade greywacke slate
- (v) RS10.5 - garnet-hornblende greywacke slate
- (vi) RS10.8 - biotite-garnet-staurolite schist.

Various minerals were analyzed semi-quantitatively from each sample (see Appendix III). X-ray maps were produced to assess the elemental distribution in each sample. The output consists of pre-set windows (corresponding to the element of interest). Iron and manganese are the relevant elements with respect to

determining the sources of bulk magnetic susceptibility. The maps also reveal spatial anisotropic distributions (ie. preferred dimensional and crystallographic orientations of iron and manganese-bearing minerals). Figures 7-5 to 7-8 display X-ray maps and electron backscatter images for the four metasedimentary samples.

The greywacke X-ray map (Fig. 7-5; sample RS9C) analysis reveals the iron-bearing minerals: chlorite, biotite, epidote, and iron-sulphide and/or ilmenite. The potassium elemental X-ray map in Figure 7-5 displays biotite laths in a sub-parallel arrangement. They make up the most volumetrically significant mineral within the iron map. Two very bright sets of grains are present only in the iron map and would then probably represent pyrite or ilmenite. These grains would raise the bulk susceptibility of the sample but are much less anisotropic than the biotite laths displaying a preferred orientation. Chlorite is the only other significant contributor to susceptibility. It is present in the iron and magnesium maps and absent in the potassium map.

A higher grade greywacke (Fig. 7-6; sample RS10) shows a stronger preferred orientation of phyllosilicates, including two generations of biotite. Analyses indicate that the iron-bearing minerals are: biotite, chlorite, ilmenite and/or iron-sulphide.

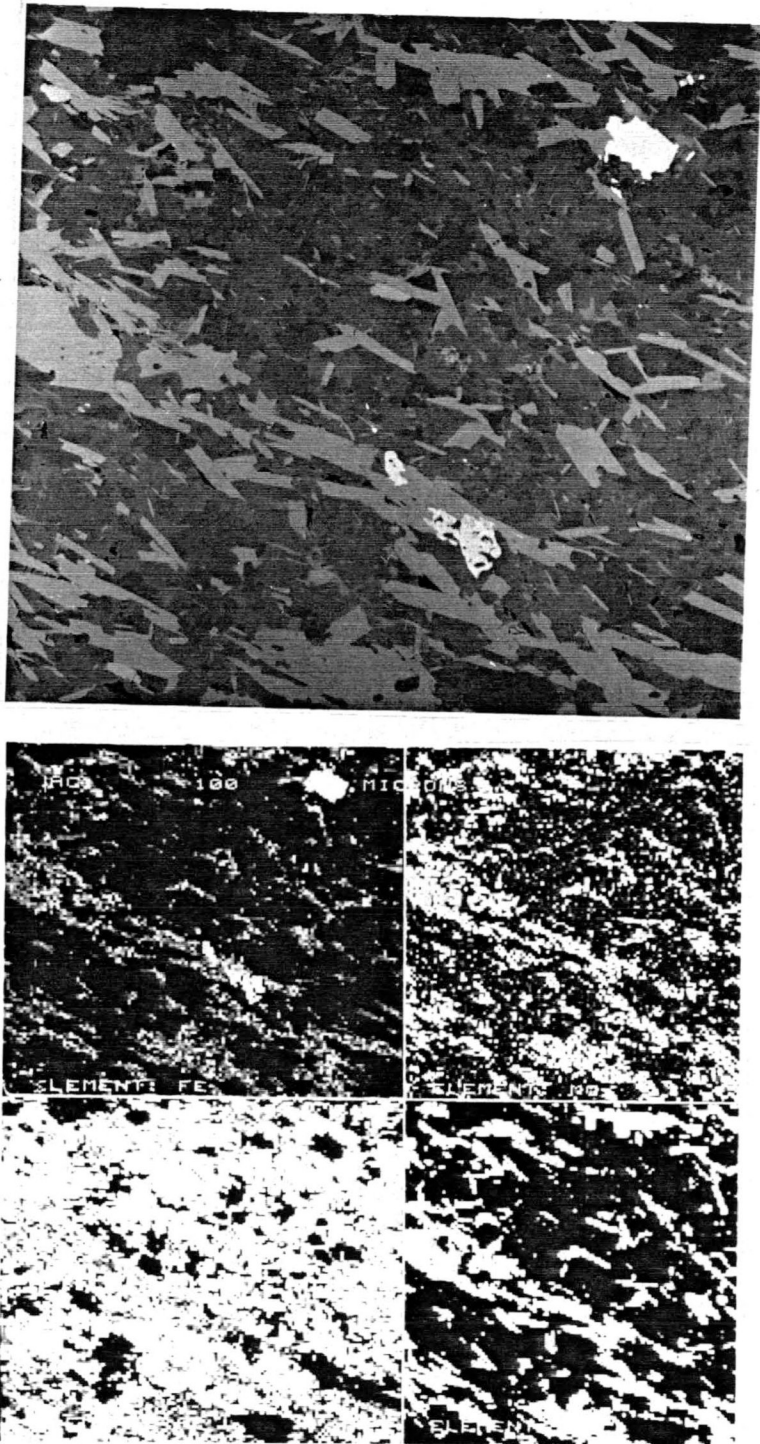


Figure 7-5: Greywacke X-ray maps (sample RS9C) for Fe, Mg, Al and K (upper photograph). Lower photograph is electron backscatter image. (Magnification = 100X; 0.1 s exp)

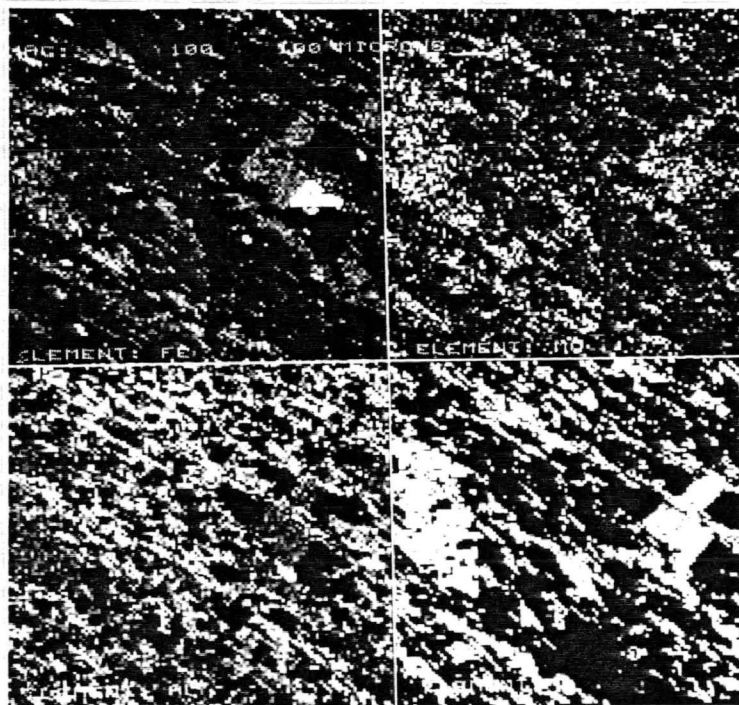
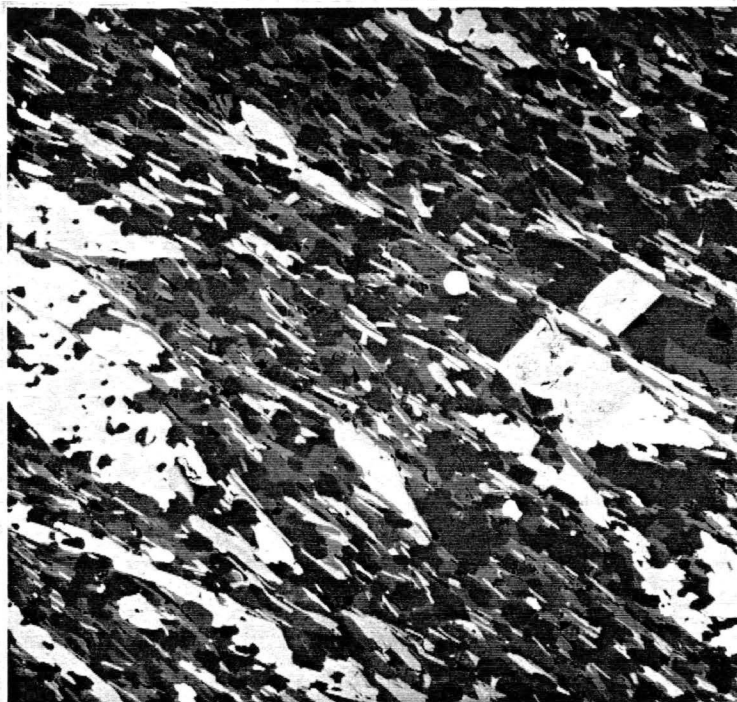


Figure 7-6: Higher grade greywacke slate X-ray maps (sample RS10) for Fe, Mg, Al and K (upper photograph). Lower photograph is electron backscatter image. (Magnification = 100X; 0.1 s exp)

As in RS9C, biotite (present in Fe, Mg and especially K elemental maps) comprises the prominent volumetric source of susceptibility as well as anisotropy. Occasional iron-sulphide or ilmenite grains show very brightly on the iron map. These grains show generally greater susceptibility and lesser anisotropy than biotite, but are aligned with the micaceous schistosity. Chlorite is relatively rare at this metamorphic grade, but a few small spots are visible on the Fe, Mg and Al maps (and not on the K map).

Figure 7-7 displays X-ray maps for the biotite-garnet schist (sample RS10.5). The iron-bearing minerals determined by semi-qualitative analyses includes: garnet, hornblende, biotite, chlorite, and ilmenite and/or iron-sulphides. Large garnet (manganese-rich spessartite) porphyroblasts are the most obvious feature on the Fe and Mn maps. Garnets are therefore, a notable contributor to bulk susceptibility in higher grade metamorphic rocks. Hornblende porphyroblasts appear faintly on the Fe and Mg maps. The occasional bright rounded grain of ilmenite and iron sulphides, visible only within the Fe map, also adds to the rock's bulk susceptibility. The major source of anisotropy lies with the aligned biotite laths visible within the K map (and the Fe and Mg maps). Some chlorite, intergrown with biotite, appears only within the Fe and Mg maps.

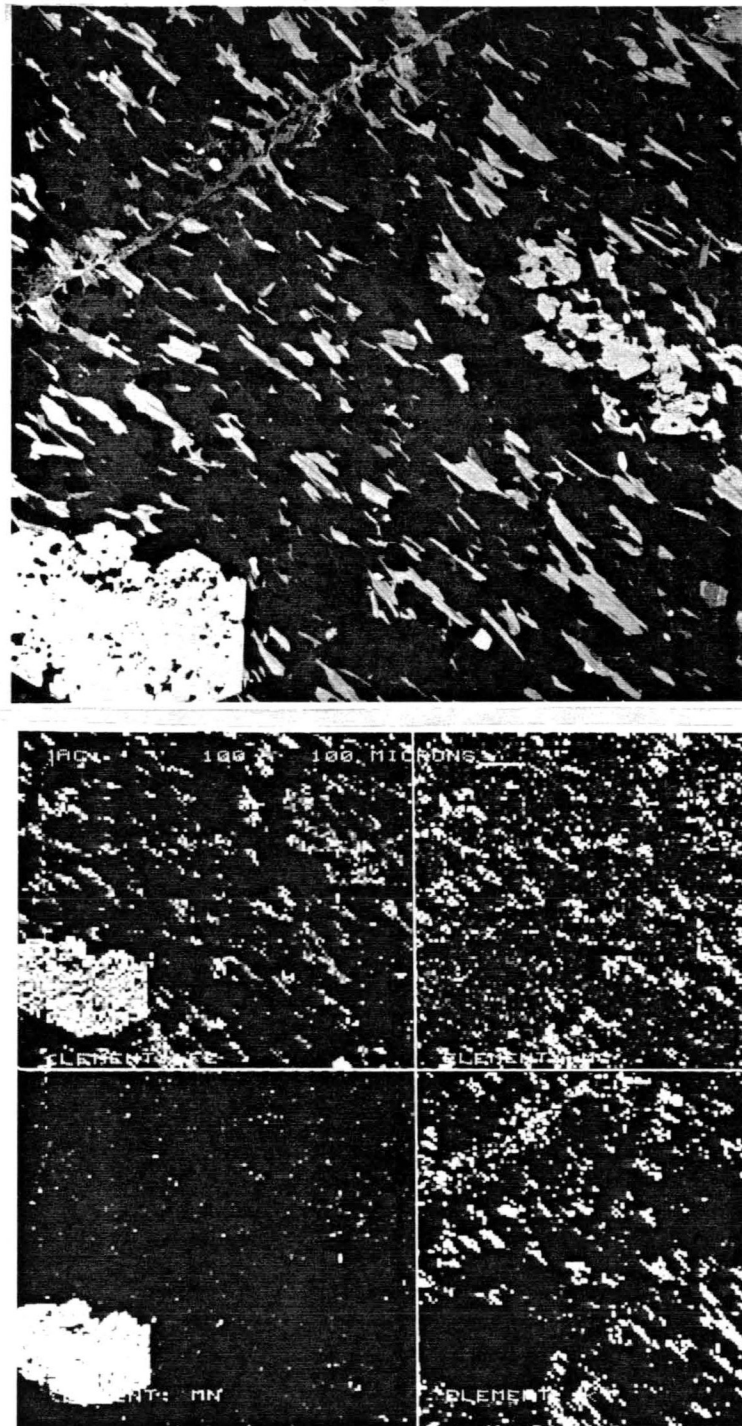


Figure 7-7: Biotite-garnet schist X-ray maps (sample RS10.5) for Fe, Mg, Mn, and K (upper photograph). Lower photograph is electron backscatter image. (Magnification = 50X; 0.1 s exp)

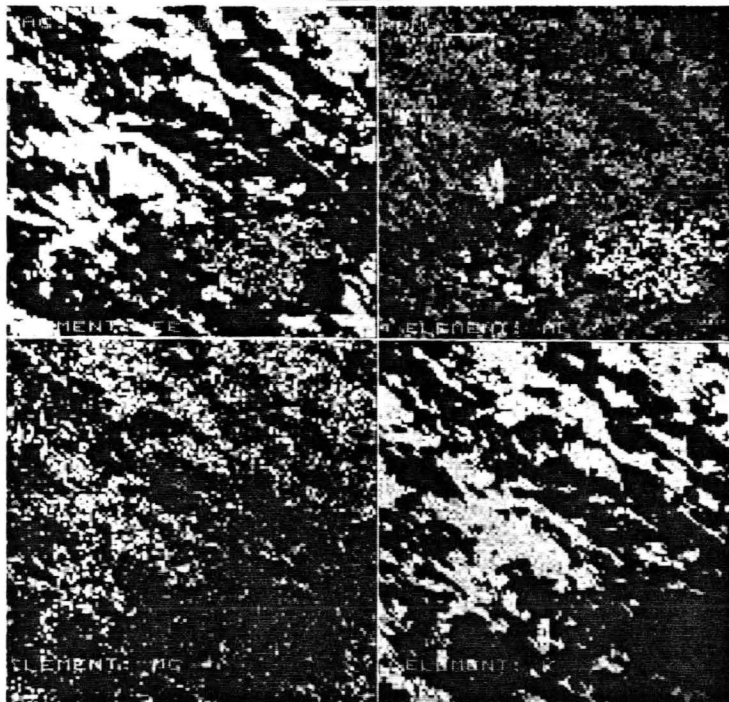
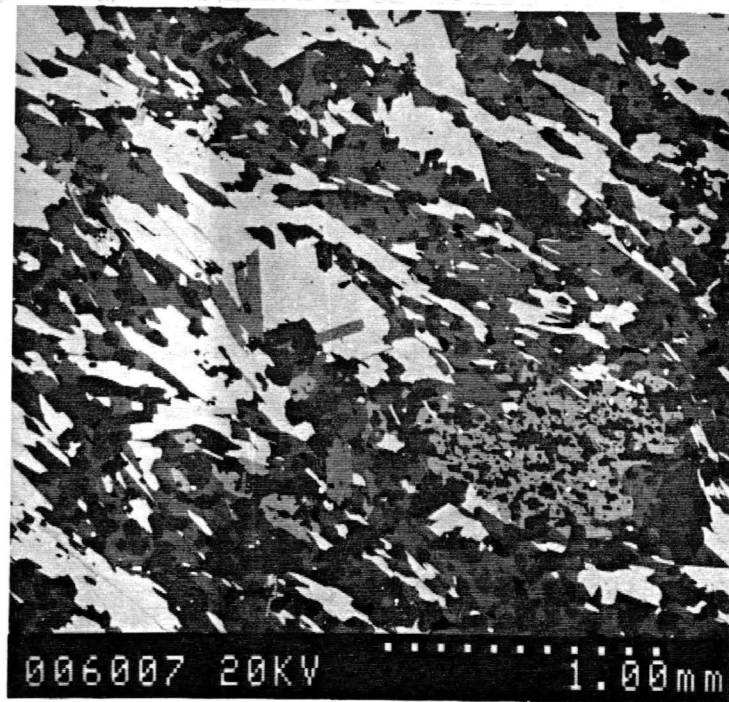


Figure 7-8: Biotite-garnet-staurolite schist X-ray maps (sample RS10.8) for Fe, Al, Mg, and K (upper photograph). Lower photograph is electron backscatter image. (Magnification = 30X; 0.1 s exp)

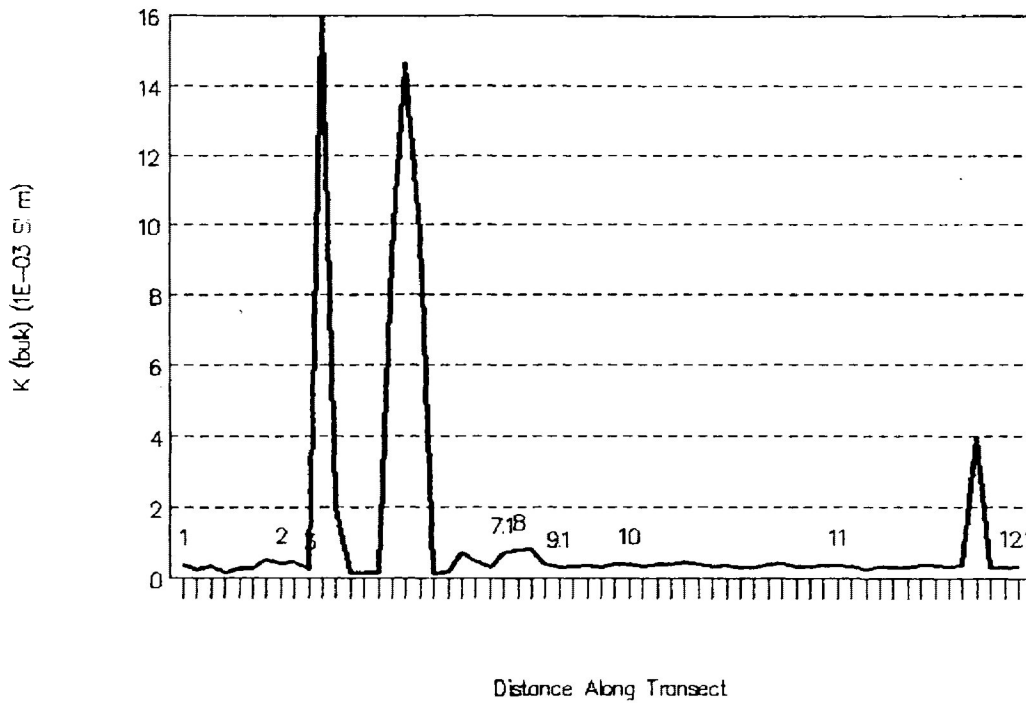
Analyses from the biotite-garnet-staurolite schist (Figure 7-8; sample RS10.8) identified the following iron-containing minerals: biotite, staurolite, pyrrhotite and/or pyrite, and cordierite. By volume, biotite comprises the most prominent source of susceptibility and anisotropy (evident especially within the K map). Staurolite porphyroblasts are much fainter, within the Fe and Al maps, and signifies a lesser influence on susceptibility. As with the other samples, fairly equant grains of pyrite and/or pyrrhotite add only to the bulk susceptibility and detract from the anisotropy. Cordierite was positively identified but is not clearly evident on these maps (it would reside within the Al, Fe, Mg maps and not the K map). Cordierite would add somewhat to the background bulk susceptibility.

7.1.4 Bulk Susceptibility In-situ Survey

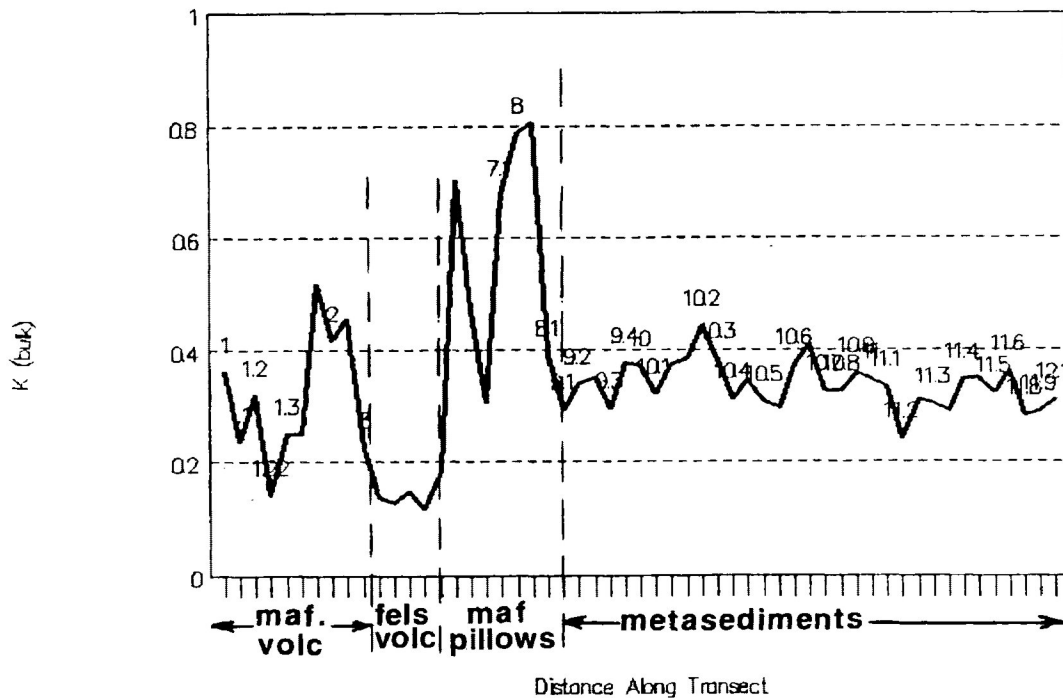
Metamorphism can influence magnetic mineralogy, by the production of more strongly susceptible phases from less susceptible minerals. For example, Rochette (1987) proposed the concept of mappable magnetic isograds within progressively metamorphosed shales. The magnetic isograds appear from rapid jumps in magnetic susceptibility due to the breakdown of detrital magnetite and the transformation of pyrite into pyrrhotite. The zonation of iron-bearing silicates, and magnetite and pyrrhotite

was proposed to correlate with "magnetic isograds" between the zeolite and amphibolite isograds. Through numerous in-situ bulk susceptibility measurements, Rochette was able to detect step-like variations producing a strong increase in the low-field bulk magnetic susceptibility caused by the appearance of ferrimagnetic monoclinic pyrrhotite. He detected only the "pyrrhotite-in" isograd and failed to establish a "magnetite-out" isograd. No jumps in susceptibility were detected due to iron-bearing paramagnetic silicates, because they appeared very gradually.

A similar study was undertaken within the thesis field area. A hand-held bulk susceptibility meter was used to produce 919 susceptibility readings across the entire thesis transect. Several readings were taken at relatively flat and unweathered outcrop surfaces and were averaged. Figure 7-9a and 7-9b show susceptibility values with each point representing an average value per station. Figure 7-9a is distorted by three enormous susceptibility values at RS3.5, RS3.7 and RS11. The first two cases involve the presence of small local metallic showings, associated with sheared felsic metavolcanics, containing gossan zones, large pyrite cubes and some chalcopyrite. The smaller spike at RS11.7 is coincident with the onset of migmatization, but dies away rapidly beyond that station. The reason for this anomaly may possibly relate to migmatization effects and accompanying reactions.



a



b

Figure 7-9: Bulk susceptibility values from "in-situ" survey across thesis transect.

- (a) - shows average values from 919 measurements taken from all outcrops (a few outcrop station numbers are included as reference).
- (b) - same data with the above three spikes removed. Only lithological variations are apparent.

Figure 7-9b shows the same data set with the three spikes removed. The only zonation visible relates to lithological and not to metamorphic controls. Mafic metavolcanics generally possess higher susceptibilities while felsic metavolcanics are generally much lower. The metasediments, despite minor compositional undulations, display no progressive increase in susceptibility with increasing metamorphic grade. This survey also failed to determine a "magnetite-out" isograd or a "pyrrhotite-in" isograd, such as that Rochette had attempted to determine elsewhere. Based on magnetic separation and scanning electron microprobe data, magnetite was seen to gradually decrease and pyrrhotite to become more prominent within this transect. Local heterogeneities presented the main problems for the bulk susceptibility in-situ survey.

7.2 MSA Results

7.2.1 Analytical Methods

Core samples for MSA studies were collected on an outcrop-by-outcrop scale along Highway #11. They were either obtained at the outcrop or from oriented hand-samples in the lab. A backpack drill was used on relatively flat, unweathered and fairly homogeneous outcrop exposures. The cores, oriented with respect to north, were drilled to a depth of about 10-15 cm,

using a one inch diameter drill bit. However, most of the MSA samples were cored in the lab using a drill press. Each hand sample was cut along a marked horizontal plane. A north arrow was drawn on the surface and a core was drilled perpendicular to the surface containing that orientation mark. The cores prepared in the laboratory tended to be of better quality. The cores were shaped to achieve dimensions comparable to a spherical sample (with core length equivalent to $0.82 \times$ diameter). These dimensions minimize any contribution of the effect of specimen shape on the intrinsic anisotropy of the rock.

The MSA of each sample was measured in a Sapphire SI-2 unit. This unit consists of a sensing coil and attached data acquisition and control circuitry (IBM Personal Computer). The coil detects anisotropies due to shape or lattice orientations of magnetically susceptible minerals. It measures the magnetic inductance in the presence of a low magnetic field along the long axis of the coil. The inductances of the coil, with and without a sample present was used in the comparison of the susceptibility of the specimen parallel to the coil with that of a standard. A calibration sample of MnO_2 was used as a standard.

Each sample was measured in twelve orientations (Figure 7-10) corresponding to nine axes (with three repeated measurements for error verification). A susceptibility tensor

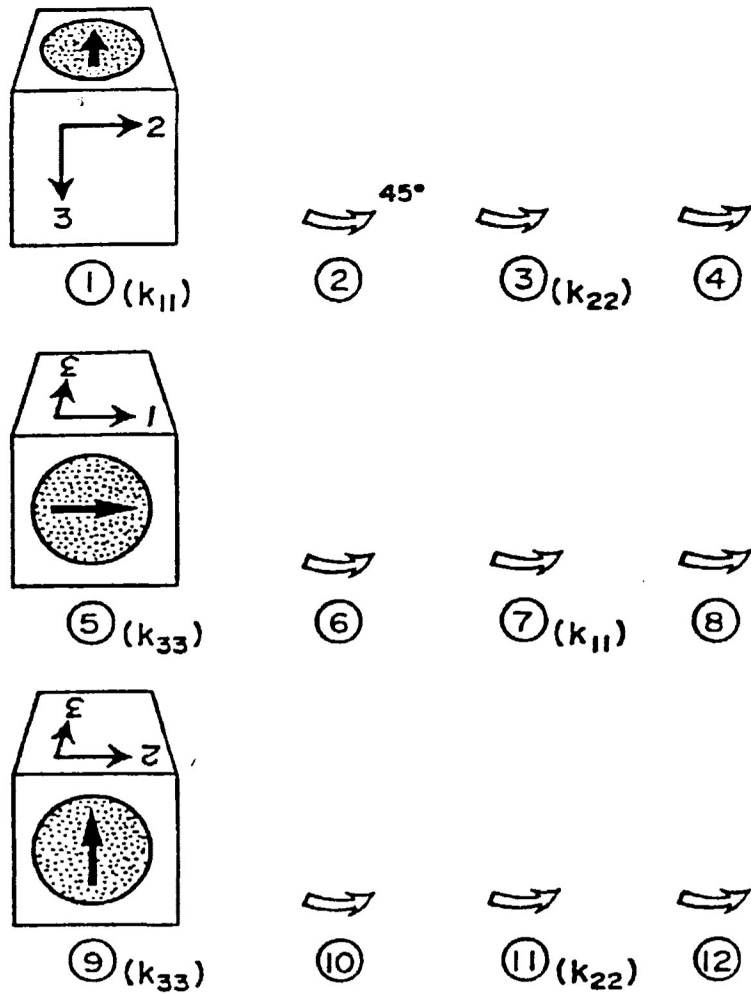


Figure 7-10: Diagrammatic representation of the twelve sample orientations used when measuring within the MSA coil. The cylindrical core sample (oriented with respect to a horizontal north arrow) is measured in a plastic cube so that the north arrow is aligned with the "k11" direction of the cube. The cube is rotated according to these 12 orientations.

was then calculated for each sample in the form of the directions and magnitudes of k_{max} , k_{int} , and k_{min} axes (data in Appendix I). Each standard-sized rock cylinder, in its various orientations takes only about fifteen minutes to measure. The entire process is quite accurate and very precise. The mafic metavolcanics and metasediments of varying metamorphic grade have a substantial bulk susceptibility ranging between $2.0E-04$ to $1.0E-03$ SI units/vol. Error is consistently low, the standard deviation is less than 2% of the actual value. In general, the samples are sufficiently anisotropic to yield principal susceptibility directions with a 95% cone of confidence radius of $<9^\circ$. The output includes calculations of R_{95} values; which are the measure of the angular deviation of the principal susceptibility directions (see Appendix I).

7.2.2 Principal Magnetic Susceptibility Directions

In strongly deformed rocks, the principal susceptibility directions tend to be parallel to prominent structural trends (the correlation between magnetic fabrics and structural field observations will be reviewed in section 7.3). The principal magnetic susceptibility directions (k_{max} , k_{int} , and k_{min}) for all the MSA samples plotted on a stereonet in Figure 7-11.

KASHABOWIE MAG DATA (ALL STATIONS)

Projection Schmidt

Number of Sample Points 117

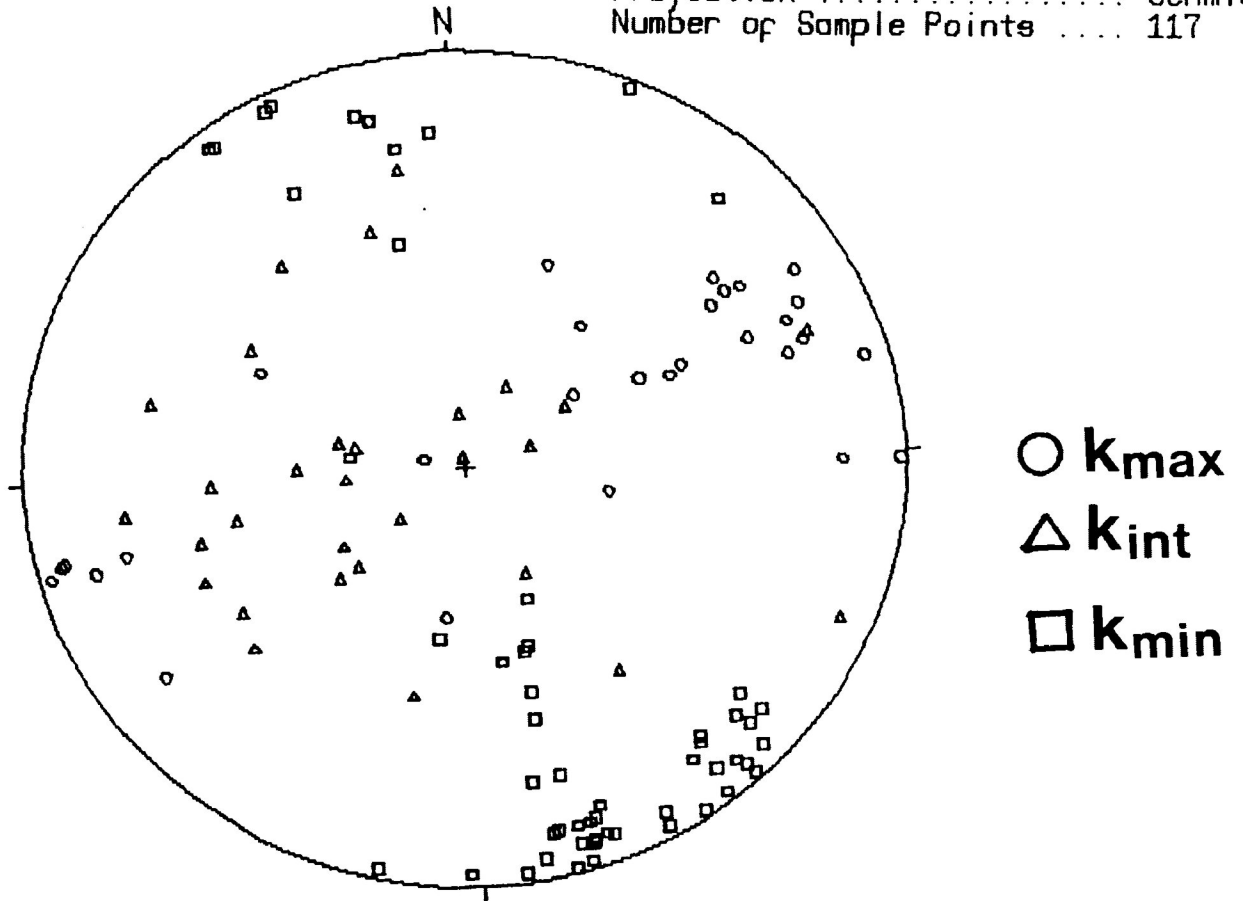
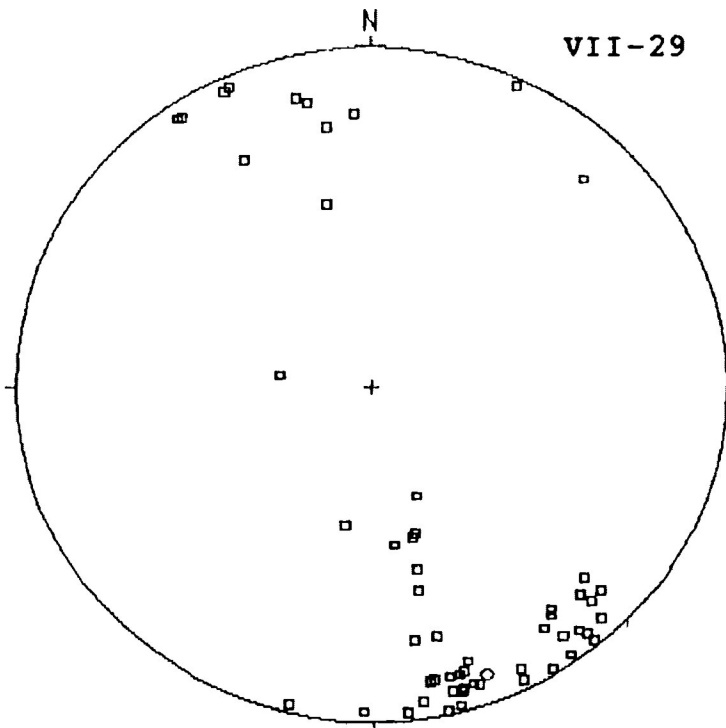


Figure 7-11: Equal area plot of all magnetic fabric axis directions (k_{max}, k_{int}, k_{min}) for all measured samples. All k_{min} axes are plotted; however, only those k_{max}/k_{int} axes with small R₉₅ values (<11°) are plotted.

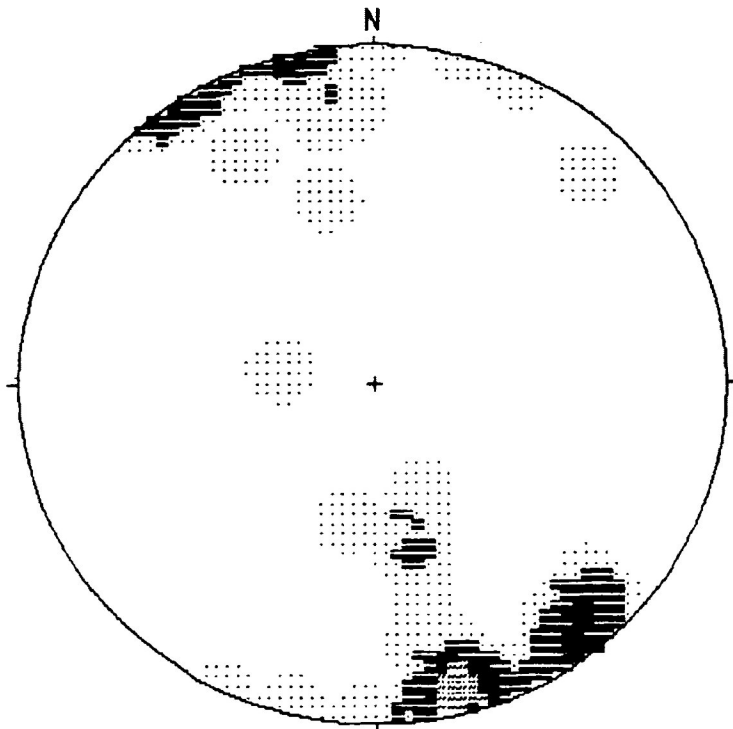
The contoured stereographs of point density distribution indicate a strong maxima of k_{min} axes with an average orientation of 160-08 and a strong clustering of data in NNW/SSE directions (Fig. 7-12). The average k_{min} point is the pole to a plane, with orientation 250/82NW, that should occupy the distribution of k_{int} and k_{max} axis points. Since many of the MSA fabrics are oblate (see sections 7.2.3 and 7.2.4), they can realistically be described in terms of minimum axes on a stereonet. These minimum axes then represent poles to these oblate MSA fabrics, or "magnetic foliations".

In many cases, the magnetic fabrics are so close to the uniaxial oblate form that a consistently oriented maximum axis cannot be determined. Therefore, the stereograms (Figures 7-13, 7-14) containing k_{max} and k_{min} data display only those cases (30 data sets out of 57) where the R_{95} value is $<11^\circ$; where actual maximum axes may be distinguished from intermediate axes. For samples that were slightly prolate ($R_{95}=11$ as a cutoff), the resultant maximum susceptibility ellipsoid axes represent "magnetic lineations". The distribution of k_{max} have well-defined sub-horizontal maxima. The average lineation is 068-22 and the axes plot along the great circle 253/77NW (which is very close to the plane (250/82NW) defined by the average k_{min} value). The 253/77NW plane contains both the k_{max} and k_{int} density distributions. In the $R_{95}<11$ cases, the k_{int} axes are distinct



MAG DATA (ALL MIN AXES)

Projection	Schmidt
Number of Sample Points	57
Mean Lineation Azimuth	159.5
Mean Lineation Plunge	8.0
1st Eigenvalue	46.51
2nd Eigenvalue	6.40
3rd Eigenvalue	4.09
LN (E1 / E2)	1.983
LN (E2 / E3)	0.448
(LN(E1/E2)) / (LN(E2/E3)) ..	4.427
Spherical variance	0.4326
Rbar	0.5674

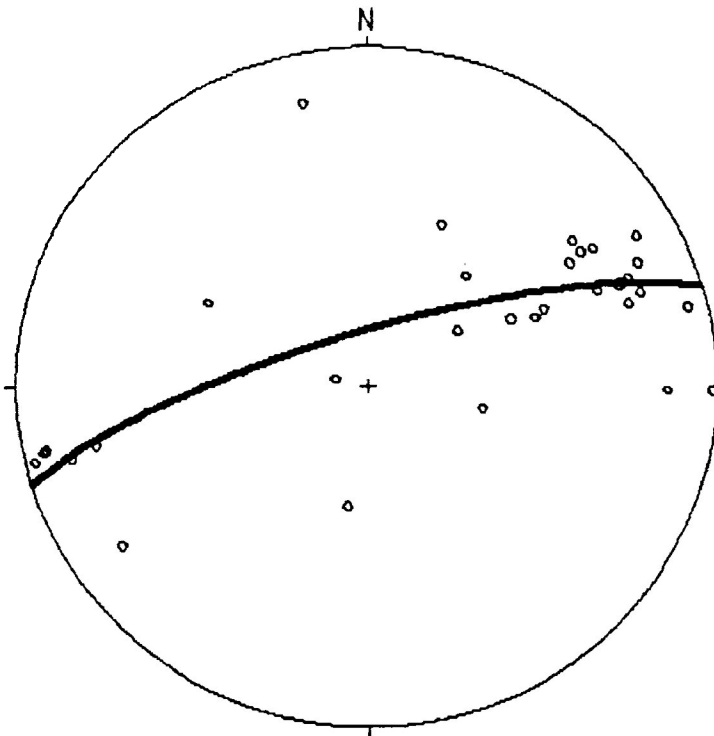


MAG DATA (ALL MIN AXES)

Step Function Grid
 Number of Sample Points 57

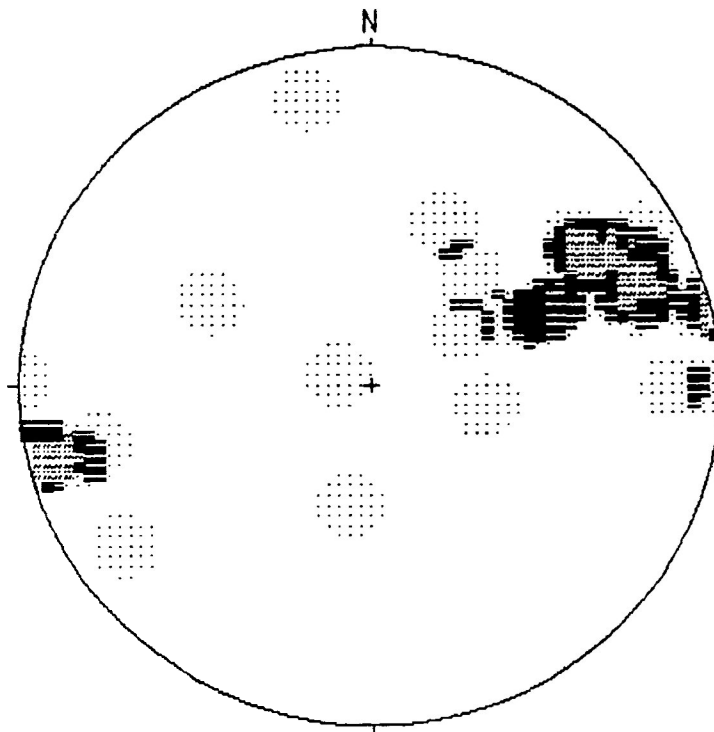
	0.0 to 7.0 %
	7.0 to 14.0 %
	14.0 to 21.0 %
	21.0 to 28.1 %

Figure 7-12: Equal area plot of all minimum susceptibility axis directions (avg. kmin = 160-08). The lower stereonet displays the contoured point density distribution of the kmin axes, representing the poles to "magnetic foliation".



MAG DATA (L-FABRIC MAX)

Projection	Schmidt
Number of Sample Points	30
Mean Lineation Azimuth	67.5
Mean Lineation Plunge	22.4
Great Circle Azimuth	253.0
Great Circle Plunge	76.8
1st Eigenvalue	21.04
2nd Eigenvalue	6.87
3rd Eigenvalue	2.09
LN (E1 / E2)	1.119
LN (E2 / E3)	1.193
(LN(E1/E2)) / (LN(E2/E3))	0.938
Spherical variance	0.4449
Rbar	0.5551

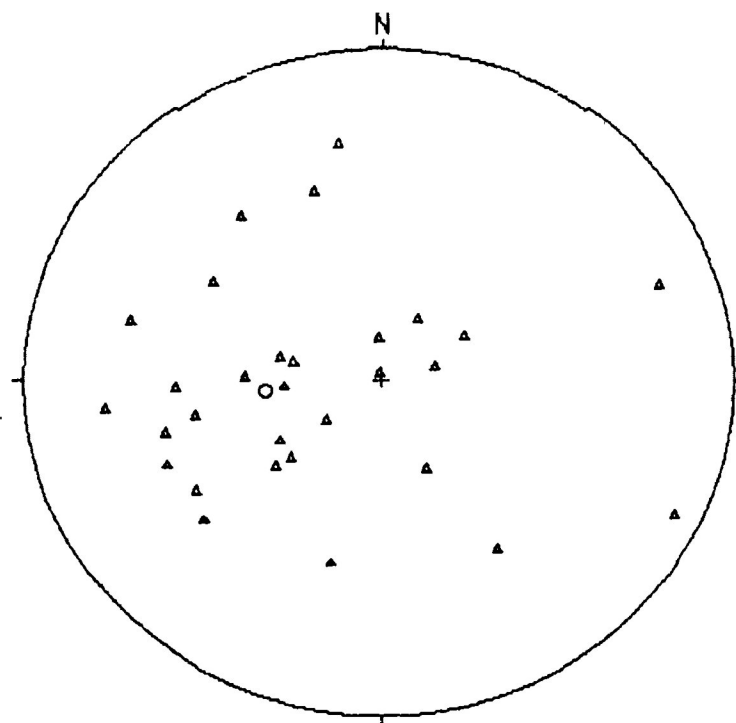


MAG DATA (L-FABRIC MAX)

Step Function Grid	
Number of Sample Points	30

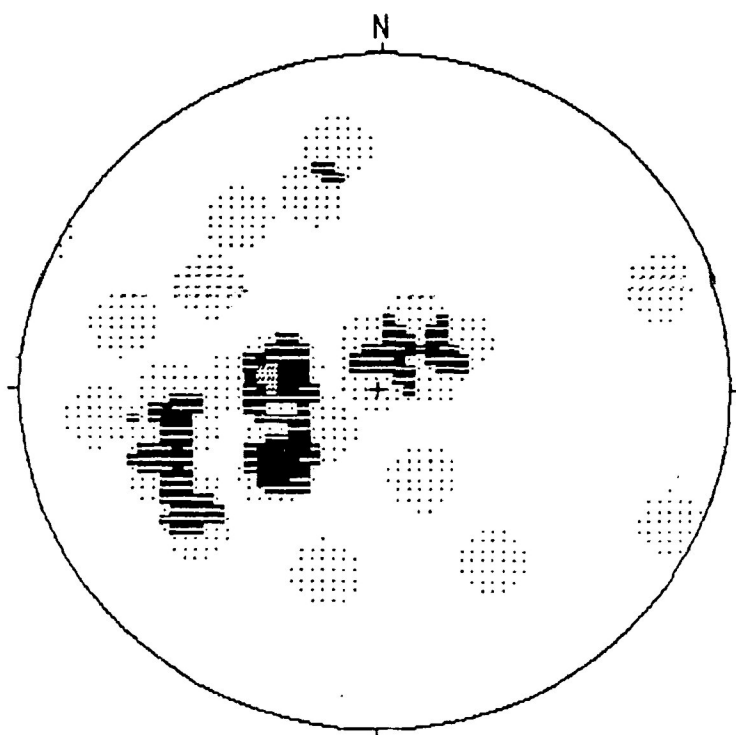
	0.0 to 4.0 %
	4.0 to 8.0 %
	8.0 to 12.0 %
	12.0 to 16.7 %

Figure 7-13: Equal area plot of all maximum susceptibility axis directions (avg. kmax = 068-22). The lower stereonet displays the contoured point density distribution of the kmax axes, representing "magnetic lineations". Only those kmax axes with small R95 values (<11°) are plotted.



MAG DATA (L-FABRIC INT)

Projection	Schmidt
Number of Sample Points	30
Mean Lineation Azimuth	264.5
Mean Lineation Plunge	63.2
1st Eigenvalue	20.00
2nd Eigenvalue	5.69
3rd Eigenvalue	4.32
LN (E1 / E2)	1.257
LN (E2 / E3)	0.276
(LN(E1/E2)) / (LN(E2/E3)) ..	4.557
Spherical variance	0.2348
Rbar	0.7652



MAG DATA (L-FABRIC INT)

Step Function Grid	
Number of Sample Points	30





	0.0 to 5.0 %
	5.0 to 9.0 %
	9.0 to 12.0 %
	12.0 to 14.0 %

Figure 7-14: Equal area plot of all intermediate susceptibility axis directions (avg. kint = 265-63). The lower stereonet displays the contoured point density distribution of the kint axes. Only those kint axes with small R95 values (<11°) are plotted.

from the contoured kmax axes which have a much shallower plunge. The kmax and kmin axes show very strong preferred directions on a regional scale across the entire transect study area. This data is quite similar to MSA results from the northern Quetico boundary with the Wabigoon subprovince (Sarvas, 1987). The Quetico/Wabigoon data have a similar magnetic foliation (256/74NW) but have no consistently oriented magnetic lineations due to complex isoclinal folding (fig. 7-15).

Some areas of the transect have more variable axis orientations than others. Figure 7-16 contains stereonet plots of the principal directions for the various lithological units. The greywacke-slates show the most tightly clustered data and correlate most closely to the average principal axes for the region. The metavolcanics plot in similar areas but have much more variable maximum axes. Very few felsic metavolcanic samples were measured, apart from a few test cores, due to very low bulk susceptibility values and high standard deviation errors. The paragneiss plots are similar to the greywacke-slate plot, but have steeper kmin axes. The migmatites show the most variable orientations and display no obvious preferred orientation, because of anatexis and recrystallization processes.

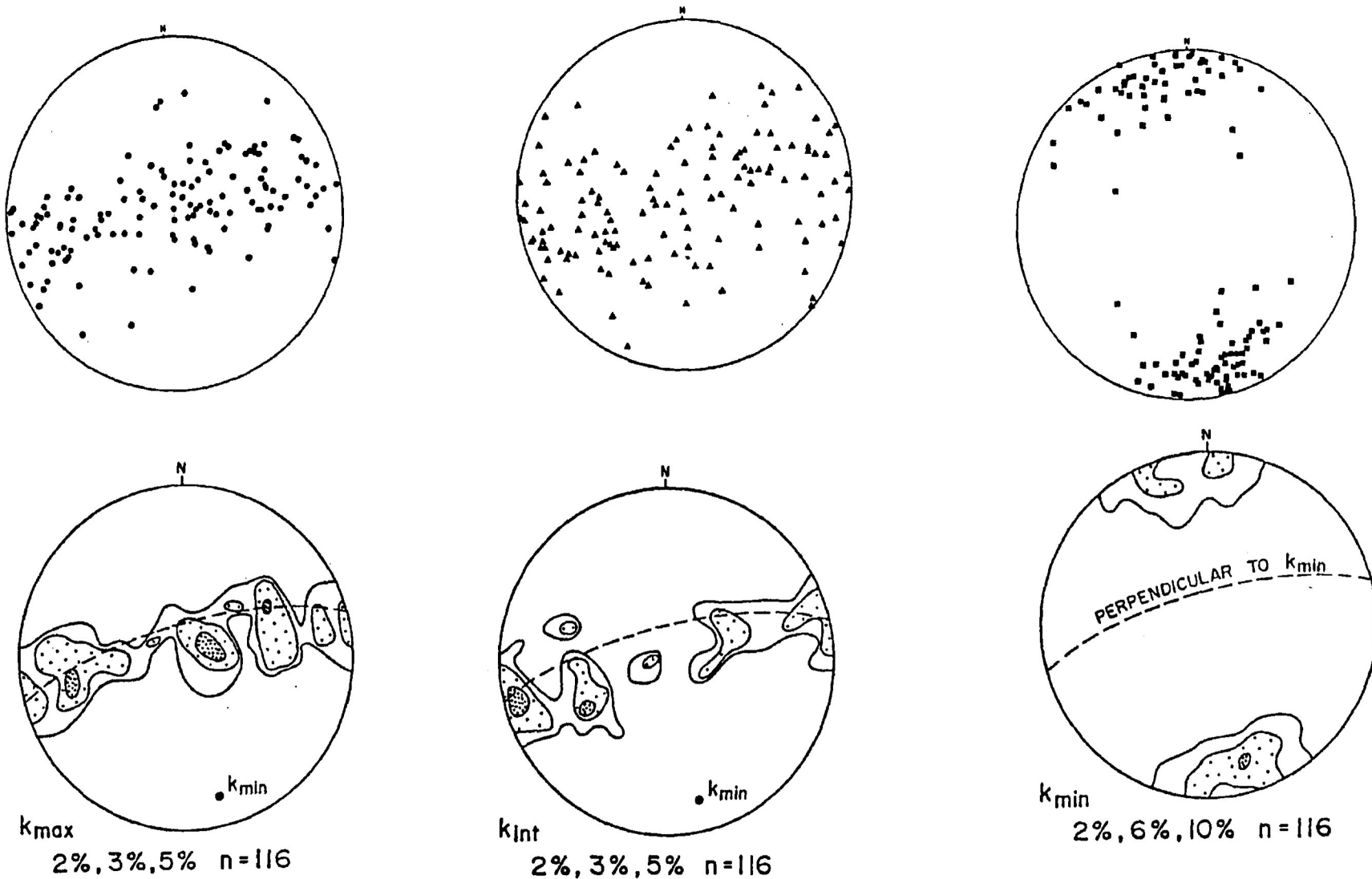
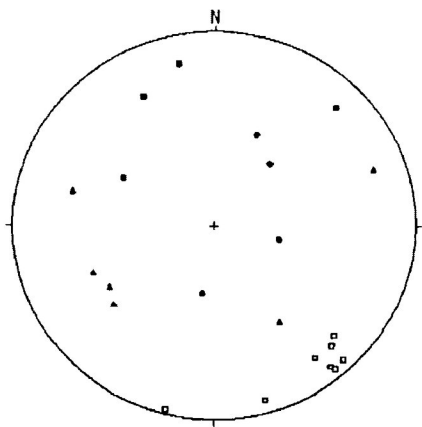
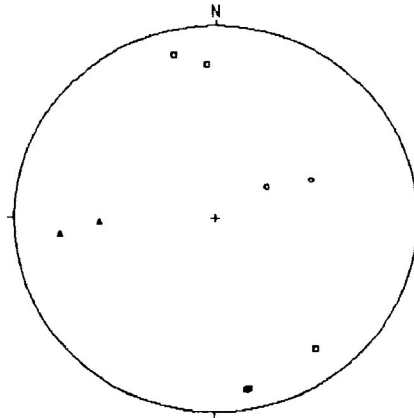


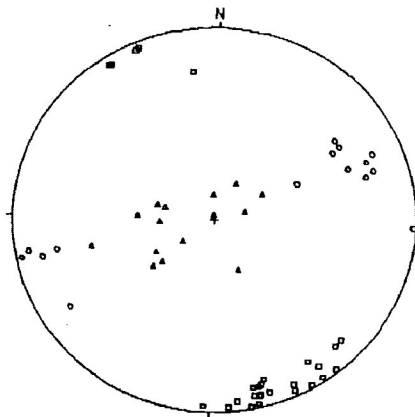
Figure 7-15: Magnetic susceptibility ellipsoid axis directions from studies at the northern Quetico boundary with the Wabigoon subprovince. (from Sarvas, 1987)



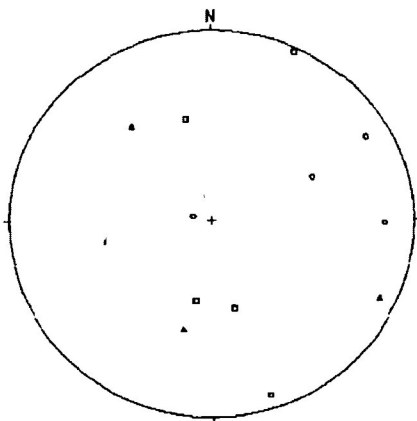
MAFIC METAVOLCANICS
 Projection Schmidt
 Number of Sample Points 23



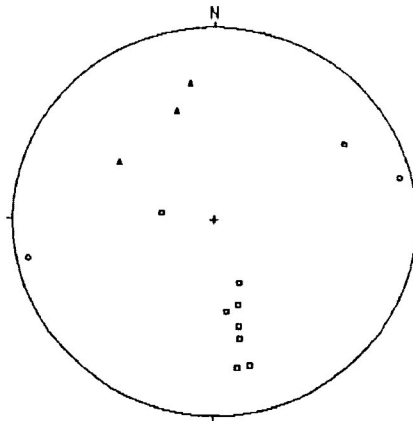
FELSIC METAVOLCANICS
 Projection Schmidt
 Number of Sample Points 5



GREYWACKE - SLATES
 Projection Schmidt
 Number of Sample Points 58



MIGMATITE
 Projection Schmidt
 Number of Sample Points 13



PARAGNEISS
 Projection Schmidt
 Number of Sample Points 14

Figure 7-16: Principal susceptibility axis directions for various rock types within the thesis transect.

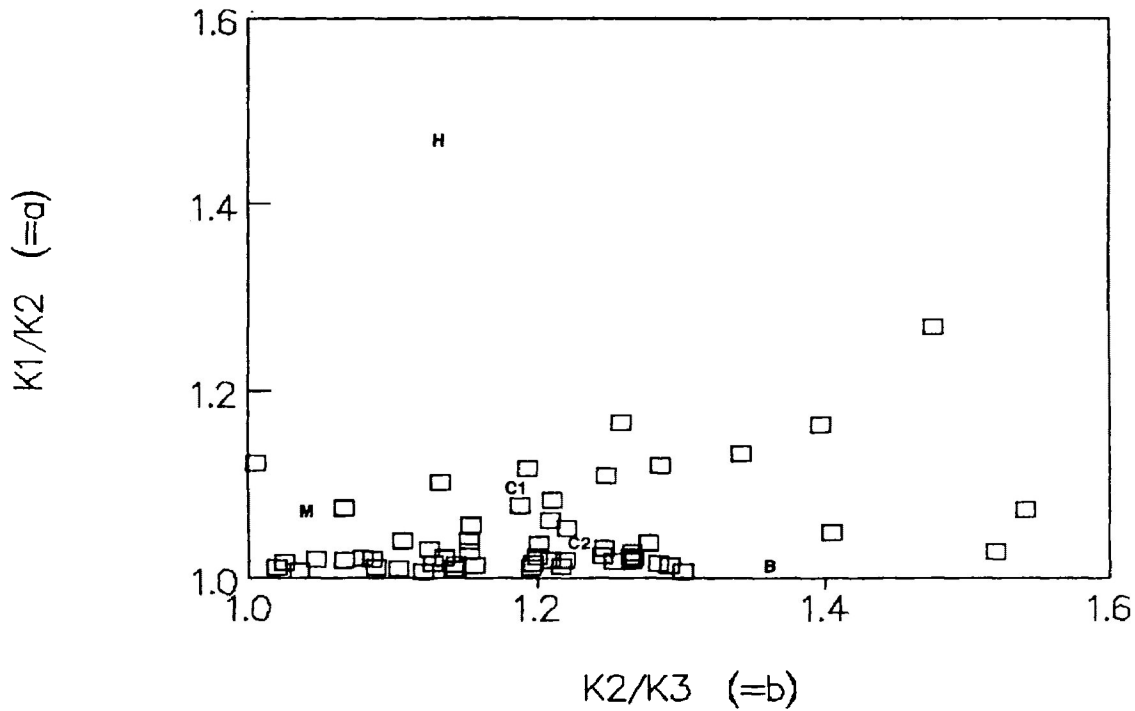
7.2.3 Flinn Diagram Fabric Analyses

Magnetic fabric analyses were derived from the calculated ellipsoids of magnetic susceptibility. The Flinn Diagram method of MSA representation of samples taken from the study area (Fig. 7-17) shows strongly oblate fabrics. The Flinn plot presents all data with respect to the axes: k_{max}/k_{int} versus k_{int}/k_{min} . In comparison with magnetic fabrics from monomineralic test data (Borradaile, 1988), the MSA whole rock samples plot closely to the biotite and chlorite positions (Fig. 7-17). The samples plot far from the very prolate hornblende position and are much more anisotropic than the metamorphic magnetite sample. This supports studies of magnetically susceptible mineralogy, presented earlier in this chapter, that the chlorite and biotite fractions predominate over the other magnetically susceptible minerals.

All the lithological varieties demonstrate a similar oblate MSA fabrics. Generally, the felsic and mafic metavolcanics have much less extreme oblate shapes (Fig. 7-18). The metasediments of the Quetico belt plot farther along the k_{int}/k_{min} axis but generally cluster between the positions held by the monomineralic chlorite and biotite samples.

Flinn Diagram

All MSA Samples



SUSCEPTIBILITY DATA FOR
COMMON METAMORPHIC MINERALS

Mineral	Kmax	Kint	Kmin	K1/K2	K2/K3	
Hornblende	1.347	0.917	0.809	1.47	1.13	"H"
Chlorite	1.093	1.060	0.864	1.03	1.23	"C2"
	1.128	1.023	0.866	1.10	1.18	"C1"
	1.063	1.020	0.921	1.04	1.11	
Biotite	1.114	1.106	0.812	1.01	1.36	"B"
	1.098	1.095	0.832	1.00	1.32	
	1.107	1.096	0.824	1.01	1.33	
	1.108	1.107	0.814	1.00	1.36	
Magnetite (metamorphic)	1.063	0.989	0.951	1.07	1.04	"M"

(data from Borradaile, 1988)

Figure 7-17: Flinn diagram representation of all MSA data relative to some monomineralic test samples (derived from data below).

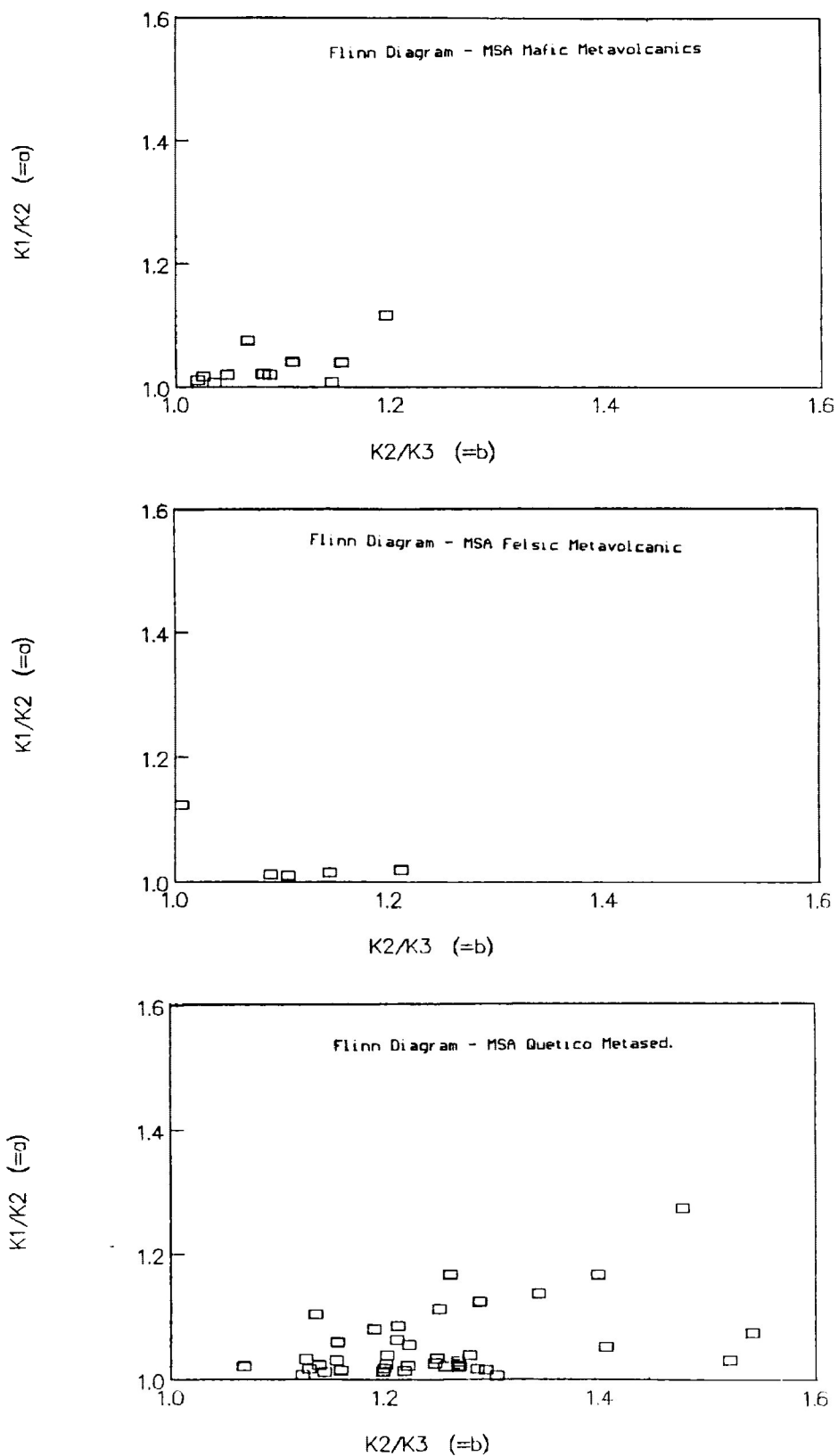


Figure 7-18: Lithological breakdown of the MSA Flinn diagram representation. Metasediment and metavolcanic samples occupy slightly different areas of the Flinn diagram.

7.2.4 Jelinek Plot Fabric Analyses

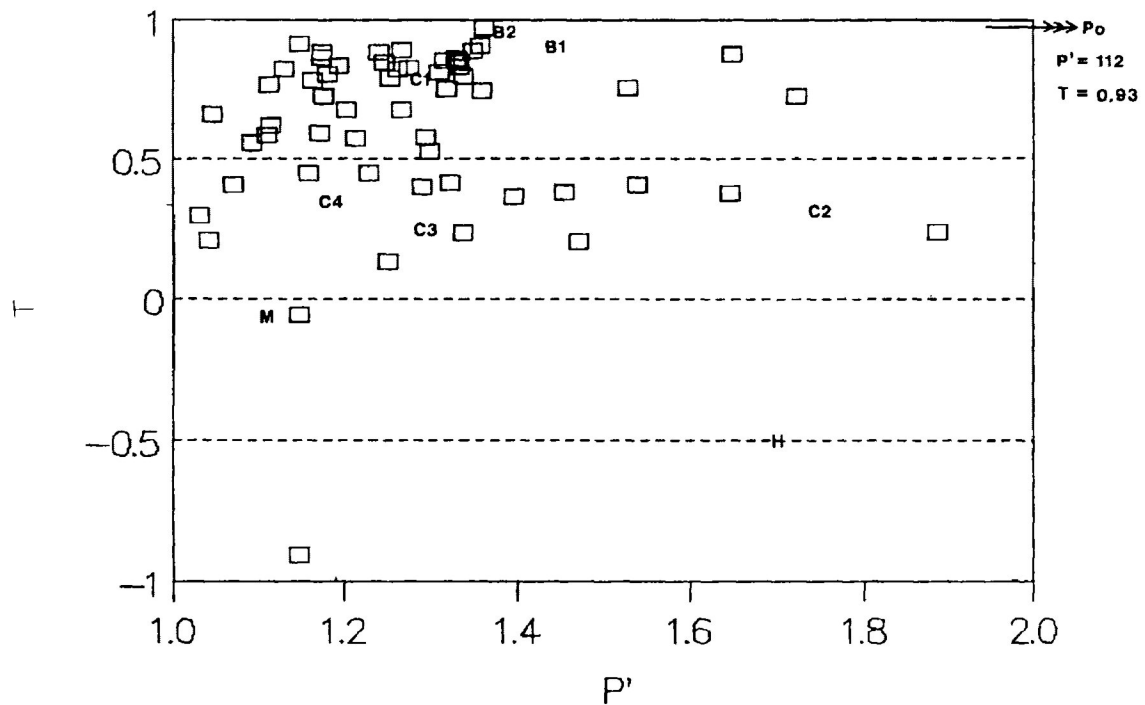
The Flinn ratios of k_{max}/k_{int} and k_{int}/k_{min} are important in describing the sense of anisotropy or shape of the magnitude of magnetic susceptibility ellipsoid. However, the degree of anisotropy, or its deviation from sphericity, is also beneficial. The Jelinek-Hrouda plot is a modern and useful representation of magnetic fabrics. Unlike the Flinn plot, it distinguishes the degree, from the sense of anisotropy. The Flinn plot poorly resolves ellipsoids with smaller degrees of anisotropy. The Jelinek parameters "P'" and "T" surmount these problems. The P'-axis represents an increasing degree of anisotropy. Positive values on the T-axis indicate more oblate ellipsoids, whereas negative T-values represent more prolate ellipsoids.

When represented by the Jelinek parameters, the sample MSA data plots well above the $T=0$ axis (Fig. 7-19). This again suggests strongly oblate fabrics. They in fact cluster between the monomineralic test sample data sites (Borradaile, 1988) of biotite and chlorite. The very magnetite-rich sample, mentioned earlier in this chapter, does plot very closely to the metamorphic magnetite position. The data seems relatively independent of the hornblende position as well as the extremely anisotropic pyrrhotite position.

VII-39

Jelinek-Hrouda Plot

All MSA samples



SUSCEPTIBILITY DATA FOR
COMMON METAMORPHIC MINERALS

Mineral	P'	I	
Hornblende	1.700	-0.50	"H"
Chlorite	1.296	0.82	"C1"
	1.752	0.30	"C2"
	1.300	0.24	"C3"
	1.190	0.33	"C4"
Biotite	1.441	0.90	"B1"
	1.378	0.96	"B2"
Magnetite (metamorphic)	1.107	-0.07	"M"
Pyrrhotite (single crystal)	112.0	0.93	

(data from Borradaile, 1988)

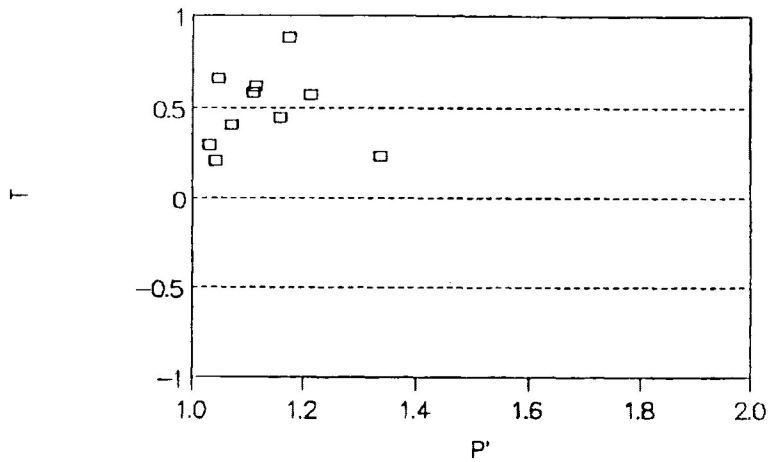
Figure 7-19: Jelinek-Hrouda diagram representation of all MSA data relative to some monomineralic test samples (derived from Jelinek parameters below).

The fact that the susceptibility of the chlorite and biotite fractions is similar to that of the MSA samples again lends support to the view that the iron-bearing phyllosilicates are the primary source of magnetic susceptibility. The biotite data points have slightly more oblate T-values and possess more anisotropic P'-values than the majority of the data in Figure 7-19. This is expected since the rock is not composed entirely of biotite (or chlorite) and does not necessarily display the perfectly induced alignment used for the monomineralic fractions (Borradaile, et al., 1986; Borradaile, 1988).

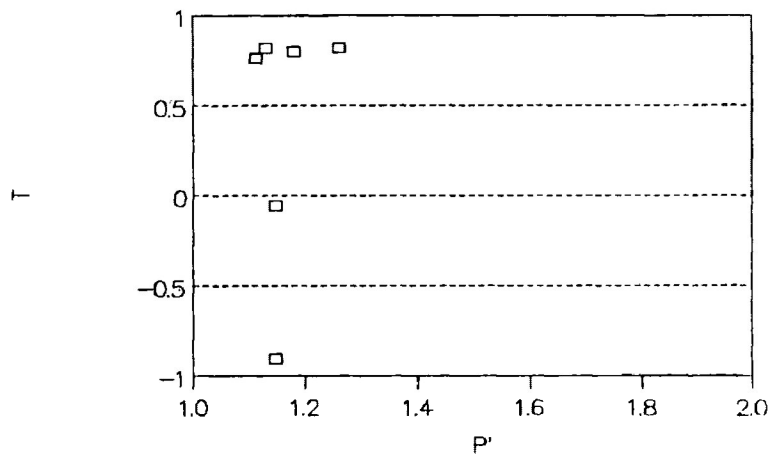
Figure 7-20 shows Jelinek plots for the various lithological groups. Generally, the Quetico metasediments plot at higher P'-values while the Shebandowan metavolcanics tend to be less anisotropic but still oblate. As expected, the chlorite and biotite-rich metasediments cluster closely to the "C" and "B" test sample points seen in Figure 7-19.

7.3 Magnetic Fabric and Field Structure Correlation

The correlation of the principal directions of susceptibility ellipsoids with mesoscopic fabric elements has been well documented (Hrouda, 1982; Borradaile et al., 1988; Stott and Schwerdtner, 1981; Rathore, 1979; Kligfield, et al., 1982) within singly deformed metamorphic rocks. A lack of



Felsic Metavolcanic Samples



Duetico Metasediment Samples

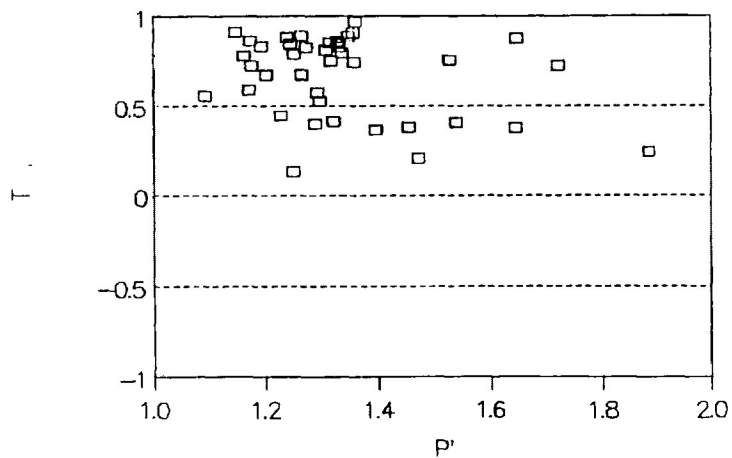


Figure 7-20: Lithological breakdown of the MSA Jelinek-Hrouda diagram representation. Metasediment and metavolcanic samples occupy slightly different areas of the Jelinek plot.

parallelism exists where multiple fabrics are superimposed (Goldstein, 1980). Another exception to the correspondence between principal strain and magnetic fabric directions arises from the interference due to combined sedimentary and tectonic fabrics (Borradaile and Tarling, 1981).

It has been demonstrated experimentally that as deformation proceeds, the principal directions of magnetic susceptibility rotate towards principal strain directions (Borradaile and Alford, 1987). However, it was emphasized that this applies only to detrital magnetic grains which consequently act as passive strain markers. This is not the case for iron-bearing phyllosilicate matrix minerals, common within metamorphic rocks. The influence of deformation mechanisms and the recrystallization of porphyroblasts during metamorphism would distort the relationship between finite strain directions and the axes of susceptibility ellipsoids.

Within strongly deformed rocks elsewhere, the direction of maximum susceptibility has been shown to be parallel to the maximum extension direction (Rathore, 1979; Kligfield, et al., 1982; Hrouda, 1976; Stott and Schwerdtner, 1981; Borradaile, 1988). Maximum susceptibility would also parallel mineral or stretched object lineations contained within a cleavage. Similarly, minimum susceptibility axes are normal to this

foliation plane and the axes cluster near the pole to the cleavage. Maximum susceptibility axes may, however, parallel the intersection lineation between bedding and cleavage (Hrouda, 1976; Borradaile, et al., 1988; Sarvas, 1987). If minimum susceptibility axes cluster near the pole of cleavage, as is the case in this study, rather than around poles to bedding; then the orientation of principle susceptibility axes are more likely to result from metamorphic deformation and are probably not due to sedimentary processes (Kligfield, et al., 1982).

The amount of data scatter of the principal directions of susceptibility and fabric orientations; and the correlation of the two is related to a certain degree of error. The major source of error is due to fabric variations and heterogeneities of magnetic mineralogy within each sample and across the region. Other possible sources of error are added during analysis: proper orientation of hand samples in the field, reorientation and drilling of cores in the lab, indication of north markings on the core, and human error associated with the orientation and measurement of cores within the MSA apparatus. The error should be less than $\pm 5^\circ$ given reasonable care to detail and choice of fairly representative outcrop sample sites.

Despite any level of analytical error, the magnetic fabrics (Fig. 7-21) correlate with visible field fabric data

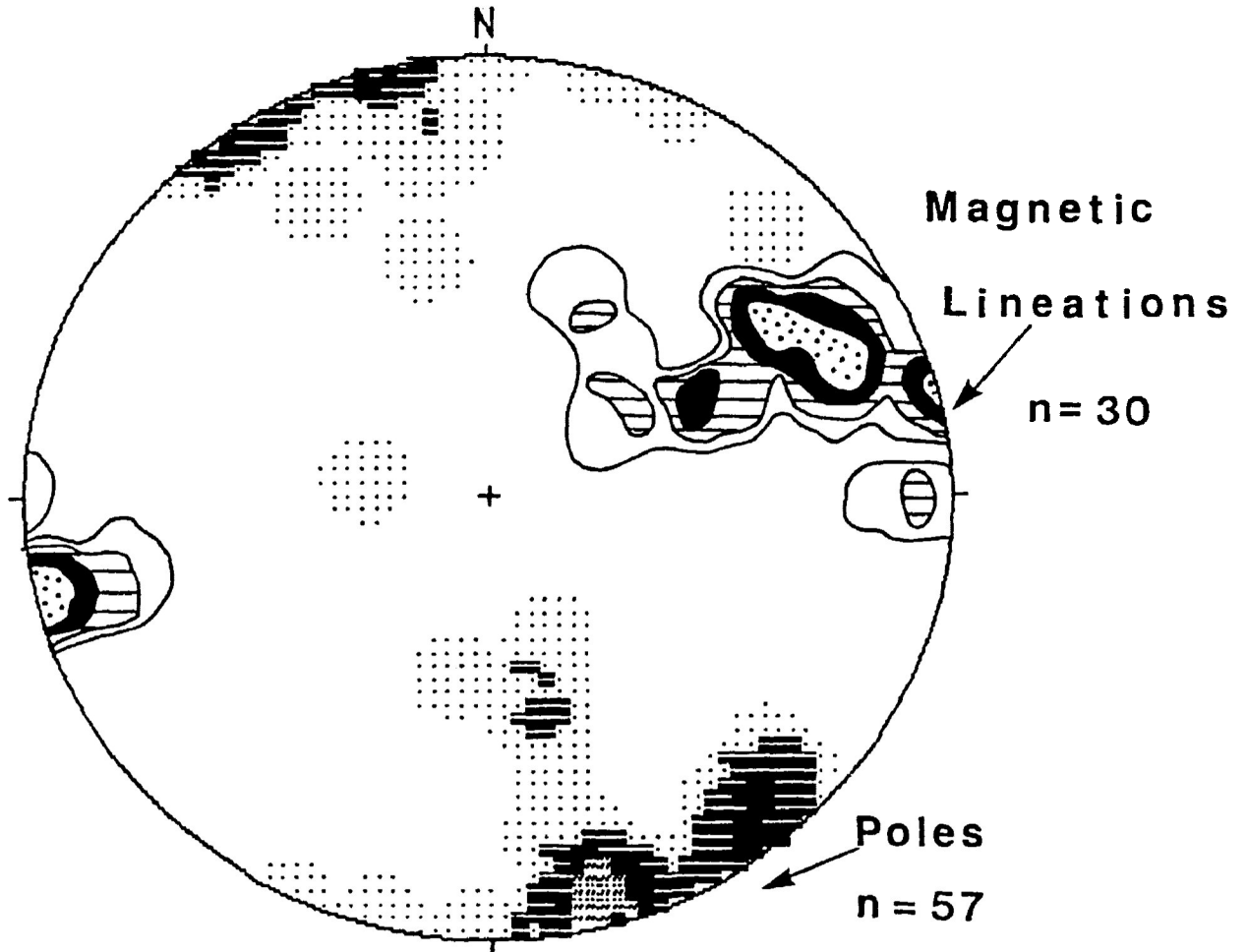


Figure 7-21: Contoured point density distribution on this equal area stereonet combines magnetic lineation (kmax axes) orientations with poles to magnetic foliation (kmin axes).

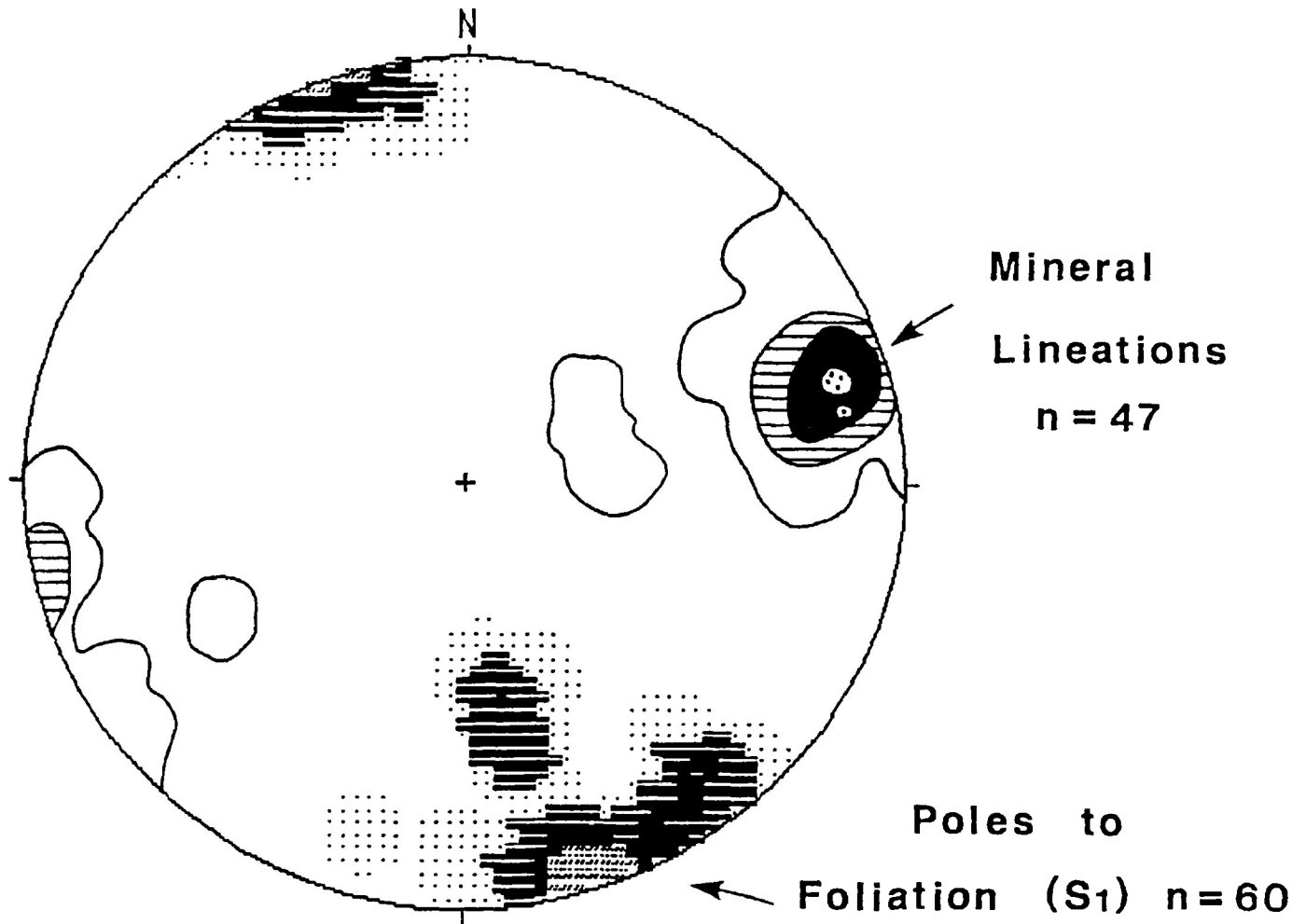


Figure 7-22: Contoured point density distribution on this equal area stereonet combines observed mineral lineation orientations with poles to measured foliations.

(Fig. 7-22). The maximum susceptibility direction is parallel to the maximum extension contained within the [S1] cleavage defined by mineral lineations. Figure 7-23 shows the close relationship between the orientations of maximum susceptibility axes and the mineral lineations for stations sampled across the transect. A similar correlation exists between the minimum susceptibility axes (poles in Fig. 7-21) and the poles to the [S1] foliation planes (Fig. 7-22).

Unlike the study by Sarvas (1987) at the northern Quetico boundary with the Wabigoon subprovince, the maximum susceptibility orientations display a tight preferred orientation close to that of the mineral lineations. Sarvas had inconsistent orientations of maximum susceptibility due to prevalent sheath folding, which is absent within this study area. The consistent correlation of the minimum susceptibility axes within [S1] cleavage poles suggests a tectonic magnetic fabric. However, since bedding fabrics are very close to local schistosity (see chapter 4), a component of bedding-controlled MSA would be difficult to totally discount in this area.

Overall, there is a close relationship between magnetic and tectonic fabrics in the area. Any differences in orientation of individual field lineations and magnetic lineations can be partially attributed to errors in measurement and outcrop

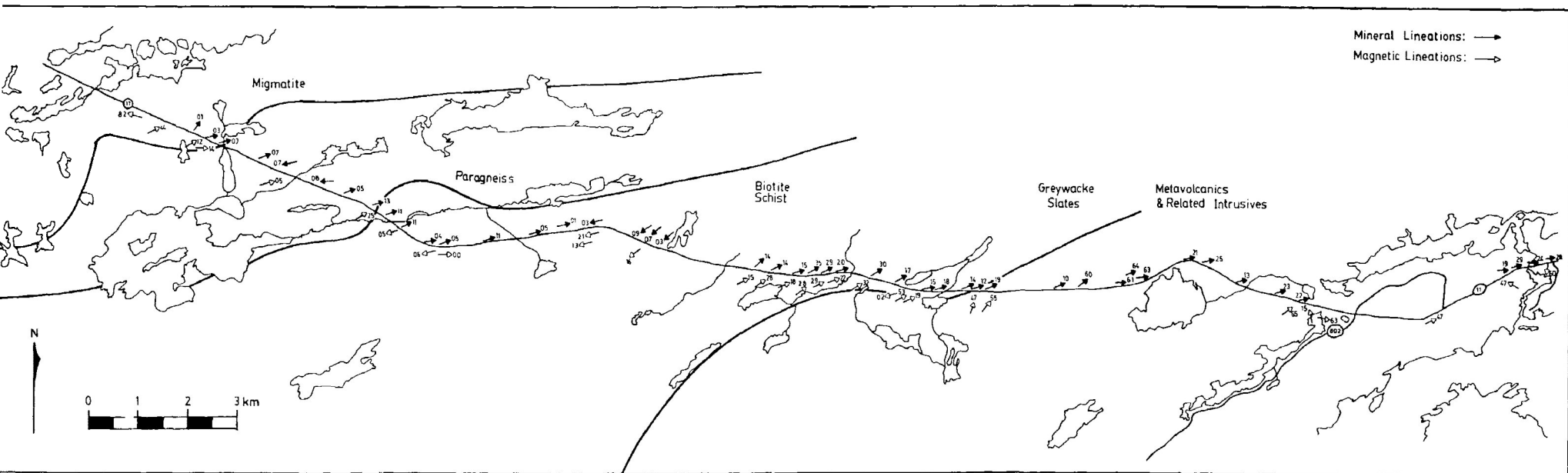


Figure 7-23: Map of the thesis area displaying the close relationship between the orientations of maximum susceptibility axes and the observed mineral lineations.

inhomogeneity. However, a definite obliquity exists in the real differences in orientation of magnetic and strain fabrics across the entire transect. The contoured stereonet in Figure 7-24 represents a large number of averaged measurements and shows an obliquity between mineral and magnetic lineations. This may be due partially to a contribution of an intersection lineation between cleavage and preserved bedding near the belt boundary. It may also relate to dextral transpressive kinematics.

A preserved depositional component of bedding and associated refracted cleavage within lower grade pelites may contribute to the obliquity in Figure 7-24. In this case, the overall magnetic fabric would represent a summation of oblate bedding-parallel sedimentary fabrics and cleavage-parallel magnetic fabric (Borradaile and Tarling, 1981). The maximum susceptibility direction would then be intermediate to bedding and cleavage planes. From the field data (chapter 4 and Appendix II), the average structural fabric elements consists of:

Bedding (S0): 074/83NW

Cleavage (S1): 070/77NW

Lineation (L1): 072-15

The observed mineral lineation appears to be a bedding-cleavage intersection lineation. However, the magnetic fabric data seems more related to cleavage than bedding:

 Mineral Lineations n = 47

 Magnetic Lineations n = 30

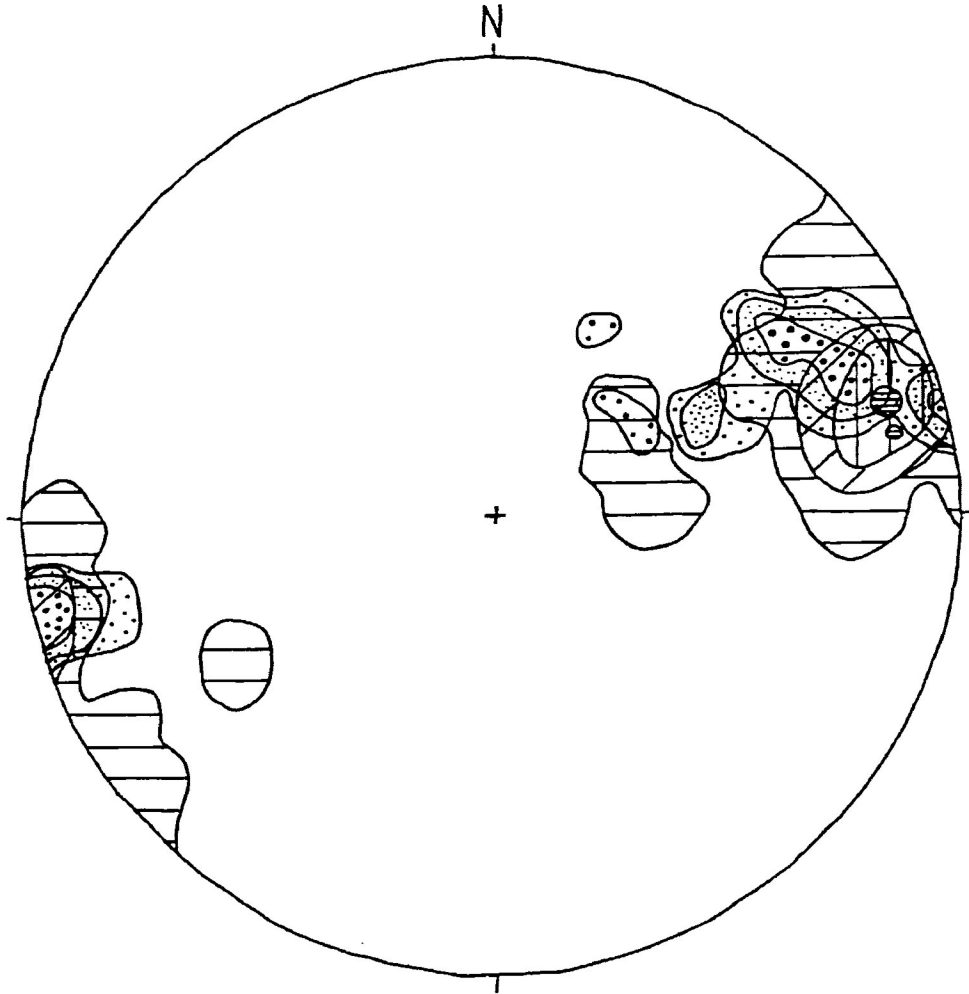


Figure 7-24: Contoured stereonet containing a large number of averaged measurements of observed mineral lineations (stripes) slightly oblique to measured magnetic kmax axis lineations (dots).

VII-50

Average kmax: 068-22

Average kmin: 160-08 (S1 avg. pole: 160-13)

(S0 avg. pole: 164-07)

The maximum susceptibility direction is not intermediate to bedding and cleavage planes. It possesses a more north-oriented obliquity apart from cleavage and lineation data clusters; whereas, bedding has an opposite obliquity to the south from average cleavage and lineation. Similarly, the average minimum susceptibility coincides well with the average cleavage pole (rather than with bedding). Bedding is preserved only in a small portion of the Quetico belt and is nearly parallel to cleavage in the field. This would suggest only a minimal bedding fabric contribution to the obliquity in Figure 7-24.

Magnetic mineralogy studies also cast some doubt on the influences of bedding fabrics on magnetic/mineral lineation obliquity. It was shown that the metamorphic paramagnetic phyllosilicate minerals dominate magnetic fabrics. These metamorphic minerals display a well-developed p.c.o. Detrital ferrimagnetic minerals would depict a more accurate strain history of the rocks. They possess a distinct p.d.o. and would naturally be influenced by their original orientation (ie. bedding fabrics). A combination of the two mineral types yields a complex superimposed susceptibility ellipsoid. Since the ferrimagnetic minerals within these rocks generally account for

<<1 wt.% of the rock, they would define a strong p.d.o. fabric. Hence, the magnetic fabric related to bedding would be overwhelmed in most localities. The relatively few ferrimagnetic grains would contribute to higher bulk susceptibilities but would have little effect on principal axis directions. Therefore, most of the rocks (especially the Quetico metasediments) have tectonic magnetic fabrics controlled by deformation mechanisms and metamorphic processes.

A tectonic magnetic fabric has important ramifications as a possible indicator of regional kinematics. An obvious obliquity, as in Figure 7-24, was not observed at the northern Quetico boundary. However, major fold axial planes at the northern boundary were observed by others to lie slightly oblique to the Quetico Fault in an anti-clockwise sense in plan view (Borradaile, et al., 1988). Their observation implies a dextral kinematic formation of the folds during transpression episodes. Major folds were not observed in this study; however, the obliquity found between magnetic and mineral lineations would similarly infer dextral kinematics.

This obliquity may arise due to progressive deformation. The mineral and magnetic lineations could represent the maximum elongation directions of different incremental strain ellipses that together define a superposed distortion and rotation of the

entire progressively sheared sequence. A structure (such as the bedding-cleavage intersection lineation) may have been initiated at a particular stage in the deformation sequence. This structure could then be superposed by new structures (ie. the progressive recrystallization of porphyroblastic micaceous minerals) arising during later stages of deformation and metamorphism. It appears that the mineral lineation observed in the field may have been dextrally rotated more extensively than the micaceous matrix. That matrix would have formed during later metamorphic increments, which were detected by MSA analyses.

CHAPTER 8 - STRAIN ANALYSIS

The analysis of strain was undertaken through the digitization of detrital quartz grains outlines taken from non-recrystallized pelites. Samples included the lowest metamorphic grade greywacke at station RS8.1, in contact with the metavolcanics, through to RS10.1 (beyond which recrystallization of quartz grains occurs). Apart from the determination of strain magnitudes and directions, the prime objective of this analysis is to attempt to correlate the anisotropy of magnetic susceptibility with strain from the same samples. Since conventional strain markers (ie. ellipsoidal markers such as large pebbles, oolites, accretionary lapilli and lava pillows) are absent, rare or poorly preserved; the grain shape analysis of (presumably) initially spheroidal quartz granules was employed.

Horizontal and vertical sections were cut, thin-sectioned and photographed in accordance with the MSA core horizontal and vertical planes from each sample. Strained quartz grains were traced from overlapping thin-section photograph enlargements. Grain outlines were recorded using a Zeiss Digitizer with a stylus and a digitizing tablet with an active area of 280 x 260 mm. Ferromagnetic wires within the tablet are arranged at regular intervals in X and Y directions. The wires emit electronically induced magnetic pulses of constant frequency at a spatial interval of 68 μm (the resolution of the tablet). When

the stylus traces an outline on the tablet, coordinate locations are determined by the computer from X and Y intercepts. The Zeiss computer performs various arithmetic functions (see Figure 8-1 for details). Among these are the calculations of major and minor axes of the elliptical markers and their orientations, used for Rf/ϕ strain analysis.

8.1 Rf/ϕ Data

The Rf/ϕ technique utilizes the axial ratio and the orientation of the long axis of elliptical markers to determine the strain of initially spheroidal or elliptical markers (Ramsay, 1967; Dunnet, 1969; Ramsay and Huber, 1983). This technique involves several pre- and post-deformational factors: R_i , R_s , θ , and ϕ (see Figure 8-2 for definitions), when determining two-dimensional strain in rocks using initially elliptical markers. Several basic assumptions underlie the Rf/ϕ technique. The three major assumptions include: (i) the particles were initially spherical or elliptical, (ii) no significant viscosity contrast exists between the elliptical markers and their surrounding matrix, (iii) homogeneity of strain with respect to the matrix (ie. particles undergo passive strain).

Additional assumptions and premises (q.v. Borradaile, 1987) are made concerning the parameters listed in Figure 8-2. The maximum principal strain direction "X" is inferred from the

VIII-3

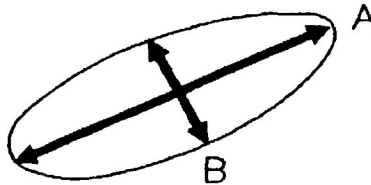
AREA



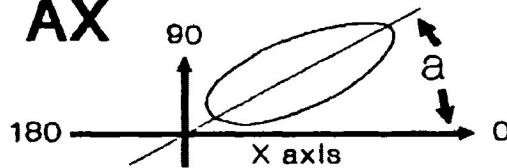
PERIM



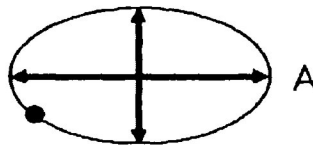
DELL. AB



ANGLE AX



FORM ELL



FORM AR

B
A
AREA

$$\pi/4 \times \text{MAJOR DIA.} \times \text{MINOR DIA.}$$

Figure 8-1: Special Arithmetic Functions on Zeiss Digitizer:

AREA: area contained within continuous trace of perimeter.

PERIMETER: continuous stylus measurement of outline.

DELL. AB: calculated major and minor axes for elliptical objects. Approximated for irregular shapes.

ANGLE AX: approximation of the angle of orientation (0-180 degrees) of the major cord length A from the X axis.

FORM ELL: aspect ratio based on B/A. Later inverted to produce the Rf value.

FORM AR: factor describing the irregularity surfaces for circular and elliptical-type structures (circle or ellipse = 1; irregular shapes <1).

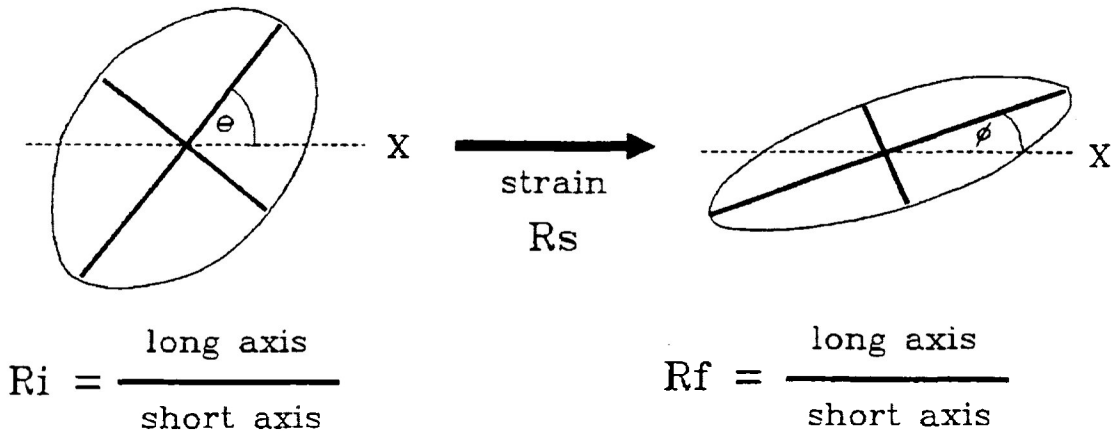


Figure 8-2: Parameters used in the R_f/ϕ Technique:
 where:

- R_i = initial undeformed particle axial ratio
- R_s = finite strain axial ratio
- R_f = final deformed particle axial ratio
- θ = angle between the R_i major axis and the maximum principle strain direction (X)
- ϕ = angle between the R_f major axis and the maximum principle strain direction (X)

maximum elongation direction of the schistose fabric (p.c.o. and p.d.o.). However, in reality, the schistosity plane has never been universally proven to have the same orientation as the principal strain direction or XY plane (Williams, 1976). The differences in maximum fabric elongation and maximum strain direction should be small in those cases. The principal strain direction cannot, however, be inferred solely from the p.d.o. of clasts since a component of an initial preferred orientation may exist. The sections measured in this study are then inferred to represent the XZ plane (horizontal sections perpendicular to p.c.o. schistosity and parallel to lineation) and the YZ plane (vertical sections perpendicular to both schistose and linear fabrics).

The θ parameter of Figure 8-2 is also subject to certain assumptions. The R_f/ϕ method assumes absolutely random initial clast orientations. The deposition of clasts usually involves some layering, represented by bedding planes, and some rotation during diagenesis and compaction processes. These preferred orientations of the clasts would largely derive from rigid body rotation and thus would not contribute any additional strain increments to that experienced during subsequent tectonic strain. Undeformed sedimentary rocks commonly display a slight preferred orientation of clast long axes when viewed in bedding-normal sections. Bedding traces were not distinguished within these sections, probably due to the close proximity of the cleavage

direction to that of bedding. Discrepancies caused by initial preferred orientations in bedding fabrics and by initial non-spheroidal clast shapes can be greatly reduced. The use of large sample sizes, of about 200 measurements, can statistically lessen primary discrepancies as well as help to reveal possible multimodal parent distributions in R_f/ϕ curves.

The R_f/ϕ passive strain theory is based on two equations relating the parameters in Figure 8-2 to the transformation of elliptical markers during passive finite strain (Ramsay, 1967; Dunnet, 1969). The first equation ([5-22] of Ramsay, 1967) describes "tan 2ϕ " as a function of R_i , R_s and θ :

$$\tan 2\phi = \frac{2\sqrt{R_s} (R_i - 1) \sin 2\theta}{(R_i + 1)(R_s - 1) + (R_i - 1)(R_s + 1)\cos 2\theta}$$

The second equation ([5-27] of Ramsay, 1967) expresses R_f as a function of R_i , R_s and ϕ :

$$R_f = \frac{\tan^2\phi(1 + R_i \tan^2\theta) - R_s(\tan^2\theta + R_i)}{R_s \tan^2\phi(\tan^2\theta + R_i) - (1 + R_i \tan^2\theta)}$$

There are too many unknown values to solve the R_f/ϕ equations Ramsay (1967) [Note: The above equations use R as max/min extension; Ramsay (1967) originally used R as $(\max/\min)^2$]. Graphical methods help alleviate this problem. The plotting of R_f against ϕ for individual clasts helps to solve the equation unknowns and, in most cases, to separate tectonic strain components from initial clast shapes and orientations (Ramsay, 1967; Dunnet, 1969; Lisle, 1977b; Ramsay and Huber, 1983).

The presence of a sedimentary fabric and its dominance relative to cleavage may be indicated in R_f/ϕ plots. The scatter along the ϕ axis represents the "fluctuation" or the range of orientation of long axes. The initial fluctuation, before deformation, is assumed to span 180° . The fluctuation after deformation remains at 180° if the tectonic finite strain ellipse has a lower ellipticity than the initial elliptical markers. The influence of the shape of the tectonic strain ellipsoid on mean clast shape increases R_f axial ratio values. Also the fluctuation decreases as grains approach more preferred orientations. Hence, scatter along the R_f axis yields information concerning the magnitudes of tectonic strain.

Scatter within the distribution of R_f/ϕ data depends upon the amount of variability of original grain shape ratios (Dunnet, 1969; Lisle, 1977b; Ramsay and Huber, 1983). Natural data often possess widespread distributions due to variable original shapes. Non-random ellipsoid orientations (ie. bedding or imbrication fabrics due to current activity) contribute to the spreading of data. Graphical analyses of R_f/ϕ involve the fitting of curves to envelope the data distribution. A series of theoretical curves representing various R_s values can be created in a symmetrical manner about the direction of the long axis of the strain ellipse. A set of standard "onion curves" were developed for the R_f/ϕ method (Dunnet, 1969). Lisle (1977b) derived "theta curves" as a more objective procedure for fitting theoretical

curves to find R_s , since initial orientations of the markers are considered. The theta curves represent the loci of all elliptical markers with the same initial θ orientation. Elliot (1970) introduced the "Shape Factor Grid" as another graphical method for strain analysis.

Regardless of the degree of fluctuation, the data will always congregate about the maximum R_f value. For the reasons described above, natural data rarely display perfect symmetry about the maximum R_f value. The ϕ orientation of the maximum frequency peak corresponds to the orientation of the strain ellipse (X) long axis. Plots of R_f/ϕ data from this study are located in Appendix V. The maximum and minimum values of best-fit envelopes can be used in the following relationships to determine R_s and maximum R_i :

case 1: Max. R_i > R_s :

$$R_s = \sqrt{(R_{fmax}/R_{fmin})}$$

$$R_{imax} = \sqrt{(R_{fmax} * R_{fmin})}$$

In this case the data can display a full 180° range of ϕ fluctuation. All data below the best-fit curve represent $R_i < R_{imax}$ data (Ramsay and Huber, 1983).

case 2: Max. R_i < R_s :

$$R_s = \sqrt{(R_{fmax} * R_{fmin})}$$

$$R_{imax} = \sqrt{(R_{fmax}/R_{fmin})}$$

In this case the R_f/ϕ data distribution field is more constricted with ϕ fluctuation $< 90^\circ$, forming an onion curve (Ramsay and

Huber, 1983).

The results of the grain shape analyses are presented for all horizontal and vertical sections in the form of R_f/ϕ plots (see Appendix V). Results from R_f/ϕ plotting are summarized in Figure 8-3. R_f values as well as the angular deviation and skewness of ϕ are also listed. The grains display great fluctuation almost spanning 180° . With increasing strain, inwards from the belt boundary, the R_f peak grows in prominence and fluctuation narrows considerably. Generally, for each sample, the horizontal sections have larger R_f maxima than their vertical counterparts. This probably reflects an $L>S$ fabric component. Large sample sizes (≈ 200) were used to reduce primary fabric discrepancies. The peaks are relatively symmetrical and no secondary peaks were detected. Bedding fabrics then do not seem to influence ϕ orientations, and may be masked by cleavage traces of similar orientation.

8.2 Statistical Determination of Strain (R_s)

This data was subjected to various statistical analytical techniques to determine the finite strain (R_s) experienced by these greywackes. Curve-fitting was not used in this study. For this data, it would be quite difficult to obtain an ideal contour envelope from the deformed markers. The process of the fitting of curves is not very precise and possesses considerable sources

VIII-10

RF-STAT	Rf	Rf	Rf	Rf	Phi	Ang.	Phi	
Sample	Min	Max	Mean	Std Dev	Mean	Dev.	Skew.	n
CV8.1	1.056	3.118	1.639	0.393	-1.10	14.83	-0.93	175
SH9	1.021	3.654	1.759	0.477	-2.74	17.66	-0.30	234
SV9	1.012	4.382	1.696	0.497	-16.69	16.83	-1.13	181
CH9.1	1.025	3.853	1.932	0.652	-0.45	13.47	-0.88	225
CV9.1	1.013	3.536	1.595	0.413	-11.16	20.42	-0.63	195
CH9.2	1.047	4.956	1.835	0.615	-6.27	15.85	-0.98	233
CV9.2	1.042	4.549	1.767	0.506	-5.64	14.22	-0.87	199
RS9.2-1H	1.021	3.960	2.128	0.616	-7.29	9.76	-1.42	218
RS9.2-1V	1.067	6.022	1.904	0.638	-2.52	12.60	-0.64	219
RS9.2-2H	1.020	4.638	1.828	0.613	-6.67	14.56	0.47	213
RS9.2-2V	1.063	4.827	1.882	0.526	-12.33	13.49	-0.27	250
RS9.25H	1.079	4.441	2.135	0.701	5.35	9.00	-1.25	213
RS9.25V	1.011	5.272	2.025	0.670	1.33	10.43	0.36	242
CH9.3	1.037	4.605	2.075	0.676	-0.53	9.38	0.02	191
CV9.3	1.049	3.851	1.897	0.501	-7.52	12.69	0.62	212
CH9.4	1.114	5.796	2.351	0.789	-2.79	10.77	-0.24	207
CV9.4	1.047	5.350	1.937	0.644	0.93	13.07	-1.01	228
RS9.4-3H	1.143	5.701	2.226	0.779	-6.47	10.78	-0.19	204
RS9.4-3V	1.086	4.360	2.061	0.683	-0.33	13.16	-1.25	161
RS10.05H	1.098	4.741	2.129	0.680	4.42	10.30	0.31	227
RS10.05V	1.024	4.064	1.874	0.577	-6.26	12.22	1.01	208
CH10.1	1.030	4.269	1.996	0.684	6.25	11.39	-0.40	160
CV10.1	1.020	3.585	1.679	0.449	17.79	16.09	0.74	186

Figure 8-3: Statistics for Rf/ ϕ analysis: Rf values, and ϕ mean, angular deviation, and skewness, and number of measurements (n). Horizontal sections contain "H" in the sample name, while vertical sections contain a "V".

of error.

8.2.1 Arithmetic, Geometric and Harmonic Mean

The calculation of mean is often used to approximate the tectonic strain ratio (R_s). Arithmetic (R_m), geometric (G) and harmonic (H) means can be computed from final strain axial ratios (R_f). Lisle (1977a) developed computer-modeled curves demonstrating how the various means depart from the actual " R_s " tectonic strain ratio (fig. 8-4). He surmised that all the means are over-estimations of R_s (where $R_m > G > H > R_s$).

The arithmetic mean is defined as the sum of all the R_f strain axial ratios, divided by the number of all deformed elliptical markers:

$$R_m = \frac{R_{f1} + R_{f2} + R_{f3} + \dots + R_{fn}}{n}$$

This method crudely approximates R_s and is generally considered as invalid (Dunnet, 1969). Of all the analytical methods, the arithmetic mean departs the farthest from true R_s . Arithmetic mean is of little value for strain estimation due to its problems with initial shape variability.

Geometric mean can estimate R_s values with slightly more accuracy. It is calculated by taking the n th root of the product of " n " number of R_f values from measured clasts:

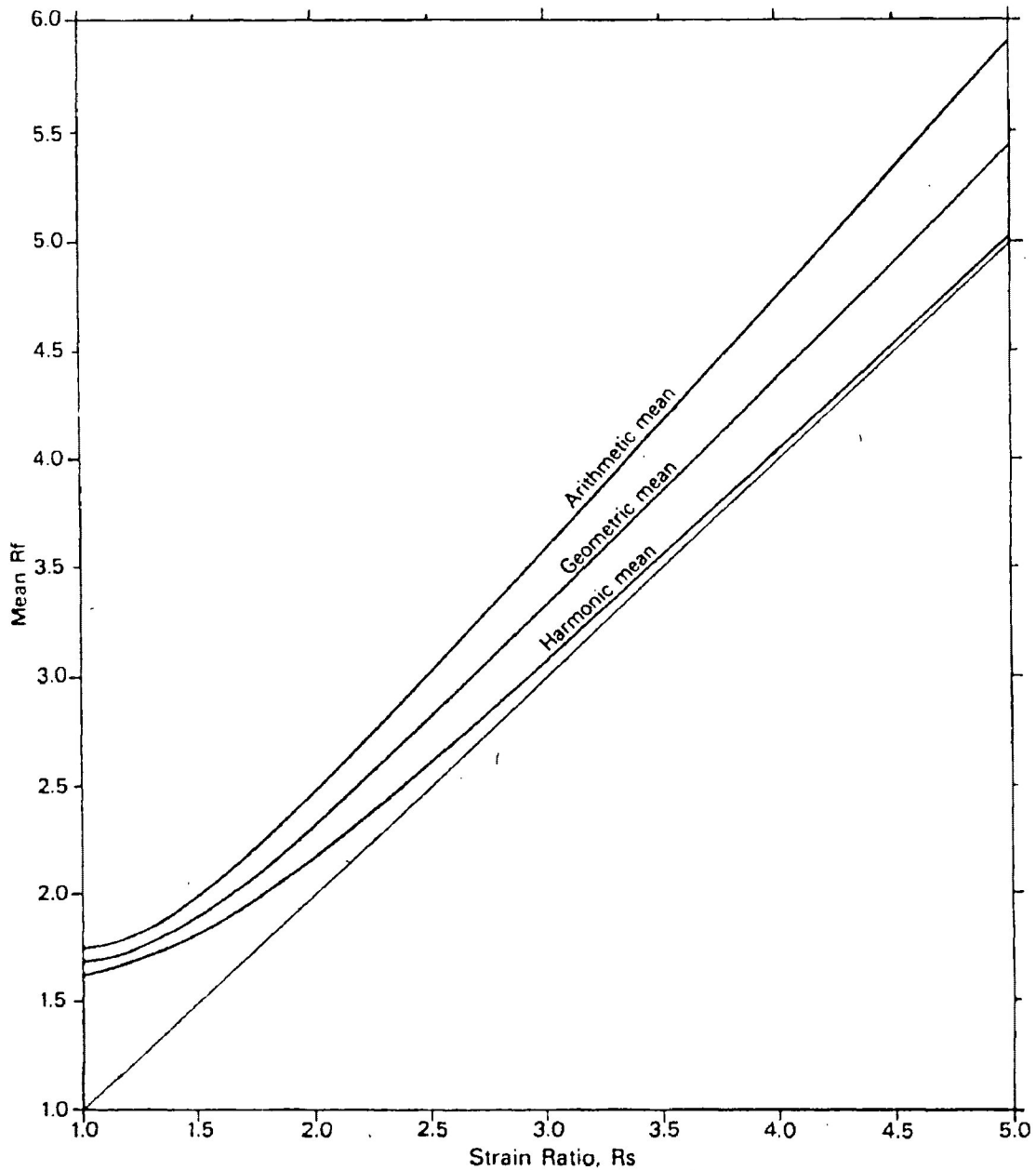


Figure 8-4: Computer-generated curves representing the relationship between the mean axial ratio of randomly oriented elliptical markers (R_f) and tectonic strain ratio (R_s). How the various means depart from actual " R_s " is demonstrated. (from Lisle, 1977a)

$$G = \sqrt[n]{(Rf1 \times Rf2 \times Rf3 \times \dots \times Rfn)}$$

As seen in Figure 8-5, the geometric mean values for tectonic strain have only negligible differences from harmonic mean values. However, the geometric mean has greater variability from R_s than does harmonic mean (Lisle, 1977a).

Harmonic mean indicates R_s more accurately than any other mean calculation. It was introduced by Lisle (1977a) as a rapid method of strain estimation; especially useful when lacking information concerning the original shapes and orientations of clasts. It is calculated by:

$$H = \frac{n}{1/Rf1 + 1/Rf2 + 1/Rf3 + \dots + 1/Rfn}$$

The R_s estimates, using harmonic mean, for each measured section are presented in Figure 8-5. Although harmonic mean usage is simple and rapid, a margin of error still exists. Generally, the error margin decreases with increasing strain. If $R_s < 2$, strain estimation errors exceed 10% of the true tectonic strain (Lisle, 1977a). This method provides more accurate results in cases of smaller R_i axial ratios and relatively large amounts of tectonic strain.

8.2.2 Robin's Analysis

Another mathematical treatment to approximate R_s from digitized planar Rf/ϕ data was developed by Robin (1977). This

VIII-14

RF-DEFM Sample	Geometric Mean	Harmonic Mean	Robin's Analysis	Linearization Strain Method	Initial "Unique Ratio"
CV8.1	1.59648	1.55754	1.351424	1.38209	1.561293
		(One-sigma limits: +1.402769 and -.2911942)			
		(Strain ratio range: 1.091 to 2.785)			
SH9	1.70225	1.650852	1.34255	1.452195	1.7331
SV9	1.63575	1.584735	1.247186	1.553445	1.84095
CH9.1	1.83335	1.743517	1.583331	1.87957	1.807053
CV9.1	1.55019	1.510782	1.16563	1.298201	1.661024
CH9.2		1.680582	1.414839	1.605587	1.811409
CV9.2	1.70657	1.653883	1.415727	1.686277	1.749728
RS9.2-1H	2.0437	1.965123	1.752466	1.912726	1.831746
RS9.2-1V	1.8417	1.746995	1.579214	1.953085	1.796688
RS9.2-2H	1.74254	1.669574	1.463112	1.697603	1.77123
RS9.2-2V		1.755146	1.459398	1.640259	1.810952
RS9.25H	2.03088	1.936682	1.779117	2.536357	2.149331
RS9.25V	1.92776	1.839306	1.721383	2.011919	1.767654
CH9.3	1.97903	1.893598	1.759764	2.089303	1.798876
CV9.3	1.83839	1.783711	1.535748	1.588557	1.715158
CH9.4	2.20298	2.072291	1.847317	2.457615	2.300084
CV9.4	1.85166	1.779433	1.506692	1.903746	1.983256
RS9.4-3H	2.10967	2.009344	1.769757	2.836335	2.494075
RS9.4-3V	1.96041	1.870191	1.624677	1.751671	1.883347
RS10.05H	2.03118	1.941423	1.747257	2.06757	1.907409
RS10.05V	1.79782	1.731537	1.540782	1.835483	1.77349
CH10.1	1.91913	1.801414	1.650925	1.904679	1.806174
CV10.1	1.62822	1.583614	1.254411	1.412653	1.716576

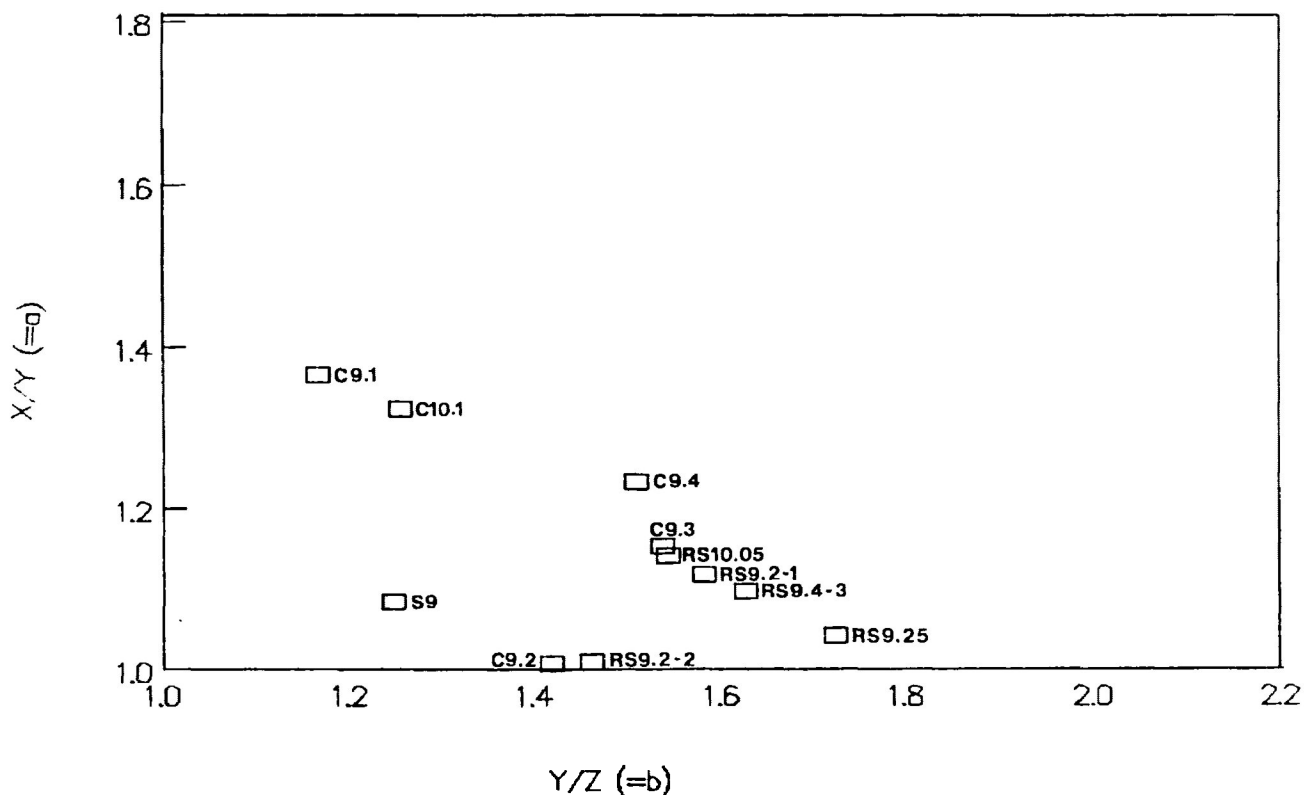
Figure 8-5: Tectonic strain ratio (Rs) estimates, for each measured section using Geometric Mean, Harmonic Mean Robin's Analysis, and Linearization Methods are presented. The initial strain ratio (Ri) estimates from the Linearization Method is given.

method still assumes a random initial orientation of passive markers. However, original shapes need not be restricted to ellipsoids, but can be arbitrarily arranged. Other premises remain during these analyses: no significant volume change (ie. pressure solution processes) and minimal competency contrast between clasts and matrix. Robin's analysis requires that, two lines parallel to the two axes of the strain ellipse evident in that section, be traced through the centre of each clast. The lines are involved in a logarithmic average process to determine the axial strain ratio (Robin, 1977).

The R_f/ϕ data from this study underwent R_s estimates using Robin's method (see results for each section; Fig. 8-5). Robin analyses were obtained for horizontal sections (XZ planes) and vertical sections (YZ planes). Values were also computed for the XY plane. These and previously obtained YZ vertical plane values were represented in three dimensions on a Flinn Plot (Figure 8-6). Using these X, Y, and Z computations for each sample, Jelinek plot parameters could then be calculated and plotted (Figure 8-7). This method is simpler and more objective than the successive approximations of curve-fitting graphical methods. Harmonic means may closely approximate and over-estimate R_s , but Robin's method has the advantage of not requiring elliptical shapes.

VIII-16

Flinn Diagram - Robin's Analyses



```

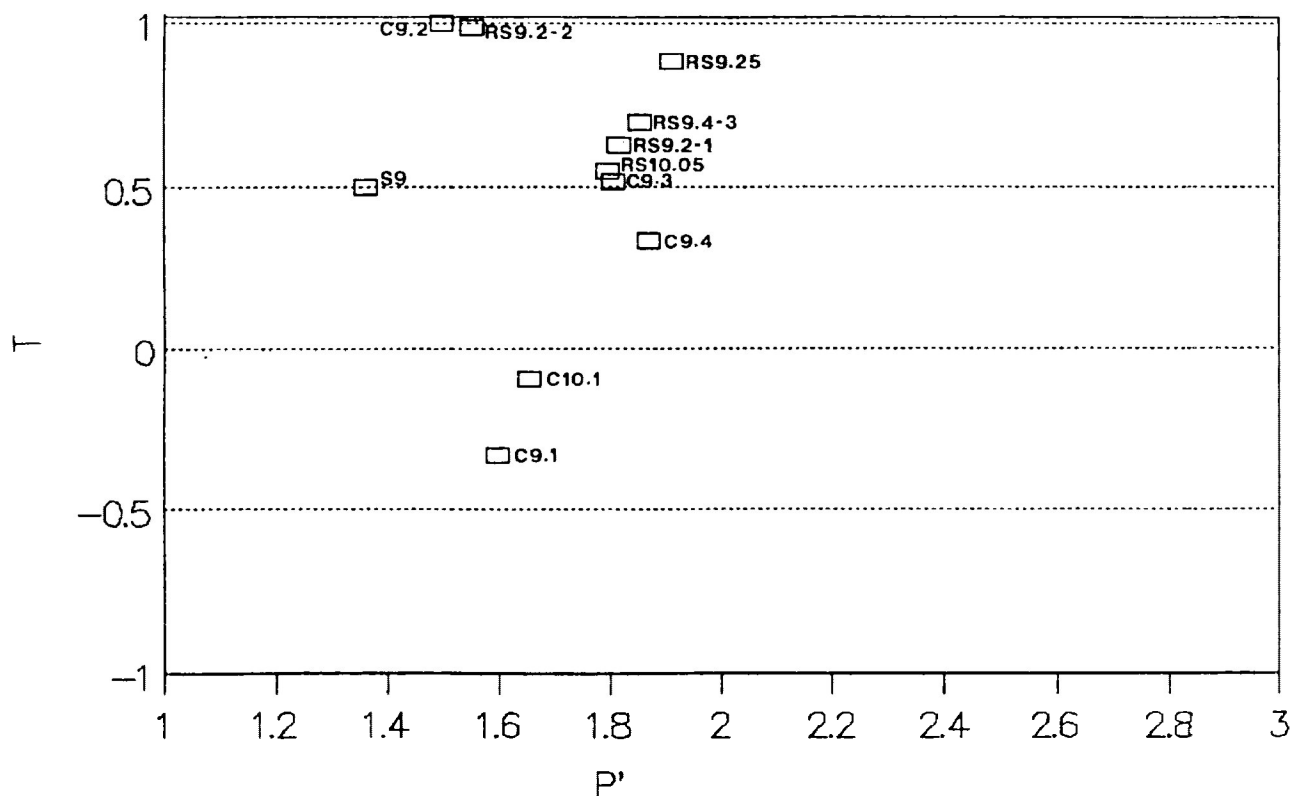
=====
DATA FROM STRAIN ANALYSIS OF DIGITIZED QUARTZ GRAINS
=====
(1) FLINN PLOT FROM ROBIN ANALYSES

```

Sample	X/Z * Z/Y = X/Y	Average Y/Z
	X/Z X/Y	Y/Z
SH9/SV9	1.34255 1.076463	1.247186
CH9.1/CV9.1	1.583331 1.358348	1.16563
CH9.2/CV9.2	1.414839 1	0.999373
RS9.2-1H/V	1.752466 1.109708	1.415727
RS9.2-2H/V	1.463112 1.002545	1.579214
RS9.25H/V	1.779117 1.033539	1.459398
CH9.3/CV9.3	1.759764 1.145868	1.721383
CH9.4/CV9.4	1.847317 1.226075	1.535748
RS9.4-3H/V	1.769757 1.089298	1.506692
RS10.05H/V	1.747257 1.134007	1.624677
CH10.1/CV10.1	1.650925 1.316096	1.540782
		1.254411

Figure 8-6: Flinn Diagram representation of X, Y, and Z computations from Robin's strain analyses of deformed detrital quartz grains.

JELINEK PLOT - Robin Strain Analyses



=====

JELINEK'S PARAMETERS FOR STRAIN RESULTS OBTAINED
FROM DIGITIZED QUARTZ GRAINS

=====

{1} JELINEK PLOT FOR ROBIN ANALYSES

Sample	K1	K2	K3	A	B	P'	T
SH9/SV9	1.131	1.050	0.842	1.076	1.247	1.359	0.500
CH9.1/CV9.1	1.291	0.950	0.815	1.358	1.166	1.597	-0.333
CH9.2/CV9.2	1.123	1.123	0.793	1.000	1.416	1.494	1.000
RS9.2-1H/V	1.248	1.125	0.712	1.110	1.579	1.816	0.629
RS9.2-2H/V	1.136	1.133	0.777	1.003	1.459	1.550	0.987
RS9.25H/V	1.225	1.185	0.689	1.034	1.721	1.910	0.885
CH9.3/CV9.3	1.263	1.103	0.718	1.146	1.536	1.804	0.518
CH9.4/CV9.4	1.313	1.071	0.711	1.226	1.507	1.868	0.336
RS9.4-3H/V	1.245	1.143	0.703	1.089	1.625	1.851	0.700
RS10.05H/V	1.256	1.108	0.719	1.134	1.541	1.796	0.549
CH10.1/CV10.1	1.295	0.984	0.785	1.316	1.254	1.652	-0.096

Figure 8-7: Jelinek plot representation of X (K1), Y (K2), and Z (K3) computations from Robin's strain analyses of deformed detrital quartz grains.

8.2.3 Linearization Method

For random initial θ values, the linearization method may give the best estimates of strain. It reorders the data in linearized space and gives a range of R_s values by the fitting of regression lines through a scatter of data points (Yu and Zheng, 1984). The linearization of the data arises from expression of the original Ramsay (1967) expressions for $\tan 2\phi$ and R_f , in terms of hyperbolic trigonometric functions:

$$\cos 2\phi = \frac{\cosh 2\epsilon_f \times \cosh 2\epsilon_s - \cosh \epsilon_i}{\sinh 2\epsilon_f \times \sinh 2\epsilon_s}$$

where:

$$\begin{aligned} \epsilon_f &= \ln(R_f) \\ \epsilon_s &= \ln(R_s) \\ \epsilon_i &= \ln(R_i) \\ &(\text{Dunnet, 1969}) \end{aligned}$$

This equation can be rewritten (Yu and Zheng, 1984) as:

$$\cosh 2\epsilon_f \times \cosh 2\epsilon_s = \sinh 2\epsilon_f \times \sinh 2\epsilon_s \times \cos 2\phi + \cosh 2\epsilon_i$$

and then divided by the hyperbolic cosine of $2\epsilon_s$:

$$\underbrace{\cosh 2\epsilon_f}_{y} = \underbrace{\tanh 2\epsilon_s}_{m} \times \underbrace{\sinh 2\epsilon_f \times \cos 2\phi}_{x} + \underbrace{\frac{\cosh 2\epsilon_i}{\cosh 2\epsilon_s}}_{b}$$

The above relationship was erroneously used in a strain analysis by Rajlich (1989), who used the term "cosh 2ϕ " in place of "cos 2ϕ ". Yu and Zheng noted the linear property (ie. $y=mx+b$) of the above relationship. It produces a fitted regression line yielding approximations for both R_s and R_i values. Least squares

regression will give a range of maximum and minimum slopes (slope is always <1). Tectonic strain is easily estimated from this slope after halving it and taking the inverse function "arctanh". A theoretical initial shape axial ratio (R_i) can be derived from the y-intercept ($\cosh 2\epsilon_i / \cosh 2\epsilon_s$) of the line.

The R_s and R_i approximations from the linearization strain method for vertical and horizontal sections are listed in Figure 8-5. The linearization plots are contained within Appendix V. The natural variability of R_i creates a clustering of data points about the mean slope. The data from this study was too variable (the only exception being sample CV8.1) to establish one-sigma limits for a strain ratio range (see CV8.1 in Fig. 8-5 and Appendix V). Both R_s and R_i strain estimates of horizontal (XZ) and vertical (YZ) planar sections from the linearization were tabulated (Figure 8-8) and plotted on a Flinn Diagram (Figure 8-9). Similarly, Jelinek parameters were computed from theoretical X, Y, and Z values (Figure 8-10) and displayed on a Jelinek plot (Figure 8-11).

8.2.4 Comparison of R_s Estimation Techniques

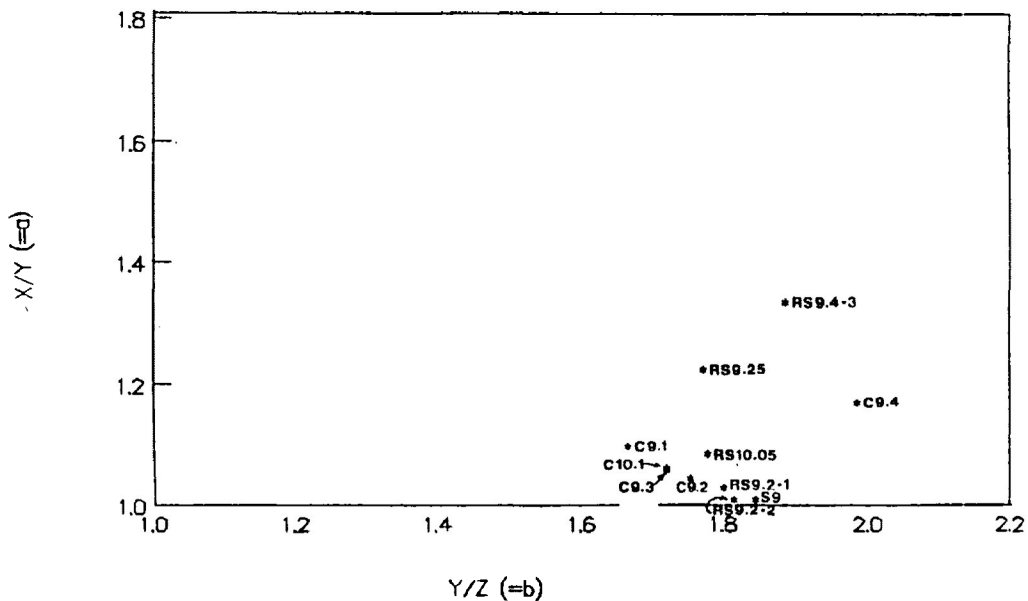
The four methods used to approximate R_s in this study (geometric mean, harmonic mean, Robin's method and linearization method) are plotted against each other in Figure 8-12 for both horizontal and vertical sections. As expected, the harmonic mean

=====						
FLINN PLOT FROM LINEARIZATION STRAIN METHOD RESULTS						
a	X/Z * Z/Y = X/Y				Average	
	Sample	X/Z	X/Y	Y/Z	Y/Z	
	SH9/SV9	1.452195	1	0.934822	S9	1.553445
	CH9.1/CV9.1	1.87957	1.447827		C9.1	1.298201
	CH9.2/CV9.2	1.605587	1	0.952149	C9.2	1.686277
	RS9.2-1H/V	1.912726	1	0.979336	RS9.2-1	1.953085
	RS9.2-2H/V	1.697603	1.03496		RS9.2-2	1.640259
	RS9.25H/V	2.536357	1.260666		RS9.25	2.011919
	CH9.3/CV9.3	2.089303	1.315221		C9.3	1.588557
	CH9.4/CV9.4	2.457615	1.290936		C9.4	1.903746
	RS9.4-3H/V	2.836335	1.619217		RS9.4-3	1.751671
	RS10.05H/V	2.06757	1.126445		RS10.05	1.835483
	CH10.1/CV10.1	1.904679	1.348299		C10.1	1.412653

b	FLINN PLOT FOR "R _i " VALUES				R _i VER.	
	R _i HOR.	X/Z	X/Y	X/Z * Z/Y = X/Y	Y/Z	Y/Z
	SH9/SV9	1.7331	1	0.941416		1.84095
	CH9.1/CV9.1	1.807053	1.087915			1.661024
	CH9.2/CV9.2	1.811409	1.035252			1.749728
	RS9.2-1H/V	1.831746	1.019513			1.796688
	RS9.2-2H/V	1.77123	1	0.978066		1.810952
	RS9.25H/V	2.149331	1.215923			1.767654
	CH9.3/CV9.3	1.798876	1.048811			1.715158
	CH9.4/CV9.4	2.300084	1.159751			1.983256
	RS9.4-3H/V	2.494075	1.324278			1.883347
	RS10.05H/V	1.907409	1.075512			1.77349
	CH10.1/CV10.1	1.806174	1.052196			1.716576

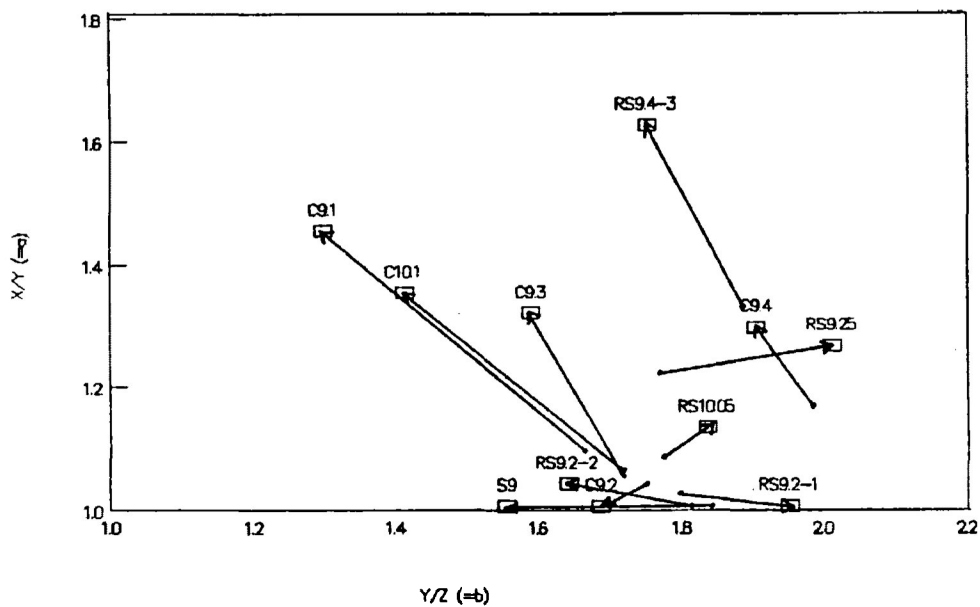
Figure 8-8: Calculated X, Y, and Z relationships for Flinn diagram representations (plotted in Fig. 8-9) for:
(a) - R_s estimates derived from Linearization Method
(b) - R_i estimates derived from Linearization Method.

Flinn Diagram - Linearization (Ri)



a

Flinn Diagram - Linearization Method



b

Figure 8-9: Flinn Diagram representation of X, Y, and Z computations from:
 (a) - R_i estimates derived from Linearization Method
 (b) - R_s estimates derived from Linearization Method.

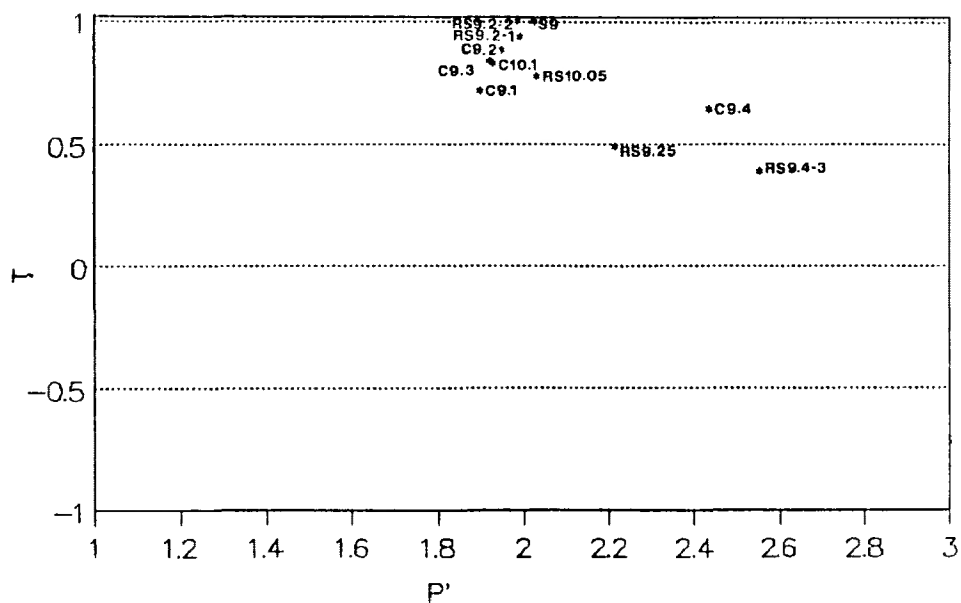
=====								
JELINEK PLOT FOR LINEARIZATION STRAIN METHOD								
a	Sample	K1	K2	K3	A	B	P'	T

	SH9/SV9	1.158	1.158	0.746	1.000	1.553	1.663	1.000
	CH9.1/CV9.1	1.396	0.964	0.743	1.448	1.298	1.885	-0.173
	CH9.2/CV9.2	1.190	1.190	0.706	1.000	1.686	1.828	1.000
	RS9.2-1H/V	1.250	1.250	0.640	1.000	1.953	2.166	1.000
	RS9.2-2H/V	1.207	1.166	0.711	1.035	1.640	1.808	0.870
	RS9.25H/V	1.473	1.169	0.581	1.261	2.012	2.635	0.502
	CH9.3/CV9.3	1.401	1.065	0.670	1.315	1.589	2.106	0.256
	CH9.4/CV9.4	1.469	1.138	0.598	1.291	1.904	2.526	0.432
	RS9.4-3H/V	1.662	1.027	0.586	1.619	1.752	2.839	0.075
	RS10.05H/V	1.325	1.177	0.641	1.126	1.835	2.179	0.672
	CH10.1/CV10.1	1.369	1.016	0.719	1.348	1.413	1.906	0.072
=====								
JELINEK PLOT FOR "R1" VALUES								
b	Sample	K1	K2	K3	A	B	P'	T

	SH9/SV9	1.226	1.226	0.666	1.000	1.841	2.023	1.000
	CH9.1/CV9.1	1.253	1.151	0.693	1.088	1.661	1.897	0.715
	CH9.2/CV9.2	1.233	1.191	0.681	1.035	1.750	1.948	0.883
	RS9.2-1H/V	1.231	1.208	0.672	1.020	1.797	1.990	0.936
	RS9.2-2H/V	1.219	1.219	0.673	1.000	1.811	1.985	1.000
	RS9.25H/V	1.377	1.133	0.641	1.216	1.768	2.214	0.489
	CH9.3/CV9.3	1.236	1.178	0.687	1.049	1.715	1.920	0.838
	CH9.4/CV9.4	1.387	1.196	0.603	1.160	1.983	2.432	0.644
	RS9.4-3H/V	1.489	1.125	0.597	1.324	1.883	2.550	0.385
	RS10.05H/V	1.271	1.181	0.666	1.076	1.773	2.029	0.775
	CH10.1/CV10.1	1.239	1.177	0.686	1.052	1.717	1.926	0.828

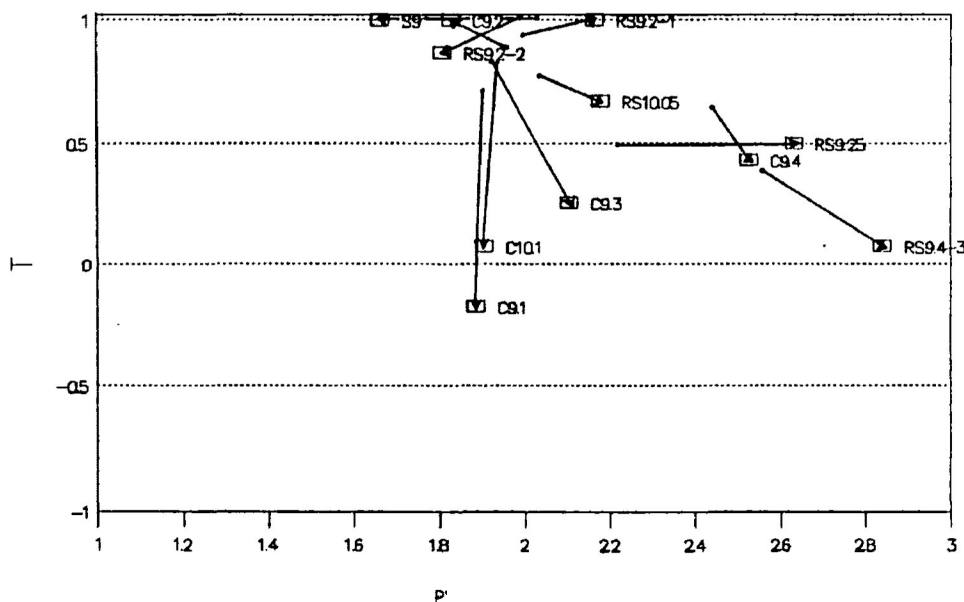
Figure 8-10: Calculated X (K1), Y (K2), and Z (K3) relationships for Jelinek plot representations (plotted in Fig. 8-11) for:
(a) - Rs estimates derived from Linearization Method
(b) - R1 estimates derived from Linearization Method.

JELINEK PLOT - Initial "Ri" Values



a

JELINEK PLOT - Linearization Method



b

Figure 8-11: Jelinek plot representation of X (K1), Y (K2), and Z (K3) computations from:
 (a) R_i estimates derived from Linearization Method
 (b) R_s estimates derived from Linearization Method.

parallels and is lower than the geometric mean. The harmonic mean is known to offer relatively accurate strain estimates in cases where the strain ratio >3.0 and where initial clast orientations were random (Lisle, 1977a). Bedding fabrics are prevalent within these rocks; however, they were not identifiable within these sections. Hence, the failure to identify bedding traces makes strain estimates slightly more difficult. The concealed preferred bedding orientations in addition to low strain values (<3.0) creates problems for the harmonic mean as a method of strain estimation.

Robin's method of strain analysis consistently provides the lowest strain estimates of all the methods used (Fig. 8-12). It is probably the preferable method for these low grade rocks since initial elliptical shapes are not required. The linearization method estimates vary within a range of strain values bounded by upper geometric mean results and lower Robin results. Within more highly strained horizontal sections, linearization results peak above the other estimates. This may indicate an ability of the linearization method to accommodate more heterogeneous fabrics. These samples contain obvious L>S p.d.o. and p.c.o. fabrics. Deviances in R_f axial ratios may influence the fitted lines of regression within linearization techniques more than any influences on the logarithmic averages of Robin's method. These heterogeneities (both in R_f and R_i) probably result in the inability of this technique, in many

STRAIN ANALYSIS COMPARISON

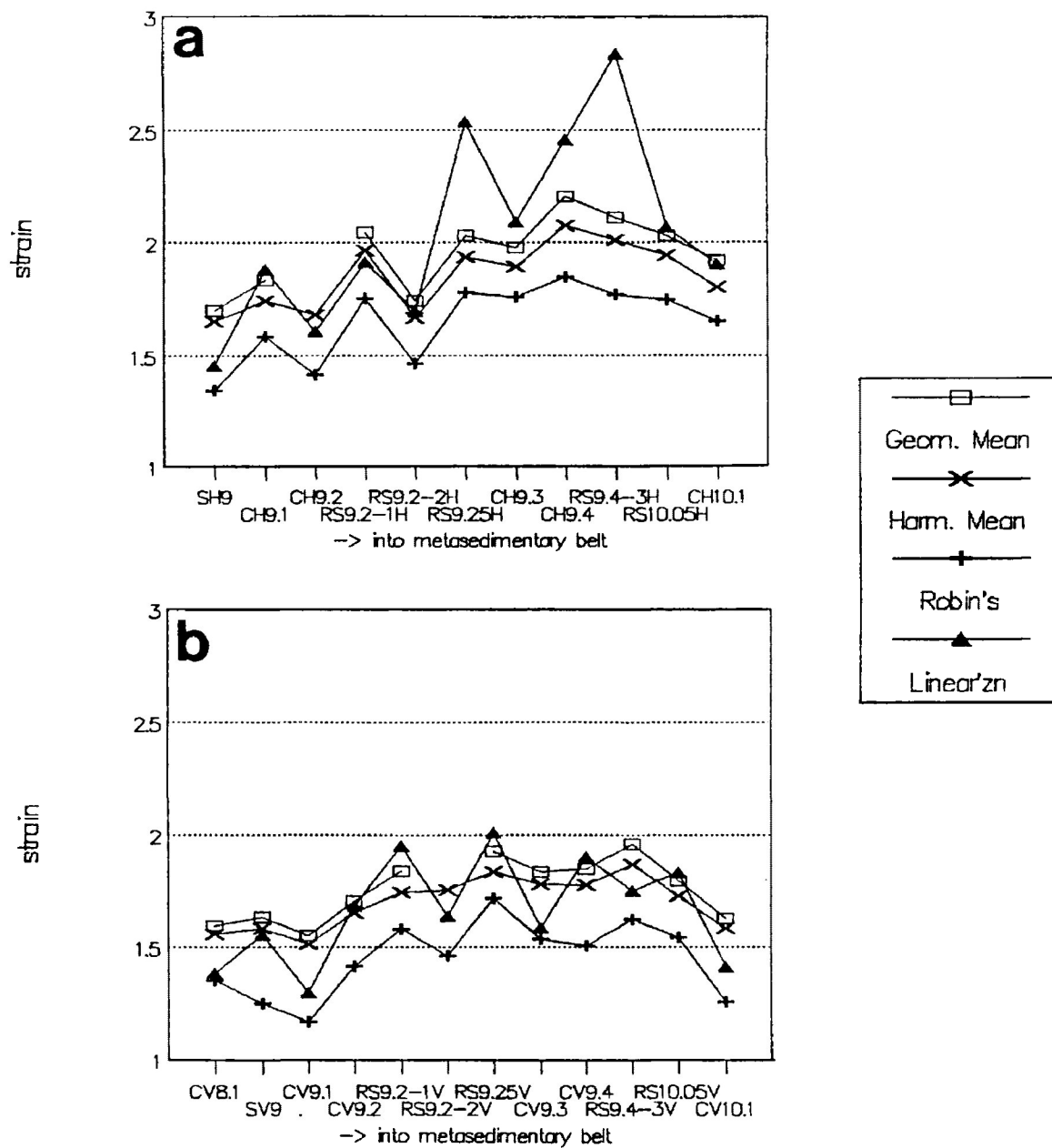


Figure 8-12: Comparative graph of range in tectonic strain ratio estimates by the above listed techniques for:

- (a) - Horizontal sample digitized quartz sections
- (b) - Vertical sample digitized quartz sections

cases, to produce valid one-sigma limits for a given strain ratio.

Overall, the strain values of low-grade metasediments at the lithological boundary with the Shebandowan metavolcanics are fairly low. Strain appears to increase inwards towards the higher grade metasediments. Strain values seem to decline again just before the onset of any visible quartz grain recrystallization. This decline may be due to metamorphic processes, associated with slightly higher metamorphic grade, such as pressure solution material transfer or recrystallization of detrital quartz clasts into more stable subgrains. Another factor worth mentioning involves the relatively high R_i values that were revealed through the linearization method. Although this value is entirely theoretical, it is of some relevance to a few of these sections. In sections of slightly higher grades, there were some difficulties distinguishing a few altered detrital feldspar granules from detrital quartz clasts. Since feldspar granules are inherently oblong and possess lath-like crystalline structure, they will contribute to higher R_i values compared to basically spheroidal quartz clasts.

8.3 Strain/MSA Correlation

Correlations were attempted for MSA and strain anisotropy parameters (Jelinek's P' and T). Anisotropy parameters for

magnetic susceptibility were derived from the principal susceptibilities ($k_1 > k_2 > k_3$). Jelinek parameters were also determined for strain anisotropy from principal strain ratios ($X > Y > Z$). From chapter 7, it was found that the principal directions of the magnitude of magnetic susceptibility ellipsoids were comparable with principal extension directions exhibited in linear and schistose macroscopic fabrics. Correlations were performed using identical oriented samples for both MSA and tectonic strain (the strain was determined by Robin's and linearization methods).

Simple linear regression plots in Figure 8-13 ($P'(k)$ vs. $P'(\epsilon)$) and Figure 8-14 ($T(k)$ vs. $T(\epsilon)$) illustrate strain/MSA relationships. In each correlation, the magnetic susceptibility parameters are specified as the "dependent" variable relative to the "independent" variable of strain. The equation of each regression line is calculated and displayed. Pearson's correlation coefficient describes the relationships of the parameters. This coefficient describes the strength of linearity using numbers between -1 and 1. A ± 1 coefficient indicates a strong linear (positive/negative) relationship; whereas a zero coefficient implies a non-existent or very weak relationship between the two variables. Correlations between T (sense of anisotropy: Jelinek parameter) for MSA and strain are quite poor (Pearson's $\rho = 0.1064$ for linearization and $\rho = 0.1464$ for Robin's method). A weak correlation does exist for the degree of

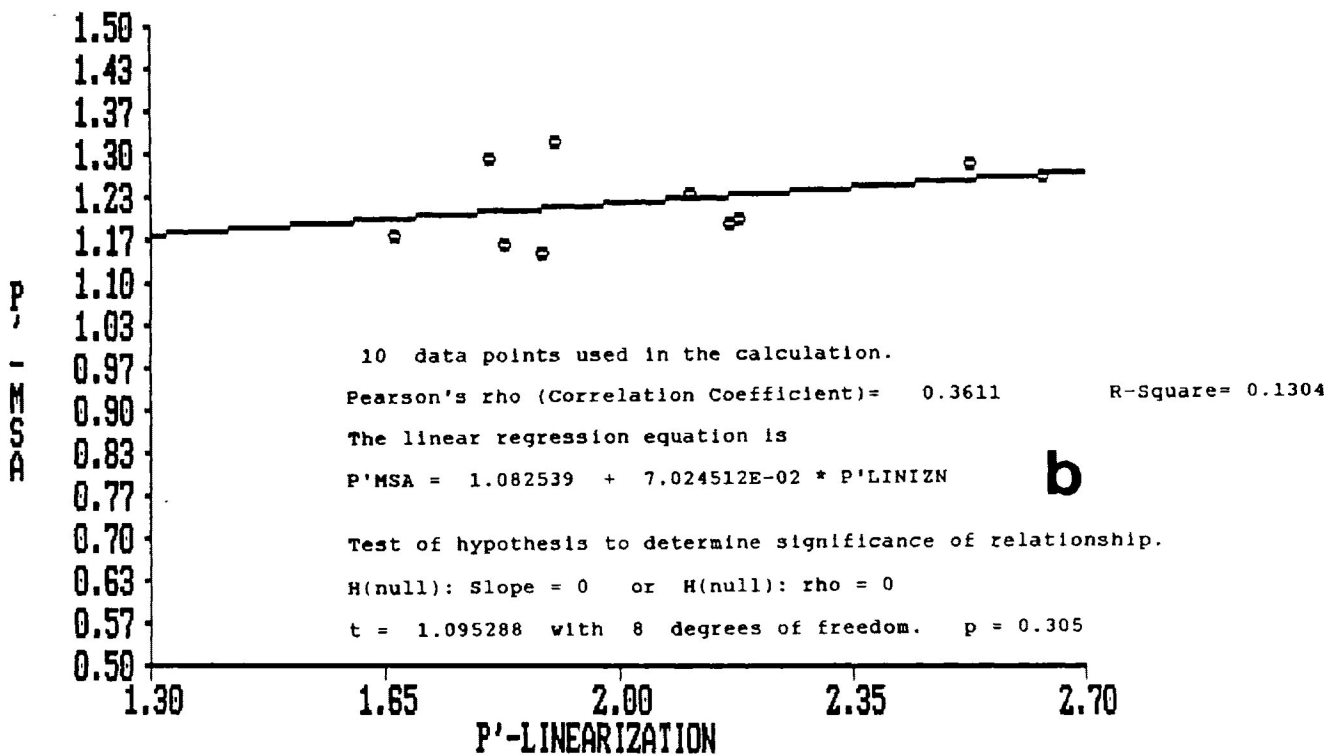
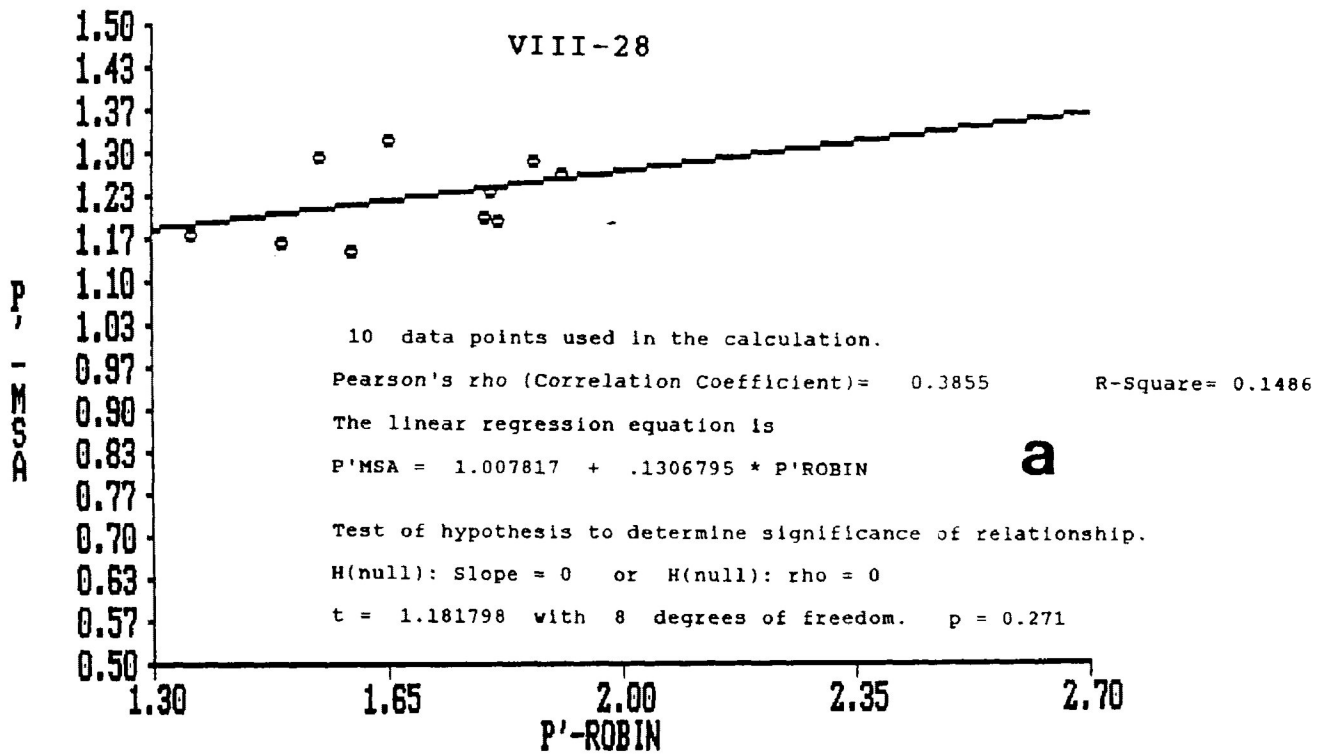


Figure 8-13: Simple linear regression plots comparing the "P'" Jelinek parameter (degree of anisotropy) between magnetic susceptibility anisotropy (vertical axis) and strain anisotropy calculated by:
 (a) - Robin's Method
 (b) - Linearization Method

10 data points used in the calculation.

Pearson's rho (Correlation Coefficient)= 0.1464 R-Square= 0.0214

The linear regression equation is

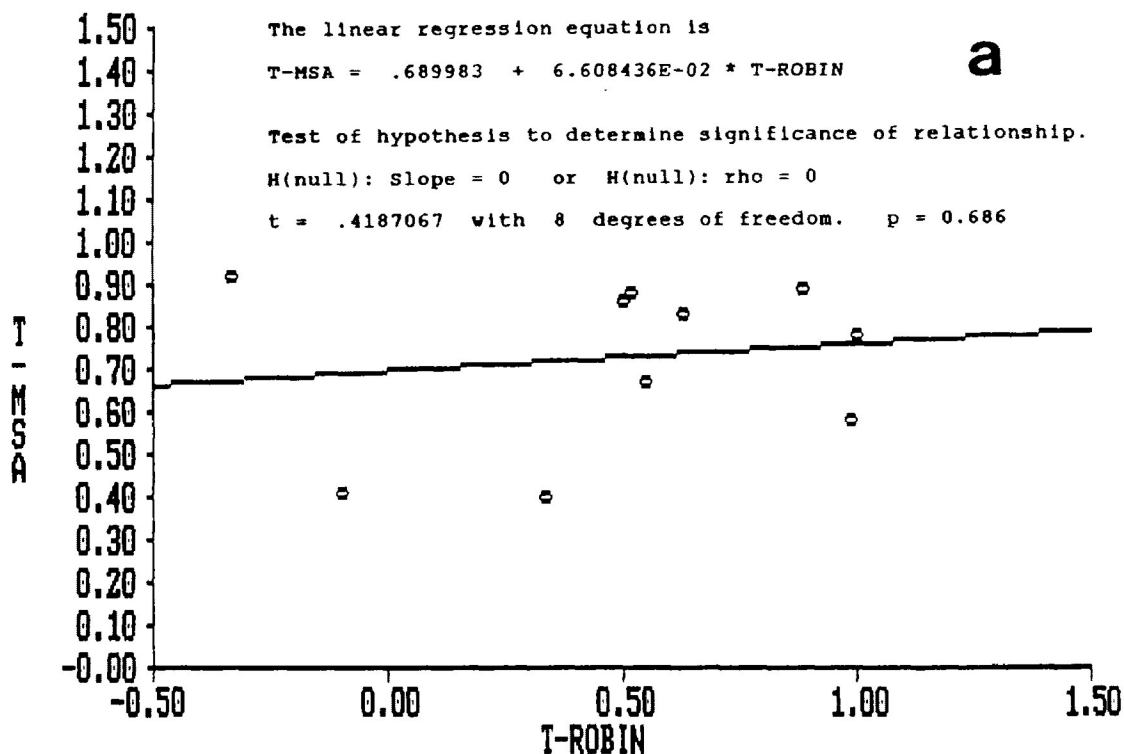
$$T\text{-MSA} = .689983 + 6.608436E-02 * T\text{-ROBIN}$$

a

Test of hypothesis to determine significance of relationship.

H(null): Slope = 0 or H(null): rho = 0

t = .4187067 with 8 degrees of freedom. p = 0.686



10 data points used in the calculation.

Pearson's rho (Correlation Coefficient)= 0.1064 R-Square= 0.0113

The linear regression equation is

$$T\text{-MSA} = .6945387 + 5.029544E-02 * T\text{-LINIZN}$$

b

Test of hypothesis to determine significance of relationship.

H(null): Slope = 0 or H(null): rho = 0

t = .302623 with 8 degrees of freedom. p = 0.770

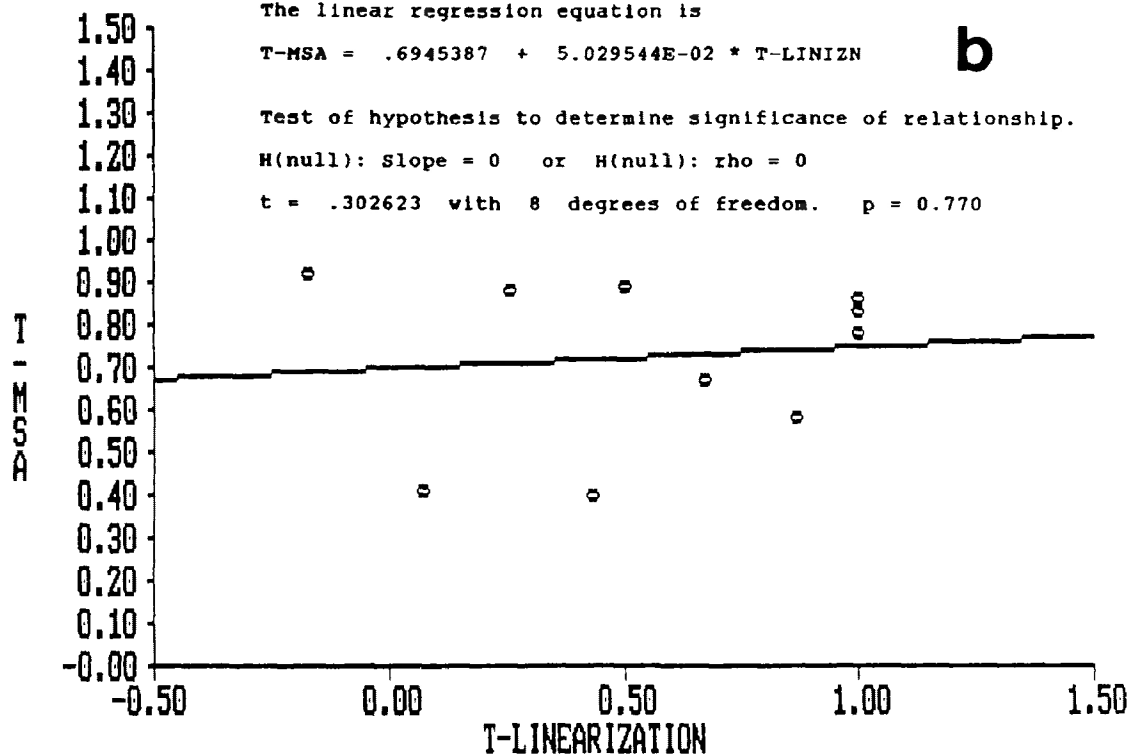


Figure 8-14: Simple linear regression plots comparing the "T" Jelinek parameter (sense of anisotropy) between magnetic susceptibility anisotropy (vertical axis) and strain anisotropy calculated by:

- (a) - Robin's Method
- (b) - Linearization Method

anisotropy (Jelinek's P' parameter) for MSA and strain (Pearson's $\rho = 0.3611$ for linearization and $\rho = 0.3855$ for Robin's method). It seems that the Robin results are more comparable to MSA results than the linearization strain estimates. T-tests for correlations that have statistically significant slope and linear relationship, result in low p-values (ie. <0.05). T-tests (Figs. 8-13 and 8-14) reaffirms that the linear regressions have insignificant slopes and linearity.

From the results described above, no clear quantitative relationship between strain and susceptibility ellipsoid shapes seems to exist. Correlations do exist in the qualitative sense; as is seen in chapter 7 stereonetts and in these regression plots. Other factors obviously effect the evolution of magnetic fabrics in a different manner than the development of strain fabrics. The strain response model (ie. whether active or passive rotation) influences the degree of correlation. Metamorphic processes (as seen in chapter 7 - magnetic mineralogy) largely influences the development of magnetic fabrics (fig. 8-15). Intergranular displacement surfaces may be invisible and may alter grain shapes. Localized mass removal, such as in pressure solution material transfer, can result in altered shapes of grains and consequently modified strain and MSA ellipsoid shapes. Similarly, the crystallization of newer metamorphic minerals at various increments of the rock's strain history is probably a major reason for discrepancies between grain shapes (MSA/strain

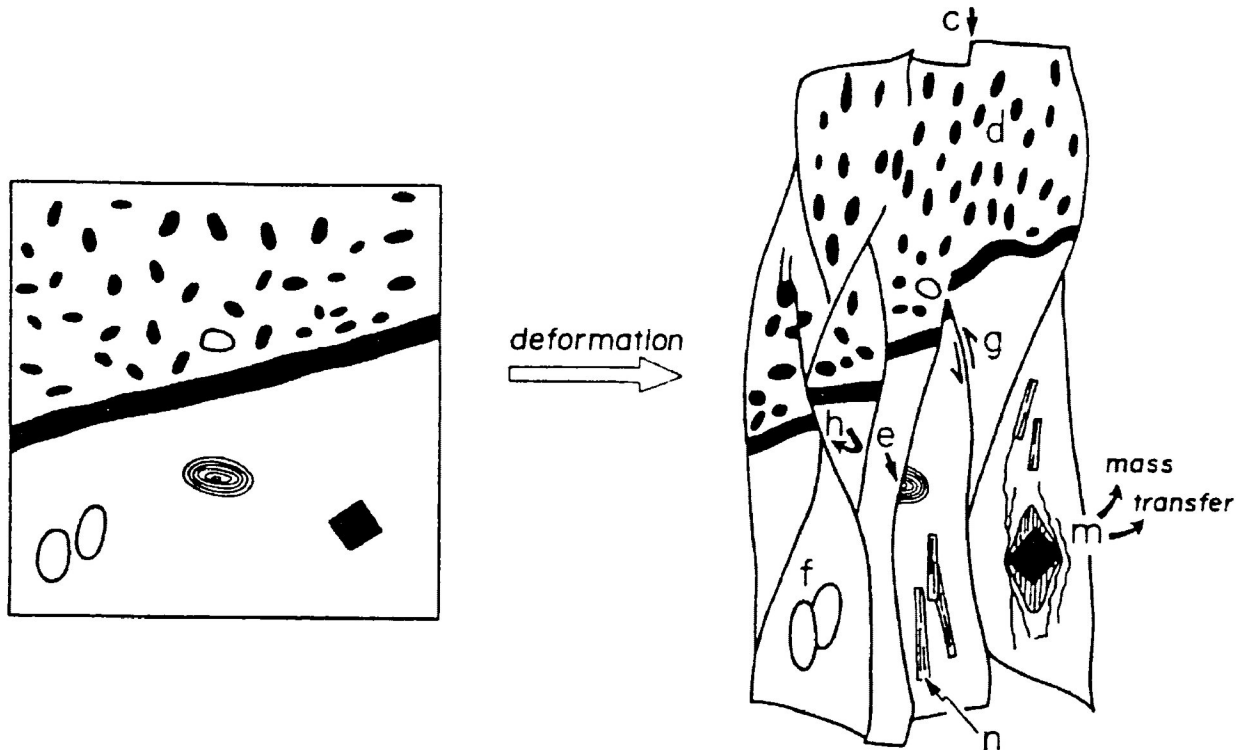


Figure 8-15: Possible metamorphic deformation processes that could influence the development of magnetic fabrics:

- (c) - intergranular displacement surfaces (may be invisible)
- (d) - ductile (may be plastic) deformation of grains
- (e) - stylolitic surfaces and grain-truncation
- (f) - penetration of grains
- (g) - microfaults (cleavage slip)
- (h) - rotations of blocks or grain groups between faults
- (m) - pressure solution material transfer
- (n) - crystallization of new minerals

(from Borradaile, 1988)

correlations) and between orientations (lineation obliquities in chapter 7). Borradaile and Tarling (1981), for example, demonstrate how pressure solution can transport carbonates and silicates while concentrating less soluble layers of magnetite and paramagnetic minerals.

As is the case for this study, many rock types possess deformation mechanisms that render strain/MSA correlations inadequate. Correlations involving simple mathematical strain estimates and those assuming single deformational episodes are not entirely applicable to many metamorphic rocks. As mentioned in section 8.1, the assumptions made for strain estimation techniques also provide extra constraints on correlations. Models assuming entirely random initial clast orientations and totally homogeneous fabrics often are insufficient to truly describe the tectonic strain of rocks that have some: (i) relict primary bedding fabrics, (ii) domainal effects of particulate flow (Borradaile and Tarling, 1984), (iii) metamorphic effects, (iv) multiple episodes of deformation and cleavage formation, (v) outcrop-scale or microscopic strain heterogeneity, or (vi) later generations of metamorphic minerals that form within contemporary strain alignments.

Even though the shapes of MSA and finite strain ellipsoids cannot be correlated quantitatively, their orientations are very similar. This helps establish the merits

of MSA techniques in the mapping of detailed and cryptic structures and as an indicator of kinematics in metamorphosed terrains such as the Superior Province of the Canadian Shield (Stott and Schwerdtner, 1981; Borradaile, et. al, 1988; this study).

CHAPTER 9 - TECTONIC IMPLICATIONS

The nature of tectonism within the Archean Superior Province has always been controversial. Early fixist models utilized diapirism as the major force of deformation. They were based on "vertical" kinematic patterns controlled by the diapirism of igneous intrusive bodies through a pre-existing sialic crust (Anhaeusser, 1973; Gorman et al., 1978). Later mobilist models using plate tectonics still retained diapiric deformation within fissured and rifted sialic cratons (Goodwin, 1977; Ayres and Thurston, 1985).

It is possible that the intrusion of diapirs within the Shebandowan and Wabigoon belts may have influenced the present deformation patterns in the form of a distant strain aureole. If this was the case, the principal extension directions would be oriented down-dip on intrusive-concordant foliations (Dixon, 1975). The resultant strain pattern would be expected to yield steeply-plunging stretching lineations, at least close to the diapir. This was demonstrated, in the laboratory, by Dixon and Summers (1983) using centrifuge models of subsiding, inter-diapir synclines. However, this area is characterized by very shallow stretching (and intersection) lineations. This is incompatible with fabrics predicted by the gravitational subsidence expected around a diapir.

It is more likely that this area experienced subhorizontal lithospheric movement. Most recently such models have been proposed to explain tectonic collages. Morphological comparisons for this style of motion were made with the lithospheric plate interactions of the Phanerozoic Cordilleran belts of western Canada (Langford and Morin, 1976). They envisaged the southern Superior subprovinces as remnants of accreted allochthonous island arc sequences with interstitial and intra-arc sedimentary basins. Blackburn (1980) generally portrayed the subprovinces as Wilson Cycle manifestations. Elsewhere in northwestern Ontario, deformation periods of early, dominantly vertical and later, dominantly horizontal motion were differentiated (Schwerdtner, et al., 1979). Both magnetic and mineral fabrics from this study area indicate only one major episode of deformation yielding subhorizontal lineations and near-vertical cleavages. This gives prominence to the "horizontal tectonics" that play a significant role in the tectonic history, especially of the subprovince boundaries. Previously, transcurrent faulting and shear zones (Schwerdtner, et al., 1979) were recognized but not emphasized to any great degree.

Deformation fabrics from the northern boundary of the Quetico belt with the Wabigoon subprovince indicate lateral stretching parallel to strike and substantial regional flattening

perpendicular to strike (Borradaile, 1982; Borradaile and Schwerdtner, 1984; Borradaile et al., 1988; Sarvas, 1987). Similarly oblate magnetic fabrics and subhorizontal magnetic and mineral lineations were observed within this study and by Stott (1985) along the southern boundary against the Shebandowan belt. Further west, along the southern boundary within Minnesota, a similar style of deformation was also found. However, it is there, a second tectonic event (Hudleston, et al., 1988). This apparently diachronous nature may reflect deformation timing differences on either side of the Quetico sedimentary trough. However, it remains unclear how the nature of the subprovince boundaries change laterally. For example, folding was observed to the east and west of this study area along the southern boundary (Kehlenbeck, 1983; Hudleston, et al., 1988). One possible method of explaining lateral differences is through transcurrent action along an undulatory shear zone or fault contact. At least it is apparent, from evidence in this study and others (Hudleston, et al., 1988; Borradaile, et al., 1988; Stott, 1985) that horizontal tectonics predominate regionally, mainly in the form of dextral strike-slip motions coupled with significant compression.

Thus it appears that some transcurrent and compressional progressive deformation may have produced the strain patterns close to the northern margin of the Quetico belt and in the

surrounding area. This style of deformation can be termed 'transpression' (Harland, 1971; Sanderson and Marchini, 1984). Dextral transpression is reported to have affected the northern and southern boundaries of the Quetico belt (Borradaile, et al., 1988; Hudleston, et al., 1988; Stott, 1985; Percival and Williams, 1989). Transpressive tectonics may be common at the Quetico and the other subprovince boundaries within the western Superior province (Mary Sanborn-Barrie, Ontario Geological Survey, personal communication, 1989). This would then suggest a tectonic style that includes repeated late Archean accretionary growth of the Superior province with oblique subduction as a possible driving force for the dextral transpression.

An accretionary arc model resulting in a fore-arc, back-arc collision has been postulated for the Quetico belt (Percival and Williams, 1989; Percival, 1989; Langford and Morin, 1976). In this hypothesis, the Quetico belt would behave as an accretionary prism between the obliquely subducting Shebandowan-Wawa arc and the Wabigoon arc or craton (Devaney and Williams, 1989; Percival and Williams, 1989). Turbiditic sediments from northern and southern areas would be deposited within the oceanic trench that would later form the Quetico belt. The trapped Quetico accretionary wedge, along with surrounding volcanic belts would then experience continued volcanism, transpressive deformation, sedimentation, and transcurrent motion and

reactivation along boundary faults. A period of thermal relaxation would occur in conjunction with static metamorphism and diapiric intrusion (Percival and Williams, 1989).

Deformation resulting from the oblique convergence at plate boundaries was termed "transpression" by Harland (1971). Transpression represents a model for the structural interpretation of zones bounded by wrench or transcurrent shears and faults; accompanied by horizontal shortening across and vertical extension along the shear plane. This style of deformation possesses several characteristic manifestations: (i) flattened oblate strain ellipsoids, (ii) steep cleavage with either vertical or horizontal stretching lineations, (iii) folds (including sheath folds) at small oblique angles to the zone, (iv) normal faults and extensional veins at high angles to the zone, and (v) vertical uplift and crustal thickening near-surface effects (Sanderson and Marchini, 1984).

A noteworthy near-surface feature of transpressive tectonics involves a vertical component of uplift or subsidence. Certain wedge-shaped uplifts, bounded by steep upward-spreading faults, combine reverse and strike-slip displacements to produce "flower structures" (Harding and Lowell, 1979). These upwards curving faults often flatten out upward (as revealed by seismic investigation elsewhere) to create "flower structures" (fig. 9-1)

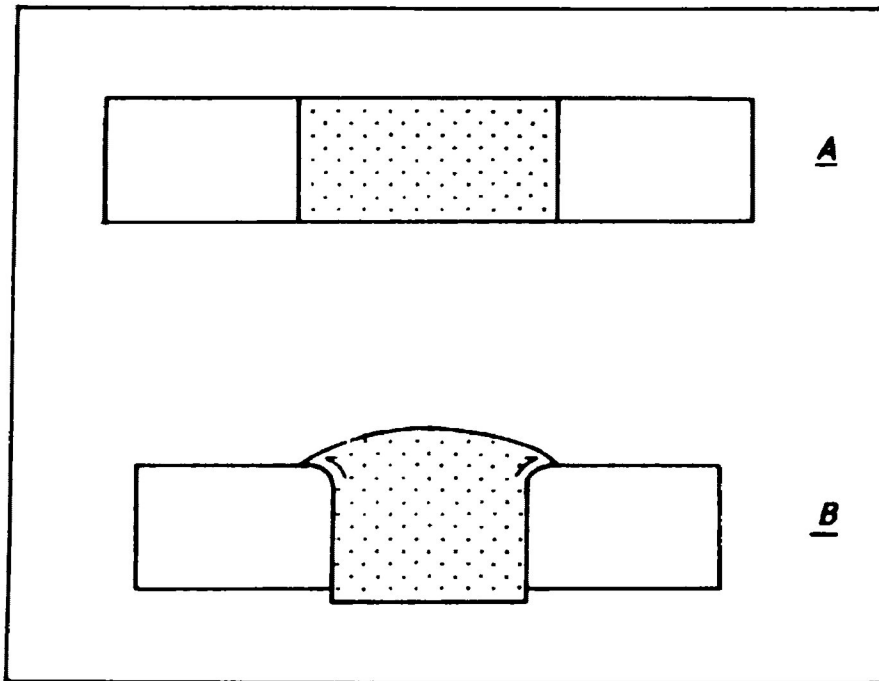


Figure 9-1: "Flower Structures" [B] that could appear as near-surface features of transpression tectonics. A vertical component of transpression results in some relative uplift or subsidence bounded by steep, upward-spreading faults.
(from Sanderson and Marchini, 1984)

when accompanying uplift or gravitational collapse of crustal blocks (Harding and Lowell, 1979). Interestingly, these structures may produce structures superficially resembling features of thrust tectonic regimes. Flower structures are entirely speculative (and may be absent in this area) but could explain tentative reports of "thrust" structures reported elsewhere within the Quetico transpressive zones. This may also reaffirm folding as the predominant deformation style at the Quetico subprovince boundaries.

Evidence from this study supports the hypothesis of north-south shortening based on some of the characteristic features listed above. Flattened oblate fabrics are recognized from magnetic fabrics, strain analyses, and general field observations. Oblate fabrics were also observed elsewhere locally at Quetico boundaries (Borradaile, et al., 1988; Sarvas, 1987; Stott, 1985). Moreover oblique, subhorizontal lineations reported here also favour a transpressive kinematic model. The mineral and magnetic lineation obliquity revealed in this study, also indicates dextral transpression deformation. Normal faults, kinks and extensional veins are found at high angles to zonal boundaries (ie. [S2] kink bands, shears, and tension gashes) and indicate compression normal to belt boundaries. Most of the brittle late-stage microstructures have also a dextral sense in plan view. These may represent the reactivation of the Quetico

Fault. Oblique subduction directed towards the northeast could explain the predominant eastward-up structural facing directions visibly dominating the metasediments in this area and on the northern Quetico boundary (Borradaile, et al., 1988). Sanderson and Marchini (1984) also suggest that slightly oblique folds are characteristic of transpression tectonics. Upright folds on the northern Quetico boundary are slightly oblique to the bounding Quetico Fault, in an anticlockwise sense when viewed in plan (Borradaile, et al., 1988). Hudleston and others (1988) observed evidence of dextral transpression through strain analyses and microstructure asymmetries at the southern Quetico boundary with the Shebandowan belt in Minnesota. North of the Quetico/Wabigoon boundary, Schwerdtner (1989) documented nine occurrences of "solid-body tilt" of deformed paleohorizontal planes. The deviation of unstrained top directions of relict primary layering from vertical orientations lends some support to transpression along the Quetico Fault zone. Overall, evidence from both boundaries of the Quetico belt indicate a dextral transpression style. This study supports those views.

CHAPTER 10 - SUMMARY

Regional strain patterns are crucial to the understanding of the nature of tectonism and the evolution of adjacent metasedimentary and greenstone belts. However, structural interpretations in these Archean rocks are hampered by patchy outcrop, the very fine-grained nature of the rocks and the paucity of strain indicators. This study utilizes the technique of magnetic susceptibility anisotropy to aid in kinematic interpretation and delineation of possible folds and enigmatic structures.

The Quetico metasedimentary subprovince and the volcanic-plutonic Shebandowan belt to the south meet along an east-west steeply dipping boundary that is believed to have been affected by dextral transpression. The exact boundary is difficult to pinpoint simply on the basis of metamorphic grade, along major faults, or between regional metavolcanic/metasedimentary interfaces. The lithologic belts in this area parallel a steep metamorphic gradient. The metavolcanics and related intrusives of the Shebandowan belt possess a single penetrative foliation of approximately east-west and subvertical orientation with some possible isoclinal folding. The Quetico metasediments consist of marginal wackes of turbiditic origin grading to schists. The steep metamorphic gradient in the area ranges from: low

greenschist facies in the Shebandowan belt, through the upper stability limit of chlorite, and through the isograds of biotite, garnet and staurolite. To the north, the metamorphic gradient peaks at medium-pressure amphibolite facies. Paragneisses form within the central Quetico belt and anatectic melt locally produces migmatites.

The measurement of magnetic susceptibility (MSA) is quite fast and simple. The instrument coil can detect anisotropies due to shape or lattice orientations of magnetically susceptible minerals within each standard-sized rock cylinder. The MSA technique sums the magnetic inductances in the presence of a low magnetic field of all the mineral constituents to create an average bulk fabric description.

The interpretation of magnetic fabrics depends upon a knowledge of the major sources of susceptibility in rocks. Previously, it had been assumed that iron-oxides, namely magnetite, are mainly responsible for MSA. However, in most metamorphic rocks, iron-oxides are present only in traces, as accessory minerals, or may even be absent. Mineral separation, leaching experiments, and scanning electron microprobe X-ray maps indicate that all the samples have multiple sources of magnetic susceptibility, dominated by iron-bearing metamorphic phyllosilicates. Additional proof of this dominance is found

within Flinn and Jelinek plots of the axes of the magnetic susceptibility ellipsoids. They show strongly oblate, flattened fabrics for all samples. The data plots closely to the positions of monomineralic test samples of biotite and chlorite. The data seems to be independent of magnetite, hornblende, and pyrrhotite monomineralic test samples.

This study has shown that the magnetic fabrics correlate with visible field fabric data. The maximum susceptibility direction is parallel to the maximum extension contained within the [S1] cleavage defined by mineral lineations. A similar correlation exists between the minimum susceptibility axes and the poles to the [S1] cleavage planes. These consistent correlations suggest a tectonic magnetic fabric.

A definite obliquity exists in the real differences in orientation of magnetic and strain fabrics across the entire transect. The slight anti-clockwise (in plan view) obliquity between mineral and magnetic lineations would imply a dextral kinematic formation during possible transpression episodes. This obliquity may arise due to progressive deformation. The mineral and magnetic lineations could represent the maximum elongation directions of different incremental strain ellipses that together define a superposed distortion and rotation of the entire progressively sheared sequence. A structure (such as a bedding-

cleavage intersection lineation) may have been initiated at a particular stage in the deformation sequence. This structure could then be superposed by newer structures arising during later stages of deformation and metamorphism. It appears that the mineral lineation observed in the field may have been dextrally rotated more extensively than the micaceous matrix. That matrix would have formed during later metamorphic increments, which were detected by MSA analyses.

Quantitative correlations between strain and MSA were very weak. Consequently it is not possible to simply relate the magnetic fabrics to strain magnitudes although the magnetic fabrics accurately monitor significant kinematic directions. Analyses of strain of low-grade detrital quartz grains, magnetic fabrics and general field observations recognize flattened oblate fabrics. Moreover oblique, subhorizontal lineations favour a transpressive kinematic model with compression normal to the belt boundary. Overall, the data from this study supports a dextral transpression hypothesis.

REFERENCES

- ANHAEUSSER, C.R. 1973. The evolution of the early Precambrian crust of Southern Africa. Philosophical Transactions of the Royal Society of London, A, 273: 359-388.
- ASHWORTH, J.R. 1985. Migmatites. Blackie & Son Ltd. Glasgow, 302 p.
- AYRES, L.D., and THURSTON, P.C. 1985. Archean supracrustal sequences in the Canadian shield: An overview ; in Ayres, L.D., et al., eds., Evolution of Archean supracrustal sequences: Geological Association of Canada Special Paper 28, p. 343-380.
- BHATAL, R.S. 1971. Magnetic anisotropy in rocks. Earth Science Review, 7: 227-253.
- BLACKBURN, C.E. 1980. Towards a mobilist tectonic model for part of the Archean of northwestern Ontario. Geoscience Canada, 7: 64-72.
- BORRADAILE, G.J. 1976. "Structural Facing" (Shackleton's Rule) and the Paleozoic rocks of the Malaguide Complex near Vélez Rubio, SE Spain. Proceedings Koninklijke Nederlandse Akademie van Wetenschappen, Amsterdam, Series B, 79: 330-336.
- BORRADAILE, G.J. 1981. Particulate flow of rock and the formation of cleavage. Tectonophysics, 72: 305-321.
- BORRADAILE, G.J. 1982. Tectonically deformed pillow lava as an indicator of bedding and way-up. Journal of Structural Geology, 4: 469-479.
- BORRADAILE, G.J. 1987a. Anisotropy of magnetic susceptibility: rock composition versus strain. Tectonophysics, 138: 327-329.
- BORRADAILE, G.J. 1987b. Analysis of strained sedimentary fabrics: reviews and tests. Canadian Journal of Earth Sciences, 24: 442-455.
- BORRADAILE, G.J. 1990. Strain analysis of homogeneously strained elliptical particles. IBM computer program version #2.4; Lakehead University, Thunder Bay, Ont.
- BORRADAILE, G.J., and ALFORD, C. 1987. Relationship between magnetic susceptibility and strain in laboratory experiments. Tectonophysics, 133: 121-135.
- BORRADAILE, G., and BROWN, H. 1987. The Shebandowan Group: "Timiskaming-like" Archean rocks in northwestern Ontario. Canadian Journal of Earth Sciences, 24: 185-188.

- BORRADAILE, G.J., KEELER, W., ALFORD, C., SARVAS, P. 1987. Anisotropy of susceptibility of some metamorphic minerals. *Physics of the Earth and Planetary Interiors*, 48: 161-166.
- BORRADAILE, G.J., and MOTHERSILL, J.S. 1984. Coaxial deformed and magnetic fabrics without simply correlated magnitudes of principal values. *Physics of the Earth and Planetary Interiors*, 35: 294-300.
- BORRADAILE, G.J., MOTHERSILL, J.S., TARLING, D., and ALFORD, C. 1986. Sources of magnetic susceptibility in a slate. *Earth and Planetary Science Letters*, 76: 336-340.
- BORRADAILE, G., and SARVAS, P. 1990. Magnetic susceptibility fabrics in slates: structural, mineralogical and lithological influences. *Tectonophysics*, 172: 215-222.
- BORRADAILE, G., SARVAS, P., DUTKA, R., STEWART, R., and STUBLEY, M. 1988. Transpression in slates along the margin of an Archean gneiss belt, northern Ontario - magnetic fabrics and petrofabrics. *Canadian Journal of Earth Sciences*, 25: 1069-1077.
- BORRADAILE, G.J., and SCHWERDTNER, W.M. 1984. Horizontal shortening of upward-facing greenstone structures in the southern Superior Province, Canadian Shield. *Canadian Journal of Earth Sciences*, 21: 611-615.
- BORRADAILE, G.J., and TARLING, D. 1981. The influence of deformation mechanisms on the magnetic fabrics of weakly deformed rocks. *Tectonophysics*, 77: 151-168.
- BORRADAILE, G.J., and TARLING, D. 1984. Strain partitioning and magnetic fabrics in particulate flow. *Canadian Journal of Earth Sciences*, 21: 694-697.
- BROWN, H.G. 1985. A structural and stratigraphic study of the Keewatin-type and Shebandowan-type rocks, west of Thunder Bay, Ontario. M.Sc. thesis, Lakehead University, Thunder Bay, Ont.
- CARD, K.D., and CIESIELSKI, A. 1986. Subdivisions of the Superior Province of the Canadian Shield. *Geoscience Canada*, 13: 5-13.
- CHORLTON, L.B., and BROWN, G.H. 1984. Gold mineralization in the Shebandowan area; in Summary of field work and other activities, 1984. Ontario Geological Survey, Miscellaneous Paper 119: 201-207.
- COGNE, J.P., and PERROUD, H. 1988. Anisotropy of magnetic susceptibility as a strain gauge in Flamanville granite, NW France. *Physics of the Earth and Planetary Interiors*, 51: 264-270.

- CORFU, F., and STOTT, G.M. 1986. U-Pb ages for late magmatism and regional deformation in the Shebandowan belt, Superior Province, Canada. *Canadian Journal of Earth Sciences*, 23: 1075-1082.
- DAVIS, D.W., POULSEN, K.H., and KAMO, S.L. 1989. New insights into Archean crustal development from geochronology in the Rainy Lake area, Superior Province, Canada. *Journal of Geology*, 97: 379-398.
- DEVANEY, J.R., and WILLIAMS, H.R. 1989. Evolution of an Archean subprovince boundary: a sedimentological and structural study of part of the Wabigoon-Quetico boundary in northern Ontario. *Canadian Journal of Earth Sciences*, 26: 1013-1026.
- DIXON, J.M. 1975. Finite strain and progressive deformation in models of diapiric structures. *Tectonophysics*, 28: 89-124.
- DIXON, J.M. and SUMMERS, J.M. 1983. Patterns of total and incremental strain in subsiding troughs: experimental centrifuged models of inter-diapir synclines. *Canadian Journal of Earth Sciences*, 20: 1843-1861.
- DUNNET, D. 1969. A technique of finite-strain analysis using elliptical particles. *Tectonophysics*, 7: 117-136.
- ELLIOT, D. 1970. Determination of finite strain and initial shape from deformed elliptical objects. *Geological Society of America Bulletin*, 81: 221-2236.
- ELLWOOD, B.B. 1979. Anisotropy of magnetic susceptibility variations in Icelandic columnar basalts. *Earth and Planetary Science Letters*, 42: 209-212.
- ELLWOOD, B.B. 1982. Estimates of flow direction for calc-alkaline welded tuffs and paleomagnetic data reliability from anisotropy of magnetic susceptibility measurements: central San Juan Mountains, southwest Colorado. *Earth and Planetary Science Letters*, 59: 303-314.
- FLINN, D. 1965. On the symmetry principle and the deformation ellipsoid. *Geological Magazine*, 102: 36-45.
- GIBLIN, P.E. 1964. Burchell Lake Area; Ontario Department of Mines, Geological Report 19, 39 p. [incl. Map #2036 - Burchell Lake Area]
- GOLDSTEIN, A.G. 1980. Magnetic susceptibility anisotropy of mylonites from the Lake Char Mylonite Zone, southeastern New England. *Tectonophysics*, 66: 197-211.

GOLDSTEIN, A.G., and BROWN, L.L. 1988. Magnetic susceptibility anisotropy of mylonites from the Brevard Zone, North Carolina, U.S.A. *Physics of the Earth and Planetary Interiors*, 51: 290-300.

GOODWIN, A.M. 1972. The Superior Province. *In*: Variations in Tectonic Styles in Canada. Geological Association of Canada Special Paper 11: 527-623.

GOODWIN, A.M. 1977. Archean basin-craton complexes and the growth of Precambrian Shields. *Canadian Journal of Earth Sciences*, 14: 2737-2759.

GORMAN, B.E., PEARCE, T.H., and BIRKETT, T.C. 1978. On the structure of Archean greenstone belts. *Precambrian Research*, 6: 23-41.

GRAHAM J.W., (1966). Significance of magnetic anisotropy in Appalachian sedimentary rocks. *In*: J.S. Steinhard and T.J. Smith (editors), *The Earth Beneath the Continents*. Geophys. Monogr. Am. Geophys. Union, 10: 627-648.

HALL, J.M., and DRURY, M.J. 1989. Greenstone belts and associated granitoids: a CCDP Workshop Report. *Geoscience Canada*, 16: 100-103.

HALVORSEN, E. 1974. The magnetic fabric of some dolerite intrusions, northeast Spitsbergen; implications for their mode of emplacement. *Earth and Planetary Science Letters*, 21: 127-133.

HAMILTON, N., and REES, A.I. 1971. The anisotropy of magnetic susceptibility of the Franciscan rocks of the Diablo Range, central California. *Geologische Rundschau*, 60: 1103-1124.

HARDING, T.P., and LOWELL, J.D. 1979. Structural styles, their plate tectonic habits, and hydrocarbon traps in petroleum provinces. *American Association of Petroleum Geologists Bulletin*, 63: 1016-1058.

HARLAND, W.B. 1971. Tectonic transpression in Caledonian Spitsbergen. *Geological Magazine*, 108: 27-42.

HARRIS, F.R. 1970. Geology of the Moss Lake area. Ontario Department of Mines and Northern Affairs. Geological Report 85, 61p. [incl. Map #2203 - Tilly Lake Sheet, scale 1:31,680]

HIRT, A.M., LOWRIE, W., CLENDENEN, W.S., and KLIGFIELD, R. 1988. The correlation of magnetic anisotropy with strain in the Chelmsford Formation of the Sudbury Basin, Ontario. *Tectonophysics*, 145: 177-189.

- HODGKINSON, J.M. 1968. Geology of the Kashabowie Area; Ontario Department of Mines, Geological Report 53, 35p. [incl. Map #2128 - Kashabowie Sheet]
- HOFFMAN, P.F. 1988. United plates of America, the birth of a craton: early Proterozoic assembly and growth of Laurentia. *Ann. Rev. Earth Planet. Sci.*, 16: 543-603.
- HROUDA, F. 1976. The origin of cleavage in the light of magnetic anisotropy investigations. *Physics of the Earth and Planetary Interiors*, 13: 132-142.
- HROUDA, F. 1982. Magnetic anisotropy of rocks and its applications in geology and geophysics. *Geophysical Surveys*, 5: 37-82.
- HROUDA, F., JACKO, S., and HANAK, J. 1988. Parallel magnetic fabrics in metamorphic, granitoid and sedimentary rocks of the Branisko and Cierna hora Mountains (E Slovakia) and their tectonometamorphic control. *Physics of the Earth and Planetary Interiors*, 51: 271-289.
- HROUDA, F., and JANAK, F. 1976. The changes in shape of the magnetic susceptibility ellipsoid during progressive metamorphism and deformation. *Tectonophysics*, 34: 135-148.
- HROUDA, F., JANAK, F., REJL, L., and WEISS, J. 1971. The use of magnetic susceptibility anisotropy for estimating the ferromagnetic mineral fabrics of metamorphic rocks. *Geologische Rundschau*, 60: 1124-1142.
- HUDLESTON, P.J., SCHULTZ-ELA, D., and SOUTHWICK, D.L. 1988. Transpression in an Archean greenstone belt, northern Minnesota. *Canadian Journal of Earth Sciences*, 25: 1060-1068.
- JOVER, O., ROCHETTE, P., LORAND, J.P., MAEDER, M., and BOUCHEZ, J.L. 1989. Magnetic mineralogy of some granites from the French Massif Central: origin of their low-field susceptibility. *Physics of the Earth and Planetary Interiors*, 55: 79-92.
- KEHLENBECK, M.M. 1983. Use of stratigraphic and structural-facing directions to delineate the geometry of refolded folds near Thunder Bay, Ontario. *Geoscience Canada*, 11: 23-32.
- KENNEDY, M.C. 1980. Metamorphism and structure across the Quetico structural subprovince, Raith, Ontario. B.Sc. thesis, Lakehead University, Thunder Bay, Ont.
- KENNEDY, M.C. 1984. The Quetico Fault in the Superior Province of the southern Canadian Shield. M.Sc. thesis, Lakehead University, Thunder Bay, Ont.

- KLIGFIELD, R., OWENS, W.H., and LOWRIE, W. 1981. Magnetic susceptibility anisotropy, strain and progressive deformation in Permian sediments from the Maritime Alps (France). *Earth and Planetary Science Letters*, 55: 181-189.
- KLIGFIELD, R., LOWRIE, W., and PFIFFNER, O.A. 1982. Magnetic properties of deformed oolitic limestone from the Swiss Alps: the correlation of magnetic anisotropy and strain. *Eclog. Geol. Helv.*, 75/1, 127-157.
- LAMARCHE, G., and ROCHETTE, P. 1987. Microstructural analysis and origin of lineations in the magnetic fabric of some Alpine slates. *Tectonophysics*, 139: 285-293.
- LANGFORD, F.F., and MORIN, J.A. 1976. The development of the Superior Province of northwestern Ontario by merging island arcs. *American Journal of Science*, 276: 1023-1034.
- LAWSON, A.C. 1913. The archean geology of Rainy Lake restudied. *Geological Survey of Canada, Memoir 40*: 115p.
- LISLE, R.J. 1977a. Estimation of the tectonic strain ratio from the mean shape of deformed elliptical markers. *Geologie en Mijnbouw*, 56: 140-144.
- LISLE, R.J. 1977b. Clastic grain shape and orientation in relation to cleavage from the Aberystwyth Grits, Wales. *Tectonophysics*, 39: 381-395.
- MCLELLAN, E. 1984. Deformational behaviour of migmatites and problems of structural analysis in migmatite terrains. *Geological Magazine*, 4: 339-345.
- MORTON, P. 1979. Volcanic stratigraphy in the Shebandowan Ni-Cu Mine area, Ontario; *in* Current Research, Part B, Geological Survey of Canada, Paper 79-1B: 39-43.
- OJAKANGAS, R.W. 1985. Review of Archean clastic sedimentation, Canadian Shield: major felsic volcanic contributions to turbidite and alluvial fan - fluvial facies associations; *in* Ayres, L.D., et al., eds., *Evolution of Archean Supracrustal sequences*: Geological Association of Canada Special Paper 28, 23-47.
- OWENS, W.H., and BAMFORD, D. 1976. Magnetic, seismic, and other anisotropic properties of rock fabrics. *Philosophical Transactions of the Royal Society of London*, A283: 55-68.
- OWENS, W.H., and RUTTER, E.H. 1978. The development of magnetic susceptibility anisotropy through crystallographic preferred orientation in a calcite rock. *Physics of the Earth and Planetary Interiors*, 16: 215-222.

- PERCIVAL, J.A. 1983. Preliminary results of geological synthesis of western Superior Province, Ontario; in Current Research, Part A, Geological Survey of Canada, Paper 83-1A: 125-131.
- PERCIVAL, J.A. 1988. Geological compilation of Quetico (52B). Geological Survey of Canada, Map 1682A, scale 1:250,000.
- PERCIVAL, J.A. 1989. A regional perspective of the Quetico metasedimentary belt, Superior Province, Canada. Canadian Journal of Earth Sciences, 26: 677-693.
- PERCIVAL, J.A., and STERN, R.A. 1984. Geological synthesis in the western Superior Province, Ontario; in Current Research, Part A, Geological Survey of Canada, Paper 84-1A: 397-408.
- PERCIVAL, J.A., STERN, R.A., and DIGEL, M.R. 1985. Regional geological synthesis of western Superior Province, Ontario; in Current Research, Part A, Geological Survey of Canada, Paper 85-1A: 385-397.
- PERCIVAL, J.A., and WILLIAMS, H.R. 1989. Late Archean Quetico accretionary complex, Superior Province, Canada. Geology, 17: 23-25.
- PETERMAN, Z.E., and DAY, W. 1989. Early Proterozoic activity on Archean faults in the Western Superior province - Evidence from pseudotachylite. Geology, 17: 1089-1092.
- PETERMAN, Z.E., and GOLDICH, S.S. 1970. Early Precambrian Geology of the Rainy Lake district. Abstract in: 16th. Annual Institute of Lake Superior Geology, held at Lakehead University; (J.L. TALBOT, et al. ed.), p.34.
- PETTIJOHN, F.J. (1975). Sedimentary Rocks. Harper & Row, New York, 628 p.
- PIRIE, J., and MACKASEY, W.O. 1978. Preliminary examination of regional metamorphism in parts of Quetico metasedimentary belt, Superior Province, Ontario; in Metamorphism in the Canadian Shield, Geological Survey of Canada Paper 78-10: 37-48.
- POULSEN, K.H., BORRADAILE, G.J., and KEHLENBECK, M.M. 1980. An inverted Archean succession at Rainy Lake, Ontario. Canadian Journal of Earth Sciences, 17: 1358-1369.
- RAJLICH, P. 1989. Strain analysis of Devonian fossils from the NE part (Rhenohercynian zone) of the Bohemian Massif. Annales Tectonicae, 3: 44-51.
- RAMSAY, J.G. 1967. Folding and fracturing of rocks. McGraw-Hill, New York, 568 pp.

- RAMSAY, J.G., and HUBER, M.I. 1983. The techniques of modern structural geology, volume 1: strain analysis. Academic Press, London, UK, 307 pp.
- RATHORE, J.S. 1979. Magnetic susceptibility anisotropy in the Cambrian Slate Belt of North Wales and correlation with strain. *Tectonophysics*, 53: 83-97.
- RATHORE, J.S. 1980. The magnetic fabrics of some slates from the Borrowdale Volcanic Group in the English Lake District and their correlations with strains. *Tectonophysics*, 67: 207-220.
- RATHORE, J.S., and BECKE, M. 1980. Magnetic fabric analyses in the Gail Valley (Carinthia, Austria) for the determination of the sense of movement along this region of the Periadriatic Line. *Tectonophysics*, 69: 349-368.
- RATHORE, J.S., COURRIOUX, G., and CHOUKROUNE, P. 1983. Study of ductile shear zones (Galicia, Spain) using texture goniometry and magnetic fabric methods. *Tectonophysics*, 98: 87-109.
- RATHORE, J.S., and HENRY, B. 1982. Comparison of strain and magnetic fabrics in Dalradian rocks from southwest Highlands of Scotland. *Journal of Structural Geology*, 4: 373-384.
- ROBIN, P.-Y.F. 1977. Determination of geologic strain using randomly oriented strain markers of any shape. *Tectonophysics*, 42: T7-T16.
- ROCHETTE, P. 1987. Metamorphic control of the magnetic mineralogy of black shales in the Swiss Alps towards the use of "magnetic isograds". *Earth and Planetary Science Letters*, 84: 446-456.
- ROCHETTE, P. 1988. Magnetic susceptibility of the rock matrix related to magnetic fabric studies. *Journal of Structural Geology*, 9(8): 1015-1020.
- ROCHETTE, P., and VIALON, P. 1984. Development of planar and linear fabrics in Dauphinois shales and slates (French Alps) studied by magnetic anisotropy and its mineralogical control. *Journal of Structural Geology*, 6: 33-38.
- ROSENBLUM, S. 1958. Magnetic susceptibilities of minerals in the Frantz Isodynamic Magnetic Separator. *The American Mineralogist*, 43: 170-173.
- RUF, A.S., NARUK, S.J., BUTLER, R.F., and CALDERONE, G.J. 1988. Strain and magnetic fabrics in the Santa Catalina and Pinaleno Mountains metamorphic core complex mylonite zones, Arizona. *Tectonics*, 7(2): 235-248.

- SANDERSON, D.J., and MARCHINI, W.R.D. 1984. Transpression. *Journal of Structural Geology*, 6: 449-458.
- SARVAS, P.A. 1987. The structure and magnetic fabric of The Quetico metasedimentary rocks in the Calm Lake - Perch Lake area, NW Ontario. M.Sc. thesis, Lakehead University, Thunder Bay, Ont.
- SAWYER, E.W. 1983. The structural history of a part of the Archaean Quetico metasedimentary belt, Superior Province, Canada. *Precambrian Research*, 22: 271-294.
- SAWYER, E.W. 1987. The role of partial melting and fractional crystallization in determining discordant migmatite leucosome compositions. *Journal of Petrology*, 28: 445-473.
- SCHWARZ, E.J. 1974. Magnetic fabric in massive sulfide deposits. *Canadian Journal of Earth Sciences*, 11: 1669-1675.
- SCHWERDTNER, W.M. 1989. The solid-body tilt of deformed paleohorizontal planes: application to an Archean transpression zone, southern Canadian Shield. *Journal of Structural Geology*, 11: 1021-1027.
- SCHWERDTNER, W.M., BENNETT, P.J., and JANES, T.W. 1977. Application of L-S fabric scheme to structural mapping and paleostrain analysis. *Canadian Journal of Earth Sciences*, 14: 1021-1032.
- SCHWERDTNER, W.M., STONE, D., OSADETZ, K., MORGAN, J., and STOTT, G.M. 1979. Granitoid complexes and the Archean tectonic record in the southern part of northwestern Ontario. *Canadian Journal of Earth Sciences*, 16: 1965-1977.
- SHACKLETON, R.M. 1958. Downward facing structures of the Highland Border. *Journal of the Geological Society of London*, 113: 361-392.
- SHEGELSKI, R.J. 1980. Archean cratonization, emergence and red bed development, Lake Shebandowan area, Canada. *Precambrian Research*, 12: 331-347.
- SINGH, J., ANDERSON, D.J., and TARLING, D.H. 1975. The magnetic susceptibility anisotropy of deformed rocks from North Cornwall, England. *Tectonophysics*, 27: 141-153.
- STEWART, R.W. 1984. The structure and lithology of the Quetico metasediments in the Chub Lake - Little McCaulay Lake area. Unpublished B.Sc. thesis, Lakehead University, Thunder Bay, Ont.

STOCKWELL, C.H. 1964. Fourth report on structural provinces, orogenies, and time-classification of rocks of the Canadian Precambrian Shield. Geological Survey of Canada, Paper 64-17(II): 1-24.

STOTT, G.M. 1985. A structural analysis of the central part of the Archean Shebandowan greenstone belt and a crescent shaped granitoid pluton, northwestern Ontario. Unpublished Ph.D thesis, University of Toronto, 281p.

STOTT, G.M., and SCHNIEDERS, B.R. 1983. Gold mineralization in the Shebandowan belt and its relation to regional deformation patterns; in The geology of gold in Ontario. Ontario Geological Survey Miscellaneous Paper 110: 181-193.

STOTT, G.M., and SCHWERDTNER, W.M. 1981. A structural analysis of the central part of the Shebandowan metavolcanic-metasedimentary belt. Ontario Geoscience Research Grant Program, Final Research Reports, Ontario Geological Survey Open File Report 5349, 315p.

STRANGWAY, D.W. 1970. History of the Earth's Magnetic Field. McGraw-Hill Book Co., New York, 168 pp.

STUBLEY, M.P. 1983. The structure and lithology of the Quetico metasediments in the Banning Lake - Seine River area. Unpublished B.Sc. thesis, Lakehead University, Thunder Bay, Ont.

TARNEY, J., DALZIEL, I.W.D., and DE WIT, M.J. 1976. Marginal basin 'Rocas Verdes' complex from S. Chile: a model for Archean greenstone belt formation; in B.F. Windley (Ed.); The Early History of the Earth, Wiley, London, p. 131-146.

THURSTON, P.C. 1985. Atikokan-Lakehead compilation project; in Summary of field work and other activities, 1985. Ontario Geological Survey, Miscellaneous Paper 126: 54-59.

THURSTON, P.C., and CHIVERS K.M. 1990. Secular variation in greenstone sequence development emphasizing Superior Province, Canada. Precambrian Research, 46: 21-58.

WALKER, R.G., 1984. Turbidites and associated coarse clastic deposits; in Facies Models (2nd. ed.): Geoscience Canada Reprint Series 1, 171-188.

WILLIAMS, P.F. 1976. Relationships between axial-plane foliations and strain. Tectonophysics, 30: 181-196.

WOOD, J. 1980. Epiclastic sedimentation and stratigraphy in the North Spirit Lake and Rainy Lake areas: a comparison. Precambrian Research, 12: 227-255.

YU, H., and ZHENG, Y. 1984. A statistical approach to the Rf/ϕ method. *Tectonophysics*, 110: 151-155.

APPENDIX I

MSA Data

Magnetic Fabric Data - MSc. Thesis
 Shebandowan/Kashabowie - Robert Spark

Drill Core	AMS File Name	Bulk Suscept's		Normalised-Principal Axes			Flinn Dgm		Jelinek-Hrouda Plot	
		K(bulk)g	K(bulk)a	Kmax	Kint	Kmin	K1/K2	K2/K3	P'	T
(1a) MAFIC CHLORITIC METAVOLCANICS										
RS1	AMRS1	7.27E-04	7.28E-04	1.0403	1.0192	0.9432	1.0207	1.0806	1.1089	0.5823
(1b) FELSIC RHYOLITE TUFF										
RS1.1	AMRS1P1	2.09E-04	2.09E-04	1.0406	1.0306	0.9324	1.0097	1.1053	1.1292	0.8243
(1a) MAFIC CHLORITIC METAVOLCANICS										
RS1.2	AMRS12	8.95E-05	9.01E-05	1.1419	1.0228	0.8562	1.1165	1.1945	1.3372	0.2345
(1b) FELSIC AGGLOMERATE/RHYOLITE & CHLORITE SCHIST										
RS1.2-2C	AMRS122C	9.40E-04	9.41E-04	1.0366	1.0249	0.9413	1.0114	1.0889	1.1112	0.7644
RS1.3	AMRS13	2.18E-04	2.19E-04	1.056	1.0408	0.9099	1.0146	1.1439	1.1785	0.8052
RS1.31	AMS1P31	1.85E-04	1.86E-04	1.0788	1.059	0.8753	1.0187	1.2099	1.2605	0.8227
(2) MAFIC TUFF & CHLORITE SCHIST										
RS2C	AMRS2C	4.73E-04	4.74E-04	1.0622	1.0214	0.9217	1.04	1.1082	1.1579	0.4478
RS2.1	AMS2P1	5.03E-04	5.04E-04	1.0415	1.0214	0.9401	1.0197	1.0865	1.1149	0.6189
(3) TEST FELSIC AGGLOMERATE/RHYOLITE										
RS3C	AMRS3C	1.13E-04	1.13E-04	1.0818	0.9641	0.9588	1.1221	1.0056	1.146	-0.9081
(6) MAFIC FLOWS + AGGLOMERATE + CHLORITE SCHIST										
RS6.2-1	AMS6P2D1	7.53E-04	7.53E-04	1.0141	1.0031	0.9831	1.011	1.0203	1.032	0.2943
RS6.2-3	AMS6P2D3	2.79E-04	2.80E-04	1.0764	1.0354	0.8973	1.0396	1.154	1.2114	0.5735
(7) MAFIC TUFFS & PILLOW BASALTS										
RS7-1	AMS7D1	2.72E-04	2.72E-04	1.0723	0.9974	0.935	1.0751	1.0667	1.1469	-0.0572
RS7-2	AMS7D2	7.06E-04	7.08E-04	1.0516	1.043	0.9117	1.0082	1.144	1.1738	0.885
RS7.1	AMRS71	6.80E-04	6.80E-04	1.0164	1.0092	0.9748	1.0071	1.0353	1.0457	0.6611
RS8.0	AMRS80	6.38E-04	6.38E-04	1.0287	1.0089	0.9635	1.0196	1.0471	1.0695	0.4057
RS8C	AMRS8C	6.40E-04	6.40E-04	1.0195	1.0029	0.978	1.0166	1.0254	1.0427	0.2086
(9) GREYWACKE SILTSTONE										
RS8.1	AMRS81	4.60E-04	4.62E-04	1.073	1.0568	0.8819	1.0154	1.1983	1.2439	0.8443
RS9C	AMRS9C	2.66E-04	2.66E-04	1.0523	1.0422	0.9119	1.0097	1.1429	1.1736	0.8648
RS9.1	AMRS91	2.19E-04	2.19E-04	1.0427	1.0374	0.9245	1.0051	1.1221	1.1457	0.9154
RS9.1	AMS9P1	5.59E-04	5.62E-04	1.108	1.0449	0.8637	1.0605	1.2097	1.2975	0.5287
RS9.2	AMRS92	2.69E-04	2.70E-04	1.0517	1.036	0.9178	1.0151	1.1287	1.161	0.7793
RS9.2-1	AMS9P2D1	3.01E-04	3.01E-04	1.0592	1.0453	0.9032	1.0133	1.1574	1.1935	0.8344
RS9.2-2	AMS9P2D2	4.70E-04	4.73E-04	1.1033	1.0479	0.8649	1.0528	1.2216	1.2924	0.5773
RS9.25	AMS9P25	3.03E-04	3.05E-04	1.076	1.0637	0.8737	1.0116	1.2175	1.2638	0.8893
RS9.3	AMRS93	2.91E-04	2.92E-04	1.0695	1.0577	0.884	1.0111	1.1966	1.2385	0.8838
RS9.4	AMRS94	3.62E-04	3.64E-04	1.1133	1.0333	0.8693	1.0774	1.1887	1.289	0.3971
(10a) GREYWACKE SLATE GRADING TO BI-Qtz-FELD SCHIST										
RS10.0	AMRS100	4.58E-04	4.64E-04	1.1735	1.0473	0.8137	1.1205	1.2872	1.4548	0.3787
RS10.05	AMS10P05	3.27E-04	3.28E-04	1.0682	1.0391	0.901	1.0281	1.1533	1.2005	0.6748
RS10.1	AMRS101	3.28E-04	3.30E-04	1.1241	1.038	0.857	1.0829	1.2111	1.3216	0.4125
RS10.15	AMS10P15	2.81E-04	2.82E-04	1.0927	1.0678	0.8571	1.0233	1.2459	1.3076	0.8105

RS10.16	AMS10P16	8.06E-04	8.32E-04	1.3349	1.0516	0.7124	1.2694	1.4761	1.8851	0.2402
RS10.2	AMRS102	8.00E-04	8.16E-04	1.2373	1.0631	0.7603	1.1638	1.3984	1.6461	0.377
RS10.3	AMRS103	4.65E-04	4.72E-04	1.1565	1.1025	0.7843	1.049	1.4057	1.5274	0.7536

(10b) BI-QTZ-FELD SCHIST / PARAGNEISS v 6T

RS10.4	AMRS104	2.78E-04	2.80E-04	1.0952	1.0907	0.8371	1.0041	1.303	1.3608	0.9693
RS10.41-1	AMS10411	3.14E-04	3.16E-04	1.0986	1.0847	0.8391	1.0128	1.2927	1.3554	0.9055
RS10.45	AMS10P45	2.95E-04	2.98E-04	1.0981	1.0819	0.8417	1.015	1.2853	1.3482	0.8881
RS10.5	AMRS105	4.66E-04	4.73E-04	1.1992	1.0582	0.7881	1.1333	1.3427	1.5388	0.404
RS10.55	AMS10P55	3.51E-04	3.54E-04	1.098	1.0739	0.8481	1.0224	1.2664	1.3315	0.8286
RS10.6	AMRS106	3.91E-04	3.93E-04	1.0782	1.0551	0.879	1.0219	1.2004	1.2516	0.7879
RS10.65-2	AMS10652	5.86E-04	5.87E-04	1.0614	1.0298	0.9149	1.0307	1.1255	1.17	0.5925
RS10.7	AMRS107	2.48E-04	2.49E-04	1.0825	1.0619	0.8699	1.0193	1.2207	1.2739	0.8247
RS10.8	AMRS108	5.17E-04	5.18E-04	1.0581	1.0366	0.9117	1.0208	1.137	1.1753	0.7239
RS10.9	AMRS109	4.78E-04	4.82E-04	1.154	1.0405	0.8328	1.1091	1.2493	1.3956	0.3648
RS10.95-1	AMS10951	1.11E-03	1.12E-03	1.1123	1.0098	0.8903	1.1015	1.1343	1.2502	0.1316

(11) MIXED SCHIST, SLATE, PARAGNEISS ZONE

RS11-1	AMS11D1	3.90E-04	3.91E-04	1.0885	1.03	0.8919	1.0568	1.1549	1.2284	0.4458
RS11.1-1	AMS11P11	4.47E-04	4.57E-04	1.2099	1.1285	0.7324	1.0721	1.5409	1.7227	0.7227
RS11.2-1	AMS11P21	1.92E-04	1.94E-04	1.0949	1.0758	0.849	1.0178	1.2671	1.3286	0.8613
RS11.3	AMS11P3	2.52E-04	2.54E-04	1.0993	1.0654	0.8539	1.0318	1.2477	1.317	0.752
RS11.35	AMS11P35	3.28E-04	3.30E-04	1.0959	1.0755	0.8484	1.019	1.2677	1.3303	0.8532
RS11.4-2	AMS11P42	3.15E-04	3.21E-04	1.1713	1.1391	0.7495	1.0282	1.5198	1.649	0.8753
RS11.45	AMS11P45	3.30E-04	3.32E-04	1.1014	1.0725	0.8465	1.027	1.267	1.3362	0.7979
RS11.5	AMS11P5	3.42E-04	3.45E-04	1.1116	1.0724	0.8388	1.0366	1.2784	1.3587	0.7447

(12) MIGMATITE ZONE

RS11.6-1	AMS11P61	3.14E-04	3.15E-04	1.0886	1.0505	0.8744	1.0363	1.2014	1.2651	0.6748
RS11.7-1	AMS11P71	9.73E-03	9.85E-03	1.1958	1.0263	0.8149	1.1652	1.2594	1.4713	0.2028
RS11.8-1	AMS11P81	1.63E-04	1.64E-04	1.0968	1.0754	0.8478	1.0199	1.2685	1.332	0.8467
RS11.9	AMS11P9	4.68E-04	4.68E-04	1.0346	1.0156	0.9517	1.0187	1.0672	1.0918	0.5573
RS12.1	AMSR12P1	3.30E-04	3.32E-04	1.0915	1.072	0.8546	1.0183	1.2543	1.3135	0.852

Magnetic Fabric Data - MSc. Thesis
 Shebandowan/Kashabowie - Robert Spark

AMS File Name	Axis	DEC	INC	R95	EV	SDEV
------------------	------	-----	-----	-----	----	------

(1a) MAFIC CHLORITIC METAVOLCANICS

AMRS1 (RS1)	Min.	331.88	24.62	4.4	6.8562E-04	5.634E-06
	Int.	69.38	15.89	4.4	7.4087E-04	7.777E-07
	Max.	9.05	-60.10	1.0	7.5618E-04	2.349E-06

(1b) FELSIC RHYOLITE TUFF

AMRS1P1 (RS1.1)	Min.	345.91	12.55	6.2	1.9504E-04	5.506E-07
	Int.	89.59	46.81	64.3	2.1557E-04	1.485E-06
	Max.	64.93	-40.56	64.7	2.1766E-04	1.083E-06

(1a) MAFIC CHLORITIC METAVOLCANICS

AMRS12 (RS1.2)	Min.	44.62	14.57	13.5	7.6618E-05	2.064E-07
	Int.	326.99	-39.49	24.0	9.1519E-05	5.679E-06
	Max.	298.52	46.85	27.5	1.0218E-04	1.819E-06

(1b) FELSIC AGGLOMERATE / RHYOLITE & CHLORITE SCHIST

AMRS122C (RS1.2-2C)	Min.	356.57	20.07	4.1	8.8480E-04	1.923E-06
	Int.	80.84	-15.30	13.5	9.6342E-04	1.282E-06
	Max.	316.10	-64.35	13.3	9.7443E-04	1.510E-06
AMRS13 (RS1.3)	Min.	322.94	-16.40	5.8	1.9839E-04	3.101E-06
	Int.	69.16	-43.51	24.4	2.2694E-04	2.893E-06
	Max.	37.62	41.92	24.4	2.3025E-04	2.265E-06
AMS1P31 (RS1.31)	Min.	348.74	-10.81	2.0	1.6213E-04	7.371E-07
	Int.	88.35	-41.19	8.4	1.9617E-04	5.463E-08
	Max.	67.02	46.80	8.3	1.9984E-04	2.675E-08

(2) MAFIC TUFF & CHLORITE SCHIST

AMRS2C (RS2C)	Min.	14.12	-1.18	1.6	4.3620E-04	8.313E-08
	Int.	284.72	27.25	8.5	4.8339E-04	7.753E-07
	Max.	281.83	-62.72	8.5	5.0270E-04	1.792E-06
AMS2P1 (RS2.1)	Min.	347.89	14.64	6.2	4.7304E-04	2.084E-06
	Int.	67.55	-34.48	14.3	5.1395E-04	1.898E-06
	Max.	277.20	-51.68	15.5	5.2408E-04	2.012E-06

(3) TEST FELSIC AGGLOMERATE / RHYOLITE

AMSR53C	Min.	349.62	-10.06	66.7	1.0829E-04	3.381E-06
(RS3C)	Int.	83.81	-22.51	75.4	1.0889E-04	1.797E-06
	Max.	57.12	65.12	43.3	1.2218E-04	1.750E-06

(6) MAFIC FLOWS + AGGLOMERATE + CHLORITE SCHIST

AMS6P2D1	Min.	321.41	-6.37	5.0	7.4007E-04	2.082E-06
(RS6.2-1)	Int.	49.40	17.44	37.8	7.5508E-04	2.894E-06
	Max.	70.74	-71.37	37.6	7.6340E-04	7.839E-06

AMS6P2D3	Min.	323.76	-15.26	2.1	2.5060E-04	1.639E-06
(RS6.2-3)	Int.	59.11	-18.85	37.1	2.8918E-04	3.589E-06
	Max.	17.25	65.37	37.2	3.0063E-04	5.416E-07

(7) MAFIC TUFFS & PILLOW BASALTS

AMS7D1	Min.	317.06	-4.69	6.2	2.5420E-04	1.070E-06
(RS7-1)	Int.	50.36	-35.08	10.1	2.7116E-04	1.260E-06
	Max.	40.45	54.51	8.2	2.9152E-04	4.171E-07

AMS7D2	Min.	316.64	-14.81	3.9	6.4397E-04	5.786E-06
(RS7-2)	Int.	47.64	-3.80	85.7	7.3667E-04	6.388E-06
	Max.	331.80	74.68	85.7	7.4274E-04	1.176E-06

AMSR571	Min.	344.09	-6.09	11.4	6.6283E-04	1.024E-06
(RS7.1)	Int.	71.94	19.38	48.8	6.8622E-04	1.920E-06
	Max.	270.76	69.61	48.4	6.9109E-04	4.831E-06

AMSR580	Min.	320.60	-3.71	1.5	6.1499E-04	1.252E-06
(RS8.0)	Int.	51.09	-7.56	22.7	6.4393E-04	5.665E-07
	Max.	24.68	81.57	22.7	6.5657E-04	2.760E-06

AMSR58C	Min.	313.59	-17.64	9.9	6.2580E-04	1.404E-06
(RS8C)	Int.	57.99	-38.02	14.9	6.4171E-04	2.981E-07
	Max.	23.91	46.65	12.3	6.5234E-04	2.057E-06

(9) GREYWACKE SILTSTONE

AMSR581	Min.	347.58	-0.06	2.5	4.0553E-04	7.609E-07
(RS8.1)	Int.	77.30	77.93	23.2	4.8594E-04	1.513E-07
	Max.	77.59	-12.08	23.2	4.9342E-04	5.643E-08

AMSR59C	Min.	334.17	-1.99	7.6	2.4241E-04	2.847E-06
(RS9C)	Int.	81.19	-83.23	71.1	2.7705E-04	2.934E-06
	Max.	63.95	6.52	70.8	2.7974E-04	1.231E-06

AMSR591	Min.	333.63	-5.54	8.7	2.0228E-04	6.123E-07
(RS9.1)	Int.	71.68	-55.31	81.7	2.2697E-04	5.635E-08
	Max.	59.86	34.13	82.1	2.2813E-04	1.077E-06

AMS9P1	Min.	341.84	-13.71	3.6	4.8250E-04	9.141E-07
(RS9.1)	Int.	285.07	66.01	4.1	5.8369E-04	7.167E-08

	Max.	66.94	19.29	1.9	6.1898E-04	8.965E-08
AMSR92	Min.	354.29	-1.11	3.7	2.4698E-04	5.711E-07
(RS9.2)	Int.	84.35	-3.23	33.8	2.7877E-04	4.903E-07
	Max.	65.50	86.58	33.9	2.8299E-04	3.321E-07
AMS9P2D1	Min.	341.49	-5.75	5.8	2.7143E-04	1.514E-06
(RS9.2-1)	Int.	75.87	-37.15	11.0	3.1416E-04	3.412E-08
	Max.	64.01	52.26	12.3	3.1833E-04	1.736E-06
AMS9P2D2	Min.	346.01	-10.82	4.4	4.0677E-04	3.470E-06
(RS9.2-2)	Int.	356.37	79.00	6.5	4.9284E-04	1.043E-07
	Max.	76.37	-1.89	7.1	5.1885E-04	2.880E-06
AMS9P25	Min.	329.00	-0.73	2.5	2.6492E-04	2.647E-07
(RS9.25)	Int.	59.60	-39.37	18.8	3.2253E-04	1.844E-06
	Max.	58.11	50.62	18.7	3.2628E-04	1.305E-06
AMSR93	Min.	316.23	-10.84	1.7	2.5728E-04	1.302E-06
(RS9.3)	Int.	47.96	-8.97	59.7	3.0785E-04	1.927E-06
	Max.	356.83	75.84	59.7	3.1128E-04	2.229E-06
AMSR94	Min.	325.82	4.14	2.6	3.1487E-04	1.084E-06
(RS9.4)	Int.	49.23	-57.76	3.3	3.7428E-04	1.360E-07
	Max.	58.40	31.91	2.5	4.0326E-04	2.854E-06

(10a) GREYWACKE SLATE GRADING TO BI-QTZ-FELD SCHIST

AMSR100	Min.	344.47	-5.15	2.0	3.7286E-04	1.690E-06
(RS10.0)	Int.	87.19	-67.75	2.5	4.7993E-04	2.105E-06
	Max.	72.43	21.59	1.8	5.3776E-04	2.197E-06
AMS10P05	Min.	343.21	-11.41	5.7	2.9478E-04	5.038E-06
(RS10.05)	Int.	272.48	58.53	4.3	3.3997E-04	1.091E-07
	Max.	66.82	28.88	6.8	3.4951E-04	2.453E-06
AMSR101	Min.	325.16	-1.45	2.1	2.8132E-04	6.227E-06
(RS10.1)	Int.	57.93	62.39	1.8	3.4072E-04	8.574E-07
	Max.	54.40	27.57	1.4	3.6897E-04	5.531E-06
AMS10P15	Min.	335.63	2.44	2.5	2.4055E-04	5.666E-06
(RS10.15)	Int.	61.21	-61.08	77.9	2.9971E-04	3.080E-06
	Max.	66.97	28.80	77.9	3.0669E-04	5.744E-06
AMS10P16	Min.	344.10	-10.57	0.5	5.7398E-04	2.661E-06
(RS10.16)	Int.	283.58	69.23	0.7	8.4725E-04	2.632E-07
	Max.	70.69	17.67	0.7	1.0755E-03	3.572E-06
AMSR102	Min.	325.22	3.69	0.6	6.0811E-04	4.466E-06
(RS10.2)	Int.	48.25	-62.05	0.5	8.5036E-04	1.272E-06
	Max.	57.15	27.67	0.6	9.8966E-04	3.905E-06
AMSR103	Min.	334.48	3.17	2.7	3.6474E-04	4.231E-06
(RS10.3)	Int.	53.06	-74.39	7.3	5.1273E-04	1.563E-06
	Max.	65.35	15.28	7.2	5.3785E-04	4.707E-06

(10b) BI-QTZ-FELD SCHIST / PARAGNEISS W GARNETS

AMRS104	Min.	320.44	-0.74	3.9	2.3254E-04	5.233E-06
(RS10.4)	Int.	54.73	-80.17	53.4	3.0301E-04	4.705E-06
	Max.	50.31	9.87	53.5	3.0426E-04	2.463E-06
AMS10411	Min.	313.43	-11.40	2.7	2.6332E-04	2.858E-06
(RS10.41-1)	Int.	60.09	-54.88	84.9	3.4040E-04	7.572E-07
	Max.	35.99	32.71	84.9	3.4476E-04	6.134E-06
AMS10P45	Min.	346.14	-5.85	1.3	2.4867E-04	7.065E-06
(RS10.45)	Int.	65.28	61.49	71.1	3.1961E-04	2.000E-06
	Max.	79.24	-27.80	71.1	3.2440E-04	2.016E-06
AMRS105	Min.	324.18	-8.03	2.3	3.6706E-04	8.809E-07
(RS10.5)	Int.	28.36	72.05	4.8	4.9285E-04	7.486E-07
	Max.	56.49	-15.95	4.2	5.5852E-04	2.523E-06
AMS10P55	Min.	326.17	-12.98	3.5	2.9783E-04	1.191E-07
(RS10.55)	Int.	339.13	76.69	74.0	3.7716E-04	1.269E-06
	Max.	56.83	-2.87	86.2	3.8560E-04	4.794E-06
AMRS106	Min.	344.23	-5.95	3.8	3.4407E-04	9.707E-07
(RS10.6)	Int.	59.45	67.78	10.6	4.1302E-04	3.648E-06
	Max.	76.57	-21.33	10.6	4.2207E-04	9.680E-07
AMS10652	Min.	345.30	-0.70	2.5	5.3602E-04	1.155E-06
(RS10.65-2)	Int.	72.21	77.19	11.0	6.0332E-04	2.188E-06
	Max.	75.46	-12.80	10.8	6.2186E-04	9.487E-07
AMRS107	Min.	351.38	-16.54	4.3	2.1544E-04	1.090E-06
(RS10.7)	Int.	308.21	67.84	40.9	2.6299E-04	4.188E-06
	Max.	77.03	14.32	40.8	2.6807E-04	1.331E-06
AMRS108	Min.	351.31	-4.38	4.7	4.7135E-04	3.759E-06
(RS10.8)	Int.	271.66	66.86	18.4	5.3594E-04	4.764E-07
	Max.	79.48	22.66	18.8	5.4708E-04	4.987E-06
AMRS109	Min.	1.49	-2.16	2.0	3.9795E-04	1.649E-06
(RS10.9)	Int.	354.57	87.81	4.4	4.9715E-04	4.433E-07
	Max.	271.49	-0.07	4.6	5.5141E-04	3.131E-06
AMS10951	Min.	350.58	22.88	0.7	9.9163E-04	8.880E-07
(RS10.95-1)	Int.	334.24	-66.26	1.4	1.1248E-03	1.422E-06
	Max.	78.04	-5.99	1.3	1.2390E-03	1.606E-06

(11) MIXED SCHIST, SLATE, PARAGNEISS ZONE

AMS11D1	Min.	338.41	-61.57	4.5	3.4775E-04	4.164E-06
(RS11-1)	Int.	350.36	27.91	8.1	4.0162E-04	2.661E-06
	Max.	77.70	-5.00	6.8	4.2441E-04	1.389E-06
AMS11P11	Min.	348.01	-36.94	1.4	3.2716E-04	5.884E-06

(RS11.1-1)	Int.	302.59	43.03	9.1	5.0411E-04	5.541E-06
	Max.	57.88	24.59	9.2	5.4044E-04	2.995E-07
AMS11P21	Min.	346.39	-23.47	4.2	1.6331E-04	1.886E-06
(RS11.2-1)	Int.	290.60	52.33	70.4	2.0693E-04	2.039E-06
	Max.	63.26	27.62	70.3	2.1062E-04	3.092E-06
AMS11P3	Min.	346.94	-42.76	4.0	2.1540E-04	1.940E-06
(RS11.3)	Int.	18.68	42.60	19.3	2.6875E-04	6.535E-06
	Max.	272.86	16.52	18.9	2.7730E-04	1.723E-06
AMS11P35	Min.	351.01	-23.26	1.2	2.7800E-04	7.369E-08
(RS11.35)	Int.	1.53	66.39	36.2	3.5242E-04	3.027E-08
	Max.	82.72	-3.95	36.3	3.5910E-04	3.618E-06
AMS11P42	Min.	344.25	-52.40	1.6	2.3612E-04	1.445E-06
(RS11.4-2)	Int.	343.03	37.59	31.7	3.5886E-04	7.569E-07
	Max.	73.49	0.59	31.7	3.6899E-04	3.974E-06
AMS11P45	Min.	352.11	-50.32	6.6	2.7904E-04	1.878E-06
(RS11.45)	Int.	341.78	39.22	4.5	3.5353E-04	1.226E-06
	Max.	75.94	5.09	8.5	3.6306E-04	1.157E-06
AMS11P5	Min.	278.10	68.40	6.3	2.8714E-04	6.092E-06
(RS11.5)	Int.	275.23	-21.58	17.7	3.6709E-04	4.638E-06
	Max.	5.62	-0.98	16.7	3.8052E-04	1.073E-06

(12) MIGMATITE ZONE

AMS11P61	Min.	10.58	-55.61	1.8	2.7456E-04	7.629E-07
(RS11.6-1)	Int.	356.82	33.62	23.1	3.2985E-04	1.841E-06
	Max.	271.10	-6.43	23.1	3.4181E-04	3.640E-06
AMS11P71	Min.	346.75	43.54	0.5	7.9259E-03	4.071E-05
(RS11.7-1)	Int.	14.76	-42.89	0.4	9.9820E-03	1.569E-05
	Max.	270.92	-14.45	0.4	1.1631E-02	1.290E-05
AMS11P81	Min.	345.50	-51.40	4.8	1.3783E-04	4.355E-07
(RS11.8-1)	Int.	321.74	36.16	12.1	1.7484E-04	3.365E-07
	Max.	60.45	11.71	11.7	1.7832E-04	2.474E-08
AMS11P9	Min.	342.21	-6.65	10.1	4.4508E-04	4.482E-06
(RS11.9)	Int.	78.99	-45.37	10.9	4.7501E-04	8.683E-07
	Max.	65.78	43.86	13.1	4.8388E-04	6.408E-07
AMSR12P1	Min.	25.07	1.35	2.9	2.8214E-04	4.907E-06
(RS12.1)	Int.	295.25	-7.67	26.8	3.5389E-04	5.848E-07
	Max.	285.16	82.21	26.7	3.6036E-04	1.459E-06

APPENDIX II

Planar [S] and Linear [L]

Outcrop Fabrics

S - DATA

STATION	[S0]	[S1]	[S2]	AVG S0	AVG S1	AVG S2
RS1		080/90	034/85		080/85	034/85
		085/81				
		081/86				
		072/82				
		085/79				
		078/90				
		072/85				
		076/88				
		256/85				
		076/90				
		081/68				
		095/85				
RS1.05		076/72	030		077/82	030
		081/85				
		072/81				
		084/82				
		073/84				
		074/88				
RS1.1		072/87			065/82	
		075/80				
		058/72				
		054/87				
RS1.2		070/84	010		080/76	010
		073/80				
		081/75				
		092/74				
		076/68				
		084/71				
		084/82				
RS1.3		283/70	017		271/74	017
		278/70				
		264/68				
		249/78				
		280/83				
RS1.31		254/81	175/78		249/81	165/77
		072/85	154/76			
		240/82				
		248/68				
		243/80				
		258/78				
RS1.32		082/80			085/76	
		088/72				
RS2	092	085/85		270/82	272/88	
	093	087/86				
	092	091/80				

S - DATA

STATION	[S0]	[S1]	[S2]	AVG S0	AVG S1	AVG S2
	267/82	274/85				
		282/84				
		086/84				
		266/76				
		278/85				
RS2.1		070/78			066/78	
		062/74				
		067/81				
RS3		070/80			073/86	
		075/90				
		078/88				
		071/81				
		081/73				
		078/82				
		067/88				
		259/80				
		244/88				
		068/90				
		061/85				
		073/87				
		080/85				
		080/88				
		075/84				
RS3.5		067/85	250/75		070/88	254/78
		070/86	257/81			
		072/90				
		070/89				
		071/88				
RS3.6		078/88	354/68		254/87	354/68
		083/90				
		257/81				
		070/84				
		249/85				
		249/85				
		251/84				
		256/86				
		256/85				
RS3.7		239/75			253/86	
		081/86				
		080/90				
RS4		080/87			072/89	
		248/82				
		074/86				
		251/84				
		073/85				

S - DATA

STATION	[S0]	[S1]	[S2]	AVG S0	AVG S1	AVG S2
		072/90				
		069/83				
		070/90				
RS4.1		262/83			075/89	
		067/80				
		074/85				
		073/83				
		079/83				
		262/73				
		068/88				
		073/85				
RS4.2		266/81			260/80	
		265/81				
		255/82				
		253/74				
RS5		065/81			253/83	
		248/80				
		240/79				
		269/85				
		256/80				
		256/86				
		256/83				
		265/81				
		244/81				
		251/80				
RS5.1		067/88			251/88	
		250/88				
		254/83				
		262/78				
		064/82				
		058/87				
		060/87				
		268/78				
		058/87				
		272/82				
RS5.2		264/81			264/87	
		068/85				
		077/86				
		265/87				
		267/85				
		265/80				
		283/84				
RS5.5		249/79			261/79	
		259/80				
		248/84				

S - DATA

STATION	[S0]	[S1]	[S2]	AVG S0	AVG S1	AVG S2
		249/85				
		252/80				
		234/84				
		243/80				
		244/82				
		257/75				
		245/86				
		230/72				
		240/70				
		240/83				
		241/80				
		229/60				
RS5.55		241/79				239/79
		227/72				
		242/74				
		251/65				
		234/88				
		057/85				
		237/80				
		240/77				
		235/82				
		244/81				
RS5.6		253/83				242/85
		252/84				
		249/79				
		242/85				
		241/75				
		245/78				
		225/74				
		057/86				
		055/84				
		051/90				
		244/86				
		243/88				
		252/90				
RS6		235/74				235/74
RS6.1		224/77				230/79
		236/80				
RS6.2		236/88				238/81
		240/78				
		259/73				
		236/54				
		043/80				
		226/86				
		250/80				
		241/88				

S - DATA

STATION	[S0]	[S1]	[S2]	AVG S0	AVG S1	AVG S2
		233/85				
RS7		202/83			230/79	
		055/90				
		226/80				
		228/70				
		210/74				
		064/80				
		223/77				
		238/83				
		235/75				
		241/60				
		246/83				
		237/77				
		235/72				
		236/84				
		231/84				
		222/75				
		229/78				
RS7.1		236/68	253/84		231/64	253/84
		237/64				
		068/85				
		219/75				
		213/84				
RS8		242/83			242/82	
		238/78				
		242/79				
		246/86				
RS8.05		245/82			252/80	
		258/78				
RS8.1	263/80			254/80		
	254/72					
	249/80					
	257/78					
	253/80					
	257/81					
	247/75					
	253/80					
	254/86					
	253/90					
RS9.1	072	062		255/83	062	
	254/86					
	256/84					
	260/78					
	255/78					
	074/88					

S - DATA

STATION	[S0]	[S1]	[S2]	AVG S0	AVG S1	AVG S2
	254/80					
	255/82					
	255/80					
	254/82					
	251/80					
	077/84					
RS9.2	251/81			255/84		
	258/83					
	259/88					
	262/88					
	257/86					
	252/83					
	255/83					
	252/82					
	254/78					
	254/88					
	253/81					
	258/84					
RS9.25	075	073	000/68	065/88	073	000/68
	246/88					
	238/89					
	067/88					
	060/88					
	238/83					
	066/87					
	244/89					
	070/84					
	068/77					
	063/84					
	059/86					
RS9.3						
RS9.4	236/84	059/80		241/83	065/87	
	243/81	068/85				
	236/79	064/88				
	245/82	059/86				
	243/81	240/90				
	237/89	071/80				
	244/85	252/82				
RS10	079	068		256/90	252/88	
	074/88	068/90				
	252/88	247/86				
	079/90	073/87				
	258/89	252/82				
	075/85	082/90				
	255/86					
	264/86					

S - DATA

STATION	[S0]	[S1]	[S2]	AVG S0	AVG S1	AVG S2
	074/84					
	257/86					
	254/88					
RS10.05	077/90			257/89		
	083/90					
	077/89					
	258/86					
	249/89					
RS10.1	068	058		067/87	061/86	
	061	066				
	069/80	067/81				
	068/90	235/85				
	063/90	060/86				
	070/86	233/85				
		056/90				
		064/86				
		242/85				
		066/88				
		064/85				
RS10.15	064	054		243/90	240/89	
	070/85	064/87				
	240/86	242/85				
	238/87					
	061/88					
RS10.16	085/90			258/89		
	078/85					
	079/85					
	078/86					
	255/88					
	254/88					
	253/81					
	258/84					
RS10.2		246/79			244/84	
		241/75				
		238/82				
		252/88				
		244/84				
		247/90				
		238/85				
		242/85				
		251/85				
		237/80				
		242/81				
		255/90				
RS10.3		238/90	336/74	230/84	328/90	

S - DATA

STATION	[S0]	[S1]	[S2]	AVG S0	AVG S1	AVG S2
		234/86	140/74			
		211/82				
		238/81				
		232/81				
		228/85				
		233/83				
		235/90				
		233/82				
		230/85				
		226/81				
RS10.4		226/85	315		225/81	323/80
		223/86	150/80			
		223/79				
		227/81				
		222/80				
		225/81				
		231/80				
		225/79				
		225/77				
		226/80				
		225/84				
		225/80				
		226/78				
		226/81				
		224/81				
RS10.41		225/83			225/81	
		225/85				
		223/79				
		226/81				
		224/80				
		227/78				
		223/80				
		227/81				
RS10.45		227/70			229/72	
		230/75				
		234/73				
		226/71				
		227/71				
		230/71				
RS10.5		232/77	314		232/78	319
		233/77	323			
		234/77				
		230/82				
		232/75				
		231/79				
		231/76				
		233/74				

S - DATA

STATION	[S0]	[S1]	[S2]	AVG S0	AVG S1	AVG S2
		229/82				
RS10.55		238/80			238/84	
		240/84				
		237/84				
		238/85				
		237/84				
		239/86				
RS10.6		255/75			256/74	
		254/73				
		257/81				
		256/71				
		258/77				
		256/67				
		254/76				
RS10.65		259/84			258/83	
		257/84				
		259/85				
		256/79				
		258/84				
RS10.7		264/82	345		256/79	345
		251/68				
		257/81				
		254/79				
		254/84				
		255/81				
		255/81				
RS10.8		255/65			256/65	
		256/70				
		255/69				
		252/64				
		254/81				
		256/62				
		258/66				
		259/61				
		260/62				
		256/60				
		257/59				
		258/55				
RS10.9	071	062		255/55	246/79	
	254/55	247/78				
	254/52	248/80				
	255/61					
	261/56					
	251/54					
	257/52					

 STATION [S0] [S1] [S2] AVG S0 AVG S1 AVG S2
 ~~~~~

253/62  
 252/64  
 253/70  
 258/49  
 260/34  
 256/60  
 253/50

RS10.95      259/64    254/78      263/65    253/78  
              270/77      252  
              259/63  
              264/54

RS11                      268/30                      264/35  
                             264/34  
                             261/40  
                             264/43  
                             260/30  
                             267/34

RS11.1                    267/53                    263/45  
                             259/43  
                             259/49  
                             259/40  
                             267/41  
                             260/43  
                             271/39  
                             265/50

RS11.2                    262/41                    261/55  
                             259/44  
                             261/60  
                             274/48  
                             253/61  
                             262/50  
                             252/78  
                             261/60

RS11.25                  262/67                    260/55  
                             253/46  
                             271/44  
                             253/66  
                             260/56  
                             258/48

RS11.3                    225/42                    250/38  
                             257/35  
                             249/35  
                             256/31  
                             261/33  
                             256/40  
                             255/42  
                             244/46

RS11.35                  263/61                    255/50  
                             258/46  
                             250/54

S - DATA

\*\*\*\*\*

| STATION | [S0] | [S1]   | [S2] | AVG S0 | AVG S1 | AVG S2 |
|---------|------|--------|------|--------|--------|--------|
|         |      | 252/56 |      |        |        |        |
|         |      | 253/54 |      |        |        |        |
|         |      | 253/45 |      |        |        |        |
|         |      | 254/48 |      |        |        |        |
|         |      | 251/48 |      |        |        |        |
|         |      | 254/46 |      |        |        |        |
|         |      | 260/47 |      |        |        |        |
|         |      | 260/47 |      |        |        |        |
| RS11.4  |      | 270/42 |      |        | 261/50 |        |
|         |      | 261/44 |      |        |        |        |
|         |      | 260/52 |      |        |        |        |
|         |      | 266/48 |      |        |        |        |
|         |      | 260/50 |      |        |        |        |
|         |      | 260/55 |      |        |        |        |
|         |      | 264/53 |      |        |        |        |
|         |      | 263/45 |      |        |        |        |
|         |      | 264/50 |      |        |        |        |
|         |      | 254/55 |      |        |        |        |
|         |      | 256/50 |      |        |        |        |
|         |      | 257/55 |      |        |        |        |
| RS11.45 |      | 255/35 |      |        | 249/42 |        |
|         |      | 248/35 |      |        |        |        |
|         |      | 235/49 |      |        |        |        |
|         |      | 241/48 |      |        |        |        |
|         |      | 243/45 |      |        |        |        |
|         |      | 260/38 |      |        |        |        |
|         |      | 250/40 |      |        |        |        |
|         |      | 260/42 |      |        |        |        |
| RS11.5  |      | 255/43 |      |        | 259/45 |        |
|         |      | 250/45 |      |        |        |        |
|         |      | 254/52 |      |        |        |        |
|         |      | 263/62 |      |        |        |        |
|         |      | 260/35 |      |        |        |        |
|         |      | 270/36 |      |        |        |        |
|         |      | 258/42 |      |        |        |        |
| RS11.6  |      | 266/40 |      |        | 267/39 |        |
|         |      | 264/42 |      |        |        |        |
|         |      | 270/34 |      |        |        |        |
| RS11.7  |      | 261/55 |      |        | 264/41 |        |
|         |      | 263/35 |      |        |        |        |
|         |      | 269/32 |      |        |        |        |
| RS11.8  |      | 050/86 |      |        | 234/72 |        |
|         |      | 237/84 |      |        |        |        |
|         |      | 222/70 |      |        |        |        |
|         |      | 246/41 |      |        |        |        |

S - DATA

\*\*\*\*\*

STATION      [S0]      [S1]      [S2]                      AVG S0    AVG S1    AVG S2  
~~~~~

RS11.9 260/58 260/58

RS12.1 285/75 285/75

STATION	[Lx]	[L1]	AVG L1
RS1	036->28	080->64 085->25 087->15 077->16 059->28 082->28 094->17	081->28
RS1.05		091->28 092->18 088->25	090->24
RS1.1		081->22 071->36	076->29
RS1.2		072->28 092->15 099->20 094->14	089->19
RS1.3		240->36??	
RS2	130->41		
RS2.2	100->10 072->08		
RS3		076->10 076->08 086->30 071->26 083->37 078->20	078->22
RS3.5		072->12 077->24 075->27 071->28	074->23
RS3.6		083->11 073->15	078->13
RS3.7			080->25
RS4	080->57	080->21	080->21
RS4.1	076->60		
RS5		090->71 086->66 076->56 084->58	084->63
RS5.1		067->78 086->64 071->54	068->64

L - DATA

STATION	[Lx]	[L1]	AVG L1
		058->67 060->56	
RS5.2		085->51 085->71	085->61
RS5.6		042->55 062->65	052->60
RS6		065->10	065->10
RS7	075->15 069->14 060->47 033->08		
RS7.1	246->11		
RS8	072->14	066->21 067->17	067->19
RS8.05		073->12	073->12
RS8.1		069->14	069->14
RS9.1		074->14 076->22	075->18
RS9.2		082->18 078->14 076->14	079->15
RS9.25		067->14 056->16 064->25 071->14	065->17
RS9.4		063->34 062->19 065->26 057->30 067->32 064->36	063->30
RS10		077->18 073->17 082->24	077->20
RS10.1		056->25 068->19 077->42	067->29

L - DATA

STATION	[Lx]	[L1]	AVG L1
RS10.15		064->42 061->27	063->35
RS10.16		085->19 074->16 071->10	077->15
RS10.2		065->17 067->14 072->12 067->14 075->14	069->14
RS10.3		058->18 056->18 041->22 060->10 050->17 055->07 044->06	052->14
RS10.4	047->07		
RS10.45		054->00 233->04 228->04	232->03
RS10.5		232->08 236->02 233->09 233->01 233->12 232->09 231->06 232->05	233->07
RS10.55		240->05 241->12 239->10 236->08	239->09
RS10.6		258->05 074->05 258->01 253->04	258->03
RS10.65		261->02 079->04 078->06 258->03	079->01

L - DATA

STATION	[Lx]	[L1]	AVG L1
RS10.7		078->07 077->04 073->12 075->04 077->04 081->04	077->05
RS10.8		076->12 071->08 073->16 073->09 077->04 072->15	073->11
RS10.9		071->08 074->03 071->04 074->02 074->00 070->15	072->05
RS10.95		081->04	081->04
RS11		066->14 072->08 070->11 063->13	068->11
RS11.1		063->12 068->12 083->06 075->13	072->11
RS11.2		073->10 074->12 071->16	073->13
RS11.3		073->06 067->03 065->09 072->03	069->05
RS11.4		268->08	268->08
RS11.45		251->05 265->08	258->07
RS11.5		067->07 071->06 071->08	070->07

L - DATA

STATION	[Lx]	[L1]	AVG L1
		071->08	
RS11.6		078->06 075->08 079->06	077->07
RS11.7		078->03 078->04 084->02	080->03
RS11.8		042->04 252->03	038->01

APPENDIX III

Semi-quantitative Microprobe

Magnetic Mineralogy Data

SEM - SEMI-QUANTITATIVE (SQ) ANALYSES

RS1.2 - Magnetite Fe3O4

	Compound%					
	[I]	[II]	[III]			
FeO	100	93.73	100			
TiO2	-----	6.27	-----			
	Atom%		Wt%			
Fe	50	77.23	45.86	72.85	50	77.23
Ti	-----	-----	2.76	3.76	-----	-----
O	50	22.27	51.38	23.38	50	22.27

RS1.2 - Chlorite (Mg,Al,Fe)12[(SiAl)8O20](OH)16

	[I]	[II]	[III]	[IV]	[V]					
SiO2	29.84	28.44	33.47	30.23	29.44					
FeO	28.74	30.86	23.1	28.7	27.96					
Al2O3	27.19	26.21	27.5	25.25	26.55					
MgO	13.51	14.34	15.68	15.29	15.61					
MnO	0.71	0.14	0.25	0.53	0.44					
Si	11.51	13.95	11.06	13.29	12.52	15.65	11.65	14.13	11.3	13.76
Fe	9.27	22.34	10.04	23.99	7.23	17.96	9.25	22.31	8.97	21.73
Al	12.36	14.39	12.01	13.87	12.13	14.55	11.46	13.36	12.01	14.05
Mg	7.77	8.15	8.31	8.65	8.75	9.46	8.78	9.22	8.93	9.41
Mn	0.23	0.55	0.05	0.11	0.08	0.19	0.17	0.41	0.14	0.34
O	58.85	40.62	58.53	40.08	59.29	42.19	58.69	40.57	58.65	40.7

RS1.2 - Epidote Ca2FeAl2Si3O12.OH

	[I]	[II]	[III]	[IV]	[V]					
SiO2	39.29	38.79	42.75	45.76	43.88					
CaO	24.12	24.31	20.86	18.54	19.73					
FeO	11.81	13.69	8.78	8.98	9.65					
Al2O3	24.78	23.21	27.61	26.72	26.74					
Si	14.98	18.37	14.93	18.13	15.89	19.99	16.9	21.39	16.32	20.51
Ca	9.85	17.24	10.03	17.37	8.31	14.91	7.34	13.25	7.86	14.1
Fe	3.76	9.18	4.41	10.64	2.73	6.82	2.77	6.98	3	7.5
Al	11.13	13.12	10.53	12.28	12.1	14.61	11.63	14.14	11.72	14.15
O	60.27	42.1	60.1	41.57	60.97	43.67	61.36	44.24	61.09	43.73

SEM - SEMI-QUANTITATIVE (SQ) ANALYSES

RS8 - Pyrite?? FeS2

	Atom%		Wt%		[I]		[II]		[III]		[IV]	
S	70.79	58.18	57.64	43.83	72.24	59.91	71.56	59.09				
Fe	29.21	41.82	41.47	54.93	27.76	40.09	28.44	40.91				
Ni	-----	-----	0.89	1.24	-----	-----	-----	-----				

RS8 - Sphalerite ZnS

	[I]	
S	50.72	33.72
Zn	46.7	63.3
Fe	2.98	2.98

RS8 - Cobaltite (Co,Fe)AsS

	[I]		[II]		[III]		[IV]		[V]	
S	38.83	23.46	34.55	20.06	36.87	21.84	39.63	23.84	34.37	19.86
Co	27.58	30.62	24.1	25.72	26.56	28.91	25.4	28.09	24.9	26.45
As	29.23	41.26	35.41	48.05	32.5	44.97	31.87	44.82	36.64	49.48
Fe	3.04	3.2	2.66	2.69	2.46	2.53	3.1	3.25	2.14	2.15
Ni	1.33	1.47	3.27	3.48	1.62	1.75	-----	-----	1.95	2.06

RS8 - Chlorite (Mg,Al,Fe)12[(SiAl)8O20](OH)16

	Compound%	
SiO2	30.75	
FeO	25.55	
Al2O3	24.51	
MgO	18.75	
MnO	0.45	
Si	11.65	14.37
Fe	8.1	19.86
Al	10.95	12.97
Mg	10.59	11.3
Mn	0.14	0.35
O	58.56	41.14

RS8 - Epidote Ca₂FeAl₂Si₃O₁₂

	[I]	[II]	[III]	[IV]	[V]					
SiO ₂	42.73	39.37	39.19	40.29	39.22					
CaO	23.27	25.27	25.23	23.46	25.53					
FeO	6.04	7.81	7.08	9.14	7.12					
Al ₂ O ₃	27.97	27.55	28.31	25.51	27.92					
MgO	-----	-----	-----	1.02	-----					
TiO ₂	-----	-----	0.19	0.19	0.2					
Cr ₂ O ₃	-----	-----	-----	0.39	-----					
Si	15.79	19.98	14.77	18.41	14.66	18.32	15.16	18.84	14.69	18.34
Ca	9.21	16.63	10.16	18.06	10.11	18.03	9.46	16.77	10.25	18.25
Fe	1.87	4.69	2.45	6.07	2.22	5.51	2.88	7.11	2.23	5.54
Al	12.18	14.8	12.18	14.58	12.48	14.98	11.31	13.5	12.33	14.78
Mg	-----	-----	-----	-----	-----	-----	0.57	0.61	-----	-----
Ti	-----	-----	-----	-----	0.05	0.11	0.05	0.11	0.06	0.12
Cr	-----	-----	-----	-----	-----	-----	0.12	0.27	-----	-----
O	60.94	43.9	60.43	42.88	60.48	43.05	60.46	42.8	60.45	42.98

RS8 - Actinolite Ca₂(Mg,Fe)₅[Si₈O₂₂](OH,F)₂

	[I]	[II]	[III]	[IV]	[V]					
SiO ₂	51.91	47.27	49.25	52.33	53.37					
CaO	12.88	12.56	13.64	14.07	12.33					
FeO	14.84	18.21	15.28	13.3	12.8					
MgO	12.16	8.33	8.22	12.38	15.43					
Al ₂ O ₃	7.58	12.52	12.91	4.22	4.88					
K ₂ O	0.29	0.4	-----	0.08	-----					
MnO	0.35	0.32	0.42	0.5	0.46					
TiO ₂	-----	0.39	0.28	2.98	0.45					
Cr ₂ O ₃	-----	-----	-----	0.15	0.28					
Si	19.38	24.27	17.97	22.1	18.49	23.03	19.62	24.46	19.72	24.95
Ca	5.15	9.2	5.12	8.98	5.48	9.75	5.65	10.05	4.88	8.81
Fe	4.63	11.53	5.79	14.15	4.8	11.88	4.17	10.33	3.95	9.95
Mg	6.76	7.33	4.77	5.02	4.6	4.96	6.92	7.46	8.5	9.31
Al	3.33	4.01	5.61	6.63	5.71	6.83	1.87	2.24	2.12	2.58
K	0.14	0.24	0.19	0.33	-----	-----	0.04	0.06	-----	-----
Mn	0.11	0.27	0.1	0.25	0.13	0.32	0.16	0.38	0.14	0.35
Ti	-----	-----	0.11	0.23	0.08	0.17	0.84	1.79	0.12	0.27
Cr	-----	-----	-----	-----	-----	-----	0.05	0.1	0.08	0.19
O	60.49	43.14	60.39	42.31	60.71	43.07	60.7	43.11	60.47	43.58

SEM - SEMI-QUANTITATIVE (SQ) ANALYSES

RS9 - Chlorite (Mg,Al,Fe)₁₂[(SiAl)₈O₂₀](OH)₁₆

Compound%									
	[I]	[II]	[III]	[IV]	[V]				
SiO ₂	32.15	30.83	29.94	30.4	30.31				
FeO	27.62	26.3	26.73	25.77	26.64				
Al ₂ O ₃	21.5	22.02	25.92	25.11	25.76				
MgO	18	20.38	16.94	18.3	16.65				
MnO	-----	0.48	0.47	0.43	-----				
CaO	0.21	-----	-----	-----	0.33				
Cr ₂ O ₃	0.51	-----	-----	-----	0.31				
Si	12.31 15.03	11.73 14.41	11.42 14	11.53 14.21	11.55 14.17				
Fe	8.84 21.47	8.36 20.44	8.52 20.77	8.18 20.03	8.49 20.71				
Al	9.71 11.38	9.87 11.65	11.65 13.72	11.23 13.29	11.57 13.63				
Mg	10.27 10.58	11.55 12.29	9.63 10.22	10.35 11.03	9.46 10.04				
Mn	-----	0.15 0.37	0.15 0.36	0.14 0.33	-----				
Ca	0.09 0.15	-----	-----	-----	0.13 0.23				
Cr	0.16 0.35	-----	-----	-----	0.09 0.21				
O	58.62 40.76	58.33 40.84	58.62 40.93	58.57 41.1	58.69 41				

RS9 - Ilmenite FeTiO₃

	[I]	[II]	[III]	[IV]	[V]				
FeO	42.84	42.08	40.5	42.4	41.72				
TiO ₂	53.19	52.77	53.51	52.76	53				
MnO	3.97	5.15	5.99	4.84	5.28				
Fe	18.06 33.3	17.76 32.71	17.05 31.48	17.89 32.96	17.59 32.43				
Ti	20.16 31.89	20.03 31.64	20.26 32.08	20.02 31.63	20.1 31.78				
Mn	1.69 3.07	2.2 3.99	2.55 4.64	2.07 3.75	2.26 4.09				
O	60.08 31.74	60.01 31.67	60.13 31.8	60.01 31.66	60.05 31.71				

RS9 - Biotite K(Mg,Fe)₃(AlSi₃O₁₀)(OH)₂

	[I]	[II]	[III]	[IV]	[V]				
SiO ₂	39.54	38.41	37.58	39.28	39.93				
K ₂ O	9.63	9.77	7.87	9.27	8.88				
Al ₂ O ₃	17.82	18.59	19.4	18.7	18.36				
MgO	12.07	10.79	12.16	11.56	11.64				
FeO	19.19	20.94	21.48	19.58	19.22				
TiO ₂	1.75	1.51	1.51	1.61	1.97				
Si	15.11 18.48	14.81 17.95	14.42 17.57	15.02 18.36	15.23 18.67				
K	4.7 7.99	4.81 8.11	3.85 6.54	4.52 7.7	4.32 7.37				
Al	8.03 9.43	8.45 9.84	8.78 10.27	8.43 9.89	8.26 9.72				
Mg	6.88 7.28	6.2 6.51	6.96 7.33	6.59 6.97	6.62 7.02				
Fe	6.14 14.92	6.75 16.28	6.9 16.7	6.26 15.22	6.13 14.94				
Ti	0.5 1.05	0.44 0.9	0.44 0.9	0.46 0.96	0.56 1.18				
O	58.64 40.84	58.54 40.41	58.66 40.69	58.72 40.89	58.88 41.11				

RS9 - Pyrite?? FeS2

	[I]		[II]		[III]		[IV]		[V]	
S	56.43	42.64	56.87	43.09	56.11	42.33	57.32	43.53	57.29	43.5
Fe	43.57	57.36	43.13	56.91	43.89	57.67	42.68	56.47	42.71	56.5

RS9 - Epidote Ca2FeAl2Si3O12.OH

	[I]		[II]	
SiO2	42.35		40.14	
CaO	23.29		23.44	
FeO	4.68		12.77	
Al2O3	29.68		23.65	
Si	15.56	19.8	15.34	18.77
Ca	9.17	16.64	9.6	16.75
Fe	1.44	3.64	4.08	9.93
Al	12.85	15.71	10.65	12.52
O	60.99	44.21	60.33	42.04

SEM - SEMI-QUANTITATIVE (SQ) ANALYSES

RS10 - Muscovite $KAl_2(AlSi_3O_{10})(OH)_2$

Compound%											
	[I]		[II]		[III]		[IV]		[V]		
SiO2	51.21		50.81		56		51.49		52.49		
K2O	10.7		10.67		8.6		10.08		9.91		
Al2O3	35.99		36.13		33.6		36.64		35.64		
FeO	1.31		1.57		1.25		1.27		1.49		
TiO2	0.79		0.82		0.56		0.52		0.47		
Atom% Wt%											
Si	18.02	23.94	17.9	23.75	19.53	26.18	18.06	24.07	18.42	24.54	
K	4.8	8.88	4.8	8.86	3.83	7.14	4.51	8.37	4.44	8.23	
Al	14.93	19.05	15.01	19.12	13.81	17.78	15.15	19.39	14.74	18.86	
Fe	0.38	1.02	0.46	1.22	0.36	0.97	0.37	0.99	0.44	1.16	
Ti	0.21	0.47	0.22	0.49	0.15	0.33	0.14	0.31	0.12	0.28	
O	61.65	46.64	61.61	46.56	62.33	47.6	61.76	46.87	61.85	46.93	

RS10 - Ilmenite $FeTiO_3$

	[I]		[II]		[III]		[IV]		[V]		
FeO	43.18		43.06		43.58		43.02		43.59		
TiO2	52.84		53.19		53.26		53.23		52.93		
MnO	3.97		3.75		3.16		3.74		3.48		
Fe	18.22	33.57	18.15	33.47	18.37	33.87	18.13	33.44	18.39	33.88	
Ti	20.05	31.68	20.17	31.89	20.19	31.93	20.18	31.91	20.08	31.73	
Mn	1.7	3.08	1.6	2.9	1.35	2.45	1.6	2.9	1.49	2.7	
O	60.03	31.68	60.08	31.74	60.09	31.75	60.09	31.74	60.04	31.69	

RS10 - Chlorite $(Mg,Al,Fe)_{12}[(Si,Al)_8O_{20}](OH)_{16}$

	[I]		[II]		[III]		[IV]		[V]		
SiO2	29.95		28.54		28.26		29.84		29.29		
FeO	29.41		27.92		30.3		27.92		27.92		
Al2O3	25.88		26.87		25.51		25.43		26.83		
MgO	14.42		16.15		15.59		16.44		15.46		
MnO	0.35		0.52		0.34		0.37		0.5		
Si	11.57	14	10.96	13.34	10.97	13.21	11.44	13.95	11.24	13.69	
Fe	9.5	22.86	8.96	21.7	9.83	23.55	8.95	21.71	8.96	21.7	
Al	11.79	13.7	12.16	14.22	11.67	13.5	11.49	13.46	12.14	14.2	
Mg	8.3	8.69	9.24	9.74	9.02	9.4	9.4	9.91	8.84	9.32	
Mn	0.11	0.27	0.17	0.41	0.11	0.27	0.12	0.29	0.16	0.39	
O	58.73	40.48	58.52	40.59	58.4	40.07	58.59	40.69	58.65	40.69	

RS10 - Pyrite?? FeS_2

	[I]		[II]		[III]		[IV]		[V]		
S	56.88	43.09	71.05	58.49	57.96	44.18	57.69	43.91	57.66	43.87	
Fe	43.12	56.91	28.95	41.51	42.04	55.82	42.31	56.09	42.34	56.13	

RS10 - Biotite -> 2nd Generation K(Mg,Fe)3(AlSi3O10)(OH)2

	[I]		[II]		[III]		[IV]		[V]	
SiO2	38.66		39.14		38.61		38.76		38.48	
K2O	9.36		9.43		8.7		9.49		9.48	
Al2O3	19.91		20.45		20.26		19.96		20.25	
MgO	10.15		9.96		9.77		9.16		9.94	
FeO	20.04		19.27		20.75		20.87		20.27	
TiO2	1.87		1.76		1.91		1.76		1.57	
Si	14.84	18.07	14.96	18.3	14.83	18.05	14.94	18.12	14.78	17.99
K	4.58	7.77	4.6	7.83	4.26	7.22	4.67	7.88	4.64	7.87
Al	9.01	10.54	9.21	10.82	9.17	10.72	9.07	10.56	9.17	10.72
Mg	5.81	6.12	5.67	6.01	5.59	5.89	5.26	5.52	5.69	6
Fe	6.43	15.58	6.16	14.98	6.67	16.13	6.73	16.22	6.51	15.76
Ti	0.54	1.12	0.51	1.06	0.55	1.15	0.51	1.05	0.45	0.94
O	58.79	40.79	58.89	41.02	58.92	40.84	58.83	40.64	58.75	40.73

RS10 - Biotite -> 1st Generation K(Mg,Fe)3(AlSi3O10)(OH)2

	[I]		[II]		[III]		[IV]		[V]	
SiO2	40.09		38.13		38.8		38.66		39.12	
K2O	9.53		9.78		9.26		8.99		8.81	
Al2O3	19.74		20.33		20.58		21.4		21.22	
MgO	10.13		10.13		10.42		10.53		11.04	
FeO	18.77		20.03		19.38		19.03		18.24	
TiO2	1.73		1.6		1.54		1.39		1.58	
Si	15.29	18.74	14.65	17.82	14.82	18.14	14.72	18.07	14.83	18.29
K	4.64	7.91	4.79	8.12	4.52	7.69	4.37	7.46	4.26	7.31
Al	8.88	10.45	9.21	10.76	9.27	10.89	9.6	11.32	9.49	11.23
Mg	5.76	6.11	5.8	6.11	5.93	6.28	5.98	6.35	6.24	6.66
Fe	5.99	14.59	6.43	15.57	6.19	15.06	6.06	14.79	5.78	14.18
Ti	0.5	1.04	0.46	0.96	0.44	0.93	0.4	0.83	0.45	0.95
O	58.95	41.16	58.66	40.66	58.82	41	58.87	41.16	58.95	41.39

SEM - SEMI-QUANTITATIVE (SQ) ANALYSES

RS10.5 - Garnet

	[I]		[II]		[III]		[IV]		[V]	
SiO2	36.63		36.19		35.78		36.55		37.25	
FeO	24.85		25.12		24.01		25.13		25.29	
CaO	5.54		5.78		6.62		5.63		5.64	
Al2O3	20.64		20.92		20.64		20.94		20.98	
MnO	9.56		10		9.9		9.59		8.95	
MgO	2.67		1.89		3.06		2.16		1.89	
TiO2	0.1		0.11		-----		-----		-----	
	Atom%	Wt%								
Si	14.74	17.12	14.63	16.92	14.4	16.72	14.73	17.09	14.97	17.41
Fe	8.36	19.32	8.49	19.52	8.08	18.66	8.47	19.53	8.5	19.66
Ca	2.39	3.96	2.5	4.13	2.85	4.73	2.43	4.03	2.43	4.03
Al	9.79	10.92	9.97	11.07	9.8	10.93	9.95	11.08	9.94	11.1
Mn	3.26	7.41	3.43	7.75	3.38	7.67	3.27	7.42	3.05	6.93
Mg	1.6	1.61	1.14	1.14	1.83	1.84	1.3	1.31	1.13	1.14
Ti	0.03	0.06	0.05	0.09	-----	-----	-----	-----	-----	-----
O	59.83	39.6	59.8	39.38	59.65	39.45	59.85	39.55	59.97	39.72

RS10.5 - Hornblende

	[I]		[II]		[III]		[IV]		[V]	
SiO2	43.95		45.16		41.9		44.31		42.92	
FeO	20.77		22.18		22.37		20.08		21.45	
CaO	11.56		10.89		12.32		11.84		11.65	
Al2O3	14.44		11.5		15.19		14.76		15.91	
MnO	1.05		1.02		0.89		0.77		0.56	
MgO	7.31		8.68		6.55		7.46		6.67	
K2O	0.31		0.27		0.4		0.45		0.46	
TiO2	0.61		0.31		0.38		0.32		0.39	
Si	16.94	20.55	17.46	21.11	16.31	19.59	17.01	20.71	16.57	20.06
Fe	6.69	16.14	7.17	17.24	7.28	17.39	6.45	15.61	6.93	16.67
Ca	4.77	8.26	4.51	7.79	5.14	8.81	4.87	8.46	4.82	8.32
Al	6.56	7.64	5.24	6.09	6.97	8.04	6.68	7.81	7.24	8.42
Mn	0.34	0.81	0.33	0.79	0.29	0.69	0.25	0.6	0.18	0.43
Mg	4.2	4.41	5	5.23	3.8	3.95	4.27	4.5	3.84	4.02
K	0.15	0.26	0.13	0.23	0.2	0.33	0.22	0.37	0.22	0.38
Ti	0.18	0.37	0.09	0.18	0.11	0.23	0.09	0.19	0.11	0.24
O	60.16	41.56	60.05	41.35	59.9	40.98	60.17	41.74	60.09	41.45

RS10.5 - Ilmenite FeTiO3

	[I]		[II]		[III]		[IV]		[V]	
FeO	42.66		44.44		46.75		43		44.03	
TiO	52.18		52.01		50.62		52.47		51.63	
MnO	5.16		3.55		2.62		4.54		4.34	
Fe	18.03	33.16	18.8	34.54	19.86	36.34	18.16	33.42	18.64	34.22
Ti	19.84	31.28	19.79	31.18	19.34	30.35	19.93	31.45	19.66	30.95
Mn	2.21	4	1.52	2.75	1.13	2.03	1.94	3.51	1.86	3.36
O	59.92	31.56	59.89	31.53	59.67	31.28	59.97	31.61	59.83	31.46

RS10.5 - Chalcopyrite CuFeS2

	[I]	
S	53.85	38.48
Fe	22.39	27.87
Cu	23.76	33.65

RS10.5 - Pyrite??

	[I]		[II]		[III]		[IV]		[V]	
S	70.21	57.5	70.51	57.85	70.46	57.8	57.36	43.58	57.64	43.86
Fe	29.79	42.5	29.49	42.15	29.54	42.2	42.64	56.42	42.36	56.14

RS10.5 - Chlorite (Mg,Al,Fe)12[(Si,Al)8O20](OH)16

	[I]		[II]		[III]		[IV]		[V]	
SiO2	28.67		31.07		31.44		30.29		30.38	
FeO	30.65		26.94		31.12		28.5		30.82	
Al2O3	22.94		24.36		21.82		22.76		25	
MgO	17.14		17.35		14.99		17.92		13.55	
MnO	0.6		0.29		0.41		0.54		0.25	
TiO2	-----		-----		0.22		-----		-----	
Si	11.16	13.4	11.85	14.52	12.26	14.7	11.65	14.16	11.81	14.2
Fe	9.97	23.83	8.59	20.94	10.14	24.19	9.17	22.15	10.02	23.96
Al	10.52	12.14	10.95	12.89	10.02	11.55	10.32	12.04	11.46	13.23
Mg	9.94	10.34	9.86	10.46	8.71	9.04	10.28	10.81	7.85	8.17
Mn	0.2	0.47	0.09	0.22	0.14	0.32	0.18	0.42	0.08	0.19
Ti	-----	-----	-----	-----	0.06	0.13	-----	-----	-----	-----
O	58.21	39.83	58.66	40.96	58.67	40.08	58.41	40.42	58.77	40.24

RS10.5 - Biotite K(Mg,Fe)3(AlSi3O10)(OH)2

	[I]		[II]		[III]		[IV]		[V]	
SiO2	35.25		36.84		38.16		38.85		36.88	
K2O	9.67		10.09		9.48		9.27		7.29	
Al2O3	16.92		16.59		17.44		18.35		18.3	
MgO	11.12		10.74		10.96		10.41		13.29	
FeO	24.36		23.19		21.57		20.72		22.24	
TiO2	2.49		2.3		2.4		2.4		1.72	
MnO	0.18		0.25		-----		-----		0.27	
Si	13.88	16.48	14.44	17.22	14.78	17.84	14.97	18.16	14.2	17.24
K	4.86	8.03	5.04	8.37	4.68	7.87	4.56	7.7	3.58	6.05
Al	7.85	8.95	7.67	8.78	7.96	9.23	8.34	9.71	8.31	9.69
Mg	6.53	6.71	6.28	6.48	6.33	6.61	5.98	6.28	7.63	8.02
Fe	8.02	18.94	7.6	18.02	6.99	16.77	6.68	16.1	7.16	17.29
Ti	0.74	1.49	0.68	1.38	0.7	1.44	0.7	1.44	0.5	1.03
Mn	0.06	0.14	0.08	0.19	-----	-----	-----	-----	0.09	0.21
O	58.06	39.26	58.21	39.55	58.56	40.25	58.78	40.61	58.53	40.47

SEM - SEMI-QUANTITATIVE (SQ) ANALYSES

RS10.8 - Biotite $K(Mg,Fe)_3(AlSi_3O_{10})(OH)_2$

Compound%											
	[I]	[II]	[III]	[IV]	[V]						
SiO2	37.33	36.92	36.39	36.82	35.95						
K2O	8.76	9.21	9	9.08	9.46						
Al2O3	20.14	20.77	20.67	20.94	19.85						
MgO	7.75	6.93	7.98	8.22	6.78						
FeO	24.24	24.2	23.64	23.42	25.82						
TiO2	1.78	1.97	2.32	1.51	2.15						
	Atom%		Wt%								
Si	14.6	17.45	14.47	17.26	14.22	17.01	14.35	17.21	14.23	16.8	
K	4.37	7.28	4.6	7.64	4.49	7.47	4.51	7.54	4.77	7.85	
Al	9.28	10.66	9.6	10.99	9.52	10.94	9.62	11.08	9.26	10.5	
Mg	4.52	4.67	4.05	4.18	4.65	4.81	4.78	4.96	4	4.09	
Fe	7.93	18.84	7.93	18.81	7.73	18.38	7.63	18.21	8.55	20.07	
Ti	0.52	1.07	0.58	1.18	0.68	1.39	0.44	0.91	0.64	1.29	
O	58.79	40.03	58.77	39.93	58.71	40	58.67	40.09	58.55	39.39	

RS10.8 - Cordierite $(Mg,Fe)_2Al_4Si_5O_{18}$

	[I]	[II]	[III]	[IV]	[V]						
SiO2	48.91	49.62	49.73	50.15	48.57						
FeO	9.79	9.65	10.34	9.85	8.86						
Al2O3	33.14	33.24	33.15	33	34.66						
MgO	7.8	6.98	6.54	6.42	7.58						
MnO	0.37	0.51	0.24	0.58	0.33						
Si	17.18	22.86	17.43	23.19	17.5	23.25	17.64	23.44	16.99	22.71	
Fe	2.88	7.61	2.84	7.5	3.04	8.04	2.9	7.66	2.59	6.89	
Al	13.72	17.54	13.77	17.59	13.76	17.55	13.68	17.46	14.29	18.34	
Mg	4.08	4.7	3.65	4.21	3.43	3.95	3.37	3.87	3.95	4.57	
Mn	0.11	0.28	0.15	0.4	0.07	0.18	0.17	0.45	0.1	0.25	
O	62.02	47	62.16	47.1	62.19	47.04	62.24	47.11	62.07	47.24	

RS10.8 - Pyrite?? FeS_2

	[I]	[II]	[III]	[IV]	[V]						
S	69.48	56.65	71.52	59.04	70.37	57.69	70.43	57.76	69.74	56.95	
Fe	30.52	43.35	28.48	40.96	29.63	42.31	29.57	42.24	30.26	43.05	

RS10.8 - Staurolite $\text{Fe}_2\text{Al}_9\text{O}_6(\text{SiO}_4)_4(\text{O},\text{OH})_2$

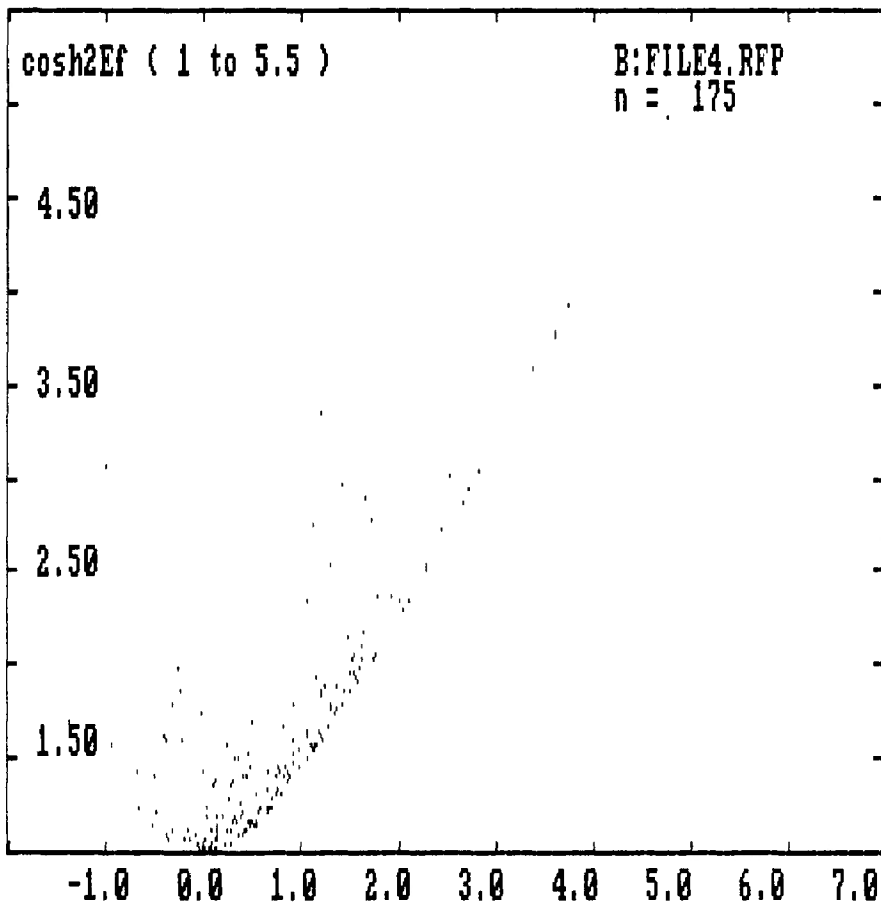
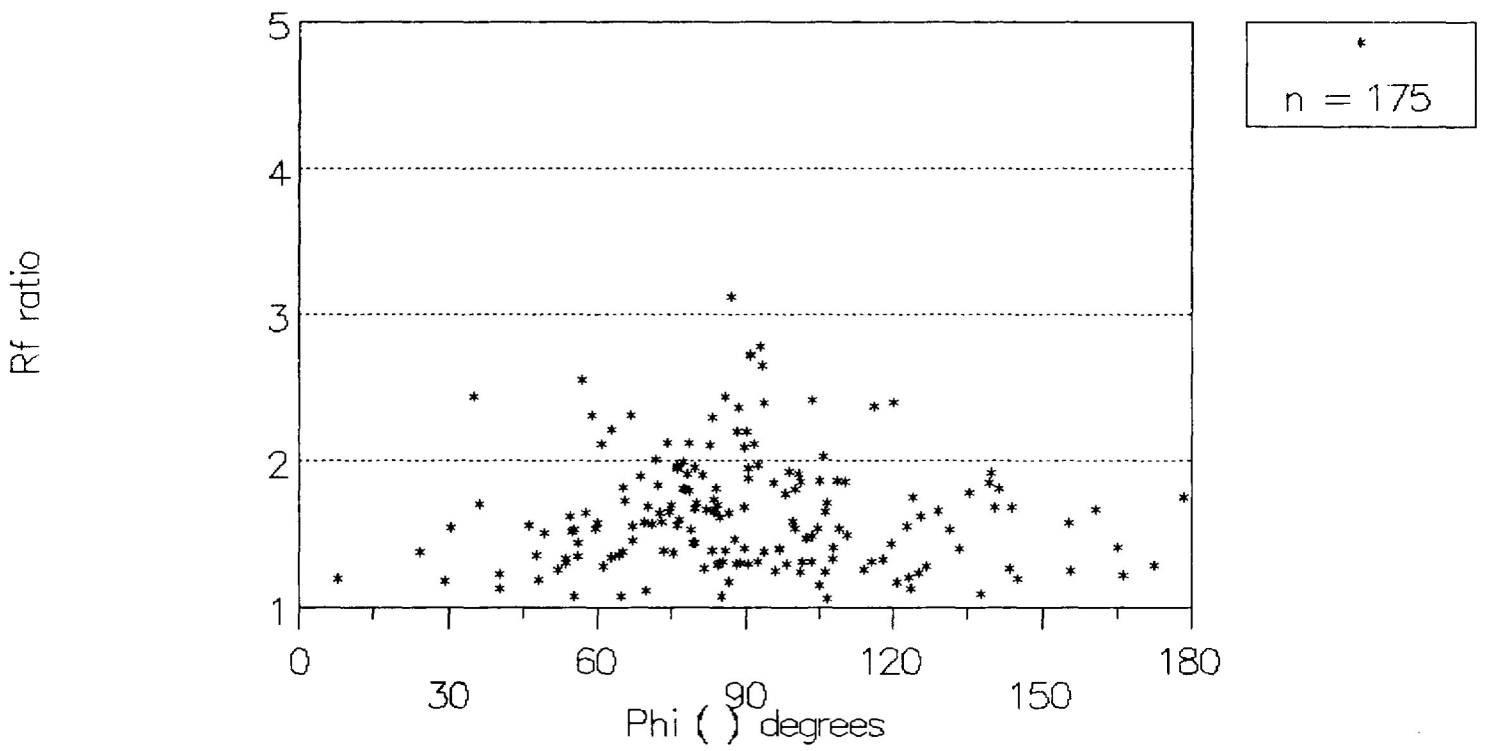
	[I]		[II]		[III]		[IV]		[V]	
SiO ₂	27.87		27.49		29.42		27.72		27.91	
FeO	15.58		14.74		14.13		15.42		15.52	
Al ₂ O ₃	53.32		53.03		54.19		53.32		53.99	
MgO	1.59		3.46		1.2		1.42		1.65	
MnO	0.47		0.63		0.32		0.45		0.45	
TiO ₂	0.56		0.65		0.27		0.78		0.48	
ZnO	0.62		-----		0.47		0.89		-----	
Si	10.15	13.03	9.95	12.85	10.62	13.75	10.11	12.96	10.13	13.05
Fe	4.75	12.11	4.46	11.46	4.27	10.99	4.7	11.99	4.71	12.06
Al	22.89	28.22	22.63	28.06	23.06	28.68	22.93	28.22	23.1	28.57
Mg	0.87	0.96	1.87	2.09	0.64	0.72	0.77	0.86	0.89	0.99
Mn	0.14	0.36	0.19	0.49	0.1	0.25	0.14	0.35	0.14	0.35
Ti	0.15	0.33	0.18	0.39	0.07	0.16	0.21	0.47	0.13	0.29
Zn	0.17	0.5	-----	-----	0.12	0.37	0.24	0.71	-----	-----
O	60.88	44.49	60.72	44.66	61.11	45.07	60.89	44.45	60.9	44.68

APPENDIX V

Strain Results From
Digitized Quartz Grains

Rf / Phi STRAIN ANALYSIS

Sample CV8.1

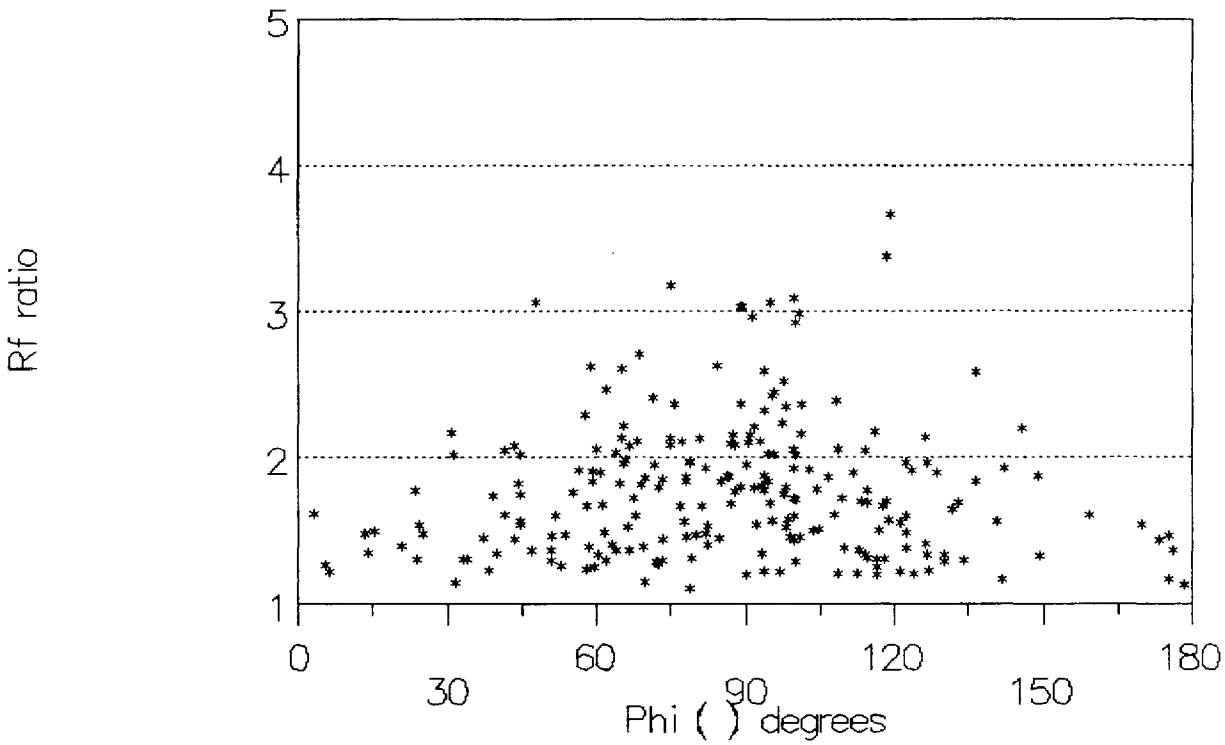


slope = 0.5698
 intercept = 1.170E+00
CV8.1

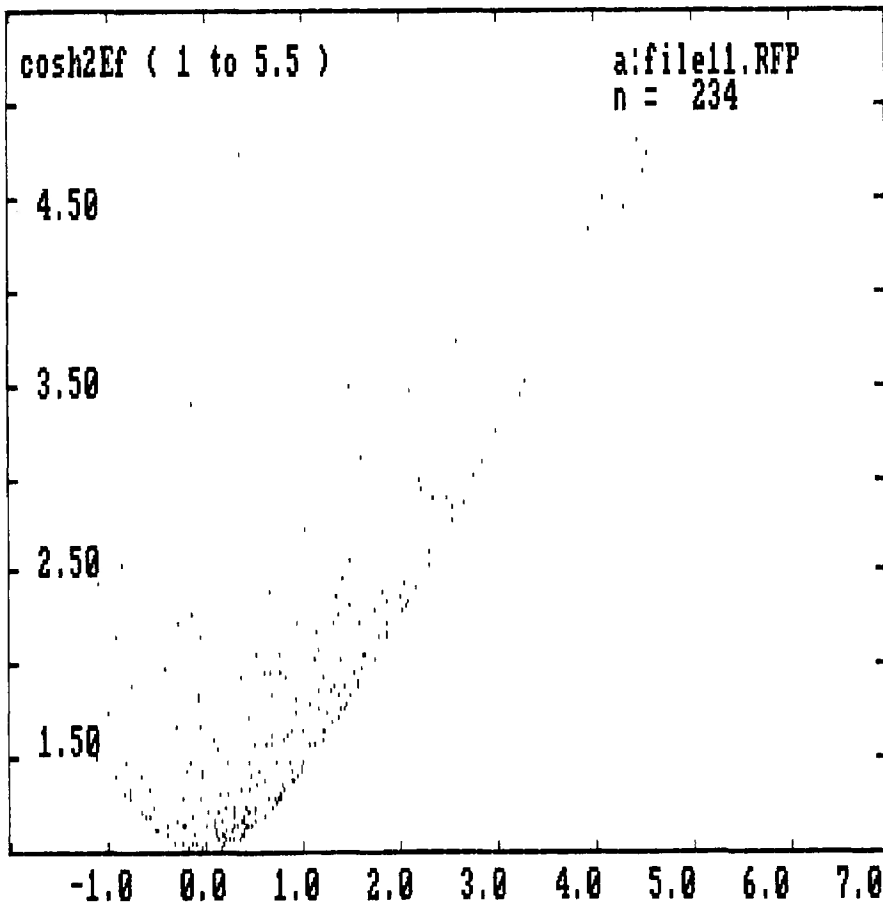
B:FILE4.RFP
 Slope of line = .5697773
 Y - intercept = 1.170188
 Supposed initial 'unique' ratio = 1.561293
 Strain ratio by linearization method = 1.38209
 One-sigma limits on strain ratio are + 1.402769
 and - .2911942
 Range of strain ratios is 1.091 to 2.785

Rf / Phi STRAIN ANALYSIS

Sample SH9



n = 234



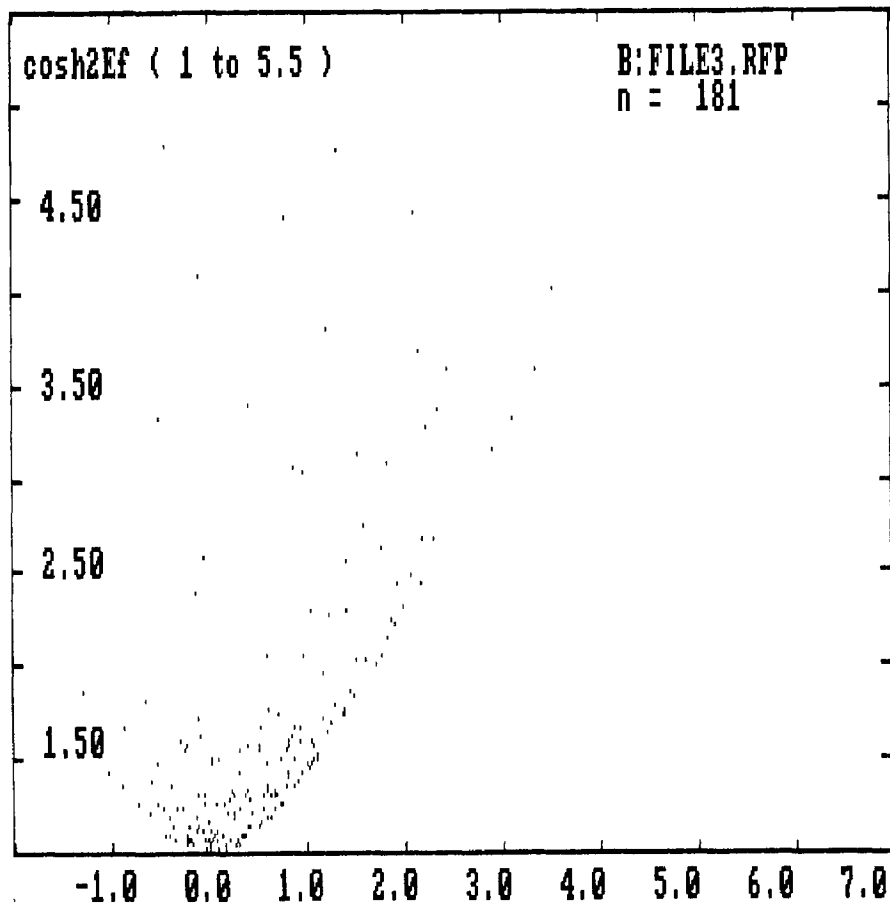
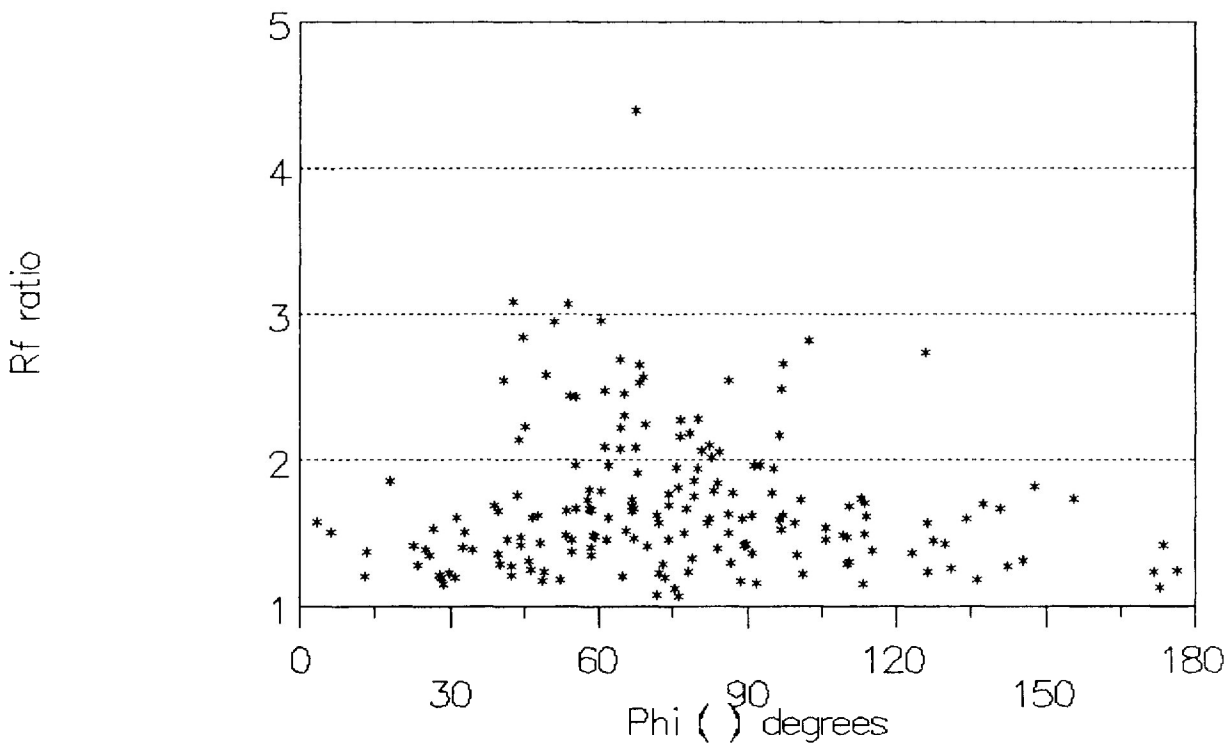
slope= 0.6328
intercept= 1.292E+00
SH9

Slope of line = .6328479
y - intercept = 1.291962
Supposed initial 'unique' ratio = 1.73331
Strain ratio by linearization method = 1.452195

sinh2Ef, cos2phi
(-2 to 7)

Rf / Phi STRAIN ANALYSIS

Sample SV9



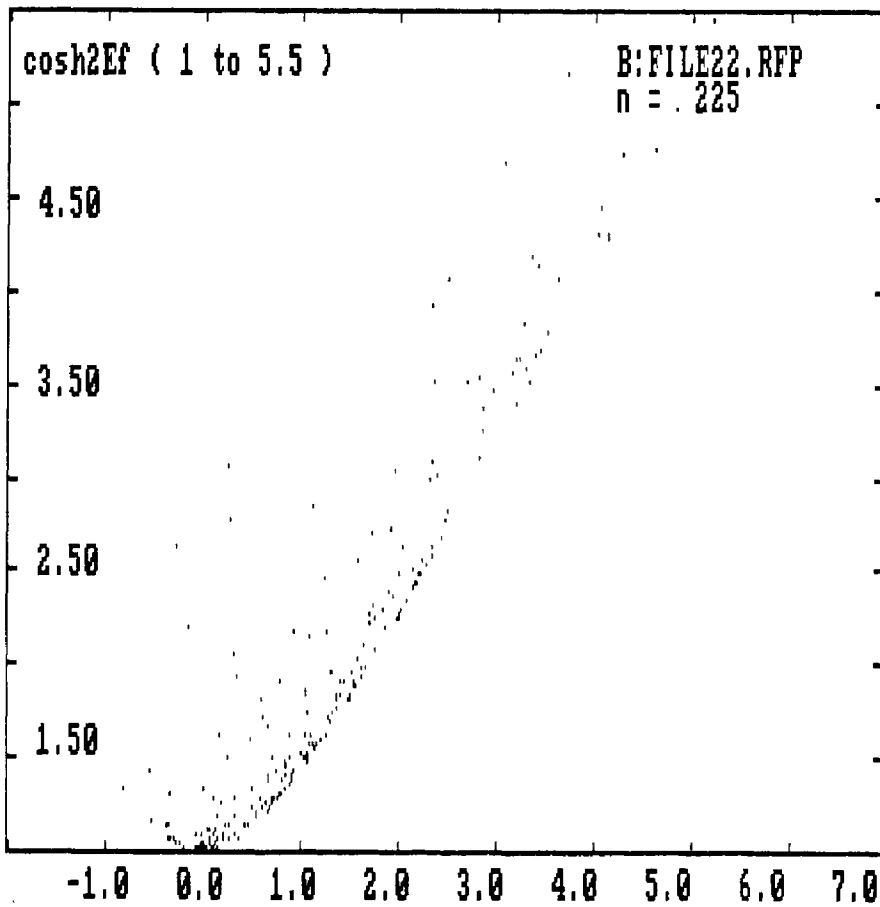
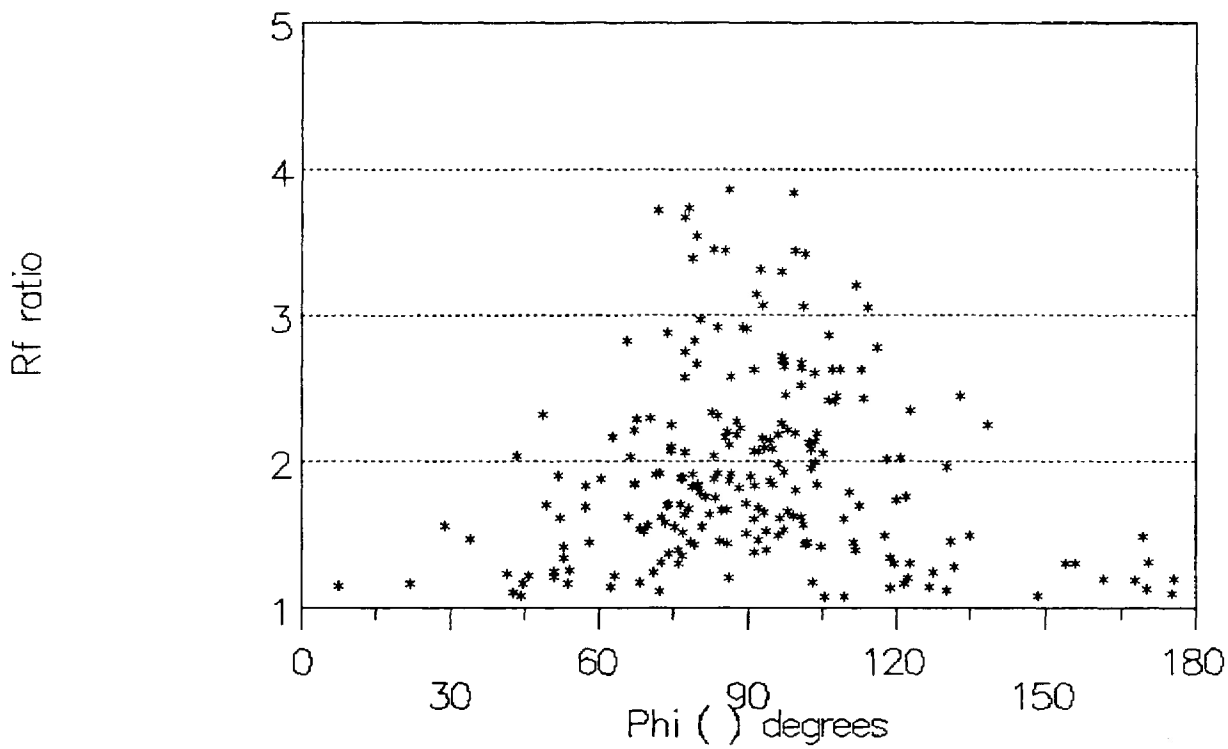
B: FILE3.RFP
n = 181

slope= 0.7069
intercept= 1.303E+00
SV9

B: FILE3.RFP
Slope of line = .7068951
y - intercept = 1.302937
Supposed initial 'unique' ratio = 1.84095
Strain ratio by linearization method = 1.553445

Rf / Phi STRAIN ANALYSIS

Sample CH9.1

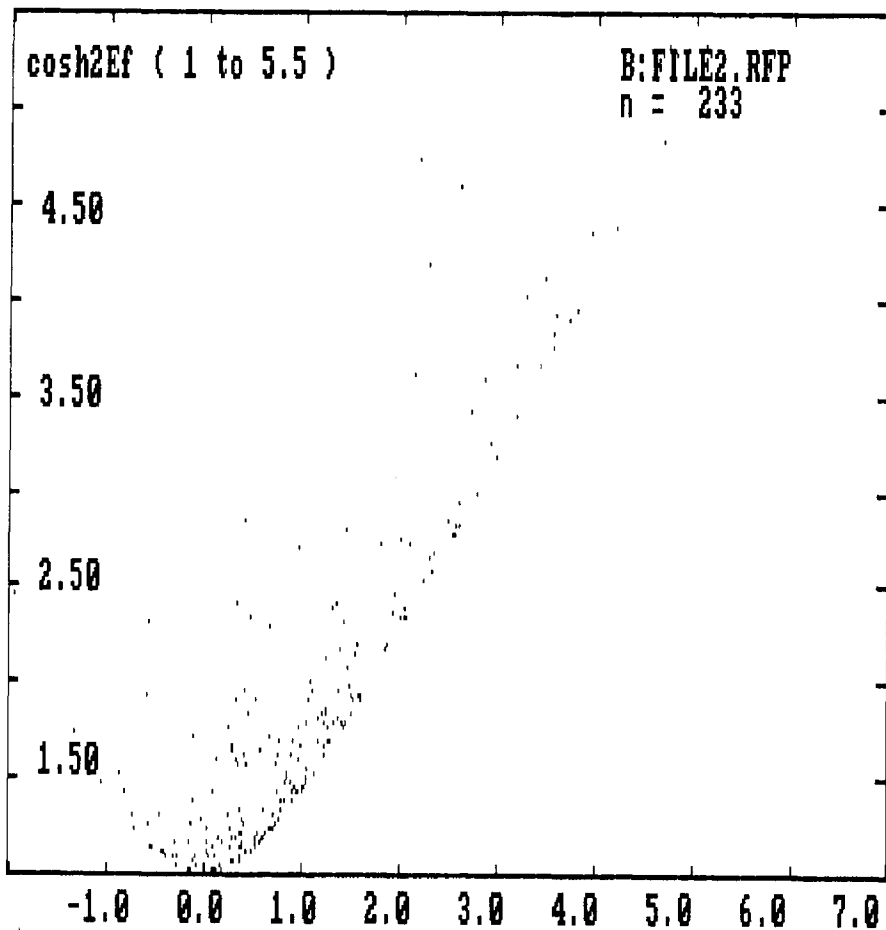
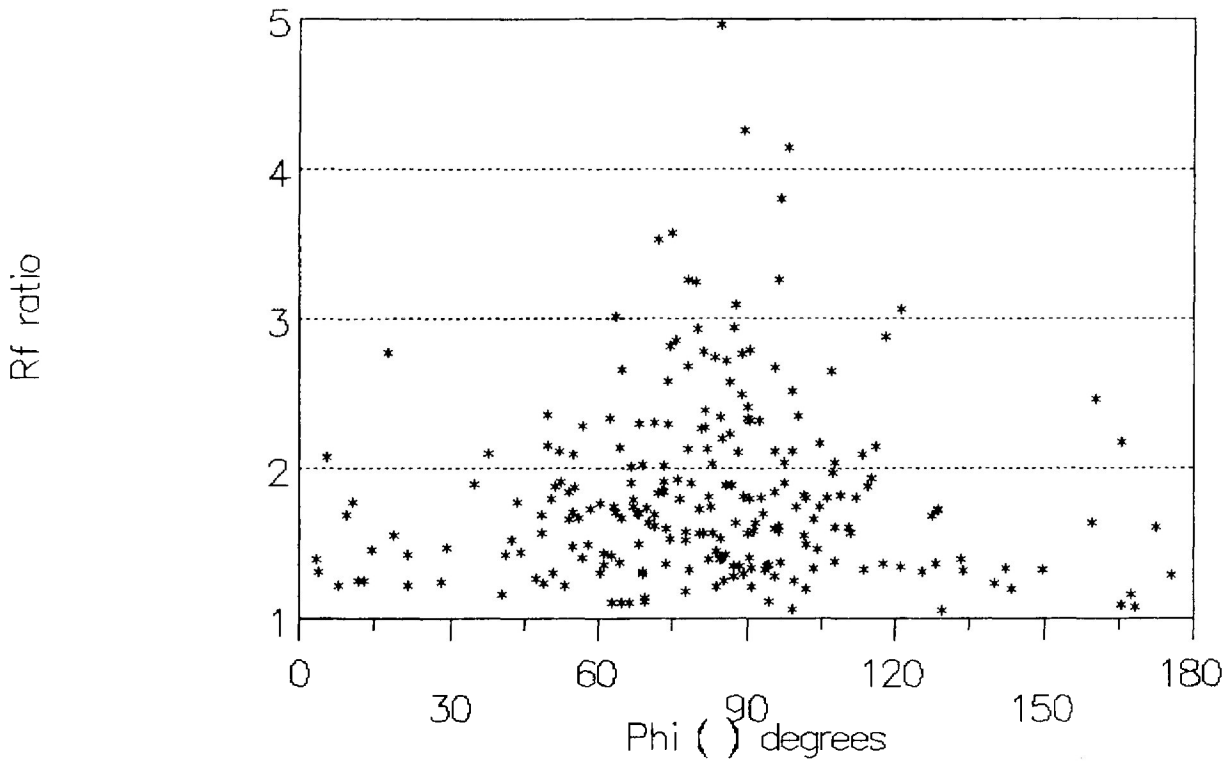


slope= 0.8516
intercept= 9.360E-01
CH9.1

B: FILE22.RFP
Slope of line = .8516381
Y - Intercept = .9360126
Supposed initial 'unique' ratio = 1.807053
Strain ratio by linearization method = 1.87957

Rf / Phi STRAIN ANALYSIS

Sample CH9.2



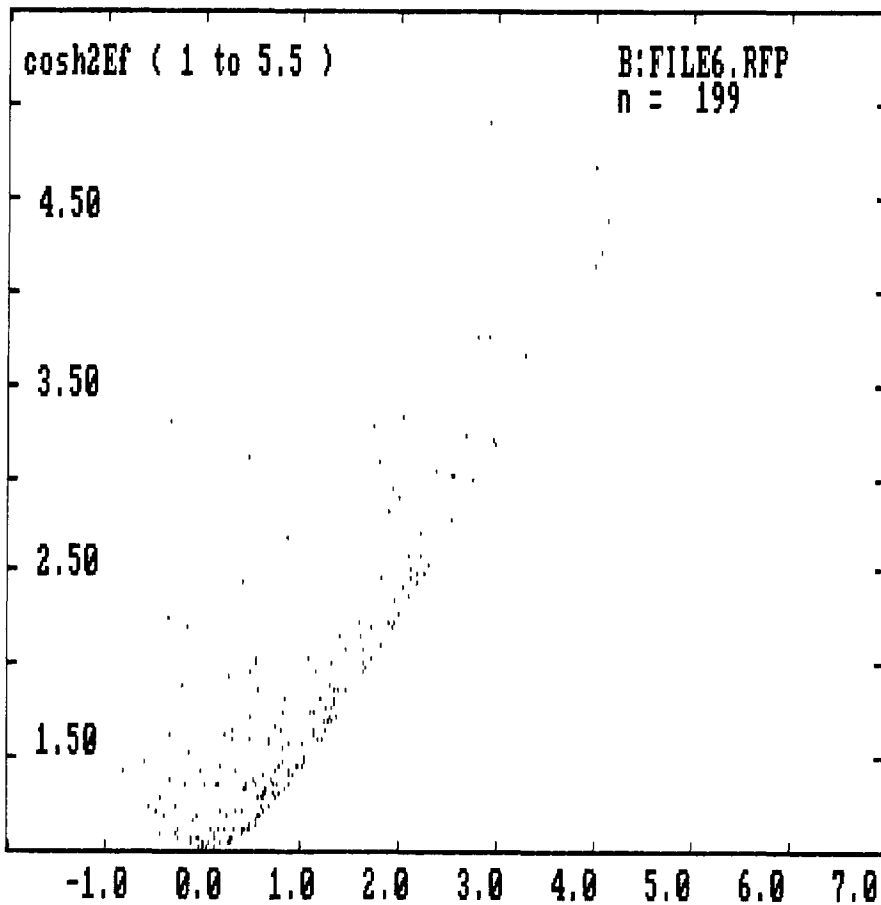
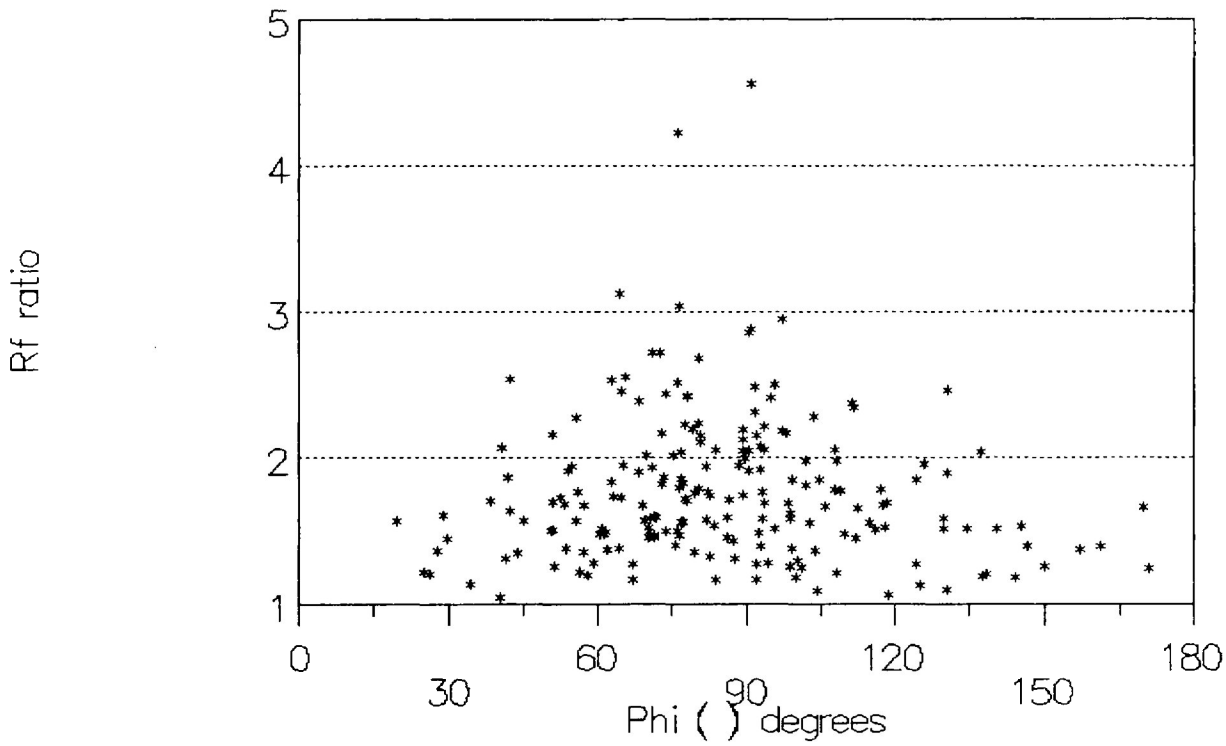
B: FILE2.RFP
n = 233

slope= 0.7384
intercept= 1.209E+00
CH9.2

B: FILE2.RFP
Slope of line = .7384125
y - intercept = 1.209098
Supposed initial 'unique' ratio = 1.811409
Strain ratio by linearization method = 1.605587

Rf / Phi STRAIN ANALYSIS

Sample CV9.2



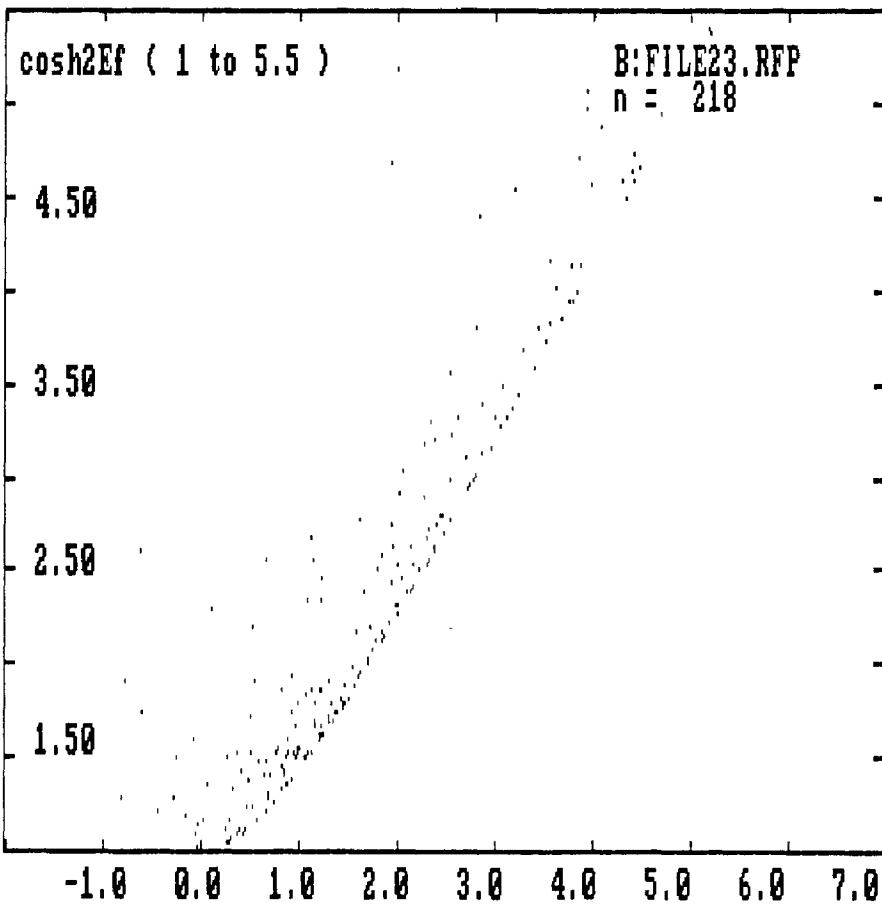
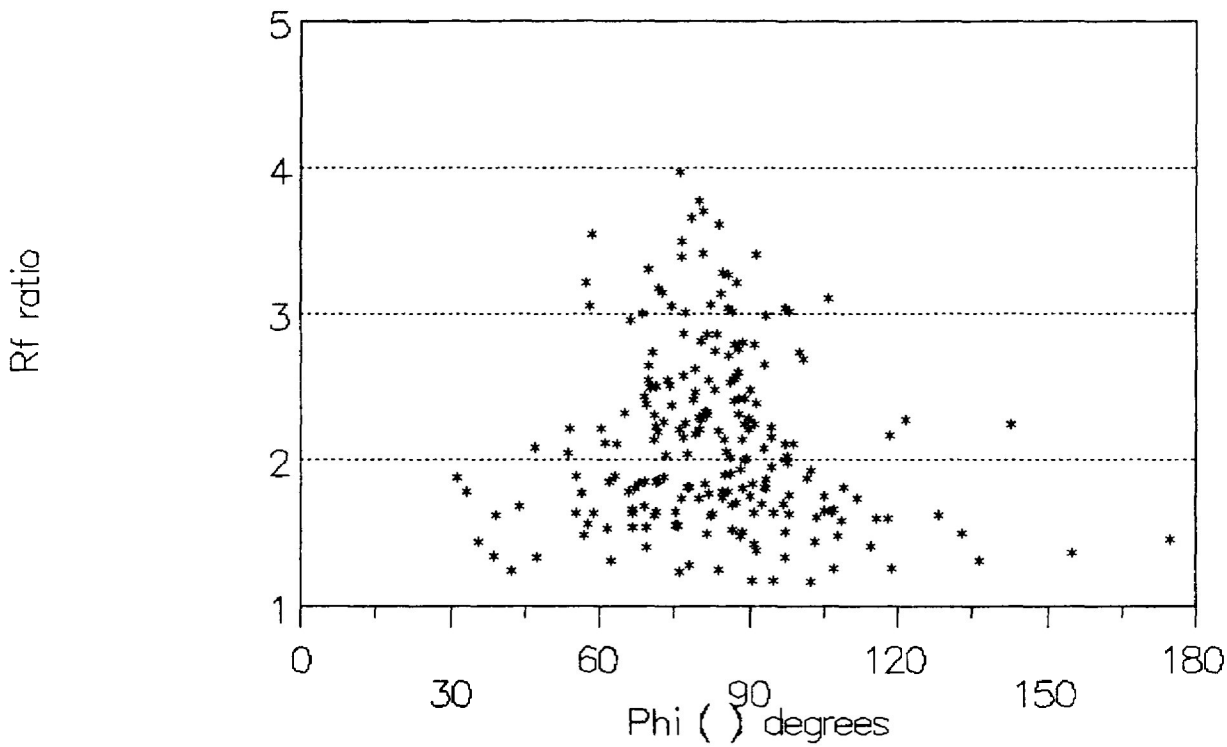
B:FILE6.RFP
n = 199

slope= 0.7799
intercept= 1.060E+00
CV9.2

B:FILE6.RFP
Slope of line = .779873
y - intercept = 1.060395
Supposed initial 'unique' ratio = 1.749728
Strain ratio by linearization method = 1.686277

Rf / Phi STRAIN ANALYSIS

Sample RS9.2-1H

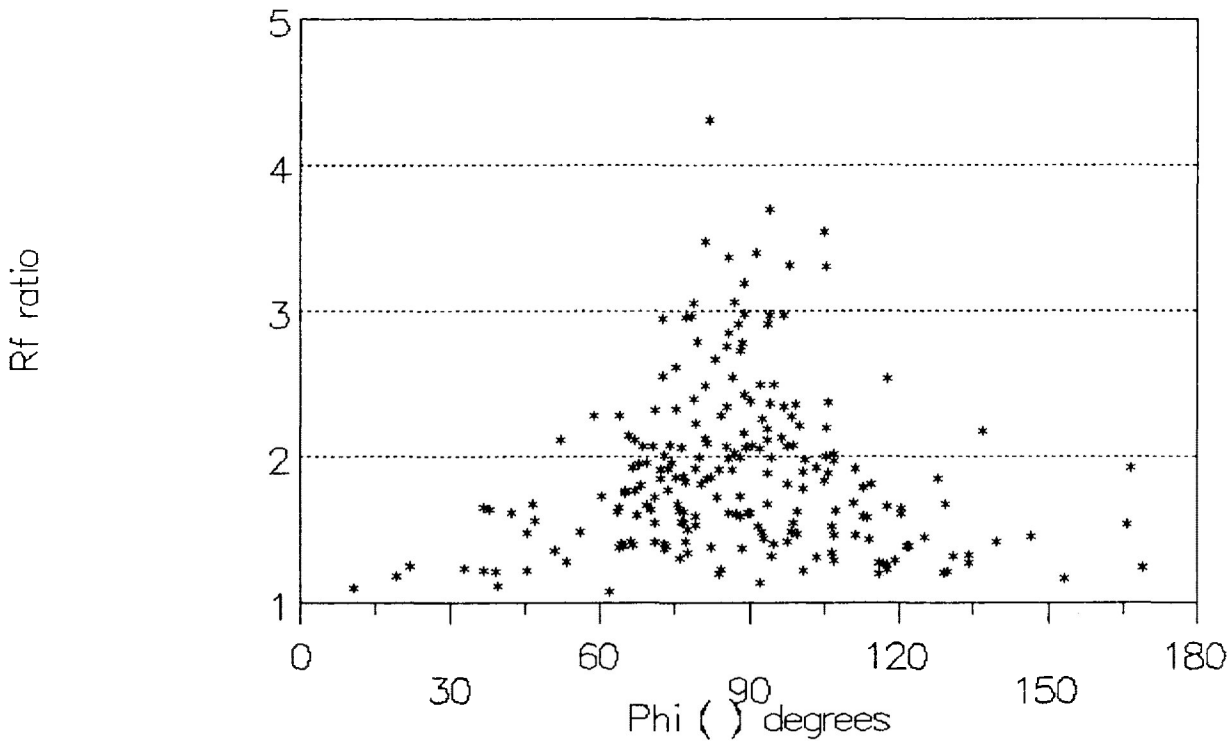


slope= 0.8610
intercept= 9.292E-01
RS9.2-1H

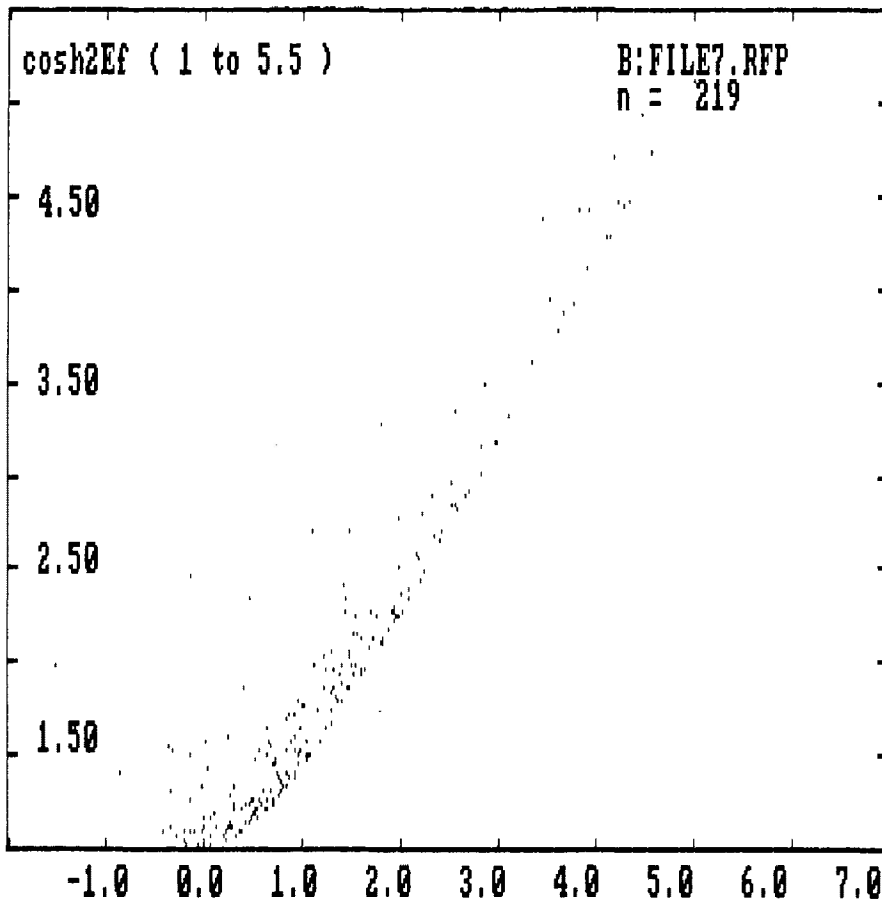
B:FILE23.RFP
Slope of line = .8609642
y - intercept = .9291612
Supposed initial 'unique' ratio = 1.831746
Strain ratio by linearization method = 1.912726

Rf / Phi STRAIN ANALYSIS

Sample RS9.2-1V



*
n = 219

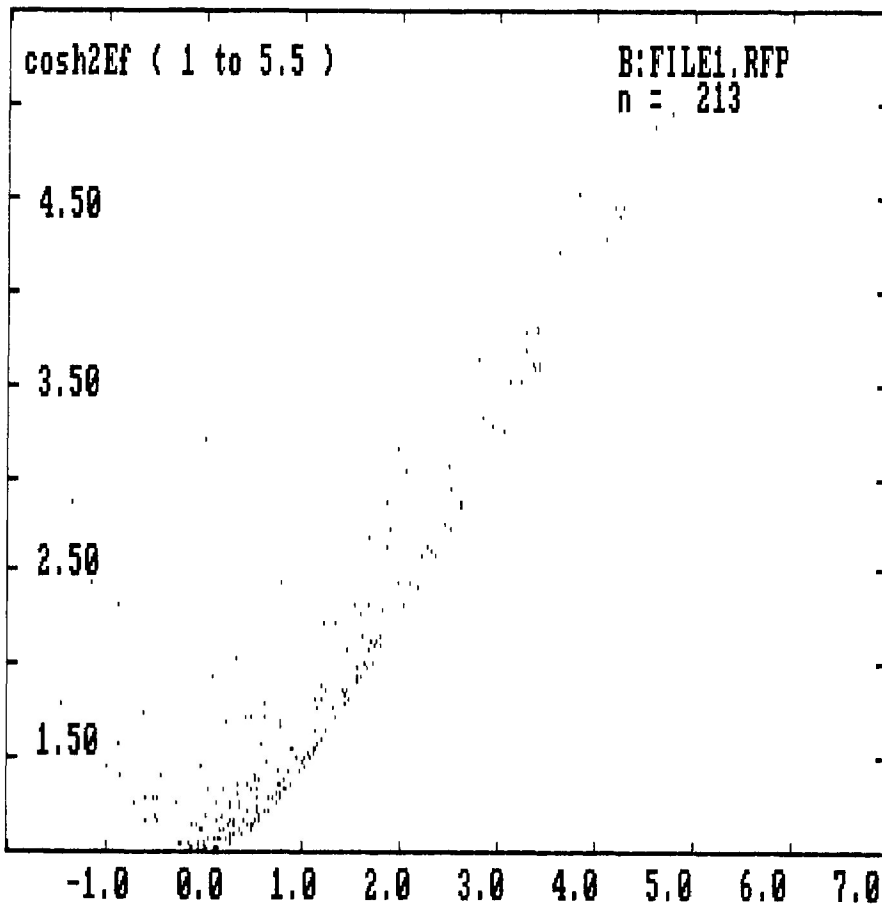
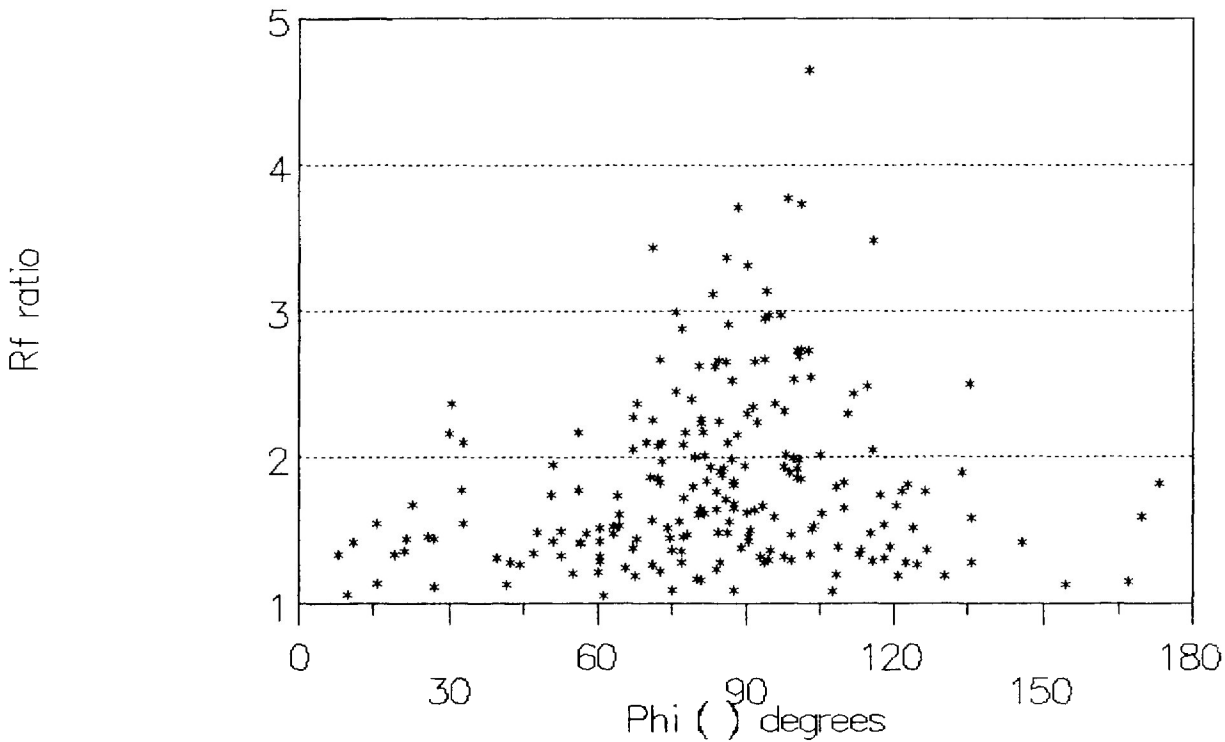


slope= 0.8714
intercept= 8.678E-01
RS9.2-1V

B: FILE7.RFP
Slope of line = .8713887
y - intercept = .8678274
Supposed initial 'unique' ratio = 1.796688
Strain ratio by linearization method = 1.953085

Rf / Phi STRAIN ANALYSIS

Sample RS9.2-2H



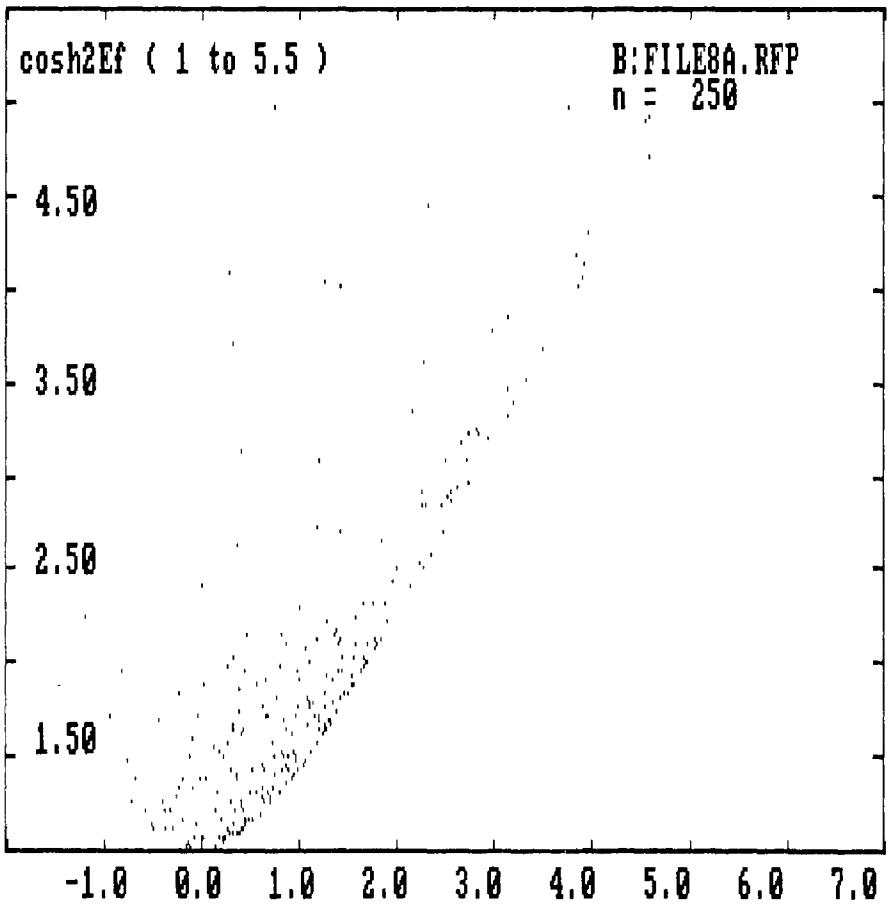
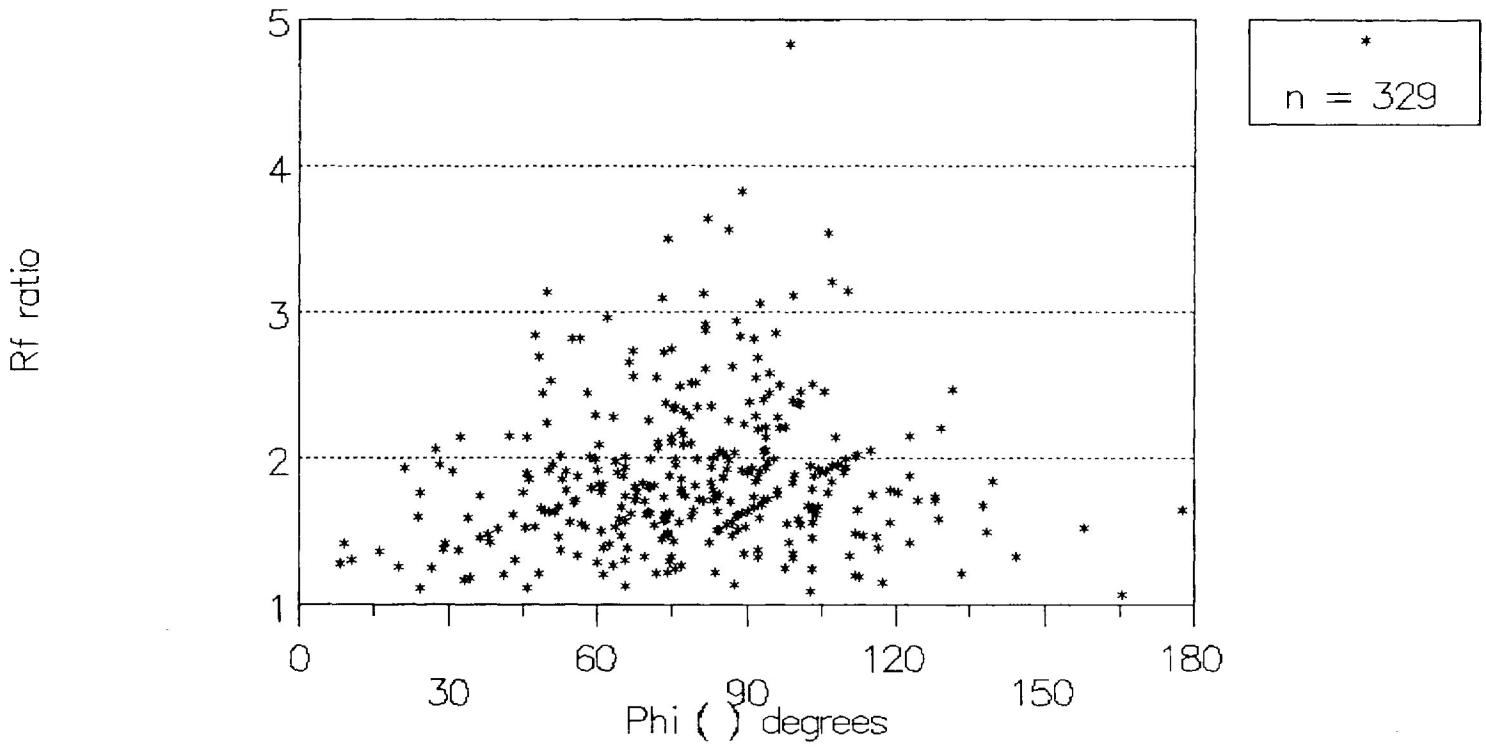
B:FILE1.RFP
n = 213

slope= 0.7851
intercept= 1.070E+00
RS9.2-2H

B:FILE1.RFP
Slope of line = .7850639
y - intercept = 1.070351
Supposed initial 'unique' ratio = 1.77123
Strain ratio by linearization method = 1.697603

Rf / Phi STRAIN ANALYSIS

Sample RS9.2-2V

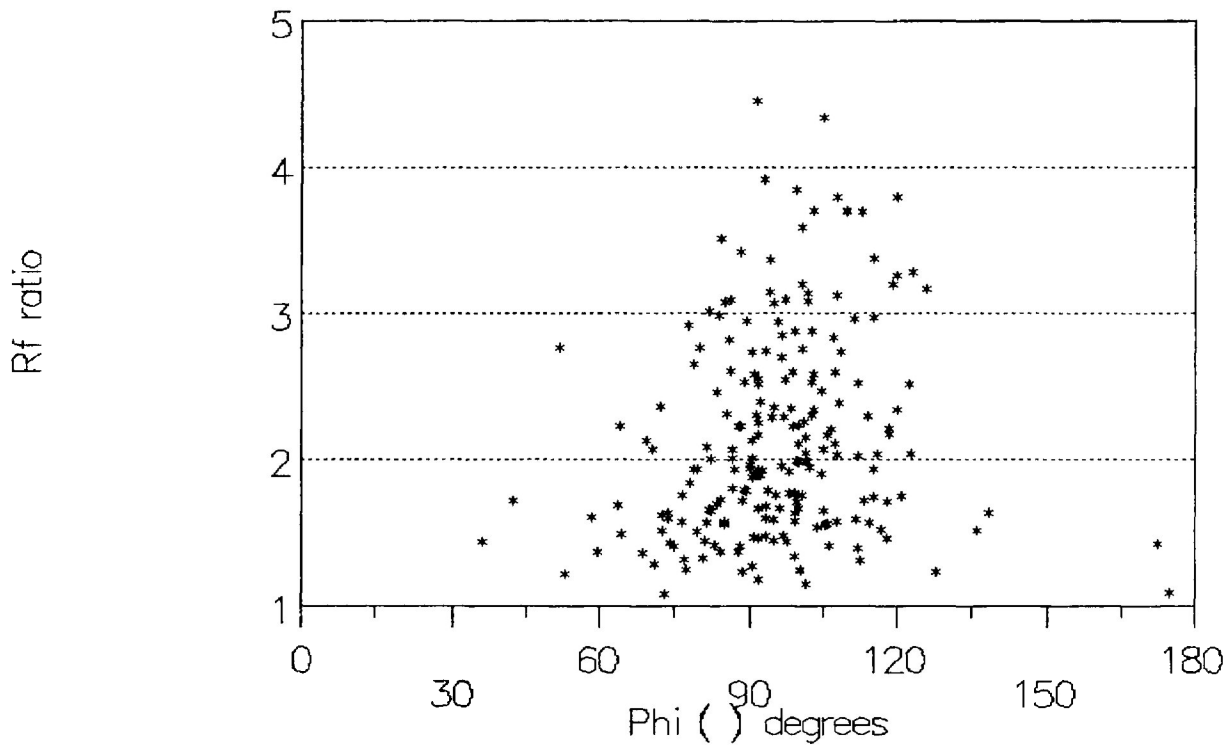


slope = 0.7572
 intercept = 1.171E+00
RS9.2-2V

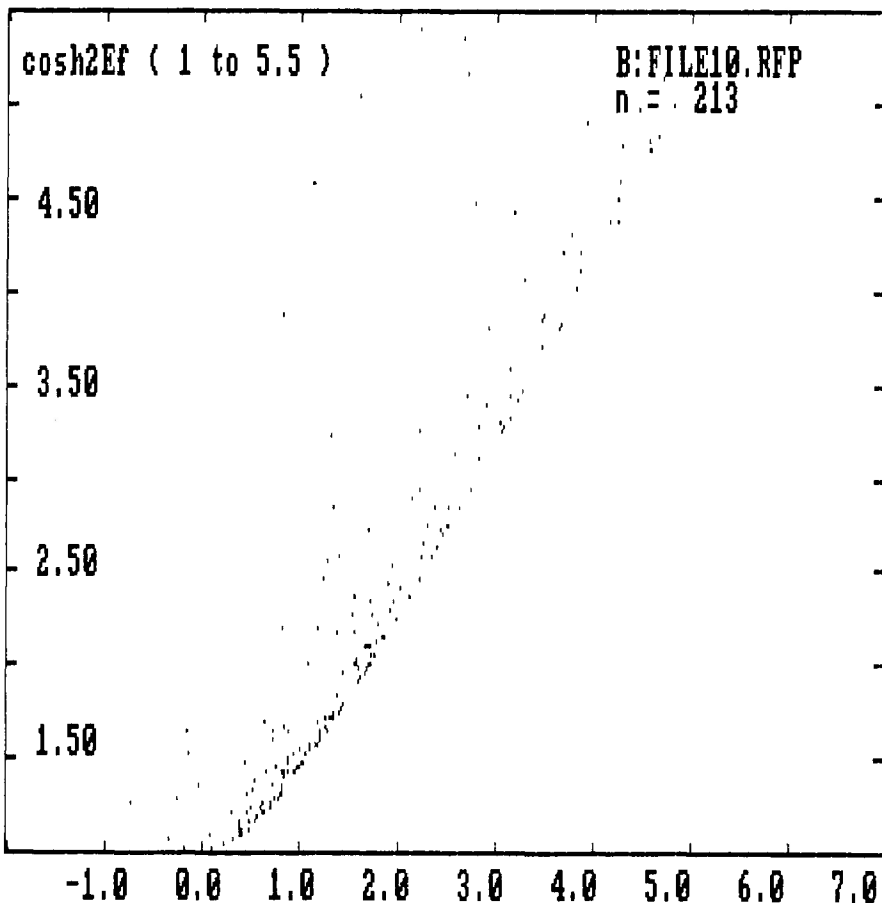
B:\FILE8A.RFP
 Slope of line = .7572378
 Y - intercept = 1.170978
 Supposed initial 'unique' ratio = 1.810352
 Strain ratio by linearization method = 1.640359

Rf / Phi STRAIN ANALYSIS

Sample RS9.25H



*
n = 213

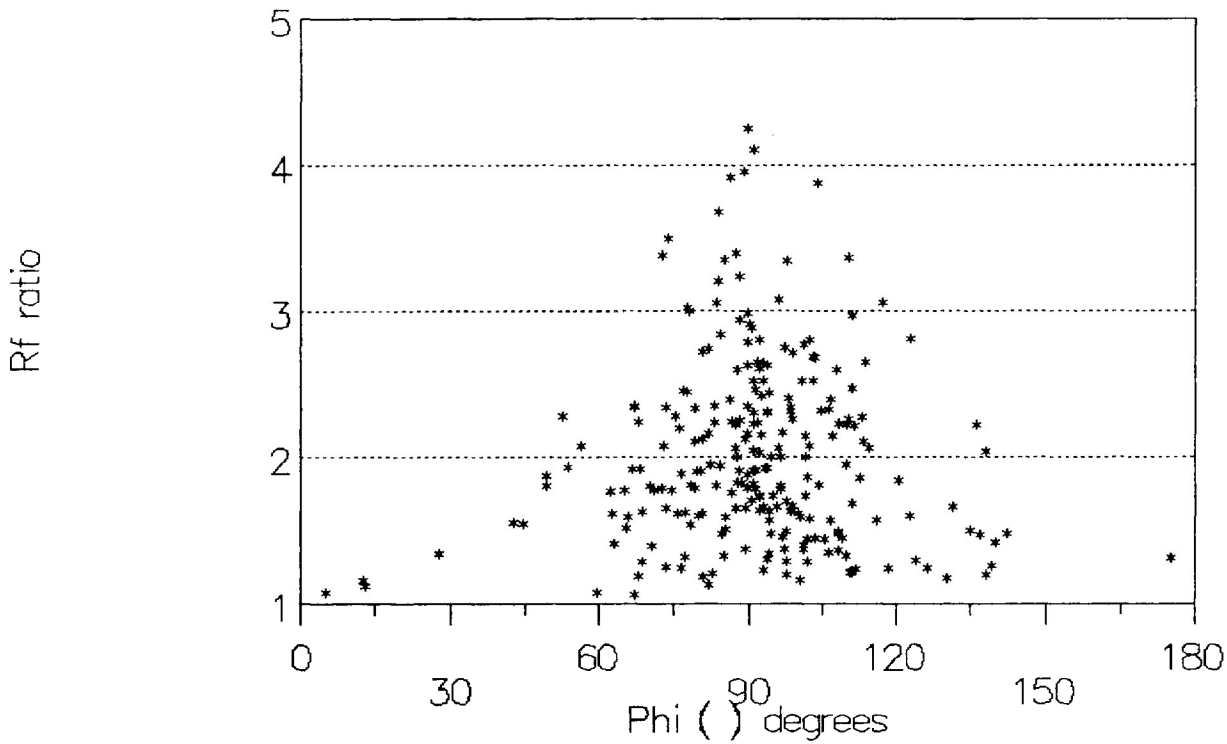


slope= 0.9528
intercept= 7.340E-01
RS9.25H

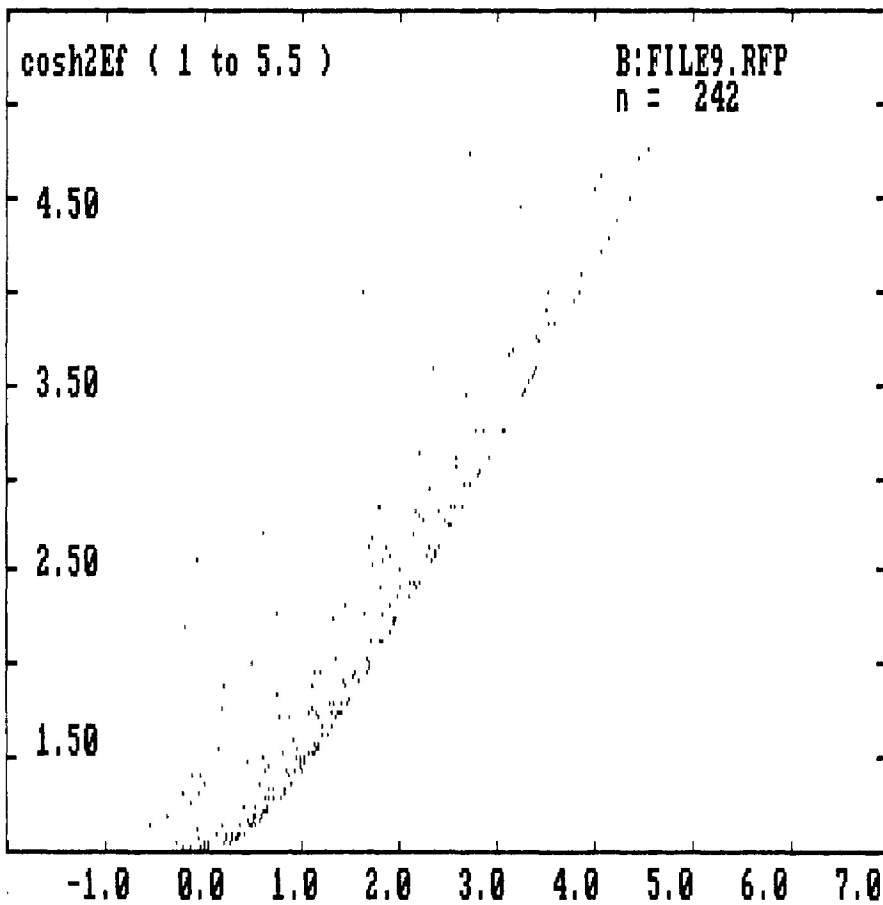
B: FILE10.RFP
Slope of line = .9528133
y - intercept = .7340142
Supposed initial 'unique' ratio = 2.149331
Strain ratio by linearization method = 2.536357

Rf / Phi STRAIN ANALYSIS

Sample RS9.25V



n = 242

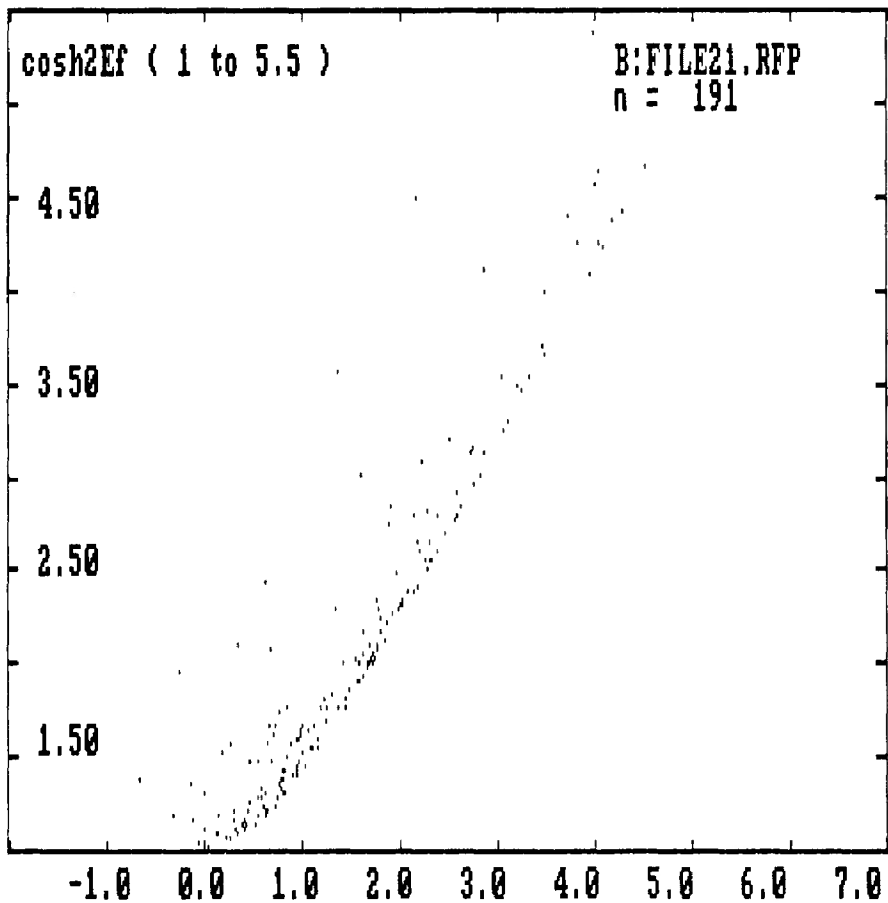
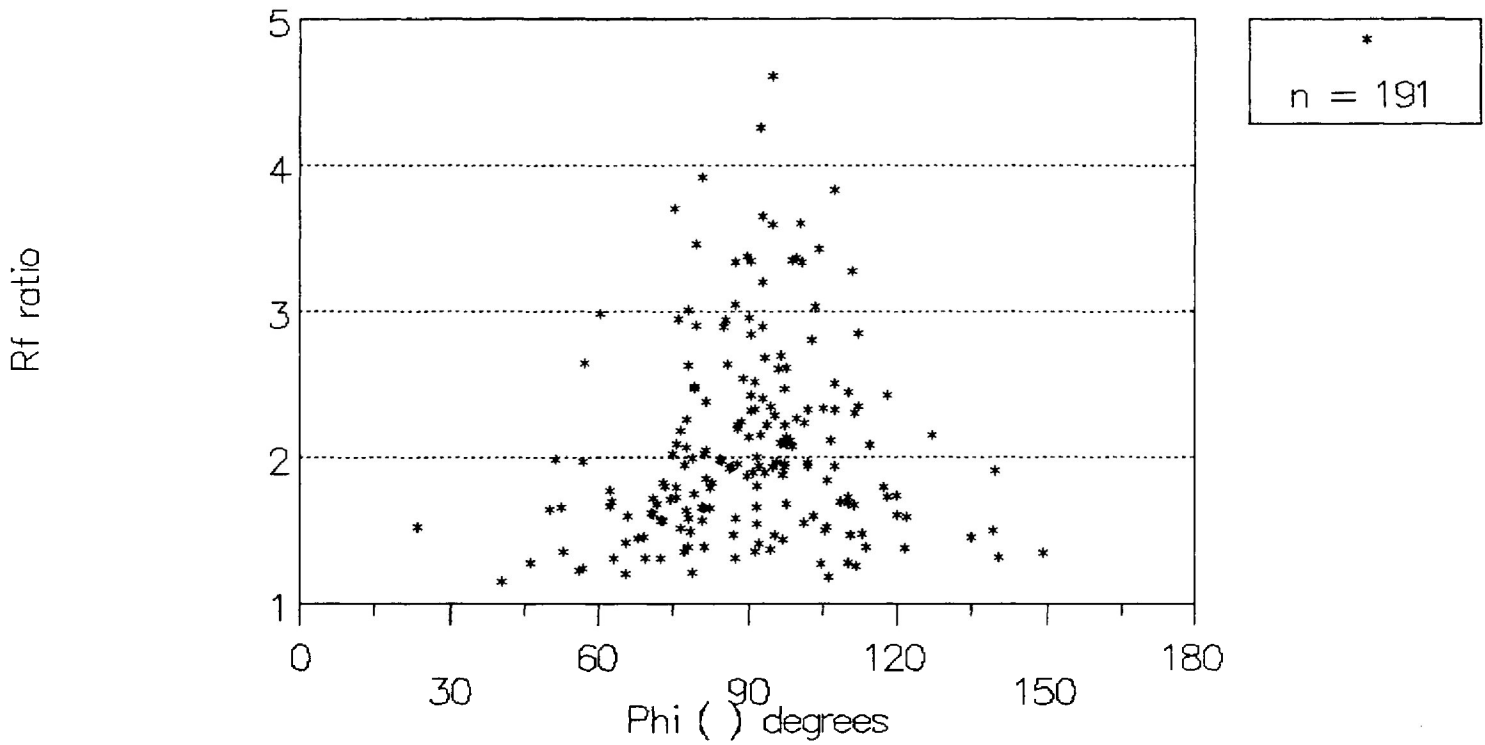


RS9.25V
slope = 0.8850
intercept = 8.020E-01

B:FILE9.RFP
Slope of line = .8849573
y - intercept = .8020366
Supposed initial 'unique' ratio = 1.767654
Strain ratio by linearization method = 2.011919

Rf / Phi STRAIN ANALYSIS

Sample CH9.3

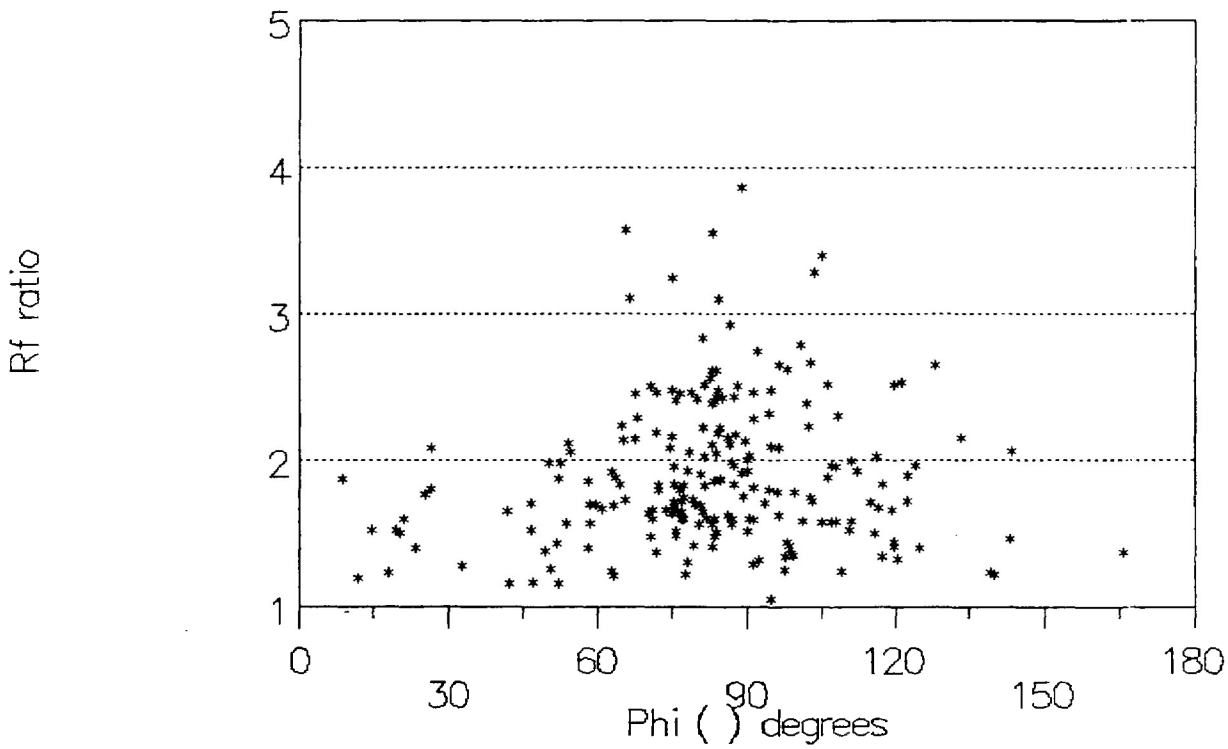


slope= 0.9003
intercept= 7.716E-01
CH9.3

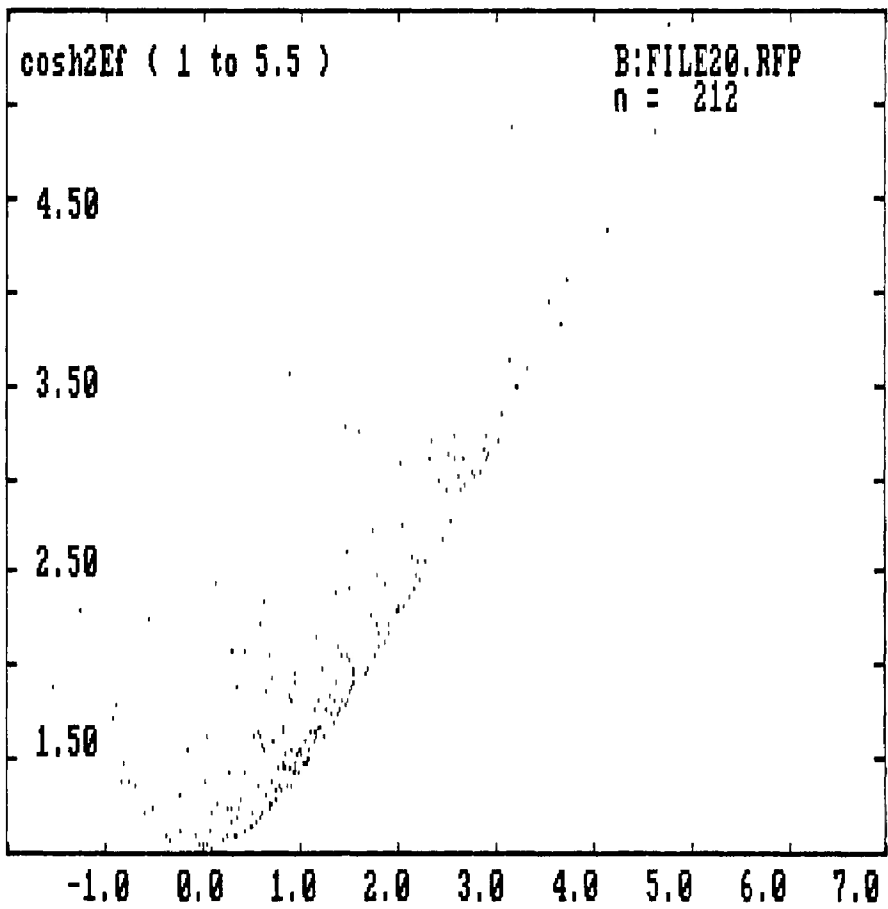
B:FILE21.RFP
Slope of line = .9002736
Y - intercept = .7716093
Strain ratio by linearization method = 2.089303
Supposed initial 'unique' ratio = 1.798876

Rf / Phi STRAIN ANALYSIS

Sample CV9.3



n = 212

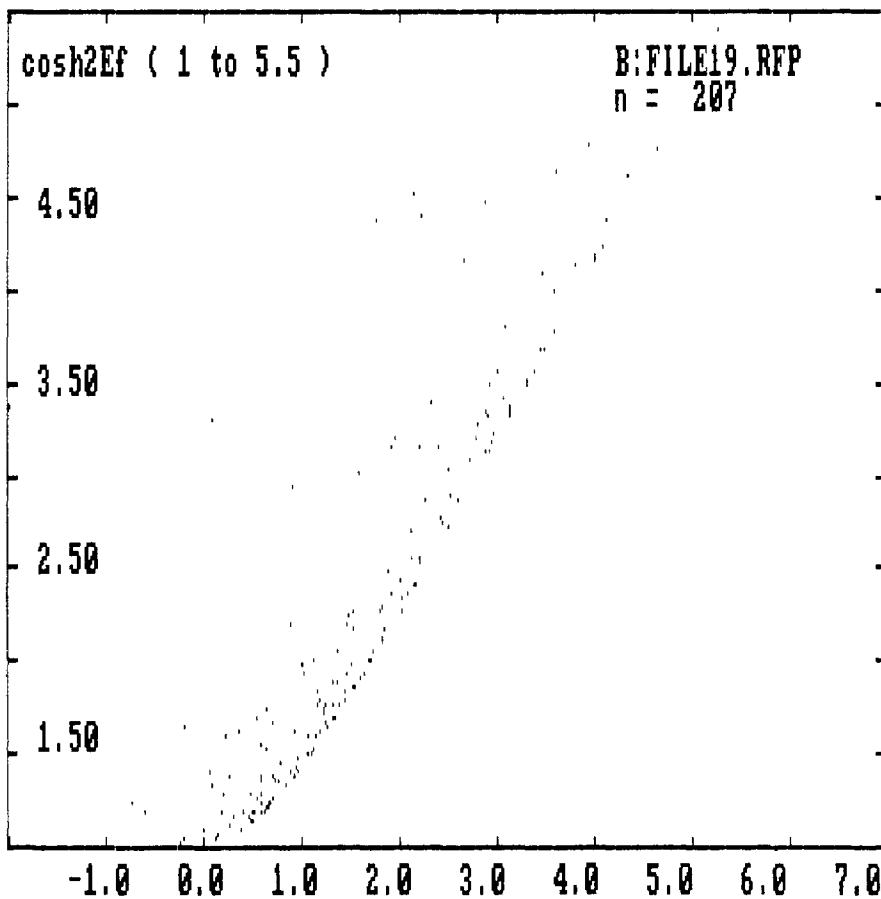
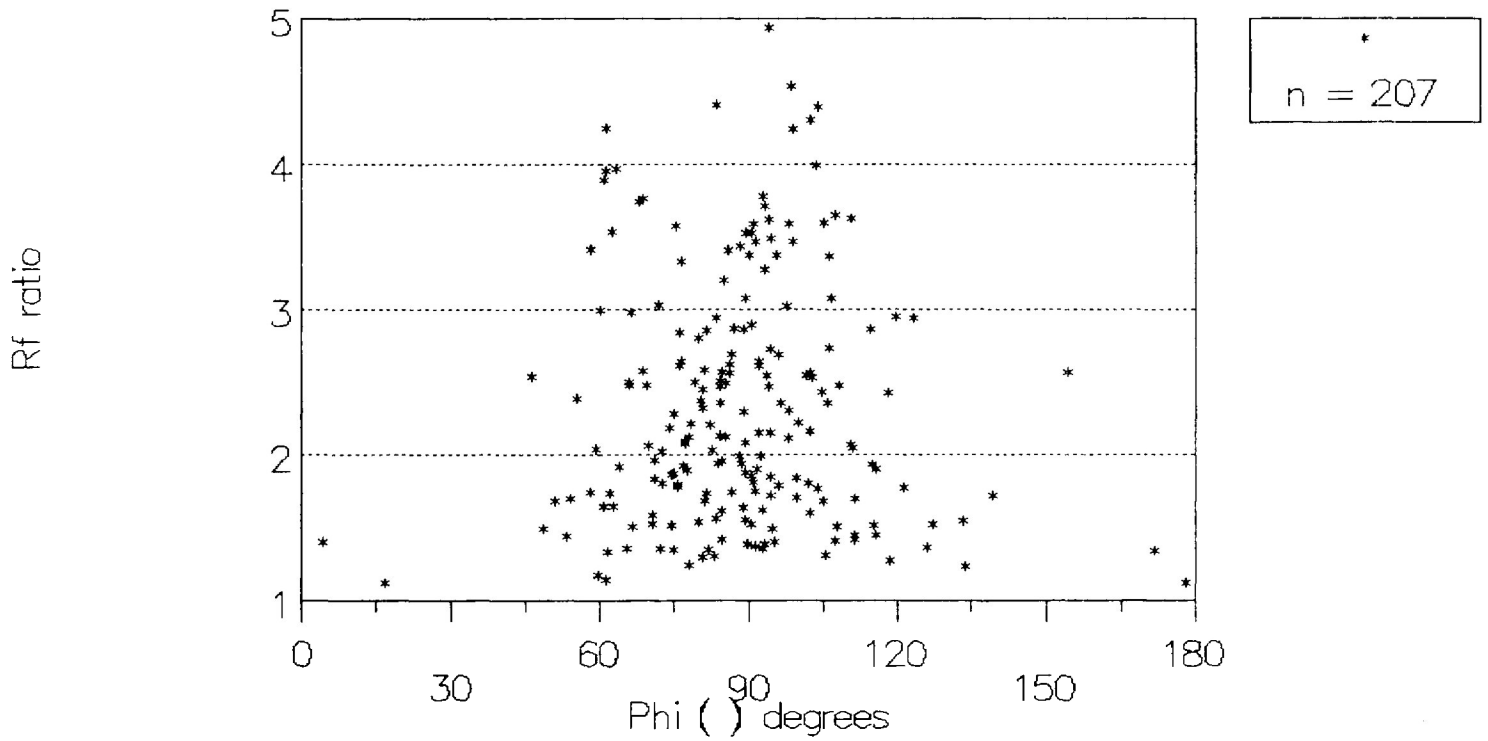


slope= 0.7286
intercept= 1.124E+00
CV9.3

B:FILE20.RFP
Slope of line = .7285603
y - intercept = 1.123952
Supposed initial 'unique' ratio = 1.715158
Strain ratio by linearization method = 1.588557

Rf / Phi STRAIN ANALYSIS

Sample CH9.4

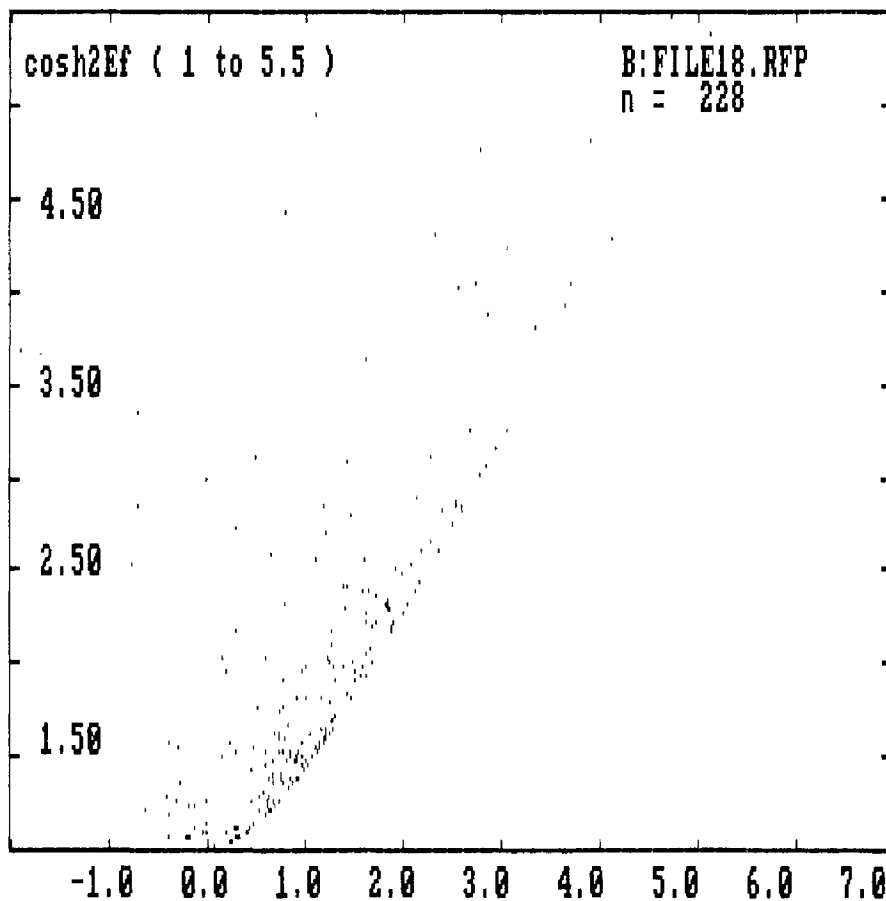
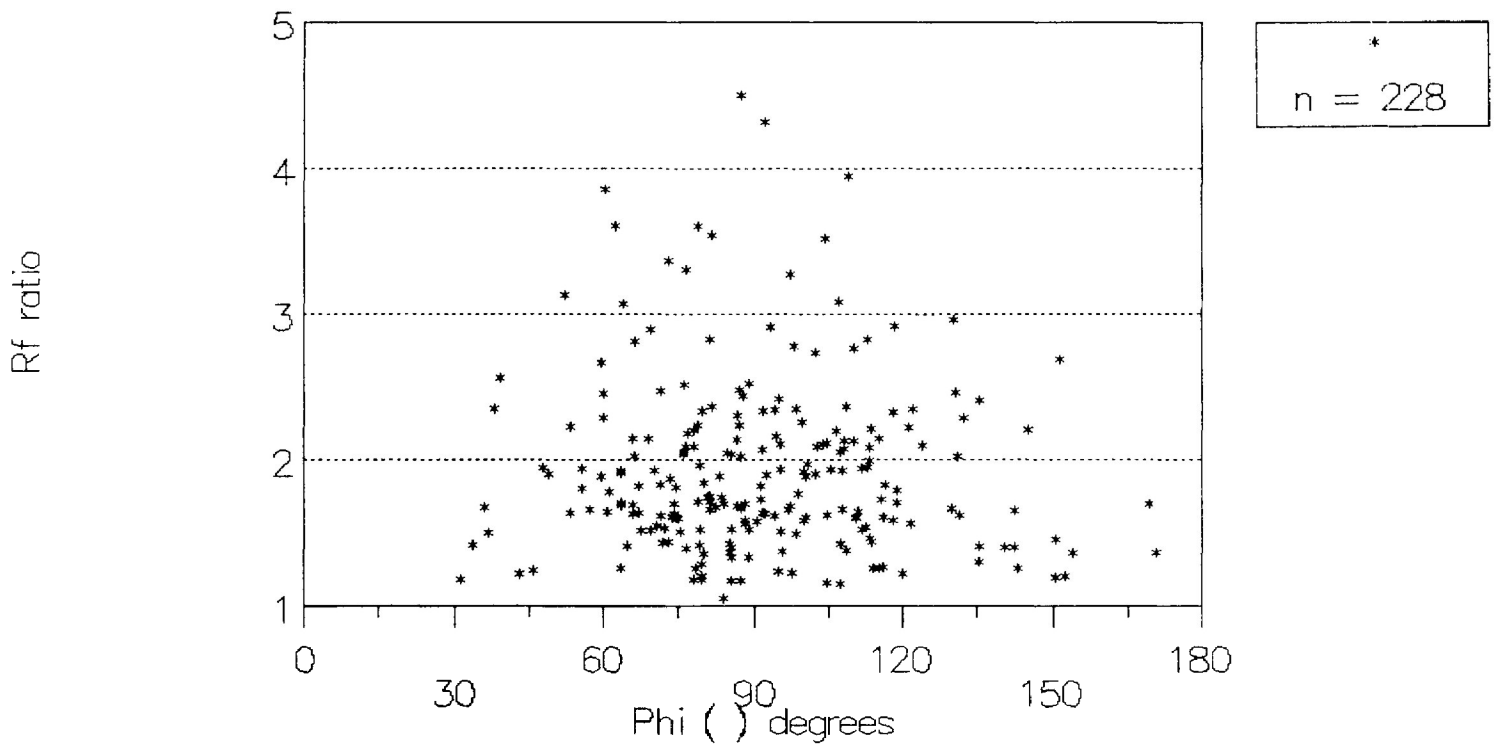


slope= 0.9466
intercept= 8.830E-01
CH9.4

B: FILE19.RFP
Slope of line = .9466283
y - intercept = .8830011
Supposed initial 'unique' ratio = 2.300084
Strain ratio by linearization method = 2.457615

Rf / Phi STRAIN ANALYSIS

Sample CV9.4



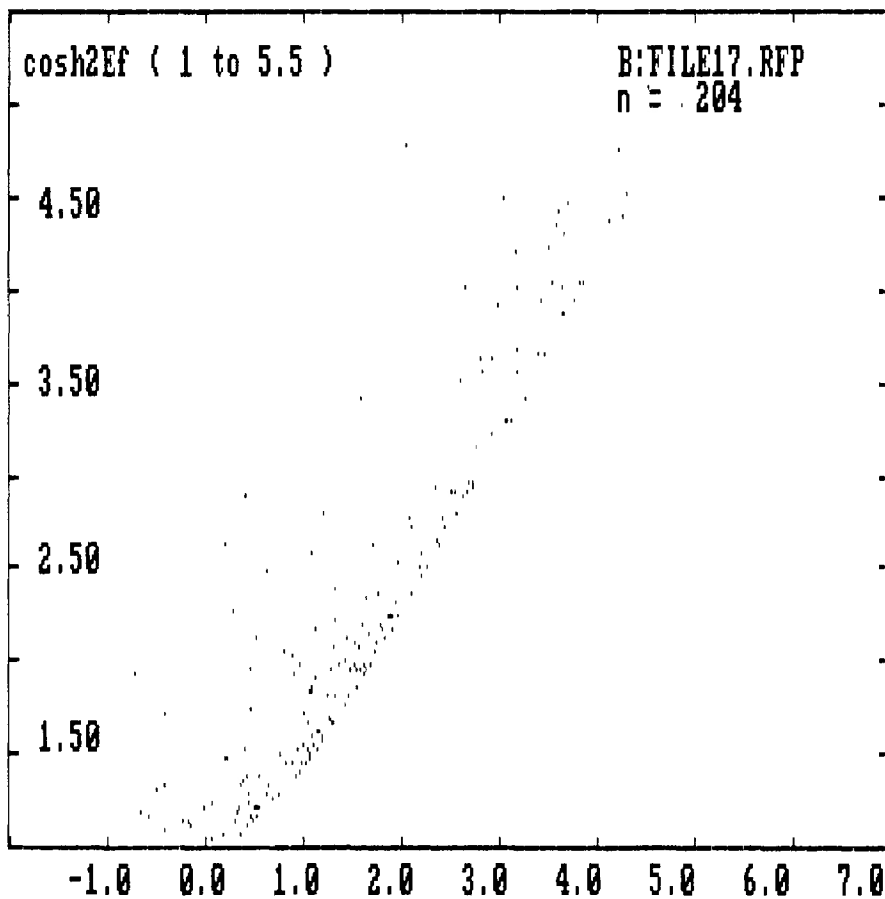
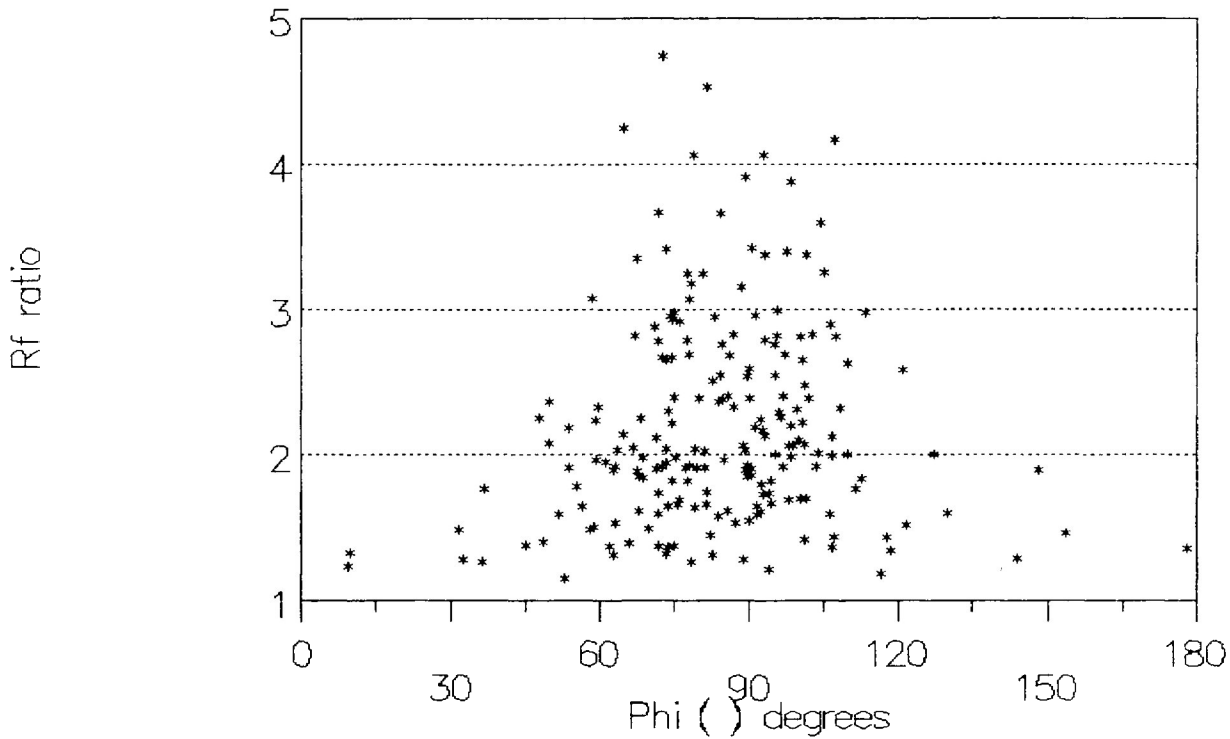
B: FILE18.RFP
n = 228

slope= 0.8585
intercept= 1.074E+00
CV9.4

B: FILE18.RFP
Slope of line = .8585091
y - intercept = 1.073693
Supposed initial 'unique' ratio = 1.983256
Strain ratio by linearization method = 1.903746

Rf / Phi STRAIN ANALYSIS

Sample RS9.4-3H

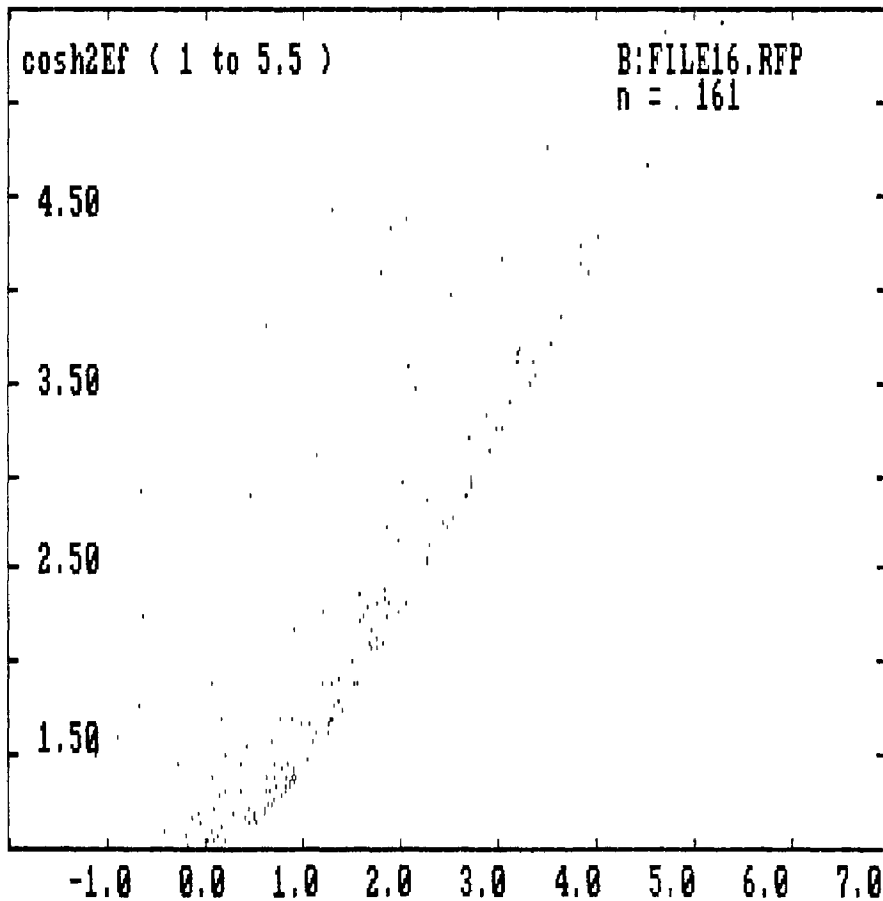
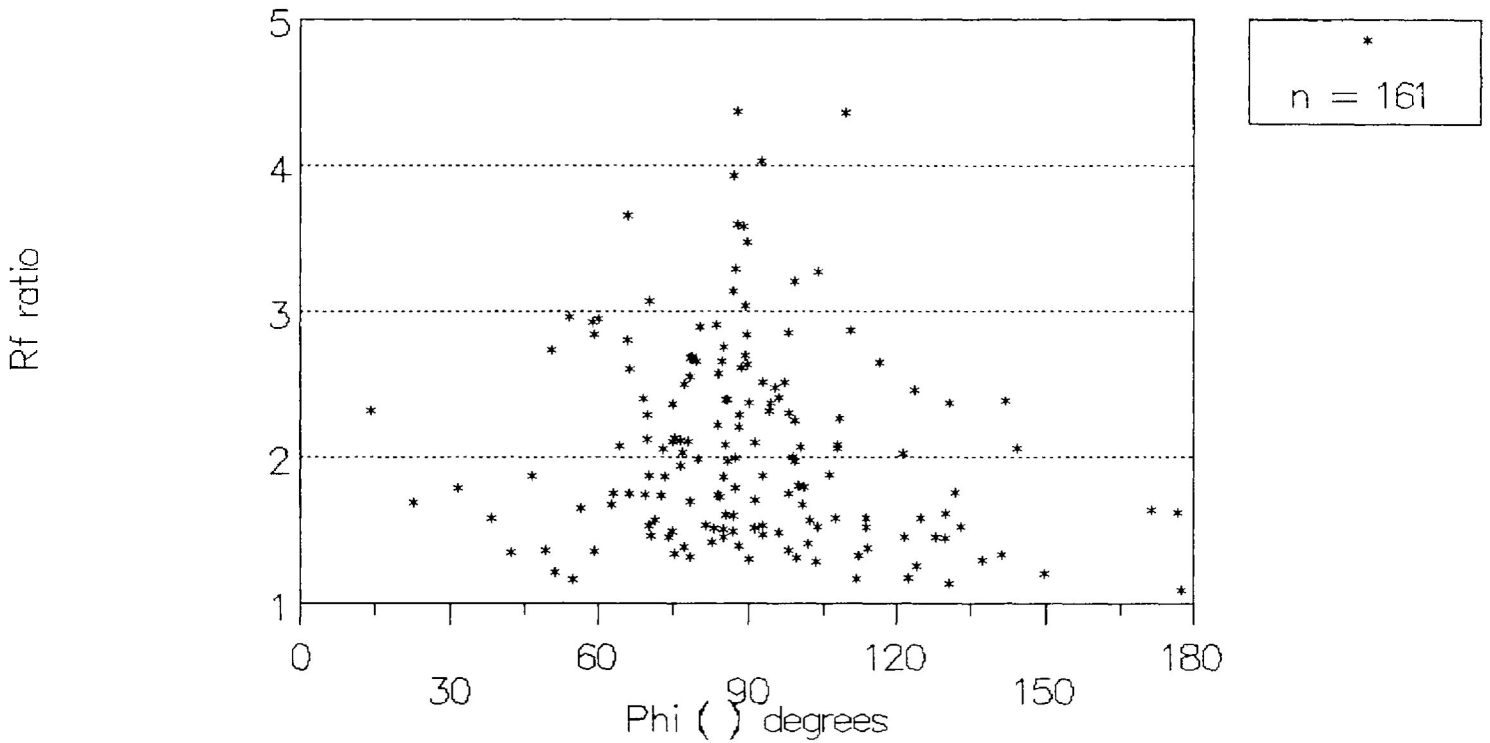


slope = 0.9696
 intercept = 7.811E-01
RS9.4-3H

R:FILE17.RFP
 Slope of line = .9695873
 y - intercept = .7811351
 Suggested initial 'unique' ratio = 2.494075
 Strain ratio by linearization method = 2.836335

Rf / Phi STRAIN ANALYSIS

Sample RS9.4-3V

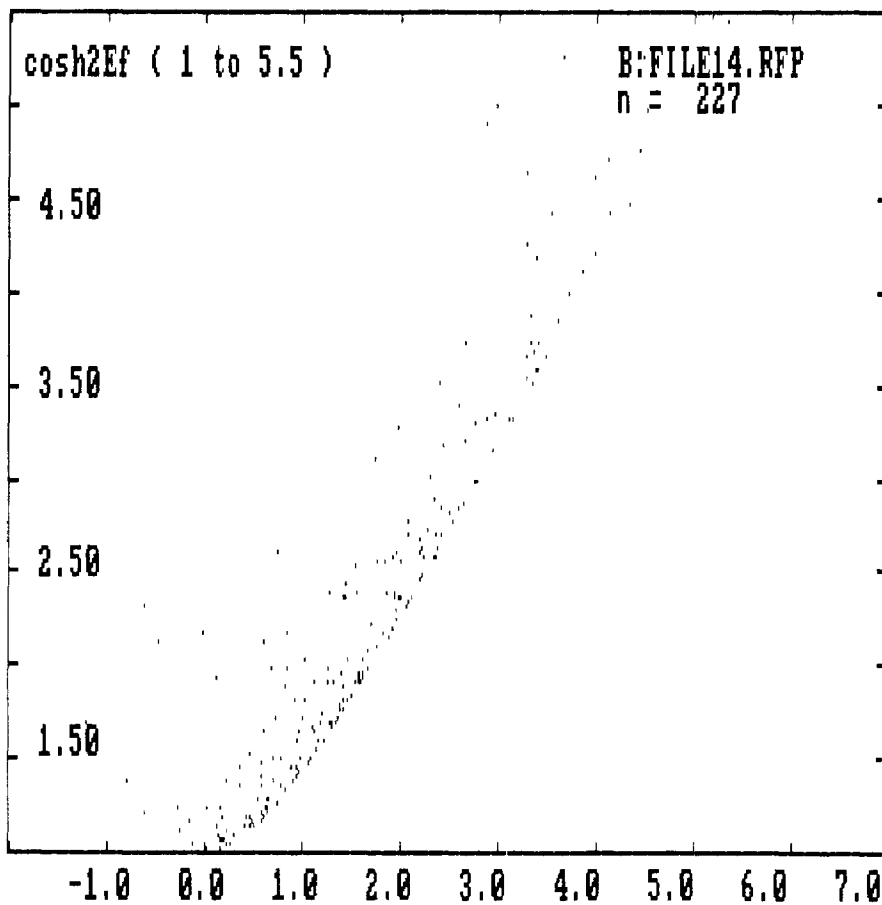
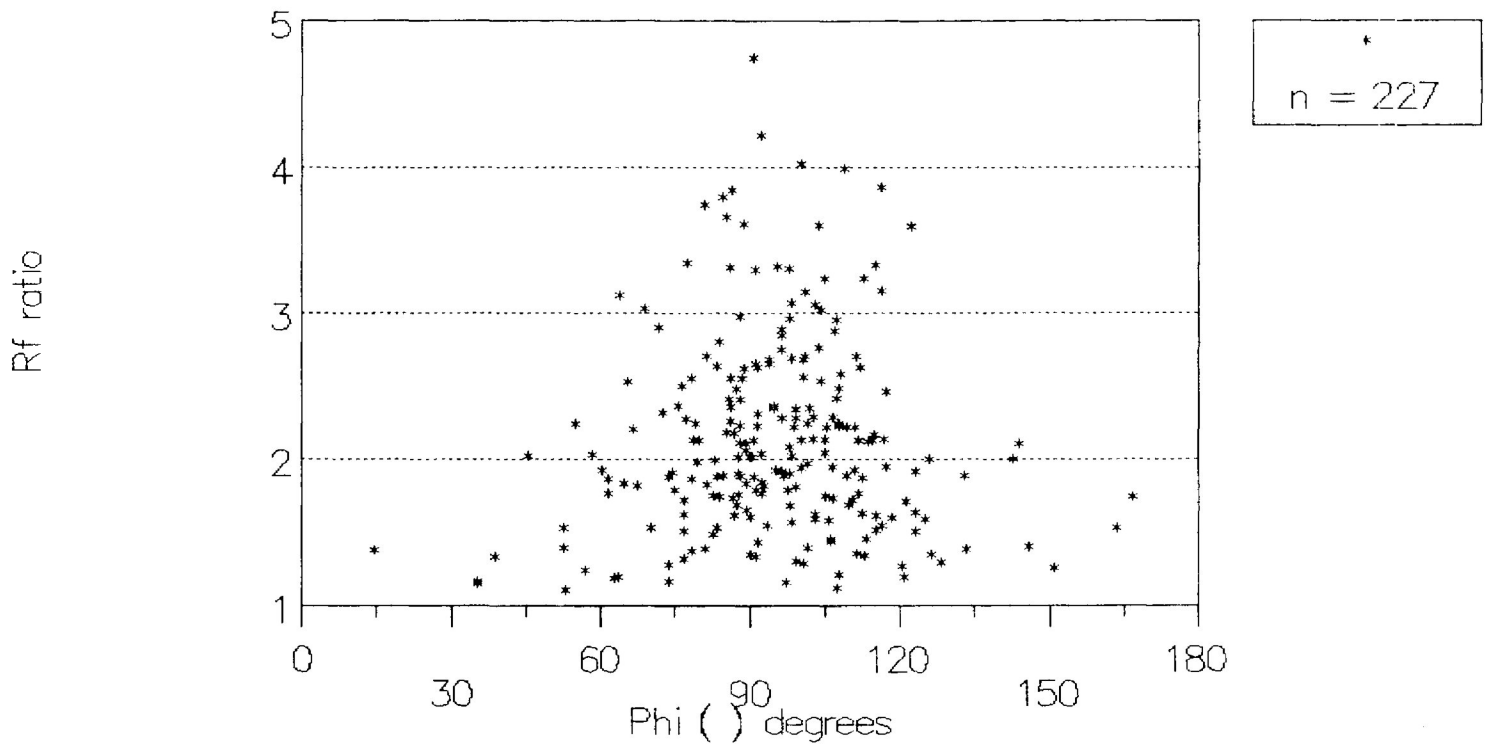


slope = 0.8080
intercept = 1.128E+00
RS9.4-3V

B:FILE16.RFP
Slope of line = .8079651
Y - Intercept = 1.12806
Supposed initial 'unique' ratio = 1.883347
Strain ratio by linearization method = 1.751671

Rf / Phi STRAIN ANALYSIS

Sample RS10.05H



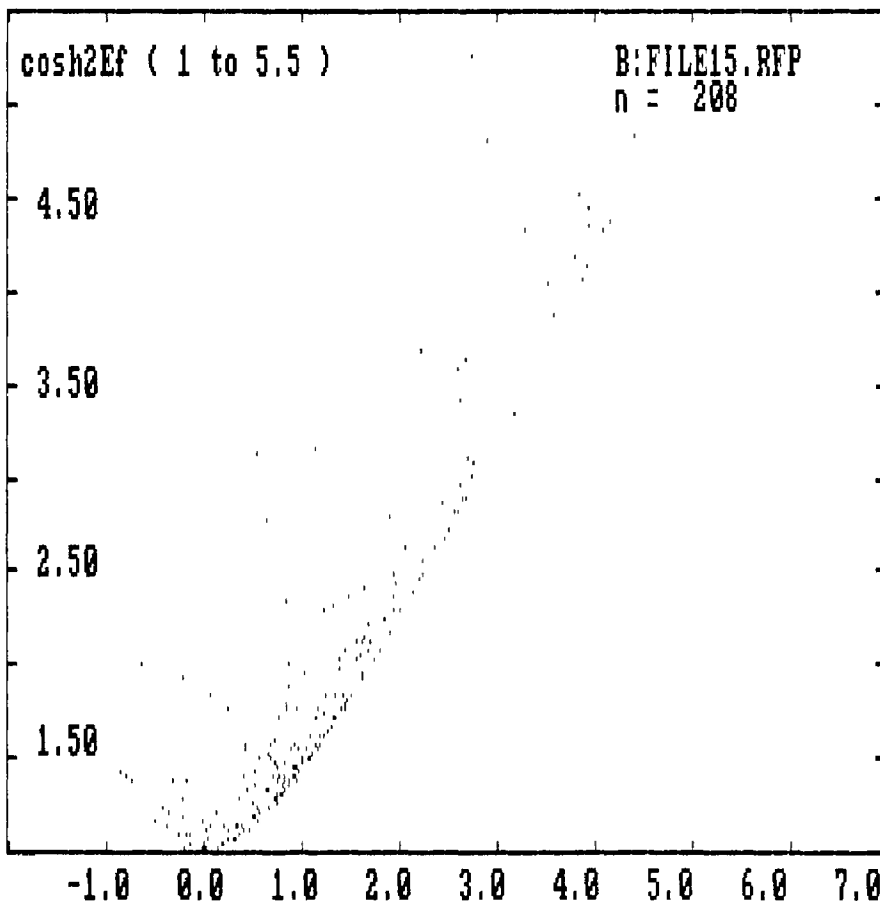
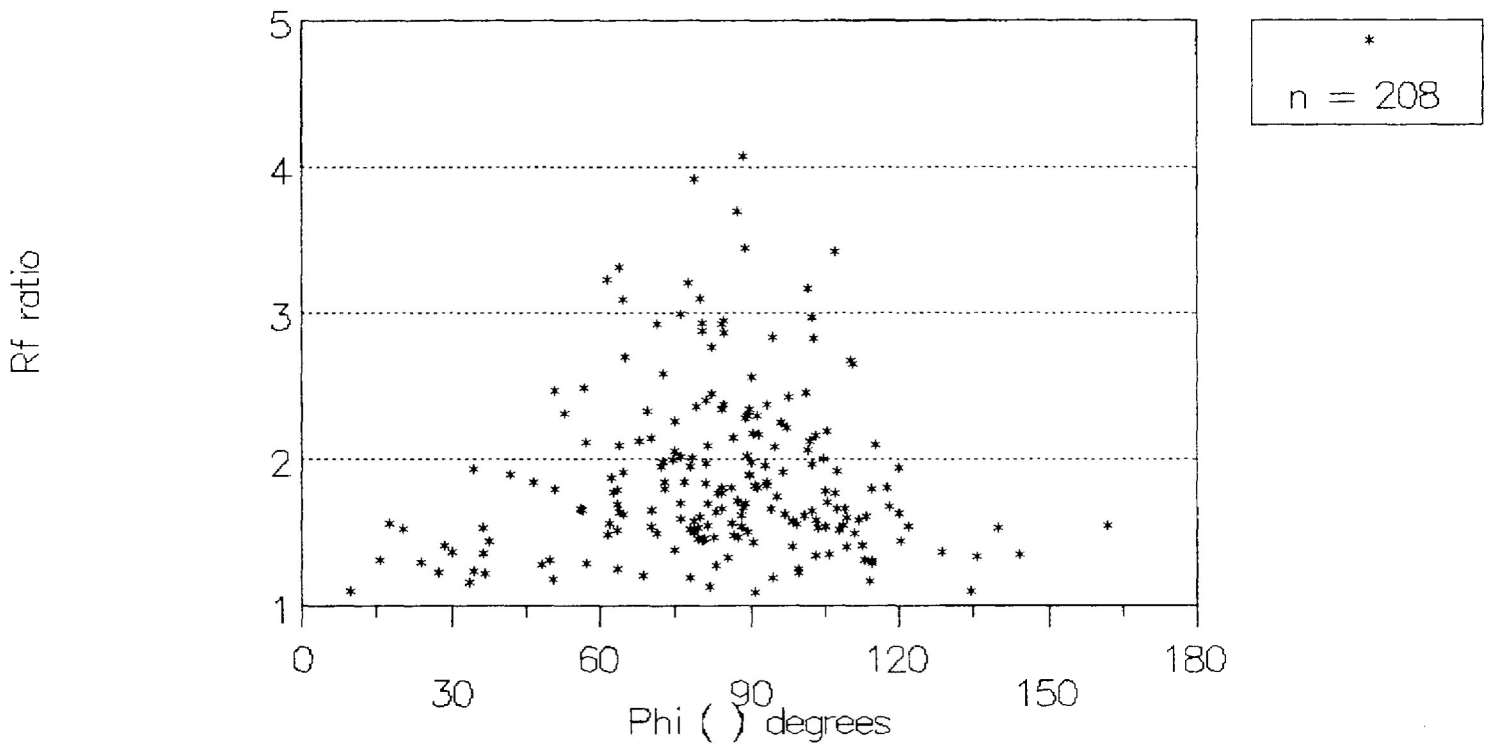
B:FILE14.RFP
n = 227

slope= 0.8962
intercept= 8.679E-01
RS10.05H

B:FILE14.RFP
Slope of line = .8962349
y - intercept = .8678796
supposed initial 'unique' ratio = 1.907409
Strain ratio by Linearization method = 2.06757

Rf / Phi STRAIN ANALYSIS

Sample RS10.05V

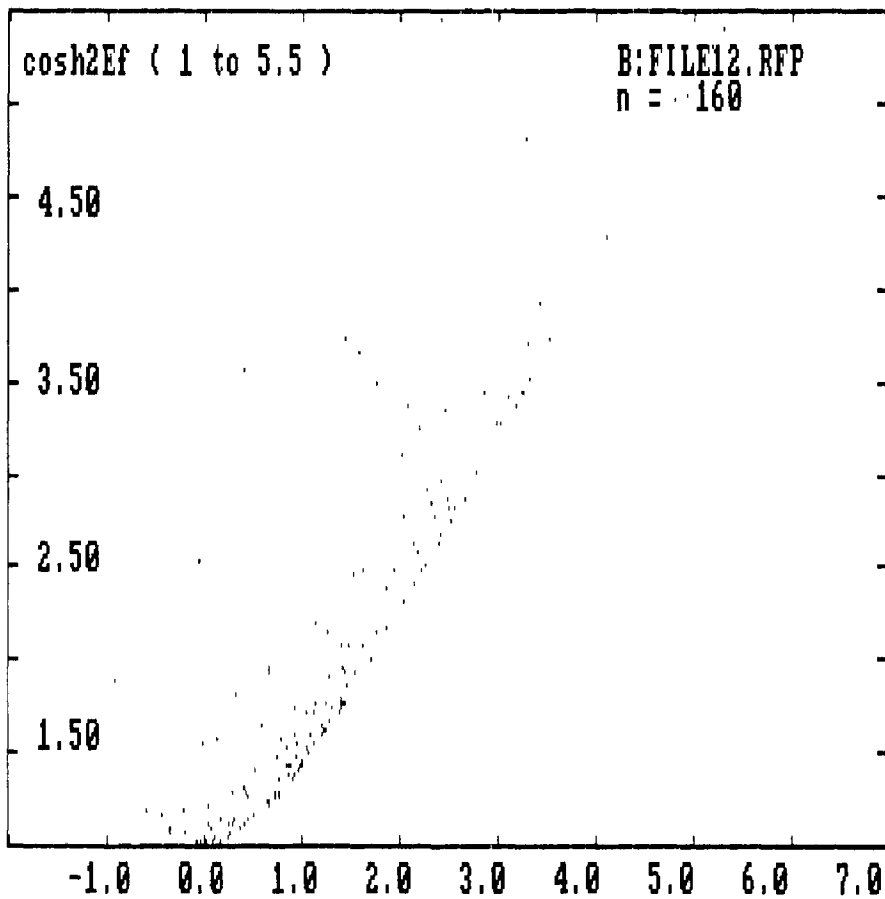
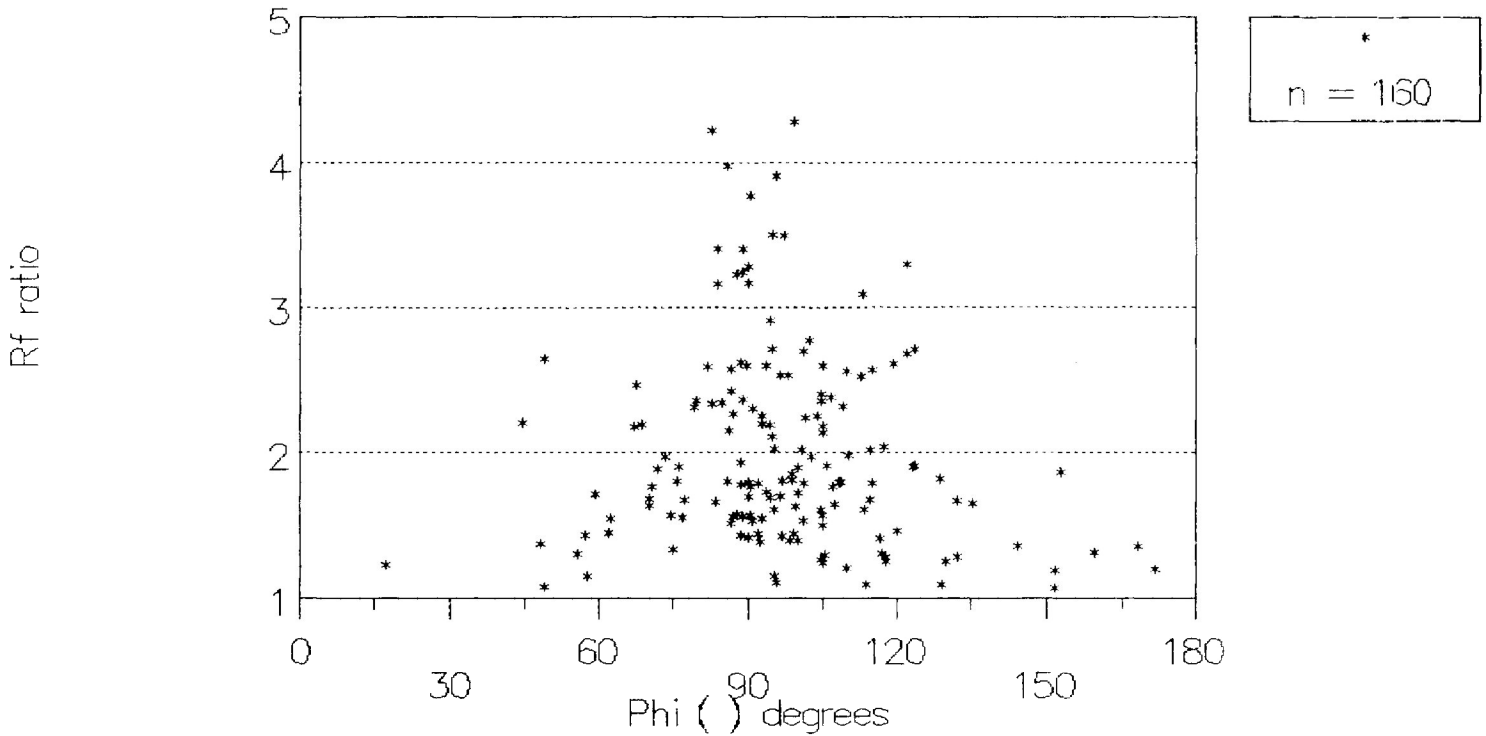


slope = 0.8381
intercept = 9.447E-01
RS10.05V

B:FILE15.RFP
Slope of line = .8380585
y - intercept = .9447286
Supposed initial 'unique' ratio = 1.77349
Strain ratio by linearization method = 1.835483

Rf / Phi STRAIN ANALYSIS

Sample CH10.1



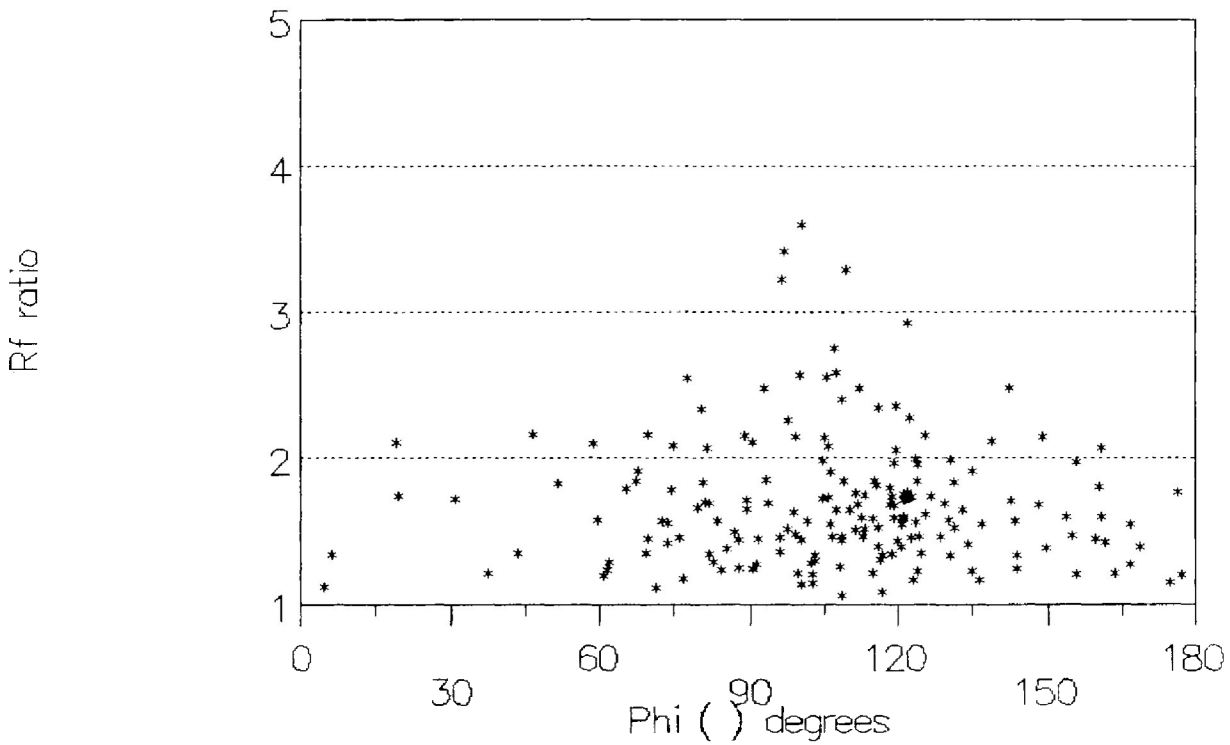
B:FILE12.RFP
n = 160

slope= 0.8588
intercept= 9.143E-01
CH10.1

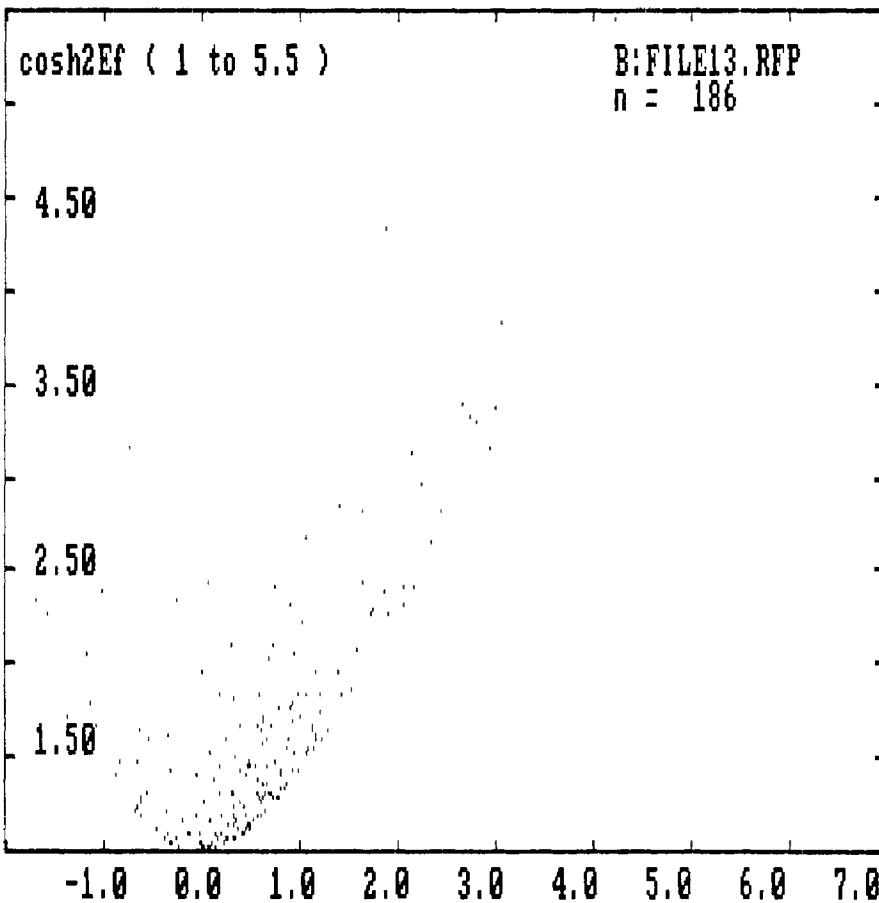
B:FILE12.RFP
Slope of line = .8587664
y - intercept = .9142679
Supposed initial 'unique' ratio = 1.806174
Strain ratio by linearization method = 1.904679

Rf / Phi STRAIN ANALYSIS

Sample CV10.1



*
n = 186



slope= 0.5986
intercept= 1.316E+00
CV10.1

B:FILE13.RFP
Slope of line = .598648
Y - intercept = 1.316142
Supposed initial 'unique' ratio = 1.716576
Strain ratio by linearization method = 1.416853

sinh2Ef.cos2phi
(-2 to 7)